

“Mg” Bone

Ink extrusion-based additive manufacturing of Mg implants

Dong, J.

DOI

[10.4233/uuid:800cbeba-7ad9-440f-acf2-68cdd5bbbb4b](https://doi.org/10.4233/uuid:800cbeba-7ad9-440f-acf2-68cdd5bbbb4b)

Publication date

2023

Document Version

Final published version

Citation (APA)

Dong, J. (2023). *“Mg” Bone: Ink extrusion-based additive manufacturing of Mg implants*. [Dissertation (TU Delft), Delft University of Technology]. <https://doi.org/10.4233/uuid:800cbeba-7ad9-440f-acf2-68cdd5bbbb4b>

Important note

To cite this publication, please use the final published version (if applicable). Please check the document version above.

Copyright

Other than for strictly personal use, it is not permitted to download, forward or distribute the text or part of it, without the consent of the author(s) and/or copyright holder(s), unless the work is under an open content license such as Creative Commons.

Takedown policy

Please contact us and provide details if you believe this document breaches copyrights. We will remove access to the work immediately and investigate your claim.

“Mg” Bone

Ink extrusion-based additive manufacturing
of Mg implants

“Mg” Bone

Ink extrusion-based additive manufacturing of Mg implants

Dissertation

for the purpose of obtaining the degree of doctor

at Delft University of Technology

by the authority of the Rector Magnificus, prof. dr. ir. T.H.J.J. van der Hagen

chair of the Board for Doctorates

to be defended publicly on

Wednesday 22 March 2023 at 10:00 o'clock

by

Jiahui DONG

Master of Science in Materials Science and Engineering,
Institute of Metal Research, Chinese Academy of Sciences, Shenyang, China
born in Shenyang, China

This dissertation has been approved by the
promotors: Prof. dr. A. A. Zadpoor and Dr. J. Zhou

Composition of the doctoral committee:

Rector Magnificus	chairperson
Prof.dr. A.A. Zadpoor	Delft University of Technology, promotor
Dr. J. Zhou	Delft University of Technology, promotor

Independent members:

Prof.dr.ir. H.H. Weinans	Delft University of Technology/Utrecht University Medical Center
Prof.dr. R. Willumeit-Römer	Helmholtz-Zentrum Hereon GmbH/ Christian-Albrechts-Universität zu Kiel
Prof.dr.ir. L.A.I. Kestens	Ghent University/Delft University of Technology
Prof.dr.ir. N.J.J. Verdonschot	Radboud University Medical Center

Other member:

Dr. G.A. Kraan	Reinier de Graaf Hospital
----------------	---------------------------

This project was financially sponsored by China Scholarship Council from
September 2018 to September 2022.



Keywords: additive manufacturing, scaffold, biodegradation, mechanical
property, biocompatibility, magnesium

Copyright © 2023 by Jiahui Dong

ISBN 978-94-6384-426-0

An electronic version of this dissertation is available at <https://repository.tudelft.nl/>.

Summary

The treatment of large bone defect remains challenging in clinics. All the clinically available bone grafts have their own limitations and are not ideal for the treatment. Therefore, developing a new generation of suitable bone substitutes is urgently needed. In the recent years, porous magnesium (Mg) has been extensively studied for orthopedic applications owing to its biodegradability, favorable mechanical properties, and osteopromotive ability. The recent advances in additive manufacturing (AM) provide unprecedented opportunities to design and fabricate porous Mg scaffolds with interconnected porous structures that are favorable for the adhesion and proliferation of bone cells. However, powder bed fusion AM, which is the most commonly used AM technique for fabricating metal structures, has encountered many difficulties in manufacturing Mg due to safety concerns, excessive oxidation, and undesirable compositional variation due to the low boiling temperature of Mg. To alleviate these difficulties, alternative AM techniques that can create highly porous structures at room temperature are highly sought after. The aim of this research was to develop a room-temperature AM technique for manufacturing porous Mg and to characterize the fabricated Mg-based scaffolds in different aspects relevant to their potential applications as bone implants.

To this end, we developed a room-temperature ink extrusion-based AM technique to fabricate geometrically ordered porous Mg scaffolds and optimized the process conditions for the successful fabrication of geometrically ordered porous Mg as described in Chapter 2. The whole procedure was composed of three steps: (i) the preparation of a Mg powder loaded ink with the desired rheological properties, (ii) the 3D printing of porous Mg scaffolds with the extrusion-based AM technique, and (iii) debinding and sintering to remove the binder in the ink followed by a liquid-phase sintering strategy to get the Mg powder particles bonded. The prepared inks, consisting of a judiciously formulated binder and 54, 58, and 62 vol% Mg powder particles, were found to possess viscoelastic properties that enable successful printing of the specimens as evidenced from shear stress sweep, frequency sweep, and creep-recovery tests. Then, the printability of the inks with different percentages of Mg powder loading were examined using the ink extrusion-based AM approach and the applicable printability windows were defined. The ink with 58 vol% Mg powder loading was finally chosen to print the scaffolds to study their debinding and sintering behavior. The choice of this ink was due to its wide printability window, high printing efficacy, and relatively high percentage of powder loading that is beneficial for obtaining high densification of the scaffold struts. A rather low carbon residue value (0.056%) and high densification of the

fabricated Mg scaffolds indicated the possibilities of debinding and sintering in one single step, which greatly minimized the operational complexity. After the optimization of the sintering conditions, a liquid-phase sintering strategy was successfully implemented for sintering the Mg scaffolds. As a result, Mg scaffolds with high porosity (78.4%), high fidelity, and a hierarchical pore structure could be obtained. This study demonstrated the feasibility of using ink extrusion-based AM techniques to produce highly porous Mg.

Based on the developed AM strategy, we made the first attempt to investigate the properties of pure Mg scaffolds, as detailed in Chapter 3. Ink extrusion-based AM could successfully manufacture pure Mg scaffolds with a macro-porosity of 55% and a strut density of 92%. However, such pure Mg scaffolds exhibited a relatively high degradation rate partly due to the highly interconnected porous structure, which could cause premature implant failure and the generation of a large amount of hydrogen gas that could trigger inflammatory responses. As a mitigation strategy, surface modification of the fabricated pure Mg was performed to decrease the degradation rate. Multifunctional MgF_2 and CaP coatings were applied to the fabricated pure Mg scaffolds, and comprehensive studies were performed regarding the microstructure, *in vitro* degradation behavior, electrochemical performance, time-dependent mechanical properties, and cytotoxicity of the fabricated specimens particularly in comparison with the uncoated Mg scaffolds. The multi-coatings not only covered all the struts through macropores, but also infiltrated into the struts through micropores, thereby decreasing the total porosity of the structures and providing enough protection from the invasion of the simulated body fluid. The MgF_2 -CaP coatings remarkably improved the corrosion resistance of the Mg scaffolds. The direct culture of the MC3T3-E1 preosteoblasts on the coated Mg scaffolds confirmed their good biocompatibility.

To further improve the corrosion resistance of the Mg scaffolds, in addition to coating, alloying Mg with a biocompatible element. The resulting Mg-Zn binary alloy geometrically ordered scaffolds with fully interconnected porous structures are presented in Chapter 4. The effects of Zn addition to Mg on the properties of the fabricated scaffolds were studied, with the pure Mg scaffolds as the reference group. The Mg-Zn alloy scaffolds (porosity of 50.3%) had a high densification rate of 93.1%. As compared to the pure Mg scaffolds, the starting *in vitro* biodegradation rate (2.3 ± 0.9 mm/y) of the Mg-Zn scaffolds was decreased by 81%. The biodegradation rate of the Mg-Zn scaffolds was reduced to 0.7 ± 0.1 mm/y over one month of immersion, because corrosion in the simulated body fluid was hindered by the compact and dense biodegradation products formed on the surface of the struts and in the space between the struts. The yield strength and Young's modulus (14.5 ± 3.0 MPa and 448.8 ± 42.4 MPa, respectively) of the Mg-Zn scaffolds were about three times as high as those of pure Mg (4.7 ± 0.7 MPa and 184.4 ± 37.3 MPa, respectively) and remained within the range of

those of the trabecular bone throughout the biodegradation tests. When directly cultured with preosteoblasts, the fabricated Mg-Zn scaffolds were moderately cytocompatible.

To improve the cytocompatibility of the extrusion-based AM scaffolds, we added bioactive ceramic particles (β -TCP) to the Mg-Zn powder (Chapter 5). The ink formulations were optimized to balance the homogeneity of the bioceramic particles with appropriate viscoelastic properties and, thus, printability. We found that the dispersion of β -TCP in the and the resulting scaffolds were the most uniform in 5 wt% β -TCP-containing inks. With the optimally formulated inks, Mg-Zn/x β -TCP (x=5, 10 and 15 wt%) composite scaffolds with a porosity in the range of 47.6 to 55.2% were successfully fabricated using the extrusion-based AM technique. We found that the reaction between β -TCP and the Mg-Zn matrix during sintering helped enhance their interfacial bonding, which greatly contributed to the properties of the composite scaffolds. The densities of the struts containing 5 wt% and 10 wt% β -TCP were higher than 99%, reaching the level usually only achieved through powder bed fusion AM. The *in vitro* biodegradation rate of the Mg-Zn/5 wt% β -TCP scaffolds decreased to 0.5 mm/y, which falls into the range (*i.e.*, 0.2-0.5 mm/y) desired for bone substitution. As compared to the monolithic Mg-Zn scaffolds, the scaffolds containing 5% and 10% β -TCP exhibited improved biocompatibility and ALP activity when cultured with preosteoblast, which confirms their osteogenic ability.

In Chapter 6, we summarize the main findings of the research. Additionally, general discussion and recommendations for future research are provided. We demonstrated the fact that extrusion-based 3D printing technique can be successfully used to fabricate biodegradable porous Mg-based implants with a hierarchical porous structure and the desired mechanical, degradable, and biological properties. Further research to assess osteogenesis *in vitro* and *in vivo* needs to be performed to confirm the potential of the developed biomaterials to promote bone formation. Overall, the work presented in this thesis is the first step towards the development of extrusion-based AM for the fabrication of biodegradable Mg-based materials. We hope that our work will provide inspiration for further exploration of this non-laser related AM technique for fabricating biodegradable Mg-based implants for bone repair and substitution.

Samenvatting

Het behandelen van grote botdefecten is tot op heden een uitdaging in klinieken. Alle klinisch beschikbare bottransplantaten hebben hun eigen beperkingen en zijn niet ideaal voor de behandeling. Daarom is de ontwikkeling van een nieuwe generatie geschikte botvervangers dringend nodig. In de afgelopen jaren is poreus magnesium (Mg) uitgebreid bestudeerd voor orthopedische toepassingen vanwege zijn biologische afbreekbaarheid, gunstige mechanische eigenschappen en osteopromotorisch vermogen. De recente ontwikkelingen in 3D printen of additieve fabricage (AF) bieden ongekende mogelijkheden om poreuze Mg-matrixen te ontwerpen en te fabriceren, die bestaan uit onderling verbonden poreuze structuren ter bevordering van de hechting en proliferatie van botcellen. Echter, de meest gebruikte AF-techniek voor het vervaardigen van metaalstructuren, poederbedfusie AF, veroorzaakt veel problemen bij het gebruik van Mg vanwege veiligheidsproblemen, overmatige oxidatie en ongewenste variaties in samenstelling vanwege de lage kooktemperatuur van Mg. Om deze moeilijkheden te verhelpen zijn alternatieve AF-technieken nodig, die in staat zijn om zeer poreuze structuren te creëren op kamertemperatuur. Het doel van dit promotieonderzoek was om een AF-techniek op kamertemperatuur te ontwikkelen voor het vervaardigen van poreus Mg en om verschillende aspecten van de gefabriceerde Mg-matrix te karakteriseren, die relevant zijn voor hun potentiële toepassingen als botimplantaten.

Hiertoe hebben we een AF-techniek op basis van inkt-extrusie op kamertemperatuur ontwikkeld om poreuze Mg-matrixen met regelmatige geometrie te fabriceren en de procesomstandigheden voor succesvolle fabricage geoptimaliseerd, zoals beschreven in hoofdstuk 2. De hele procedure bestond uit drie stappen: (i) bereiding van een inkt met Mg-poeder met de gewenste reologische eigenschappen, (ii) 3D-printen van poreuze Mg-matrixen met de inkt-extrusie techniek, en (iii) ontbinden om het bindmiddel in de inkt te verwijderen en vloeibare fase sinteren om vervolgens de Mg-poederdeeltjes te verbinden. De bereide inkten, bestaande uit een zorgvuldig geformuleerd bindmiddel met 54, 58 en 62 vol.% Mg-poederdeeltjes, bleken visco-elastische eigenschappen te hebben waardoor het succesvol printen mogelijk was, zoals bleek uit tests voor de schuifspanning, frequentiezwaaai en kruipherstel. Vervolgens werd de printbaarheid van inkten met verschillende percentages Mg-poeder onderzocht met behulp van de inkt-extrusie AF-techniek en werden de grenzen waarbinnen printen mogelijk was gedefinieerd. De inkt met 58 vol.% Mg-poeder werd uiteindelijk gekozen om de matrix

te printen om hun ontbind- en sintergedrag te onderzoeken, vanwege de ruime printbaarheidsgrenzen en het relatief hoge percentage van poeder dat gunstig is voor het verkrijgen van een hoge verdichting van de matrix structuur. Ontbinden en sinteren konden in één enkele stap gecombineerd worden, door een verwaarloosbaar lage koolstofresiduwaarde (0,056%) en een hoge verdichting van de gefabriceerde Mg-matrix, wat de operationele complexiteit aanzienlijk minimaliseert. Na het optimaliseren van de sintercondities werd een succesvolle vloeibare fase sinterstrategie geïmplementeerd voor het sinteren van Mg-matrixen. Als resultaat konden Mg-matrixen met hoge porositeit (78,4%), hoge betrouwbaarheid en een hiërarchische poriestructuur worden geproduceerd. Dit werk toonde de haalbaarheid aan van het gebruik van de op inkt-extrusie gebaseerde AF-techniek om zeer poreus Mg te produceren.

Op basis van de ontwikkelde AF-strategie hebben we een eerste poging gedaan om de structurele kenmerken en eigenschappen van zuivere Mg-matrixen te onderzoeken, zoals beschreven in Hoofdstuk 3. De zuivere Mg-matrixen konden met succes vervaardigd worden met behulp van inkt-extrusie AF, met een macroporositeit van 55% en een structuurdichtheid van 92%. Dergelijke zuivere Mg-matrixen vertoonden echter een relatief hoge degradatiegraad, deels vanwege de sterk onderling verbonden poreuze structuur, die voortijdig falen van het implantaat zou kunnen veroorzaken, en de vorming van een grote hoeveelheid waterstofgas, die ontstekingsreacties zou kunnen veroorzaken. Als mitigatiestrategie werd oppervlaktemodificatie van de gefabriceerde zuivere Mg-matrixen ontwikkeld om de degradatiegraad te vertragen. Multifunctionele MgF₂- en CaP-coatings werden aangebracht en uitgebreide studies naar microstructuur, in vitro degradatiegedrag, elektrochemische prestaties, tijdsafhankelijke mechanische eigenschappen en cytotoxiciteit werden uitgevoerd, ter vergelijking met de ongecoate Mg-matrixen. De multifunctionele coatings bedekten niet alleen de gehele structuur via macroporiën, maar infiltreerden ook in de stutten via microporiën, wat resulteerde in een afname van de totale porositeit en bescherming bood tegen het binnendringen van gesimuleerd lichaamsvocht. De MgF₂-CaP-coatings verbeterden de corrosieweerstand van de pure Mg-matrixen opmerkelijk. Directe kweek van MC3T3-E1 preosteoblasten op de gecoate Mg-matrixen bevestigde hun goede biocompatibiliteit.

Om de corrosieweerstand van de Mg-matrixen te verbeteren, werd naast het coaten ook het legeren van Mg met een biocompatibel element als een andere strategie geprobeerd. Matrixen van een Mg-Zn binaire legering met een geometrisch regelmatige en volledig onderling verbonden poreuze structuur werden gefabriceerd, zoals gepresenteerd in Hoofdstuk 4. Het effect van het toevoegen van Zn aan Mg op de eigenschappen van de gefabriceerde matrixen werd bestudeerd, waarbij de zuivere Mg matrixen functioneerden als referentiegroep. De matrixen van de Mg-Zn-legering (porositeit van 50,3%) hadden een hoge verdichtingssnelheid van 93,1%. De initiële in vitro

biodegradatie graad ($2,3 \pm 0,9$ mm/j) van de Mg-Zn-matrixen was na één dag onderdompeling in gemodificeerde, gesimuleerde lichaamsvloeistof met 81% verminderd, vergeleken met de zuivere Mg-matrixen. De biodegradatie graad van de Mg-Zn-matrixen werd teruggebracht tot $0,7 \pm 0,1$ mm/j gedurende een maand onderdompeling, omdat de corrosie in gesimuleerde lichaamsvloeistof werd gehinderd door de vorming van compacte en dichte biodegradatie producten op het oppervlak van de structuur en in de ruimte ertussen. De vloeigrens en Young's modulus (respectievelijk $14,5 \pm 3,0$ MPa en $448,8 \pm 42,4$ MPa) van de Mg-Zn-matrixen waren ongeveer drie keer zo hoog als die van de zuivere Mg-tegenhangers (respectievelijk $4,7 \pm 0,7$ MPa en $184,4 \pm 37,3$ MPa) en bleven binnen het bereik van die van trabeculair bot gedurende de 28-daagse in vitro biodegradatie testen. Wanneer ze direct werden gekweekt met preosteoblasten vertoonden de gefabriceerde Mg-Zn-matrixen een matige cytocompatibiliteit.

Om de cytocompatibiliteit van de met extrusie gefabriceerde AF-matrixen te verbeteren, hebben we bioactieve keramische deeltjes (β -tricalciumfosfaat, d.w.z. β -TCP) aan het Mg-Zn-poeder toegevoegd, zoals gepresenteerd in Hoofdstuk 5. De formuleringen van de inkt werden geoptimaliseerd om een balans te vinden tussen de homogeniteit van biokeramische deeltjes in de inkt en de visco-elastische eigenschappen, wat van cruciaal belang is voor de printbaarheid. We ontdekten dat de dispersie van β -TCP-deeltjes in de 5 gew.% β -TCP-bevattende inkten en de resulterende matrix het meest uniform was. Met de optimaal geformuleerde inkten werden Mg-Zn/x β -TCP (x=5, 10 en 15 gew.%) composiet matrix met een porositeitsbereik van 47,6 tot 55,2% met succes vervaardigd met behulp van de extrusie AF-techniek. We ontdekten dat de reactie tussen β -TCP en de Mg-Zn-matrix tijdens het sinteren hun binding op het grensvlak hielp te verbeteren, wat in hoge mate bijdroeg aan de eigenschappen van de composiet-matrix. De dichtheden van de stutten die 5 en 10 gew.% β -TCP bevatten, waren hoger dan 99% en bereikten het niveau dat gewoonlijk alleen wordt bereikt door poederbedfusie AF. De in vitro biodegradatie graad van de Mg-Zn/5 gew.% β -TCP-matrix daalde tot 0,5 mm/j, wat binnen het bereik valt (d.w.z. 0,2 - 0,5 mm/j) dat gewenst is voor botssubstitutie. In vergelijking met de monolithische Mg-Zn-matrixen vertoonden de matrixen die 5% en 10% β -TCP bevatten verbeterde biocompatibiliteit en ALP-activiteit die op osteogeen vermogen duiden, wanneer ze werden gekweekt met preosteoblasten.

In hoofdstuk 6 vatten we de belangrijkste bevindingen van het onderzoek samen. Daarnaast worden algemene discussies en aanbevelingen voor toekomstig onderzoek gegeven. De inkt-extrusie 3D-printtechniek kan met succes worden gebruikt om biologisch afbreekbare implantaten te fabriceren die op Mg gebaseerd zijn, met een hiërarchische poreuze structuur en de gewenste mechanische, afbreekbare en

biologische eigenschappen. Verder onderzoek om osteogenese in vitro en in vivo te beoordelen moet worden uitgevoerd, om de potentie van het bevorderen van botvorming te bevestigen. Over het algemeen is het werk dat in dit proefschrift wordt gepresenteerd de eerste stap in de richting van de ontwikkeling van de inkt-extrusie AF-techniek die werd gebruikt voor de fabricage van biologisch afbreekbare Mg-materialen. We hopen dat ons werk inspiratie zal bieden voor verdere verkenning van deze AF-techniek die niet op lasers gebaseerd is, om biologisch afbreekbare Mg-implantaten te fabriceren voor botherstel en -substitutie.

CONTENTS

1 Introduction

1.1 Background	2
1.2 Biodegradable Mg metallic biomaterials	2
1.3 Additive manufacturing of Mg scaffolds	3
1.4 Ink extrusion-based 3D printing	4
1.5 Thesis Aim	4
1.6 Thesis outline	5
References	8

2 Ink extrusion-based additive manufacturing of Mg-based scaffolds

2.1 Introduction	14
2.2 Material and methods	14
2.3 Results	20
2.4 Discussion	32
2.5 Conclusions	42
References	44
Supplementary material	47

3 Ink extrusion-based additive manufacturing of pure Mg scaffolds

3.1 Introduction	50
3.2 Material and methods	51
3.3 Results	59
3.4 Discussion	79
3.5 Conclusions	86
References	88
Supplementary material	93

4 Ink extrusion-based additive manufacturing of Mg-Zn scaffolds

4.1 Introduction	98
4.2 Material and methods	98
4.3 Results	105
4.4 Discussion	118
4.5 Conclusions	125
References	127

Supplementary information	131
5 Ink extrusion-based additive manufacturing of Mg-Zn/bioceramic scaffolds	
5.1 Introduction	134
5.2 Material and methods	136
5.3 Results	144
5.4 Discussion	159
5.5 Conclusions	167
References	169
Supplementary information	175
6 General conclusions, discussion, and recommendations	
6.1 General conclusions	190
6.2 General discussion.	191
6.3 Recommendations.	198
References	202
Curriculum Vitae	207
List of Publications	208
Acknowledgements	210

1

Introduction

1.1. Background

Bone is well-known for its self-healing capability [1]. However, when high-energy trauma, disease, tumor resection, or osteomyelitis occurs, resulting in large bony defects, the large bony defect could not heal without intervention and progresses to non-union [2]. To address this clinical issue, bone grafting is necessary for bone regeneration. Over two million bone grafting procedures are performed annually worldwide [3] and the market size of bone grafts is increasing and expected to grow 4.3% annually by 2028 [4]. Among all the clinically available bone grafts, autografts that are harvested from the patients' own bodies are still considered the gold standard to treat bony defects. Allografts harvested from a deceased donor and xenografts obtained from an animal are alternative treatment options [5]. However, these strategies have some shortcomings and limitations, such as a lack of autograft source, donor site complications, and disease transmission. [6] More importantly, given our increasingly aging societies and prevalent obesity, the quantities of available natural bone grafts are far from meeting the clinical demands [7]. The above-mentioned challenges have triggered the blossom of synthetic bone substitutes. Products containing hydroxyapatite (HA), tricalcium phosphate (TCP), dicalcium phosphate, calcium sulphate, or bioactive glasses are currently available for use in orthopedic surgery. However, these products usually have their own clinical limitations, such as long time required for complete integration and new bone replacement as well as insufficient biomechanical support [8]. Therefore, developing a new generation of suitable bone substitutes is highly desired.

An ideal bone substitute or implant should: (i) be able to degrade *in vivo* within an appropriate period of time until the newly grown bone tissue has replaced the substitute's function [9], (ii) exhibit osteogenic, osteoconductive, and osteoinductive properties for new bone formation [10], (iii) be biomechanically stable and match the mechanical properties of the host bone to avoid stress shielding [9, 10], prior to losing its mechanical functionality, and (iv) present a highly porous structure with fully interconnected pore networks to allow for bony ingrowth and facilitate the transport of nutrients and metabolic waste [11].

1.2. Biodegradable Mg metallic biomaterials

Metallic biomaterials with outstanding mechanical properties are considered some of the most suitable candidates for load-bearing implants. Some traditional metals, such as stainless steel, Co-, and Ti-based alloys, have been successfully used for such applications in orthopedic and trauma surgeries [12]. However, non-biodegradable implants often require a second operation for removal after their services in human bodies are no longer required, which exposes patients to further risks and brings additional pain to these

patients. In addition, the surface conditions of these metallic implant materials, whilst biocompatible, are bioinert, being not active in the cellular process for bone healing [13]. Therefore, biodegradable metals are becoming the rising stars as a new generation of metallic biomaterials for orthopedic applications.

In recent years, magnesium (Mg)-based biodegradable metals have been extensively investigated for potential use as bone-substituting biomaterials. A few medical products made of Mg alloys have been already launched in the market [14]. In general, Mg possesses the following advantages over other metals. First, Mg ions play an important functional role in physiological systems [15]. Second, Mg ions released from Mg implants stimulate bone formation [16]. Third, Mg possesses appropriate mechanical properties that are close to those of the natural bone [17]. In addition, through alloying or adding other types of components to form composites, Mg can be flexibly tuned to possess the mechanical, degradation, and biological performances needed for bone defect regeneration [18]. Thus, Mg-based materials can satisfy the first three requirements mentioned above for biodegradable implants aimed to regenerate the bone. Incorporating porosity into Mg-based implants is of critical importance to meet the last requirement of an ideal bone substitute for orthopedic and traumatological applications.

1.3. Additive manufacturing of Mg scaffolds

Several techniques to fabricate porous Mg scaffolds have been already developed, including melt foaming [19-21], preform infiltration [22-26], pattern casting [27, 28], and powder metallurgy with the space holder technology [29-32]. However, these traditional fabrication techniques permit neither complex exterior 3D architectures nor fully interconnected interior pore networks. Recent advances in additive manufacturing (AM) offer great potential to achieve a much greater degree of design and manufacturing flexibility and efficiency over the traditional techniques, making it possible to design and fabricate fully interconnected porous structures with precisely controlled topological parameters [33, 34].

Recently, employing AM techniques to fabricate Mg-based materials has been started in a small number of university research groups [35, 36]. Selective laser melting (SLM) in the category of powder bed fusion, according to the ASTM classification, is a commonly chosen AM technique for porous Mg fabrication [36-45] as compared to other AM techniques [46, 47]. The success in fabricating porous Mg alloy scaffolds with SLM has, however, been relatively limited [42-45]. The primary challenge encountered is associated with the safety in operation, considering the high flammability of Mg powder with a large collective surface area. The other difficulties encountered concern the undesirable compositional variation in the final parts are due to the relatively low melting and boiling temperatures of Mg and to the rapidly increased vapor pressure of Mg at its

boiling temperature [38, 48] and excessive oxidation throughout the whole chain of scaffold fabrication due to the high affinity of fine Mg powder particles to oxygen [38]. Furthermore, due to the high reflectivity of Mg powder, high laser power is required, which makes the SLM equipment costly [38], increases the chance of Mg evaporation, and creates significant thermal gradients during SLM, leading to metallurgical defects and residual stresses [49]. Recently, a few attempts have been made to develop binder jetting [50-53] and fused filament fabrication (FFF) techniques [54], followed by a sintering step, as alternatives to SLM. However, utilizing these techniques for the fabrication of geometrically-ordered porous Mg scaffolds has not yet been reported.

1.4. Ink extrusion-based 3D printing

Ink extrusion-based 3D printing is another interesting alternative to SLM in which an ink containing metallic or any other powder particles together with a binder system (composed of polymer, volatile solvent, and/or additive) is extruded through a nozzle and printed into a designed structure. The 3D printed structure is then subjected to debinding and sintering. The extrusion-based 3D printing technique has been demonstrated to be feasible in the case of AM steel [55, 56], iron [57, 58], titanium-based [59], and nickel-based [58, 60, 61] micro-trusses.

Ink extrusion-based 3D printing has a great potential to overcome the material, technical, and structural limitations of the other AM techniques currently applied to fabricate porous Mg scaffolds, as mentioned in subsection 1.3. It offers multiple advantages, including (i) 3D printing at ambient conditions, (ii) easy adjustment of the components of the ink, (iii) low equipment investment, and (iv) the potential to fabricate complex structures with hierarchical pores and desired alloy compositions. In addition, while no natural support is present for overhung parts in this 3D printing process, a precise match of the evaporation rates of solvent and printing parameters allows for printing stacked lattice structures with overhang parts and enables the fabrication of helically freeform structures without any synthetic support [62].

1.5. Thesis Aim

Up to now, we have discussed the importance of developing a novel AM technique to fabricate porous Mg-based scaffolds with desired properties for potential use in orthopedics. As previously mentioned, ink extrusion-based 3D printing techniques eliminate the need for high-power lasers. There are, therefore, no concerns regarding the issues encountered in powder bed fusion AM of porous Mg. The application of ink extrusion-based 3D printing for manufacturing geometrically-ordered porous Mg can, therefore, be considered be a major breakthrough in the development of biodegradable Mg-based materials as ideal bone substitutes. To the best of our knowledge, there have

been no reports on the successful fabrication of ink extrusion-based 3D printed Mg scaffolds, let alone the related characterization.

The aim of this dissertation was to demonstrate the feasibility of fabricating Mg-based scaffolds using the ink extrusion-based 3D printing technique and to tune their properties to meet the requirements for ideal bone substitutes through base material modification or surface modification. Toward this aim, we identified the following research questions that will be addressed in this thesis:

“Can we use ink extrusion-based 3D printing techniques to manufacture biodegradable Mg-based scaffolds with geometrically-ordered and fully interconnected porous structure successfully?”

“Can we fabricate porous Mg-based scaffolds with the desired properties for potential use as bone substitutes?”

1.6. Thesis Outline

The systematic, stepwise research carried out to answer the various aspects of both abovementioned research questions is presented in Chapters 2 – 5. Each subsequent chapter follows up on the work presented in the previous chapters and tries to resolve the issues identified in the preceding research or improve certain properties desired for the targeted applications.

In Chapter 2, we demonstrate that ink extrusion-based 3D printing techniques presents unprecedented possibilities to produce Mg scaffolds. 3D printing of pure Mg scaffolds was taken as the first attempt to explore the viable fabrication methods and identify the optimal processing conditions. Mg scaffolds with high fidelity and interconnected hierarchical pores were successfully fabricated. With the first research question answered, we were ready to evaluate the performance of the fabricated pure Mg scaffolds.

Chapter 3 presents a comprehensive study on the microstructure, biodegradation behavior, mechanical properties and biocompatibility of the fabricated pure Mg scaffolds. Pure Mg with a highly porous structure was found to degrade rapidly in simulated physiological environments and exhibit limited biocompatibility. Therefore, surface modification aiming at inducing multiple types of functions is applied to the scaffolds. Considering the geometric complexities of the surfaces in the 3D structure, the quality of the coatings on and inside the scaffolds and the effects of the coatings on the properties of the coated pure Mg scaffolds are investigated.

While surface modifications could, indeed, significantly improve the corrosion resistance of pure Mg scaffolds, the Mg substrate exposed after the coatings are degraded or penetrated through dominates the overall biodegradation process. To address this challenge, the corrosion resistance of the porous Mg substrate must be improved.

Therefore, in the follow-up research presented in Chapter 4, a Mg alloy powder (Mg-Zn) is chosen as the starting material and Mg-Zn binary alloy scaffolds with a geometrically-ordered and fully interconnected porous structure are fabricated using the same printing technique. The effects of the addition of the alloying element (Zn) on the microstructure, degradation behavior, mechanical properties, and biocompatibility of the Mg scaffolds are studied.

While alloying could, indeed, enhance the corrosion resistance of the porous Mg scaffolds, the fabricated Mg alloy scaffolds exhibited moderate cytotoxicity due to the excessive release of Zn ions from the scaffolds. The biocompatibility would, therefore, need to be enhanced by adding bioactive components or/and by decreasing the degradation rate of the scaffolds.

Then, further research, presented in Chapter 5, was carried out to add a bioactive ceramic (β -TCP) to the Mg-Zn scaffolds and the Mg-Zn/ β -TCP nanocomposite scaffolds were additively manufactured using the same technique. The homogeneous dispersion of β -TCP micro-particles and the printability of the ink were optimized and balanced. The effects of the addition of β -TCP micro-particle on the microstructure and properties of the Mg-Zn scaffolds were comprehensively studied.

Finally, Chapter 6 concludes this thesis by providing a brief summary and discussion of our findings. A reflection upon the whole project to reach the overall aim presented in Chapter 1 is provided. In addition, we present an outlook on future research.

The structure of the research presented in this thesis is visualized below:

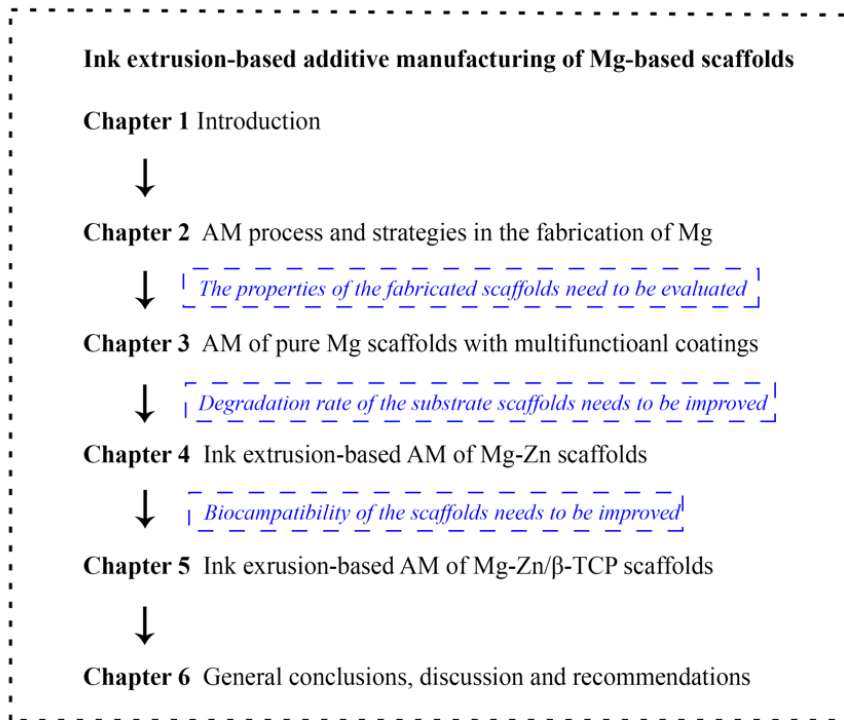


Figure 1.1 The structure of the dissertation.

References

- [1] S. M. Ahmad Oryan, And Amin Bigham-Sadegh, Bone injury and fracture healing biology, *Biomed. Environ. Sci.* 28 (2015) 57-71.
- [2] L. Claes, K. Eckert-Hubner, P. Augat, The fracture gap size influences the local vascularization and tissue differentiation in callus healing, *Langenbecks Arch Surg.* 388 (2003) 316-322.
- [3] L. Zhang, G. Yang, B. N. Johnson, X. Jia, Three-dimensional (3D) printed scaffold and material selection for bone repair, *Acta Biomater.* 84 (2019) 16-33.
- [4] <https://www.researchandmarkets.com/reports/5394240/bone-grafts-and-substitutes-market-by-product-and>
- [5] A. Kolk, J. Handschel, W. Drescher, D. Rothamel, F. Kloss, M. Blessmann, M. Heiland, K. D. Wolff, R. Smeets, Current trends and future perspectives of bone substitute materials - from space holders to innovative biomaterials, *J Craniomaxillofac Surg.* 40 (2012) 706-718.
- [6] R. Bonithon, A. P. Kao, M. P. Fernandez, J. N. Dunlop, G. W. Blunn, F. Witte, G. Tozzi, Multi-scale mechanical and morphological characterisation of sintered porous magnesium-based scaffolds for bone regeneration in critical-sized defects, *Acta Biomater.* 127 (2021) 338-352.
- [7] W. Wang, K. W. K. Yeung, Bone grafts and biomaterials substitutes for bone defect repair: A review, *Bioact Mater.* 2 (2017) 224-247.
- [8] G. M. Calori, E. Mazza, M. Colombo, C. Ripamonti, The use of bone-graft substitutes in large bone defects: any specific needs?, *Injury.* 42 Suppl 2 (2011) S56-63.
- [9] S. Bose, M. Roy, A. Bandyopadhyay, Recent advances in bone tissue engineering scaffolds, *Trends Biotechnol.* 30 (2012) 546-554.
- [10] P. Janicki, G. Schmidmaier, What should be the characteristics of the ideal bone graft substitute? Combining scaffolds with growth factors and/or stem cells, *Injury.* 42 Suppl 2 (2011) S77-81.
- [11] A. A. Zadpoor, Bone tissue regeneration: the role of scaffold geometry, *Biomater. Sci.* 3 (2015) 231-245.
- [12] Q. Chen, G. A. Thouas, Metallic implant biomaterials, *Mater. Sci. Eng. R: Rep.* 87 (2015) 1-57.
- [13] M. Song, R. Zeng, Y. Ding, R. W. Li, M. Easton, I. Cole, N. Birbilis, X. Chen, Recent advances in biodegradation controls over Mg alloys for bone fracture management: A review, *J. Mater. Sci. Technol.* 35 (2019) 535-544.
- [14] D. Zhao, F. Witte, F. Lu, J. Wang, J. Li, L. Qin, Current status on clinical applications of magnesium-based orthopaedic implants: A review from clinical translational perspective, *Biomaterials.* 112 (2017) 287-302.
- [15] C. Palacios, The role of nutrients in bone health, from A to Z, *Crit. Rev. Food Sci. Nutr.* 46 (2006) 621-628.
- [16] Y. Zhang, J. Xu, Y. C. Ruan, M. K. Yu, M. O'Laughlin, H. Wise, D. Chen, L. Tian, D. Shi, J. Wang, S. Chen, J. Q. Feng, D. H. Chow, X. Xie, L. Zheng, L. Huang, S. Huang, K. Leung, N. Lu, L. Zhao, H. Li, D. Zhao, X. Guo, K. Chan, F. Witte, H. C. Chan, Y. Zheng, L. Qin, Implant-derived magnesium induces local neuronal production of CGRP to improve bone-fracture healing in rats, *Nat. Med.* 22 (2016) 1160-1169.

- [17] M. P. Staiger, A. M. Pietak, J. Huadmai, G. Dias, Magnesium and its alloys as orthopedic biomaterials: A review, *Biomaterials*. 27 (2006) 1728-1734.
- [18] F. Witte, The history of biodegradable magnesium implants: a review, *Acta Biomater.* 6 (2010) 1680-1692.
- [19] X. C. Xia, X. W. Chen, Z. Zhang, X. Chen, W. M. Zhao, B. Liao, B. Hur, Effects of porosity and pore size on the compressive properties of closed-cell Mg alloy foam, *J. Magnes. Alloy.* 1 (2013) 330-335.
- [20] D.-H. Yang, B.-Y. Hur, S.-R. Yang, Study on fabrication and foaming mechanism of Mg foam using CaCO₃ as blowing agent, *J. Alloys Compd.* 461 (2008) 221-227.
- [21] H. J. Luo, L. Zhang, Z. G. Xu, Y. S. Yang, Effect of technological parameters on preparation of Mg-Based foam materials, *Materials Science Forum.* 749 (2013) 356-360.
- [22] M. P. Staiger, I. Kolbeinsson, N. T. Kirkland, T. Nguyen, G. Dias, T. B. F. Woodfield, Synthesis of topologically-ordered open-cell porous magnesium, *Mater. Lett.* 64 (2010) 2572-2574.
- [23] K. Lietaert, L. Weber, J. Van Humbeeck, A. Mortensen, J. Luyten, J. Schrooten, Open cellular magnesium alloys for biodegradable orthopaedic implants, *J. Magnes. Alloy.* 1 (2013) 303-311.
- [24] J. O. Osorio-Hernández, M. A. Suarez, R. Goodall, G. A. Lara-Rodriguez, I. Alfonso, I. A. Figueroa, Manufacturing of open-cell Mg foams by replication process and mechanical properties, *Mater. Des.* 64 (2014) 136-141.
- [25] X. Wang, Z. Li, Y. Huang, K. Wang, X. Wang, F. Han, Processing of magnesium foams by weakly corrosive and highly flexible space holder materials, *Mater. Des.* 64 (2014) 324-329.
- [26] N. Kleger, M. Cihova, K. Masania, A. R. Studart, J. F. Löffler, 3D printing of salt as a template for magnesium with structured porosity, *Adv. Mater.* 31 (2019) e1903783.
- [27] G. Jiang, G. He, A new approach to the fabrication of porous magnesium with well-controlled 3D pore structure for orthopedic applications, *Mater. Sci. Eng. C.* 43 (2014) 317-320.
- [28] M. Q. Cheng, T. Wahafu, G. F. Jiang, W. Liu, Y. Q. Qiao, X. C. Peng, T. Cheng, X. L. Zhang, G. He, X. Y. Liu, A novel open-porous magnesium scaffold with controllable microstructures and properties for bone regeneration, *Sci. Rep.* 6 (2016) 24134.
- [29] Y. Z. Bi, Y. Zheng, Y. Li, Microstructure and mechanical properties of sintered porous magnesium using polymethyl methacrylate as the space holder, *Mater. Lett.* 161 (2015) 583-586.
- [30] M. M. C.E. Wen, Y. Yamada, K. Shimojima, Y. Chino, T. Asahina, T. Asahina, Processing of biocompatible porous Ti and Mg, *Scr. Mater.* 45 (2001) 1147-1153.
- [31] G. L. Hao, F. S. Han, W. D. Li, Processing and mechanical properties of magnesium foams, *J. Porous Mater.* 16 (2008) 251-256.
- [32] J. Capek, D. Vojtech, Properties of porous magnesium prepared by powder metallurgy, *Mater. Sci. Eng. C-Mater. Biol. Appl.* 33 (2013) 564-569.
- [33] O. Al-Ketan, R. Rowshan, R. K. Abu Al-Rub, Topology-mechanical property relationship of 3D printed strut, skeletal, and sheet based periodic metallic cellular materials, *Addit. Manuf.* 19 (2018) 167-183.

- [34] X. Y. Zhang, G. Fang, J. Zhou, Additively manufactured scaffolds for bone tissue engineering and the prediction of their mechanical behavior: A review, *Materials (Basel)*. 10 (2017) 50-78.
- [35] N. Sezer, Z. Evis, M. Koç, Additive manufacturing of biodegradable magnesium implants and scaffolds: Review of the recent advances and research trends, *J. Magnes. Alloy*. 9 (2021) 392-415.
- [36] Y. Qin, P. Wen, H. Guo, D. Xia, Y. Zheng, L. Jauer, R. Poprawe, M. Voshage, J. H. Schleifenbaum, Additive manufacturing of biodegradable metals: Current research status and future perspectives, *Acta Biomater*. 98 (2019) 3-22.
- [37] S. Gangireddy, B. Gwalani, K. Liu, E. J. Faierson, R. S. Mishra, Microstructure and mechanical behavior of an additive manufactured (AM) WE43-Mg alloy, *Addit. Manuf.* 26 (2019) 53-64.
- [38] V. Manakari, G. Parande, M. Gupta, Selective laser melting of magnesium and magnesium alloy powders: A review, *Metals*. 7 (2016) 2-35.
- [39] N. A. Zumnick, L. Jauer, L. C. Kersting, T. N. Kutz, J. H. Schleifenbaum, D. Zander, Additive manufactured WE43 magnesium: A comparative study of the microstructure and mechanical properties with those of powder extruded and as-cast WE43, *Mater. Charact.* 147 (2019) 384-397.
- [40] D. Hu, Y. Wang, D. Zhang, L. Hao, J. Jiang, Z. Li, Y. Chen, Experimental investigation on selective laser melting of bulk net-shape pure magnesium, *Mater. Manuf. Process.* 30 (2015) 1298-1304.
- [41] C. Chung Ng, M. Savalani, H. Chung Man, Fabrication of magnesium using selective laser melting technique, *Rapid Prototyp. J.* 17 (2011) 479-490.
- [42] Y. Li, J. Zhou, P. Pavanram, M. A. Leeflang, L. I. Fockaert, B. Pouran, N. Tumer, K. U. Schroder, J. M. C. Mol, H. Weinans, H. Jahr, A. A. Zadpoor, Additively manufactured biodegradable porous magnesium, *Acta Biomater*. 67 (2018) 378-392.
- [43] Y. Wang, P. Fu, N. Wang, L. Peng, B. Kang, H. Zeng, G. Yuan, W. Ding, Challenges and solutions for the additive manufacturing of biodegradable magnesium implants, *Engineering*. 6 (2020) 1267-1275.
- [44] A. Kopp, T. Derra, M. Muther, L. Jauer, J. H. Schleifenbaum, M. Voshage, O. Jung, R. Smeets, N. Kroger, Influence of design and postprocessing parameters on the degradation behavior and mechanical properties of additively manufactured magnesium scaffolds, *Acta Biomater*. 98 (2019) 23-35.
- [45] B. J. L. L. Jauer, M. Voshage, W. Meiners, Selective laser melting of magnesium alloys, *Eur Cell Mater* (2015) 1.
- [46] H. Takagi, H. Sasahara, T. Abe, H. Sannomiya, S. Nishiyama, S. Ohta, K. Nakamura, Material-property evaluation of magnesium alloys fabricated using wire-and-arc-based additive manufacturing, *Addit. Manuf.* 24 (2018) 498-507.
- [47] J. Guo, Y. Zhou, C. Liu, Q. Wu, X. Chen, J. Lu, Wire arc additive manufacturing of AZ31 magnesium alloy: Grain refinement by adjusting pulse frequency, *Materials (Basel)*. 9 (2016) 823.
- [48] S. Das, Physical aspects of process control in selective laser sintering of metals, *Adv. Eng. Mater.* 5 (2003) 701-711.

- [49] Y. Yang, P. Wu, X. Lin, Y. Liu, H. Bian, Y. Zhou, C. Gao, C. Shuai, System development, formability quality and microstructure evolution of selective laser-melted magnesium, *Virtual Phys. Prototy.* 11 (2016) 173-181.
- [50] M. Salehi, S. Maleksaeedi, M. a. B. Sapari, M. L. S. Nai, G. K. Meenashisundaram, M. Gupta, Additive manufacturing of magnesium–zinc–zirconium (ZK) alloys via capillary-mediated binderless three-dimensional printing, *Mater. Des.* 169 (2019) 107683.
- [51] M. Salehi, S. Maleksaeedi, M. L. S. Nai, M. Gupta, Towards additive manufacturing of magnesium alloys through integration of binderless 3D printing and rapid microwave sintering, *Addit. Manuf.* 29 (2019) 100790.
- [52] M. Salehi, H. L. Seet, M. Gupta, H. Farnoush, S. Maleksaeedi, M. L. S. Nai, Rapid densification of additive manufactured magnesium alloys via microwave sintering, *Addit. Manuf.* 37 (2021) 101655.
- [53] K. X. Kuah, D. J. Blackwood, W. K. Ong, M. Salehi, H. L. Seet, M. L. S. Nai, S. Wijesinghe, Analysis of the corrosion performance of binder jet additive manufactured magnesium alloys for biomedical applications, *J. Magnes. Alloy.* 10 (2021) 1296-1310.
- [54] T. M. M. Wolff, A. Bals, T. Ebel, and R. Willumeit-RöMer, FFF of Mg-Alloys for Biomedical Application, in *Magnesium Technology 2019, Proceedings of Magnesium Technology Symposium at the 148th TMS Annual Meeting, San Antonio, Texas, 2019*, edited by V. V. Joshi, J. Brian Jordon, D. Orlov, and N. R. Neelameggham, The Minerals, Metals & Materials Society, Pittsburgh, PA, 2019, pp. 43-49.
- [55] C. Xu, A. Bouchemit, G. L'esperance, L. L. Lebel, D. Therriault, Solvent-cast based metal 3D printing and secondary metallic infiltration, *J. Mater. Chem. C* 5 (2017) 10448-10455.
- [56] C. Xu, Q. Wu, G. L'espérance, L. L. Lebel, D. Therriault, Environment-friendly and reusable ink for 3D printing of metallic structures, *Mater. Des.* 160 (2018) 262-269.
- [57] C. Yang, Z. G. Huan, X. Y. Wang, C. T. Wu, J. Chang, 3D printed Fe scaffolds with HA nanocoating for bone regeneration, *ACS Biomater. Sci. Eng.* 4 (2018) 608-616.
- [58] S. L. Taylor, A. E. Jakus, R. N. Shah, D. C. Dunand, Iron and nickel cellular structures by sintering of 3D-printed oxide or metallic particle inks, *Adv. Eng. Mater.* 19 (2017) 8.
- [59] J. P. Li, J. R. De Wijn, C. A. Van Blitterswijk, K. De Groot, The effect of scaffold architecture on properties of direct 3D fiber deposition of porous Ti6Al4V for orthopedic implants, *J. Biomed. Mater. Res. Part A*. 92A (2010) 33-42.
- [60] S. L. Taylor, A. J. Lbeh, A. E. Jakus, R. N. Shah, D. C. Dunand, NiTi-Nb micro-trusses fabricated via extrusion-based 3D-printing of powders and transient-liquid-phase sintering, *Acta Biomater.* 76 (2018) 359-370.
- [61] S. L. Taylor, R. N. Shah, D. C. Dunand, Ni-Mn-Ga micro-trusses via sintering of 3D-printed inks containing elemental powders, *Acta Mater.* 143 (2018) 20-29.
- [62] S. Z. Guo, M. C. Heuzey, D. Therriault, Properties of polylactide inks for solvent-cast printing of three-dimensional freeform microstructures, *Langmuir*. 30 (2014) 1142-1150.

2

Ink extrusion-based additive manufacturing for Mg-based scaffolds

*We present a room-temperature extrusion-based AM method for the fabrication of topologically ordered porous Mg scaffolds. It is composed of three steps, namely (i) preparing a Mg powder loaded ink with desired rheological properties, (ii) solvent-cast 3D printing (SC-3DP) of the ink to form scaffolds with 0 °/ 90 °/ 0 ° layers, and (iii) debinding and sintering to remove the binder in the ink and then get Mg powder particles chemically bonded by applying a liquid-phase sintering strategy. Rheological analysis of the prepared inks with 54, 58 and 62 vol% Mg powder loading was performed to reveal their viscoelastic properties. Thermal-gravimetric analysis (TGA), Fourier transform infrared spectroscopy (FTIR), carbon/sulfur analysis and scanning electron microscopy (SEM) indicated the possibilities of debinding and sintering at one single step for fabricating pure Mg scaffolds with high fidelity and densification. The resulting scaffolds with high porosity contained hierarchical and interconnected pores. This study, for the first time, demonstrated that the SC-3DP technique presents unprecedented possibilities to fabricate Mg-based porous scaffolds that have the potential to be used as a bone-substituting material.*¹

¹ The chapter is based on a scientific paper: J. Dong, Y. Li, P. Lin, M. A. Leeflang, S. Van Asperen, K. Yu, N. Tumer, B. Norder, A. A. Zadpoor, J. Zhou, Solvent-cast 3D printing of magnesium scaffolds, Acta Biomater. 114 (2020) 497-514.

2.1. Introduction

The SC-3DP method has been demonstrated to be feasible in the case of the AM of steel [1, 2], iron [3, 4], titanium-based [5], and nickel-based [4, 6, 7] micro-trusses. To the best of our knowledge, there have been no reports on SC-3DP of Mg scaffolds. It is worth noting that unlike relatively less reactive metals, fabricating Mg-based materials through the SC-SDP approach could present a different set of challenges, including (i) limited choice of binder components due to the high reactivity of Mg powder, leading to interactions during the printing and debinding processes and the exclusion of the use of water-based and PLGA-containing binder systems that are suitable for SC-3DP of other metals, (ii) the poor sinterability of Mg powder in the absence of external pressure, because of the inevitable presence of a stable oxide film on Mg powder particle surface, which acts as a barrier to diffusion.

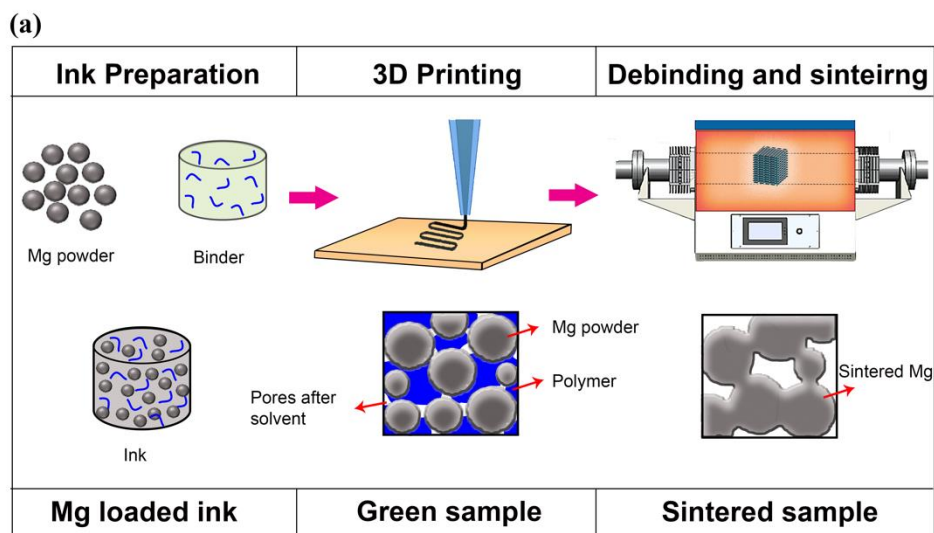
In the present study, we attempted to overcome these challenges and apply the SC-3DP technique to build topologically ordered biodegradable pure Mg scaffolds. Pure Mg was chosen in this first attempt to make the material system simple and avoid unexpected interactions between the alloying elements and binder. This work was aimed to demonstrate the viability of using the SC-3DP technique to produce Mg scaffolds and to find applicable and optimized process conditions for successful fabrication of porous Mg scaffolds with high fidelity. First, the prepared inks, consisting of a judiciously formulated binder and Mg powder particles, were evaluated in their rheological behavior. Rheological characterization was intended to lay the basis for initial screening of inks prior to time-consuming trials of 3D printing and also to provide quantitative support for the evaluation of printability and for the description of observed behavior during the printing process. Second, the inks with different percentages of Mg powder loading were printed by applying the SC-3DP approach and the applicable printability windows were defined. Finally, the effects of sintering temperature and holding time on the density of struts were investigated in light of maintaining the shape fidelity of the scaffolds.

2.2. Material and methods

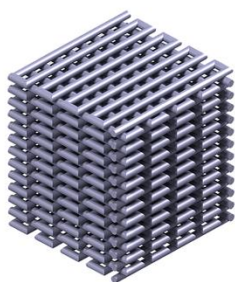
2.2.1. Fabrication strategy

The SC-3DP approach to the fabrication of porous Mg scaffolds consisted of three steps (Figure 2.1a): ink preparation, 3D printing of Mg scaffolds with a designed structure, and debinding and sintering. First, inks containing a binder system (polymer, volatile solvent, and additive), and different percentages of Mg powder loading were prepared. Second, the prepared ink with the required rheological properties was extruded through a micro-nozzle under an applied pressure and at an appropriate printing speed. The volatile

solvents in the extruded struts rapidly evaporated upon extrusion, enabling the condensation of the remaining polymer and increasing the rigidity of the deposited Mg powder loaded struts. This allowed the struts to hold their shape and support the subsequent layers. The presence of the additive prevented the solvent from excessively fast drying, due to its lower vapor pressure, thereby permitting adjacent layers to merge during deposition. Green scaffold samples with Mg powder particles, polymer, and additives were created. Finally, the green scaffold samples were transformed into pure Mg scaffolds through a thermal treatment, during which polymer and additives were thermally decomposed and Mg powder particles were sintered together.



(b)



(c)

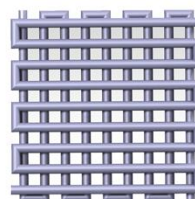


Figure 2.1 A schematic diagram of the fabrication steps and the designed structure of Mg scaffolds: (a) the fabrication process consisting of ink preparation, 3D printing, and post-processing, (b) the CAD model of the scaffold, and (c) the lay-down pattern of the scaffold.

2.2.2. Ink preparation and characterization

2.2.2.1. Powder characterization

Atomized pure Mg powder with a purity of 99.8 wt% (Zn: 0.0081 wt%, Fe: 0.0085 wt% and others: 0.17 wt%) (Tangshan Weihao Magnesium Powder Co., China) had a particle size range of 25 to 80 μm ($D_{10} = 31.11 \mu\text{m}$, $D_{50} = 44.96 \mu\text{m}$ and $D_{90} = 67 \mu\text{m}$). The morphology of the powder was examined with a scanning electron microscope (SEM, JSM-IT100, JEOL, Japan). The microstructure of the Mg powder was observed with an optical microscope (OM, VH-Z250R, KEYENCE, USA) after grinding, polishing, and etching in a solution composed of nitric acid, acetic acid, water, and ethanol at a volume ratio of 1:3:4:12. The average grain size was determined by using the line intercept method.

2.2.2.2. Ink preparation

Mg powder loaded inks were synthesized through mixing of (i) Mg powder particles and (ii) a binder system composed of polystyrene (Sigma-Aldrich), chloroform (Sigma-Aldrich) and dibutyl phthalate (Sigma-Aldrich). Mg powder particles were added into the already made binder in a glove box to prevent Mg powder particles from becoming oxidized during ink preparation. Inks with 54, 58, and 62 vol% powder loading were prepared. The binder and Mg powder mixtures were further mixed by applying magnetic stirring for improvements in homogeneity. The synthesized inks were then centrifuged at 102 rad/s for 1 min and at 25 °C to remove air bubbles.

2.2.2.3. Rheological characterization

The rheological properties of the 54, 58, and 62 vol% Mg powder loaded inks were determined by using a rheometer (Physica MCR 301, Anton Paar, Germany) with a plate-plate geometry (25 mm diameter, 1 mm distance). A shear stress ramp, ranging from 1 to 10000 Pa at 1 Hz, was applied to the ink and the linear viscoelastic range (LVR) was determined. Rotational shear rate-viscosity measurements were performed in the flow mode at shear rates varying between 0.1 and 220 s^{-1} . The linear trend when plotting the results on a double-logarithmic scale was fitted into a power law equation to quantify the degree of shear thinning:

$$\eta = K\dot{\gamma}^{n-1} \quad (1)$$

where η is the viscosity, $\dot{\gamma}$ the shear rate, K the consistency index, and n the flow behavior index.

The storage (G') and loss (G'') moduli were obtained from a frequency sweep test over a frequency range of 0.1 to 10 Hz at a constant stress selected from the LVR ($\tau = 10$

Pa). In the creep experiment, a constant shear stress selected within the LVR ($\tau = 10$ Pa) was applied for 60 s and the resulting strain was measured. Then, in the recovery test, the stress was removed and the strain was recorded for another 180 s. The compliance (J) was obtained from the ratio of the measured strain to the applied stress. The degree of recovery (R) of the ink (*i.e.*, the ability to recover from deformation) was calculated as:

$$R = \frac{J_{max} - J_{\infty}}{J_{max}} \quad (2)$$

where J_{max} and J_{∞} are the compliance at the end of the creep and the recovery tests, respectively.

2.2.3. 3D printing

2.2.3.1. Flow rate measurement

The 54, 58, and 62 vol% Mg powder loaded inks were transported into plastic syringes (EFD, Nordson, Germany) with a 410 μm tapered nozzle (EFD, Vieweg, Germany), which were mounted on a 3D Bioscaffolder printer (BS 3.2, GeSim, Germany). To determine the flow rates of the inks with different percentages of Mg powder loading, the inks were extruded under applied pressures of 60, 80, 100, and 500 kPa for 5, 10, and 15 min. Because the 62 vol% ink could not be extruded at the applied pressures of 60, 80 or 100 kPa, an additional extrusion pressure of 600 kPa was applied for evaluating 62 vol% ink flow rate. The extruded Mg powder containing struts were collected and weighed using a high-precision balance after drying in a fume hood. Then, the mass flow rate was determined by dividing the total weight (the weight of the evaporated solvents was also included in calculation) of the extruded struts dispensed at various time points along a certain dispensing time (5, 10, or 15 min) to obtain an average mass flow rate. The average volumetric flow rate was then obtained by converting the mass flow rate using the respective ink density. The induced shear rate, as the ink flew through the nozzle tip, was correlated with the flow rate and was estimated by

$$\dot{\gamma} = \frac{3n+1}{4n} \cdot \frac{4\dot{Q}}{\pi R^3} \quad (3)$$

where $\dot{\gamma}$ is the shear rate, R the radius of the nozzle, n the shear-thinning coefficient, and \dot{Q} the volumetric flow rate.

2.2.3.2. Scaffold structure design

A cuboidal architecture (dimensions: 7 mm \times 7 mm \times 8 mm) with a strut size of 410 μm , a spacing distance of 390 μm and a lay-down pattern of 0°/90°/0° (Figure 2.1b), and a relative density of 53.7% (the design value, calculated by Solidworks), was designed using the GeSim custom software. A linear infill pattern (Figure 2.1c) was adopted for the designed structure, since it is the most reliable pattern to create uniform porous

structures and allows for a fast and facile fabrication process. This designed structure was meant to determine the printability of the created Mg powder loaded inks and the formability of the scaffolds easily and quickly, as well as the optimized printing process parameters.

2.2.3.3. 3D printing and printability window

The 54, 58, and 62 vol% Mg powder loaded inks were extruded under various applied pressures at room temperature. The extruded struts were deposited on a glass slide as the substrate. The distance between the glass slide and the nozzle tip, and the layer height were both set to be 320 μm in the system, which was almost 80% of the inner diameter of the nozzle. Considering the capacity of the printer used, applied pressures ranging between 1 and 600 kPa (the maximum pressure of the printer) and printing speeds varying between 1 and 18 mm/s were used to determine the printability windows of the three Mg powder loaded inks to realize the desired architecture. First, the operating process parameters (applied pressure and printing speed) that enabled the width of extruded struts in a range of 300 to 500 μm were chosen as the preliminary parameters. Considering the difficulties to obtain the struts having exactly the same diameter as the nozzle size, a relatively large range of 300 to 500 μm was empirically chosen to make the resultant printing window suitable for different printing cases of Mg scaffolds, since inevitable experimental errors could greatly affect the size of extruded struts during the printing process. Then, these parameters were further screened through building 3D structures and evaluating them. Finally, the printability windows of the inks to fabricate the designed Mg scaffolds were determined. The criteria for the printability of the scaffolds were as follows (i) the deflection degree (δ_z) of spanned struts must be less than 5% of the extruded struts diameter [8], and (ii) there should be no apparent defects or displacements of the printed struts. After the printability windows were constructed, a number of printing process parameter sets were selected for these zones and marked as A, B, C, D, E and F in the windows, and then the resultant scaffolds were imaged under SEM and taken as the examples.

2.2.4. Debinding and sintering

The samples with 58 vol% Mg powder loading, a strut size of $350 \pm 10 \mu\text{m}$, and an interspace of $450 \pm 9 \mu\text{m}$, printed with the parameters selected from the defined printability window, were subjected to debinding and sintering. The debinding and sintering processes were conducted in a tube furnace with a controlled atmosphere of high-purity argon (purity $\geq 99.9999\%$). The printed materials were heated at 5 $^\circ\text{C}/\text{min}$ from room temperature to 650 $^\circ\text{C}$ with various dwelling times (5, 10, and 35 min), followed by furnace cooling to room temperature. To investigate the effect of sintering temperature, part of the 3D printed samples was sintered at 660 and 670 $^\circ\text{C}$.

2.2.5. Material characterization

To determine the exact temperature of binder removal, thermal-gravimetric analyses (TGA 8000, PerkinElmer, USA) of pure binder samples and green samples with 58 vol% Mg powder loading were conducted by heating the samples to 650 °C at a rate of 5 °C/min and at an Ar flow rate of 40 mL/min. The as-received Mg powder and the as-sintered Mg samples were also subjected to TGA, following the same procedure as above. The analyses were performed in triplicate. The adsorption spectra of the green samples and those heated to 220, 450, and 650 °C were generated using a Fourier transform-infrared spectroscope (FTIR, Spectrum 100, PerkinElmer, USA). A portion of the green sample was placed on the diamond attenuated total reflection (ATR) crystal. The spectra over a range of 4000 to 600 cm^{-1} were obtained by 30 scans with a spectral resolution of 4 cm^{-1} . Phase constituents in pure Mg powder, printed and sintered scaffolds were identified by using an X-ray diffractometer (XRD, Bruker D8 Advance diffractometer Bragg-Brentano geometry). The diffractometer was equipped with a Lynxeye position sensitive detector and operated at 45 kV and 40 mA with a scan range of 10 -110° and a step size of 0.030° using Cu K α radiation. Quantitative analysis of magnesium oxide (MgO) was performed using the Bruker software (Diffrac.Suite EVA, 5.2). Chemical analyses of the as-received Mg powder and sintered parts in terms of carbon content were performed using a carbon/sulfur analyzer (CS744, LECO, USA). Three repeat samples for each group were measured.

The printed 2D pattern and the cross section of the sintered samples were imaged under the optical microscope. The green samples and sintered samples were also examined using SEM. The relative density of the sintered struts was measured from the optical images of the polished cross sections using the ImageJ software (National Institutes of Health, US). The shrinkage of the sintered samples was determined by measuring the dimensions of the samples before and after sintering using a digital caliper. The sintered scaffolds were imaged by using X-ray micro-computed tomography (μ CT, Nanotom 180NF, Phoenix) at a current of 140 μ A and a voltage of 140 kV, and resolutions of 5 μ m and 2 μ m. To calculate the porosity, struts size, and pore size of the sintered samples, the scanned images were exported to Fiji (National Institutes of Health, US). The regions of interest (ROIs) were then defined. Subsequently, the BoneJ [9] plugin software was used for the calculations.

2.2.6. Statistical analysis

Statistical analysis was performed using ANOVA (one way or two way) or the Scheirer-Ray-Hare test with post-hoc Tukey's multiple comparison test. $p < 0.05$ was considered statistically significant.

2.3. Results

2.3.1. Characteristics of the Mg powder

Atomized pure Mg powder particles appeared to be spherical (Figure 2.2a) under SEM, typical of the characteristics of an argon-protected centrifugally atomized powder. On the cross-sections of powder particles, the average grain size was $8.6 \pm 1.7 \mu\text{m}$ (Figure 2.2b).

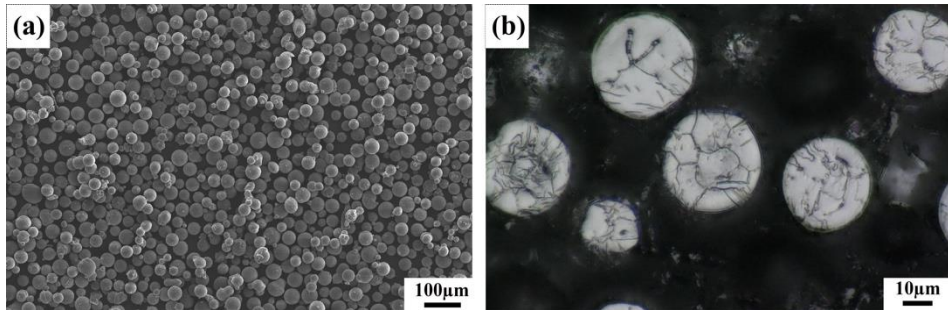


Figure 2.2 The characteristics of the Mg powder: (a) a SEM image showing spherical powder particles and (b) the microstructure of the Mg powder.

2.3.2. Rheological characteristics of the inks

The viscosity-shear stress curve of each of the three prepared inks (with 54, 58 and 62 vol% Mg powder loading) showed a steep drop in viscosity at a certain shear stress (Figure 2.3a). A relative steady region was observed before reaching the critical shear stress, known as the yield stress (τ_y). The yield stress was determined at the intersection of the two tangents: one in the stable region of viscosity where the material was deformed elastically and another in the region where the viscosity dropped and the material started to flow. The yield stress of the ink with a higher percentage of Mg powder loading was higher than that of the ink with a lower percentage of Mg powder loading (Table 2.1). Figure 2.3b shows the decreases in viscosity with increasing shear rate for all the three samples, which is known as the shear-thinning behavior, being of great importance for the inks to be extruded through fine nozzle and at the same time to retain the shape after deposition. Over the full shear rate range, the viscosity value of the ink with a higher percentage of Mg powder loading was higher than that of the ink with a lower percentage of Mg powder loading (Figure 2.3b). The shear-thinning degrees of the three inks were similar (Figure 2.3b), which could be observed from the fitted results (*i.e.*, the values of the shear-thinning coefficient, n) (Table 2.1).

The storage (G') and loss (G'') moduli were determined through a frequency sweep test to examine the viscoelastic properties of the prepared inks, which were considered crucial for successful printing. In the frequency sweep testing, both the storage and loss moduli increased with rising Mg powder loading and frequency (Figure 2.3c). For all the inks with the three percentages of Mg powder loading, the storage moduli were all higher than the loss moduli, indicating that the inks showed elastic or solid-like behavior, which was necessary for retaining the shape of extruded part and supporting its own weight and the layers on top during SC-3DP. The creep-recovery testing was also performed to characterize the viscoelastic properties of the inks, expressed by the compliance J as a function of time (Figure 2.3d). The results showed a nonlinear growth trend in the creep test and an exponential decay in the recovery region. The ink with different percentages of Mg powder loading showed a similar degree of recovery (Table 2.1).

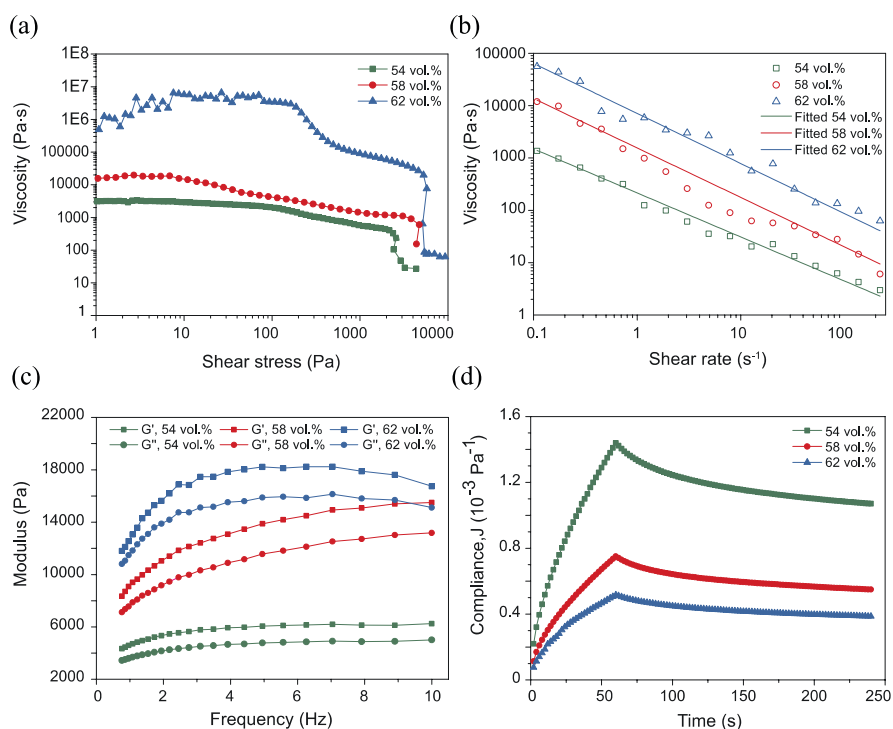


Figure 2.3 The rheological characteristics of the Mg powder loaded inks: (a) the results obtained from the shear stress sweep tests at 1 Hz, (b) the results obtained from the shear rate sweep tests at 10 kPa, (c) the G' and G'' values determined from the frequency-sweep tests, and (d) the compliance values determined from the creep-recovery tests.

Table 2.1 Rheological parameters of the inks with different percentages of Mg powder loading, in which n is the shear-thinning coefficient and K the consistency index.

Ink	Yield stress (Pa)	n	K	Recovery degree
54 vol% ink	2677 ± 87^A	0.18 ± 0.03^A	240 ± 36^A	$26\% \pm 1\%^A$
58 vol% ink	4753 ± 6^B	0.06 ± 0.01^A	1313 ± 337^A	$29\% \pm 3\%^A$
62 vol% ink	5917 ± 76^C	0.05 ± 0.01^A	6782 ± 419^B	$27\% \pm 3\%^A$

A-C: different uppercase letters represent statistically significant difference among the groups of the different percentages of Mg powder loading at $p < 0.05$ (comparison in column); The same letter indicates that the values are not significantly different.

2.3.3. 3D printing

Figure 2.4a shows that the flow rates of the inks steadily increased with rising applied pressure. When the flow rates of the inks with different percentages of Mg powder loading at a given applied pressure were compared, the ink with 54 vol% Mg powder loading exhibited the highest flow rate, while the ink with 62 vol% Mg powder loading had the lowest flow rate. It should be noted that the ink with 62 vol% Mg powder loading could not be extruded out of the nozzle when a pressure less than 350 kPa was applied. We used the measured flow rates to calculate the predicted shear rates and subsequently the corresponding viscosity values (at the point when the inks were extruded through the nozzle) using Equation 3 (Table 2.2). Clearly, the shear rate is dependent on the flow rate at a given external pressure. An increase in the applied pressure results in a significant increase in shear rate, accompanied by a decrease in viscosity (Table 2.2).

Three separate operating windows (Figure 2.4b) were defined as guidelines for selecting the printing process parameters (*i.e.*, applied pressure and printing speed) for the designed Mg scaffolds with different percentages of Mg powder loading. In each plot, four regions are presented, in which scaffolds with different qualities can be obtained. Zone I indicates that one dimensional (1D) struts with widths in the range of 300 to 500 μm and 2D array can be successfully fabricated. As part of zone I, zone II represents the real printable region for 3D printed Mg scaffolds, while zone III and zone IV represent the unprintable regions, in which the widths of struts were out of the defined range of 300 to 500 μm as a result of the mismatch of printing parameters.

Table 2.2 Predicted shear rate values and corresponding viscosity values during the extrusion of the inks at different applied pressures.

Inks		80 kPa	120 kPa	500 kPa
54 vol%	Shear rate (s ⁻¹)	419 ± 17 ^{A 1}	589 ± 12 ^{B 1}	4598 ± 10 ^{C 1}
	Viscosity (Pa·s)	1.70 ± 0.05 ^{A 1}	1.29 ± 0.02 ^{B 1}	0.24 ± 0.00 ^{C 1}
58 vol%	Shear rate (s ⁻¹)	358 ± 2 ^{A 2}	559 ± 84 ^{B 1}	8459 ± 98 ^{C 2}
	Viscosity (Pa·s)	5.23 ± 0.02 ^{A 2}	3.46 ± 0.50 ^{B 2}	0.26 ± 0.00 ^{C 1}
62 vol%	Shear rate (s ⁻¹)	0 ^{A 3}	0 ^{A 2}	159 ± 2 ^{B 3}
	Viscosity (Pa·s)	∞ ^{A 3}	∞ ^{A 3}	54.94 ± 0.50 ^{B 2}

A-C: different uppercase letters represent statistically significant difference among the groups of different applied pressures at $p < 0.05$ (comparison in row);

1-3: different Arabic numbers represent statistically significant difference among the groups of different percentages of Mg powder loading at $p < 0.05$ (comparison in column);

The same letter or number indicates that the values are not significantly different.

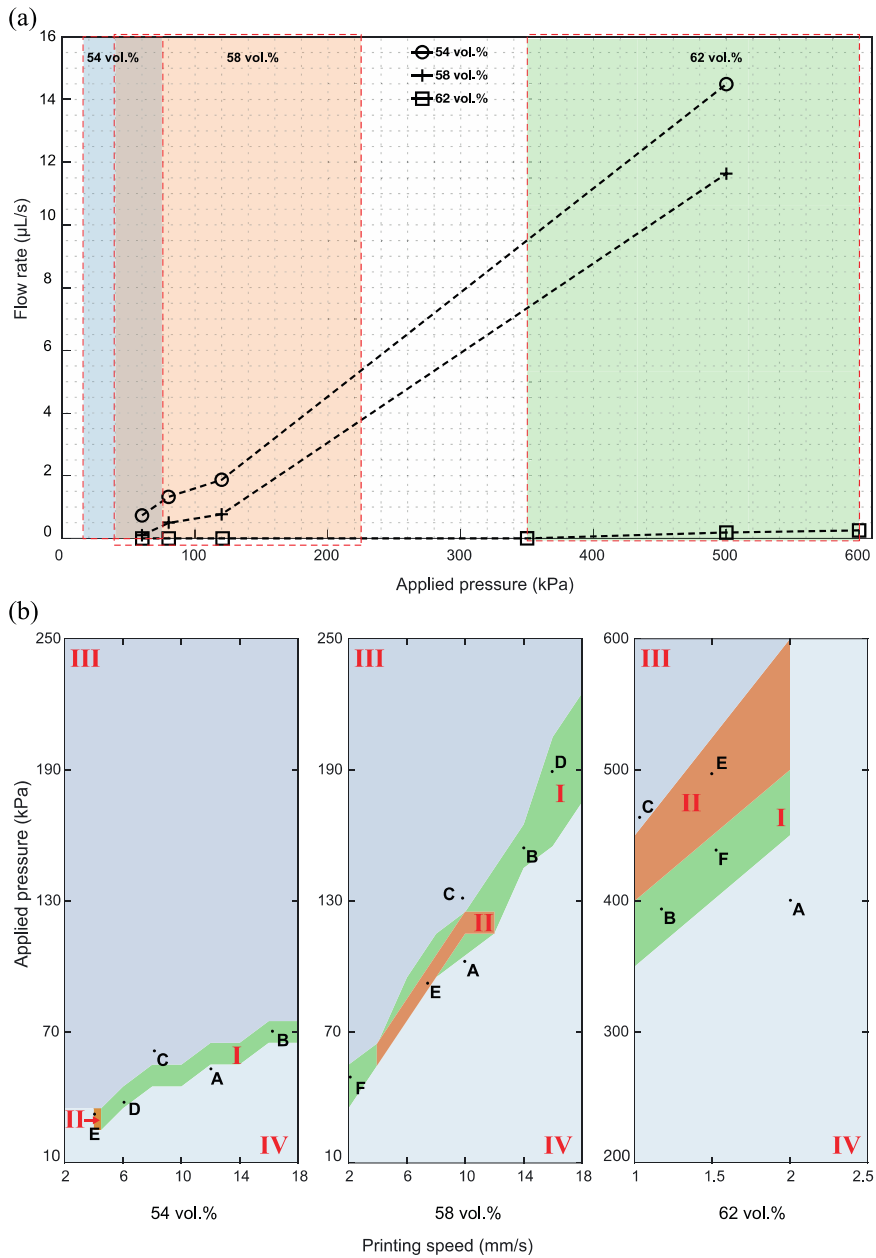


Figure 2.4 The characteristic printing behavior of the Mg powder loaded inks: (a) flow rate as a function of the applied pressure* and (b) the printability windows (II: 3D printable zone; I: 2D printable zone; III and IV: unprintable zones). *The standard deviations of the flow rate values measured were all less than 1%.

Several combinations of the process parameters selected from the different zones were adopted for 3D printing trials and the resulting specimens were considered as the representatives of the regions (Figure 2.4b). The struts printed with the process parameters at point A in zone IV were much thinner than the expected struts (Figure 2.5a) and the lower applied pressure (or higher printing speed) resulted in the displacement of the deposited struts. On the other hand, point C selected in zone III led to the fabrication of much thicker struts (Figure 2.5c) and the closure and fusion between adjacent struts. Point B in zone I enabled the successful fabrication of 1D struts or 2D arrays with a desired gap between two struts, without any displacements or fusion (Figure 2.5b). The green scaffold samples fabricated with the process parameters at point D in the zone I of the 54 and 58 vol% windows had a collapsed surface with a large degree of deflection (Figure 2.5d), while the scaffold samples printed with the process parameters at point F in Zone I of the 58 and 62 vol% windows possessed excessive defects (Figure 2.5f). The SEM image of the scaffold fabricated with the process parameters at point E in zone II of the three ink windows showed that the adjacent layers cohered well together and the struts aligned accurately (Figure 2.5e).

The differences in macro-morphology between the struts printed from the inks with 54, 58, and 62 vol% Mg powder loading could be observed through the close-up views of the struts in the scaffolds (Figure 2.5g-i). As compared to 58 vol% struts (Figure 2.5h), in the 54 vol% struts, Mg powder particles were well covered and bonded by excessive binder (Figure 2.5g), while the surface of 62 vol% struts was rough due to insufficient coverage by the binder (Figure 2.5i).

The macrographs of the printable scaffold samples (Figure 2.5e) showed that the top layer of struts perpendicularly stacked on the layer underneath accurately. Furthermore, there was an overhung part outside the outermost wall of the scaffolds, which was printed without any additional supporting structure. It did not bend or deform during 3D printing or subsequent handling. The shrinkage of the printed scaffold samples was less than 5%, as compared with the designed structure.

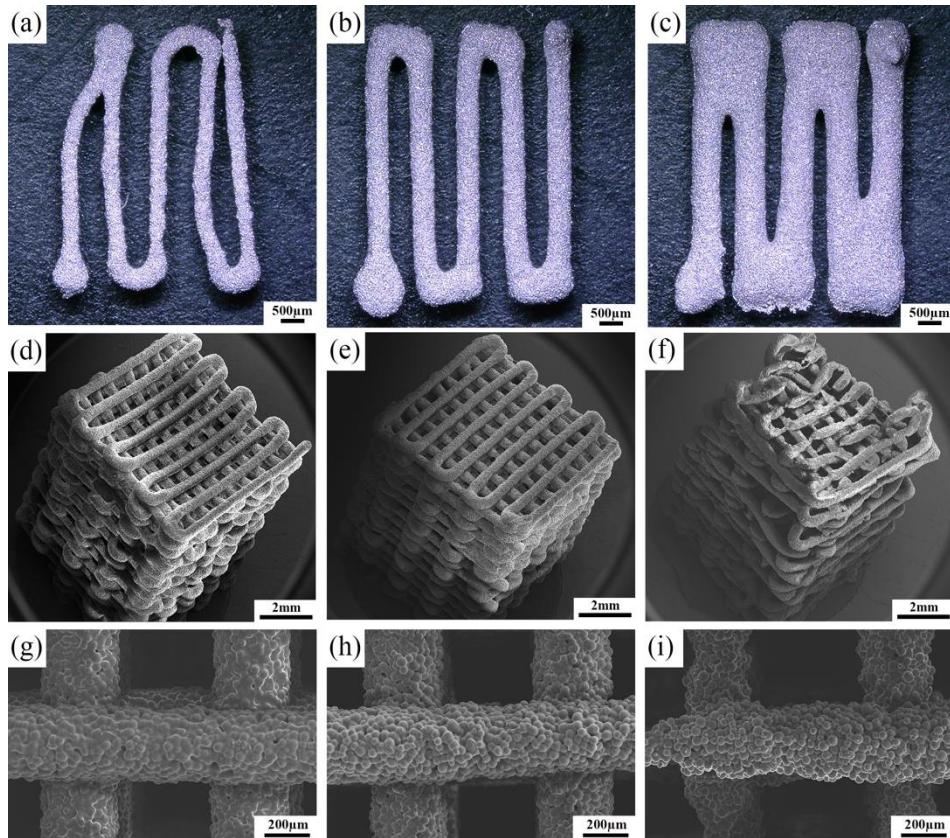


Figure 2.5 The results obtained from the printing trials of Mg scaffolds: (a)-(c) printed single-layer struts with the printing process parameters corresponding to points A-C in the printability windows (Figure 2.4), respectively, (d)-(f) the representative samples showing samples with deflected surface, accurate alignment and excessive defects, printed with the process parameters corresponding to points D-F in the printability windows (Figure 2.4), respectively, and (g)-(h) the microstructures of the printed struts initially with 54, 58, and 62 vol% Mg powder loading, respectively.

2.3.4. Debinding and sintering

2.3.4.1. Debinding

TGA of the pure binder without Mg powder added revealed two-step weight losses (Figure 2.6a). The binder was almost totally decomposed after being heated up to 410 °C and thus above 410 °C, the curve remained steady. FTIR analysis showed that at room temperature, there was no new peak appearing in the spectrum of the ink with 58 vol% Mg powder loading after the Mg powder was added to the binder solution (Figure 2.6c),

as compared with the spectrum of the pure binder. With increasing temperature, TGA of the as-printed sample with 58 vol% Mg powder loading (Figure 2.6b) showed a similar trend to that of the pure binder (Figure 2.6a). The first step of thermal decomposition started to occur at around 115 °C and progressively continued to 210 °C, indicating the removal of plasticizers. Indeed, the peaks stemming from the plasticizers disappeared in the FTIR spectrum of the material after the green samples had been heated to 220 °C, corresponding to the first step debinding, as compared to the spectrum of the ink at room temperature. The leftover peaks at wavelengths of 1492, 1452, 743, and 679 cm^{-1} corresponded to the characteristic absorption frequencies of backbone polymer (Figure 2.6c). The second step of binder decomposition occurred in the range of 320 to 440 °C, where the pyrolysis of polymer occurred with the evidence of the absence of the absorption bands that displayed after the material was heated to 220 °C (Figure 2.6c). The total weight loss of the 58 vol% Mg powder loaded sample between 115 and 440 °C was found to be around 20 wt%. As compared with the spectrum of the sintered Mg powder without the binder, there were no differences between the scaffolds and pure Mg powder samples heated to 650 °C. Due to the absence of vibrations or rotations of organic groups in these samples, both of them showed a nearly steady spectrum (Figure 2.6c).

Unlike the TGA curve of the as-printed sample, the TGA curves of the as-received Mg powder and as-sintered samples did not show any pronounced two-step weight losses, but maintained the weight percentage at around 100% before being heated up to 400 °C (Figure 2.6b), indicating the absence of the binder in the sintered scaffolds. Above the debinding temperature, the TGA curves of all the three samples showed slight increases prior to decreasing. TGA of the as-received Mg powder and the as-printed sample revealed a weight gain of 6.5 ± 1.3 wt% over a temperature range of 400 to 630 °C and a weight gain of 2.0 ± 0.3 wt% ($p < 0.01$, compared to the as-received Mg powder group), respectively, while the weight gain of the as-sintered Mg sample started from 500 °C and ended at 625 °C with a weight gain of 2.8 ± 0.4 wt% ($p < 0.01$, compared to the as-received Mg powder group) (Figure 2.6b). XRD showed that only the pure Mg phase was present in the as-received Mg powder and in the as-printed Mg sample, while in addition to the pure Mg phase, 1 - 2 wt% MgO phase was detected in the as-sintered sample (Figure 2.6d). From the elemental carbon measurement, there was 0.056 ± 0.004 wt% carbon residue in the sintered Mg samples after sintering at 650 °C, compared to 0.011 ± 0.006 wt% carbon measured from the as-received Mg powder ($p < 0.001$).

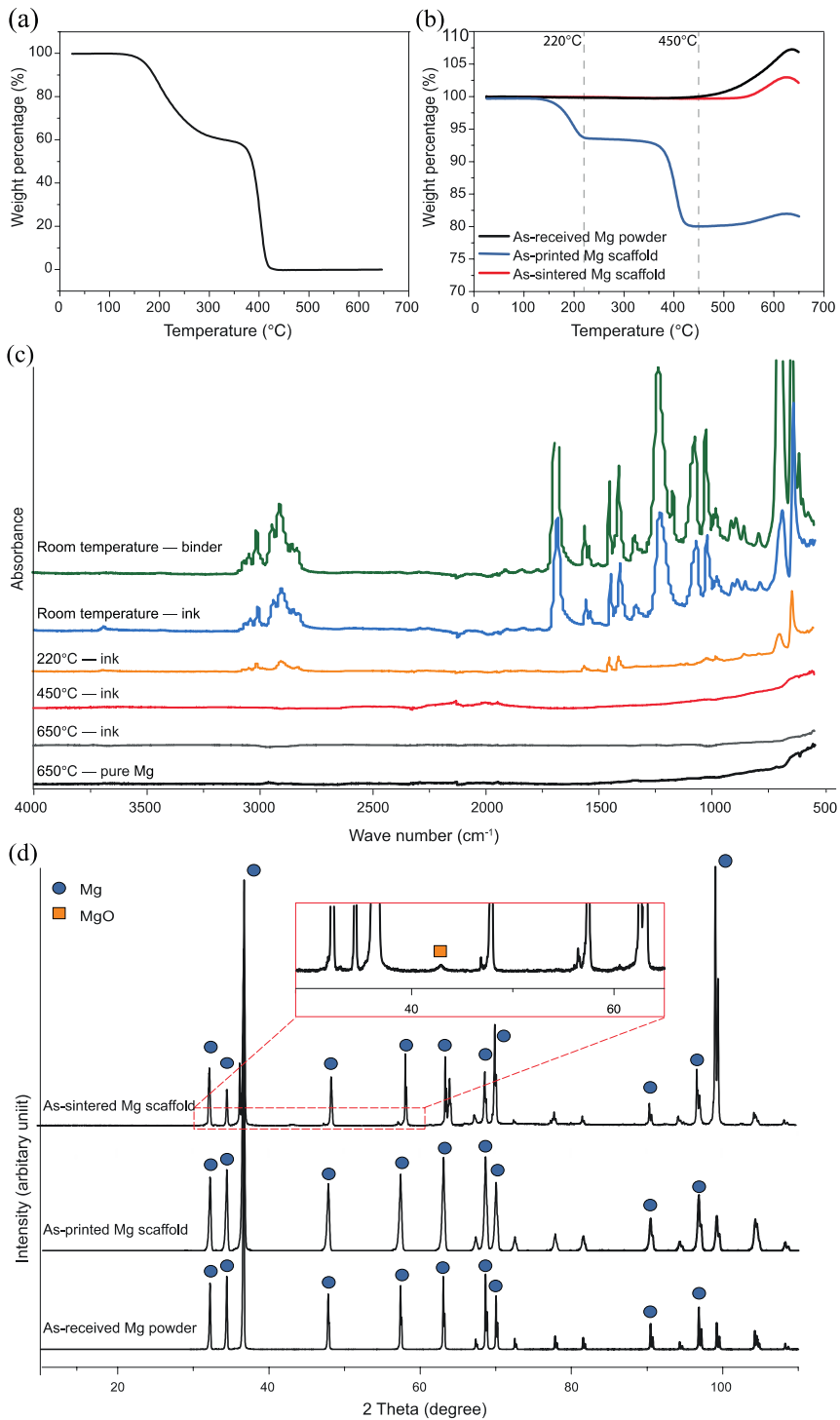


Figure 2.6 The characteristics of the decomposition and interaction in the 58 vol% Mg powder loaded scaffold during fabrication process: (a) TGA results of the pure binder, (b) TGA results of the as-received Mg powders, as-printed and as-sintered scaffolds, (c) FTIR analysis results after the ink was subjected to heating to different temperatures and (d) XRD results of the as-received Mg powders, as-printed and as-sintered scaffolds.

2.3.4.2. Sintering

The effects of the sintering temperature and time on the fidelity of sintered 58 vol% Mg powder loaded scaffolds and the sintering neck evolution within struts were examined under SEM and optical microscope. During sintering at 650 °C, necks formed within struts in scaffolds (Figure 2.7a2-e2). The sintering results of the Mg scaffolds affected by the sintering temperature and time could be seen from the cross-section close-up micrographs of the struts (Figure 2.7a4-e4). Near-net struts were created with necks formed between Mg powder particles and the relative density of struts (excluding the nodules to be described below) increased with increasing holding time and sintering temperature (Table 2.3).

Table 2.3 Relative density values of struts after sintering under different conditions.

Sintering temperature (°C)/ dwelling time (min)	650/35	650/10	650/5	660/5	670/5
Relative density	70% ±	61% ±	54% ±	58% ±	63% ±
of struts	6% A	4% B	6% C 1	7% 12	7% 2

A-C: different uppercase letters represent statistically significant difference among the groups of different sintering times at $p < 0.001$;

1-2: different Arabic numbers represent statistically significant difference among the groups of different sintering temperatures at $p < 0.001$;

The same letter or number indicates that the values are not significantly different.

Interparticle neck formation proceeded greatly after sintering at 650 °C for 35 min and some powder particles were found to have merged together to form a larger body (Figure 2.7a2). Reducing the holding time enabled the alleviation of the merging phenomenon of Mg powder particles, but interparticle necks were still well maintained. The growth of necks, the reduction of micropores, and powder particle merging tended to progress further as the sintering temperature increased (Figure 2.7d2 and Figure 2.7e2).

Due to the excessive flow of molten Mg and poor wettability between molten Mg and solid Mg powder particles, some nodules appeared in the fabricated Mg scaffolds (Figure 2.7a1-e1) sintered under certain sintering conditions. Large nodules could be found on the surface of the struts and between the struts of the scaffolds sintered at 650 °C for 35 min (Figure 2.7a1). The nodules could be large enough to fill the space or macropores between adjacent struts, which could be observed from the cross-section view of the sintered samples (Figure 2.7a3). The size of the nodules decreased as the holding time decreased, while no nodules were observed when the holding time was only 5 min (Figure 2.7c1-c4). However, they appeared when the temperature was increased from 650 to 660 °C and even to 670 °C, although the holding time was only 5 min (Figure 2.7d1 and Figure 2.7e3). Many of the macropores between the struts were filled by spherical nodules after sintering at 670 °C, adversely affecting the scaffold fidelity (Figure 2.7e3).

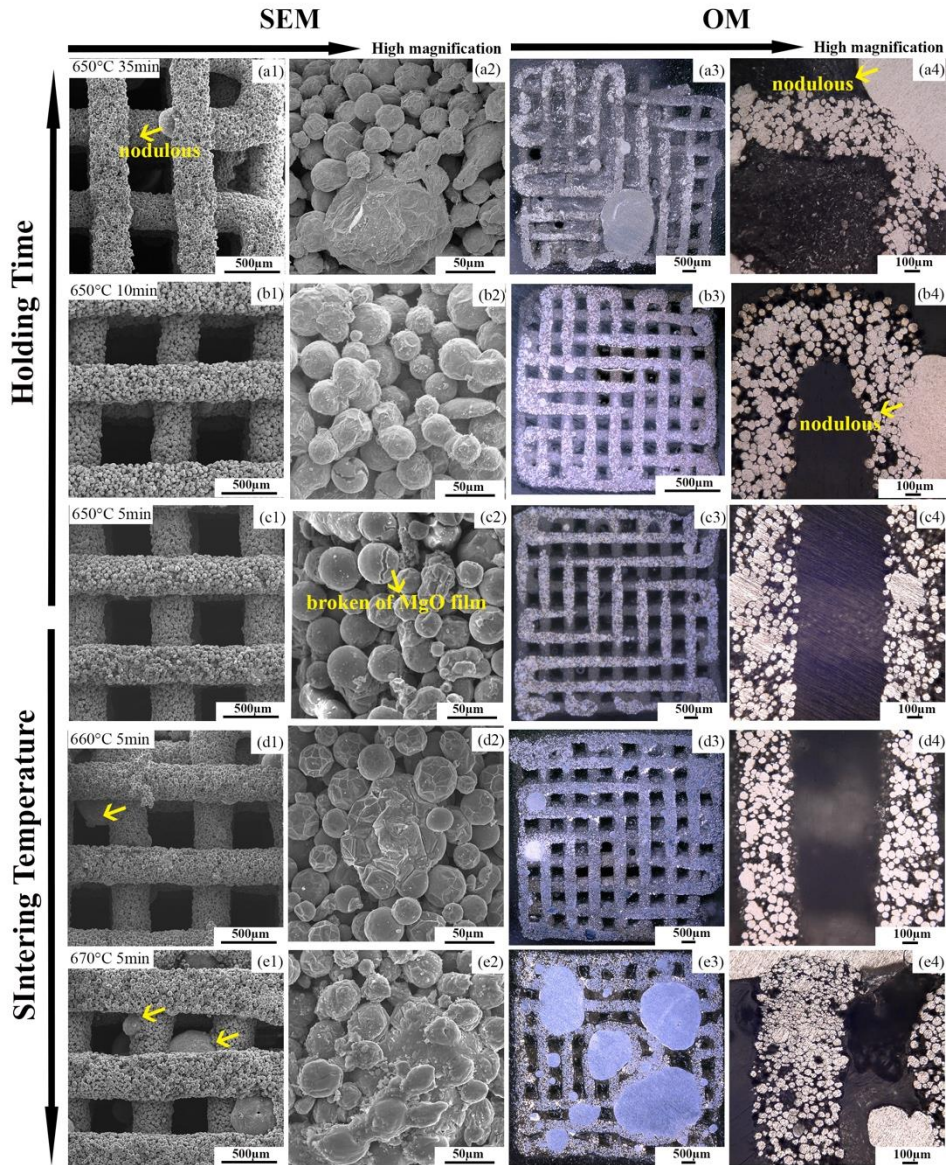


Figure 2.7 The sintering behavior and fidelity of the scaffolds initially with 58 vol% Mg powder loading in relation to sintering temperature and holding time.

2.3.4.3. Hierarchical structure of scaffolds

The macrograph of the sample after sintering at 650 °C for 5 min (Figure 2.8b) showed the retention of the shape with high fidelity, as compared to the 3D printed sample (Figure 2.8a). The strut size after sintering was $323 \pm 15 \mu\text{m}$. The designed macropores remained

open after sintering, as confirmed by the 3D reconstruction of μ CT images (Figure 2.8c). The pore size was $476 \pm 11 \mu\text{m}$. The micro-channels and surrounding necks within the struts were clearly visible from the reconstructed models (Figure 2.8c) and the micropores in the struts were in a range of 19 to $100 \mu\text{m}$, according to the calculation of ROI from the μ CT images. The porosity of the sintered samples was 78.4%. Both macropores and micropores are mostly interconnected (Figure 2.8c). The shrinkage of the sintered sample, relative to the 3D printed sample, was $2.0 \pm 0.8\%$.

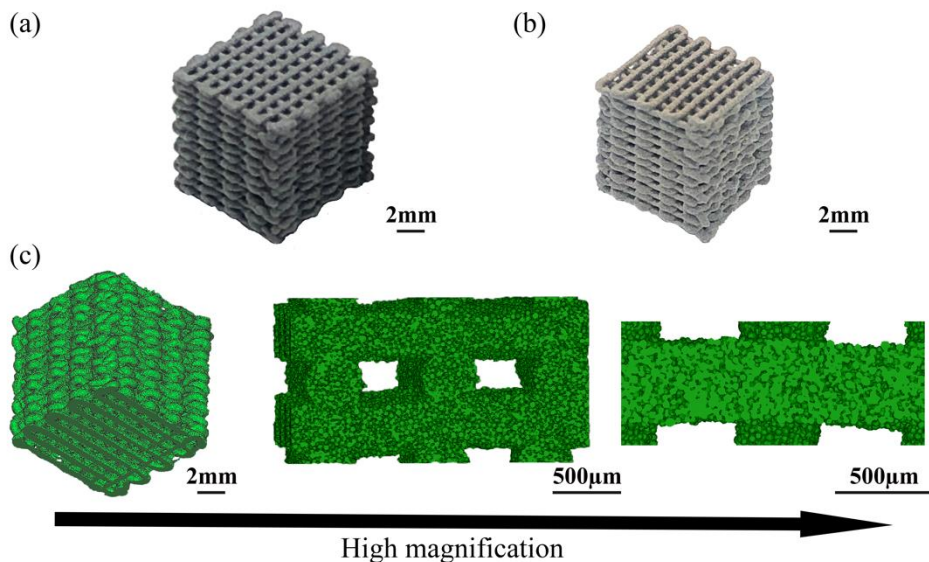


Figure 2.8 The macrographs of the fabricated samples: (a) 3D printed sample, (b) sample sintered at $650 \text{ }^\circ\text{C}$ for 5 min, and (c) reconstructed sintered sample from μ CT images.

2.4. Discussion

In this study, for the first time, an extrusion-based 3D printing technique was utilized to manufacture porous Mg scaffolds. The major challenges involved in applying this technique, namely the limited number of binder choices and poor sinterability of Mg in the absence of external pressure, were overcome. These achievements open up many possibilities to exploit this approach further.

2.4.1. Ink preparation

The core of fabricating Mg scaffolds through the SC-3DP process is the design of Mg powder loaded inks that should be chemically stable and exhibit required rheological properties to allow the 3D printing of defect-free Mg scaffolds under ambient conditions.

The selection of binder, the rheological properties of the ink, and the relationship between the ink and printing process are discussed below.

2.4.1.1. Selection of binder

The selection of a proper binder is a challenging task and also a critical step prior to the fabrication of Mg-based scaffolds with the SC-3DP technique. First, considering the intrinsic properties of Mg powder, any water-based binder should be excluded. That is because Mg powder reacts with an aqueous binder and produces a great amount of hydrogen in the ink feedstock. Bubbles were easily observed when Mg powder was mixed with a water-based PVA binder (Figure S2.1, see the supplementary material), which resulted in discontinuous extrusion and severe defects in the manufactured struts. Second, any possible interactions between the Mg powder and the by-products of polymeric binder during debinding should be carefully considered. For instance, commercially available PLGA (polylactide-co-glycolide) has been widely utilized as a binder in combination with volatile solvents for producing various other materials, such as iron [4], nickel-based alloys [6, 7], tungsten [10], graphene [11], and ceramic [12] using the SC-3DP technique. In the case of the Mg powder loaded ink with PLGA as the binder, however, we found that during the debinding process, either the ester group (-COOH) of PLGA or thermally-evolved PLGA fragments adhered to the surfaces of Mg powder particles inevitably containing the hydroxyl (-OH) group, probably leading to the formation of an intermediate compound, magnesium carboxylate (Figure S2.2, see the supplementary material). Similar reactions were found on the surfaces of the alumina [13] and lead titanate [14] samples where poly (methyl methacrylate) (also containing the ester group) was involved. This reaction produced organic residues anchored on Mg powder particle surfaces (Figure S2.3, see the supplementary material), resulting in the retention of non-volatile char on Mg powder particle surfaces and hindering the sintering of Mg powder, although metal carboxylate was not stable at high temperatures.

Finally, apart from the concerns about the possible interactions between the binder and the Mg powder, the temperature of the pyrolysis process and the amount of binder residue should also be considered, because the applicable sintering temperatures of pure Mg with a melting point of 650 °C are relatively low, as compared to those applicable to other metals, such as iron and nickel.

Based on the above considerations and the lessons learned from many experimental trials, we designed a graded volatile binder system that consisted of polymer, volatile solvents, and additives for fabricating Mg scaffolds. From the results obtained from the FTIR analysis and TGA, it was confirmed that this binder system did not react with the Mg powder during 3D printing or debinding. This is because unlike water-based PVA binder, the solvent we used is a kind of water-free organic solvent, and unlike PLGA

containing binder, the backbone polymer used in this study did not include the functional group that might react with Mg powder. After debinding, almost no binder residue retained, which could otherwise have hindered the sintering of Mg (Figure 2.6). Moreover, the carbon residue results confirmed that there was very little carbon residue (0.056%) in the sintered samples. Therefore, the chosen binder system would not affect further sintering process.

2.4.1.2. Rheological properties of the inks

The viscoelastic properties of a viable ink are of critical importance for the success of the SC-3DP approach. A high degree of shear-thinning behavior is particularly important, which enables the ink material to be extruded through fine nozzles, on the one hand, and to possess a sufficiently high rigidity for shape retention on the other hand [15]. Meeting these criteria requires proper control of ink formulation and rheological properties to generate a stable suspension that promotes the “fluid-to-gel” transition, thereby ensuring the retention of the printed shape and the fusion with the previously deposited layer. The fluid-to-gel transition can be achieved by applying different approaches to different 3D printing techniques, such as temperature-controlled transition [16, 17], gelling of precursor solution [18], and solvent evaporation, which was applied to the present printing technique (*i.e.*, SC-3DP). Solvent evaporation is the most commonly used approach for increasing the rigidity of materials right after extrusion, and offers a number of benefits, such as simplicity, room-temperature processing, *etc.* In addition, by carefully adjusting the ink composition, tailorable rheological properties of the ink can be obtained to maximize its printability.

Solids loading is commonly used to quantify the amount of suspended solids in a substance. In the present study, this is referred to as the amount of Mg powder loaded into the binder to form feedstock or ink for SC-3DP. The volume fraction of solids loading (ϕ) is closely related to the viscosity of a spherical particle loaded ink [19]. When ϕ increases towards a maximum packing fraction (ϕ_m), the relative viscosity tends to be infinite and the suspension exhibits yield stress behavior. Usually, spherical particles with unimodal sizes, no matter what their sizes may be, can achieve a typical value of $\phi_m=0.64$ for random close packing [20]. This was confirmed experimentally by printing the 64 vol% Mg powder loaded ink and as expected, its flow was totally hindered even though the maximum pressure of the printer, 600 kPa, was applied. Therefore, 54, 58, and 62 vol% Mg powder loading were used in the present study for the optimization of the solids loading in the inks.

In the present case, the rheological behavior of the inks could be tailored by varying the percentage of Mg powder loading (54, 58, and 62 vol%) (Figure 2.3). The results obtained from the shear stress sweep, frequency sweep, and creep-recovery tests all

showed the viscoelastic properties of the inks. First, in the shear stress sweep test, the obtained yield stress revealed an “at-rest” viscoelastic characteristic, below which the material behaved as a solid. It is reported that the “yield behavior” really exists in highly filled viscous polymers [20]. A suspension composed of a low-viscosity fluid or equivalently a high concentration of solids ($\phi > 0.5$) usually exhibits a high yield stress that must be exceeded in order to initiate the flow, which is attributed to the particle interaction forces within materials [20]. However, it has been observed that suspensions with particles larger than 10 μm in diameter (non-colloidal suspensions) or volume fraction less than 0.3 usually do not show a sign of yield stress due to the less significant interaction forces among larger particles. Although Mg powder particles with diameters in a range of 25 to 80 μm were used in this study, the “yield behavior” was obvious for the Mg powder loaded inks (Figure 2.3), which was most likely due to the addition of plasticizers to the inks. The plasticizers could activate the surface of solid powder particles and, therefore, increase the interfacial interaction between powder particles [21], which promoted the viscoelastic properties of the Mg powder loaded inks. The yield stress of the ink with a higher percentage of Mg powder loading is higher than that of the ink with a lower percentage of Mg powder loading, indicating that a higher printing pressure is required for initiating the flow of the ink with a higher percentage of Mg powder loading (Figure 2.4).

Second, in the frequency sweep test, all the three inks conformed to the $G' > G''$ relationship in the linear region (Figure 2.3c). The phase angle, δ ($\tan \delta = G''/G'$), is an indicator of the elastic or viscous behavior of an ink. When δ falls in the range of $0^\circ < \delta < 90^\circ$, the material presents viscoelastic behavior, in which the material with $\delta > 45^\circ$ is more viscous and that with $\delta < 45^\circ$ is more elastic [22]. Therefore, the inks with various percentages of Mg powder loading showed dominantly elastic behavior featured by a phase angle smaller than 45° . In the present study, a minimum elastic modulus G' value that is required to have a midpoint deflection of no greater than 5% of the strut diameter was considered, based on a simple elastic beam model [8]. This assessment was widely adopted by other researchers to evaluate the rigidity of the inks to support the entire structure [22-24]. A minimum G' value of 7.05 - 7.28 Pa was required, based on the calculation with the ink density values of 1.50 - 1.55 g/ml for 54 - 62 vol% Mg powder loading, 410 μm in strut diameter, and 390 μm in spacing distance. The G' values of all the inks obtained from the frequency sweep tests (Figure 2.3c) were all more than 4 orders of magnitude larger than the required value and, therefore, theoretically satisfied the criterion.

Finally, the viscoelastic properties of the inks were confirmed by the creep-recovery tests, where a quick viscosity recovery with no shear stress applied was required (Figure 2.3d). All the prepared inks showed viscoelastic characteristics with about 25% recovery

degree. The shear thinning of the inks is a prerequisite for extrusion-based 3D printing. All the prepared inks exhibited the shear-thinning behavior (Figure 2.3c), and the degree of shear thinning did not show large differences between the inks with different percentages of Mg powder loading (Table 2.1). This agrees with the findings of other researchers, showing that n remains unchanged upon the addition of various volume fractions of spherical solids due to the presence of the particulates [25].

The viscosity of the suitable inks for extrusion-based 3D printing varies case by case. In the present study, the shear rates for extruding different inks at various applied pressures were derived from the measured flow rates. The corresponding viscosity values of the inks experiencing extrusion for suitable 3D printing (Figure 2.4) were between 1 and 60 Pa·s (Table 2.2), which is in the same viscosity range as reported before [22].

Although the rheological properties are of help in gaining a fundamental understanding of the printability of the inks, the real printing process is significantly more complex than what can be captured from the shear-viscosity measurements. Nevertheless, rheological evaluation can provide a guideline for initial screening or optimizing the suitable inks prior to time-consuming trials of 3D printing. Indeed, in the present research, the rheological characterization of the prepared inks with three different percentages of Mg powder loading provided theoretical support for describing the printability and printing behavior, which will be discussed in the next subsection.

2.4.2. 3D printing process

The dimensional accuracy of material deposition during the 3D printing process is strongly dependent on the flow rate of the ink (*i.e.*, the extrusion rate of the ink from the nozzle under an external pressure). The flow rate is influenced primarily by three factors, namely the physical and rheological properties of the ink, the geometry of the nozzle, and user-imposed conditions, such as the temperature, which was not included in the present study. First, under the same applied pressure, the flow rate of the ink with a lower percentage of Mg powder loading was found to be larger than that of the ink with a higher percentage of Mg powder loading (54 vol% > 58 vol% > 62 vol%). That is because the flow rate is usually inversely proportional to viscosity. The viscosity value of the ink at the shear rate induced by extruding was in the ascending order: 54 vol% < 58 vol% < 62 vol% (Table 2.2). Combined with the printability window (Figure 2.4b), the appropriate flow rate for printing struts with a fidelity tolerance below 25% (the width of struts in a range of 300 to 500 μm , when a 410 μm nozzle was used) was at a level of 10^{-4} to 10^{-3} ml/s with printing speeds in a range of 1 to 18 mm/s (Figure 2.4a). A wide range of flow rates (*i.e.*, 0.07 nL/s - 4 mL/s) were reported for various inks suitable for extrusion-based 3D printing [26]. The flow rates in the present case were, therefore, considered reasonable. Second, the nozzle size and geometry could affect the flow rate. A tapered

nozzle was used for 3D printing in the present study, since it is better suited for achieving high-pressure gradients or higher flow rates than a cylindrical nozzle [27].

The applicable printing parameters are determined by the flow rate of the ink. For a given ink, as flow rate increases at a given printing speed, nozzle size, and geometry, the width of the resultant strands increases. In this case, an increased printing speed is needed to ensure that the struts width remains within a desired range. This correlation can give a reasonable explanation for the inclined region of the printability window, especially zone I for 2D strut printing. The selection of suitable process parameters that could be used for successful fabrication of 3D scaffolds is much stricter than that for 2D printing, since maintaining structural integrity would have to be considered in the 3D printing process (Figure 2.4b). Two criteria would have to be met for structural integrity: (i) smooth transitions between adjacent layers, which requires enough liquidity for deposited layers to enable seamless fusion with the subsequent layers, and (ii) enough rigidity of firstly deposited layers to support the whole structure, which requires rapid evaporation of solvents right after extrusion. It was observed that the evaporation of the inks played an important role in meeting these two criteria for building the designed structure without distortions or defects, although the presence of additive (*i.e.*, the remaining low vapor pressure solvent) already imparted the liquidity to a certain extent. At a high printing speed, point D in the 54 and 58 vol% windows led to insufficient evaporation of solvents from the deposited layers, resulting in the slumps of the structure (Figure 2.5d). A lower printing speed (for example, point F in the 58 vol% window) or a thin strut resulting from an insufficient applied pressure (point F in the 62 vol% window) resulted in too much drying of the layers and, thus, the unmerged or discontinuous layers with poor adhesion (Figure 2.5f). In the printability windows of the 54 and 62 vol% Mg powder loaded inks, the printable zones were located at low printing speeds (below 5 mm/s) for the designed 3D scaffolds (Figure 2.4b). The 54 vol% Mg powder loaded ink needed more time for evaporation than the ink with a higher percentage of powder loading to reach the same level of rigidity, because the former had more solvents. A lower printing speed means a longer time for the nozzle to reach the same displacement and, therefore, a longer time for the solvent evaporation from the deposited struts before the deposition of next layers. By contrast, the applicable printing speed for the ink with 62 vol% Mg powder loading was limited to a very low speed due to a very low flow rate. In comparison with the inks with 54 and 62 vol% Mg powder loading, the ink with 58 vol% Mg powder loading could be printed over the widest range of printing speeds (*i.e.*, 4-12 mm/s).

In summary, the flow rate (affected by the applied pressure), the evaporation rate (a physical property of the ink) and the deposition rate (determined by printing speed) must be matched with each other for printing the desired 3D structure successfully. The established operating window can be used as a quick guidance for fabricating 3D porous

scaffolds with structure sizes on a millimeter scale. It is important to note that the operating window depends on the size and geometry of the designed structure in the evaporation-controlled printing process. In the present study, the printed structure showed a high fidelity without defects and the side pores remained open even over a long spanning length (Figure 2.8a). The main limitation of the printing process is that the inks must be printed within 1.5 - 2 h after having been loaded into the cartridge due to the continuous evaporation of the inks in the cartridge and, thus, an altered viscosity that could affect the printing process.

Apart from the considerations regarding the printability of Mg powder loaded inks, a higher percentage of Mg powder loading is beneficial for the subsequent steps (*i.e.*, debinding and sintering), as a high relative density of struts can be obtained and the retention of strut/scaffold shape can be ensured after binder removal. However, the ink with 62 vol% Mg powder loading is not the most promising one, because of its narrow printability window and low printing efficiency (*i.e.*, the low permissible printing speeds). Therefore, the printed scaffolds with 58 vol% Mg powder loading were chosen for further study on the debinding and sintering behavior of the scaffolds.

2.4.3. Debinding and sintering

Debinding and sintering of porous Mg scaffolds are even more challenging than the 3D printing step. The main challenge involved in debinding is mostly related to the binder selection that has already been discussed earlier. TGA and FTIR analysis (Figure 2.6) confirmed the proper choice of the binder, as the vast majority of the binder had been degraded before reaching the sintering temperature and no interaction was found between the reactive Mg powder and the pyrolysis products of the binder during the debinding process.

Apart from the advantages of the seamless attachment of layers during 3D printing, a binary-component binder system is also beneficial for debinding. The plasticizer was removed first to open the paths for further diffusion of the degraded gaseous products (Figure 2.6). The major polymer, which served as backbone, retained the strut shape until being almost totally decomposed before the sintering temperature, 650 °C, was reached, with low ash residue (Figure 2.6). Around 20 wt% of the binder was thermally decomposed during the 2-step degradation, which was nearly all the binder in the initial feedstock (Figure 2.6b). As the backbone polymer was mostly removed before 450 °C was reached, the ash or carbon residue content was of paramount importance for retaining the shape and preventing the scaffolds from slumping and distorting before the formation of the inter-particle necks occurred during sintering. Such a strategy (*i.e.*, a multi-component binder system) is often used in the debinding of metal injection molding (MIM) [28]. A heating rate of 5 °C/min was chosen for debinding and sintering, which was

relatively high as compared with that typically applied in MIM. In general, a high heating rate is not preferred in MIM because integrity loss may occur during the debinding process when sudden evaporation of a binder fraction occurs with no clear exit path. In solvent-cast 3D printing applied in the present study, however, the backbone binder accounted only for 37 vol% of the binder and the rest were solvent and plasticizer. As a result, the evaporation of the solvent and the decomposition of plasticizer provided sufficient paths for the evaporation of polymer. Sudden internal stress that may cause the collapse of the structure would unlikely occur. In addition, the carbon residue on the surfaces of Mg powder particles played a vital role in increasing the friction between Mg powder particles. In other studies on solvent-cast 3D printing of metals, scaffolds could be fabricated successfully even at a heating rate of 10 °C/min during the debinding process [6, 7]. Considering a relatively long debinding time being typical in MIM, a single-step protocol was employed in the present study by combining debinding and sintering, during which no dwelling time for debinding was allocated. The relatively quick debinding might be attributed to the pressure-free thin struts that enabled fast diffusion paths for pyrolysis products to move to the green body surfaces where the decomposed binder under argon gas flow could quickly escape [29]. This one-step treatment greatly increased the fabrication efficiency and reduced the operational complexity, as compared with the usual practice in the case of MIM.

The changes of the Mg powder throughout the fabrication process were also studied. XRD revealed that the Mg powder in the as-printed samples remained the same as the as-received powder in phase constitution (Figure 2.6d), which was also confirmed by the FTIR results (Figure 2.6c). In the sintered sample, however, the MgO phase was found. In TGA, above 400 °C, weight gain occurred to all the tested samples (Figure 2.6b) due to the oxidation of Mg. In another study, it was also observed that the oxidation of Mg accelerated above a critical temperature (*i.e.*, 400 °C) at various heating rates even in an ultra-high-purity Ar gas atmosphere (Ar purity: 99.9999%) [30]. After being heated above 400 °C in TGA, the as-printed sample appeared to be less oxidized (with a weight gain of 2.0 wt%), when compared with pure Mg powder (with a weight gain of 6.5 wt%). This was probably because a small amount of carbon residue from the binder covered some surfaces of Mg powder particles in the as-printed sample, while the as-received Mg powder particles possessed more exposed surfaces. The weight gain of the as-sintered Mg sample was also lower than that of the as-received Mg powder over the temperature range of 400 to 650 °C. This was because the as-sintered Mg sample had already been oxidized once during the sintering process prior to XRD analysis, while pure Mg powder particles still had “relatively clean” surfaces to react with oxygen during XRD analysis. Therefore, compared with the as-received pure Mg powder, the Mg powder in the as-printed Mg scaffolds did not change chemically after being mixed with the binder, while that in the

as-sintered Mg scaffolds presented only small increases in MgO content (1-2 wt%) and carbon content (0.045 wt%).

Sintering of the porous Mg scaffolds was challenging, as the presence of an oxide layer on Mg powder particle surfaces severely retarded the sintering process. Unlike other metals, such as iron and copper [31], the diffusion coefficient of Mg atoms (*i.e.*, 5.25×10^{-24} at 650 °C) through the oxide layer is about 12 orders of magnitude lower than their self-diffusivity (3.01×10^{-12} at 650 °C) [32]. Furthermore, the magnesium oxide (MgO) layer on Mg powder particle surfaces is rather stable even beyond the evaporation temperature of Mg. In addition, there is no real possibility of reducing MgO into Mg during sintering. Therefore, solid-state sintering of loose Mg powder is not feasible and breaking up the oxide layer is the only way to allow for effective sintering kinetics, which will provide paths for the diffusion of Mg atoms. With respect to this, the compaction of Mg powder is usually used in order to mechanically rupture the oxide layer in the conventional powder metallurgy techniques. However, the sintering of the designed porous scaffolds excludes the possibility of applying external mechanical pressure on the 3D printed samples. Nevertheless, hot isostatic pressing (HIP) which has been once tried to consolidate a magnesium alloy solid part [33] may be still applicable.

Liquid-phase sintering offers a possibility for the sintering of loose Mg powder, in which the presence of a small volume fraction of the liquid phase facilitates the disruption of the oxide layer and enhances the diffusion. This strategy has been also utilized in the sintering of ZK60 scaffolds fabricated by powder-bed inkjet 3D printing [32]. The control of the presence of a solid-liquid coexistence zone enabled the liquid fraction in the ZK60 alloy to vary from 14 to 43 vol% over a temperature range of 535 to 610 °C, which gave a wide range for the selection of sintering temperature. In comparison with that Mg alloy, it is much more difficult to take advantage of the formed liquid phase for the sintering of with a liquid monophasic zone. That is because sintering at or above the melting point of Mg is necessary to generate the liquid phase, but it involves the risk of disrupting the shape of the specimens and even total collapse of the scaffolds.

With the above considerations, in the present study, we proposed a short sintering process to overcome the challenge involved in pure Mg sintering. It was found that a 5 min holding time was enough to form inter-particle necks at 650 °C. Generally, 650 °C is the melting point of pure Mg. Although the sintering temperature reached the melting point of Mg, the shape of scaffolds was still well retained without any collapse (Figure 2.8), owing to the presence of a MgO film on the surfaces of Mg powder particles. A depicted model (Figure 2.9) displays how pure Mg can be successfully sintered within a short holding time. Before the occurrence of sintering, an oxide layer covered Mg powder surfaces, which severely impedes diffusion (Figure 2.9a). During heating towards 650 °C, the liquid phase appeared along grain boundaries or some defects inside Mg powder

particles. As temperature increased to the melting point of Mg, a greater volume fraction of the liquid phase formed inside powder particles. The volumetric expansion of Mg powder particles caused a gradual increase of internal pressure inside Mg powder particles until the oxide layer ruptured. The cracks on the surface of powder particles (Figure 2.7c2) provided short-circuit paths for the interior liquid Mg to seep onto the surfaces of powder particles. The released liquid was then drawn into the inter-particle neck regions due to the capillary force, leading to the formation of necks. In summary, the enveloping MgO film enabled the retention of Mg powder particles and scaffold shape, while the cracks of the MgO film gave the melt a chance to flow out and consequently to form necks.

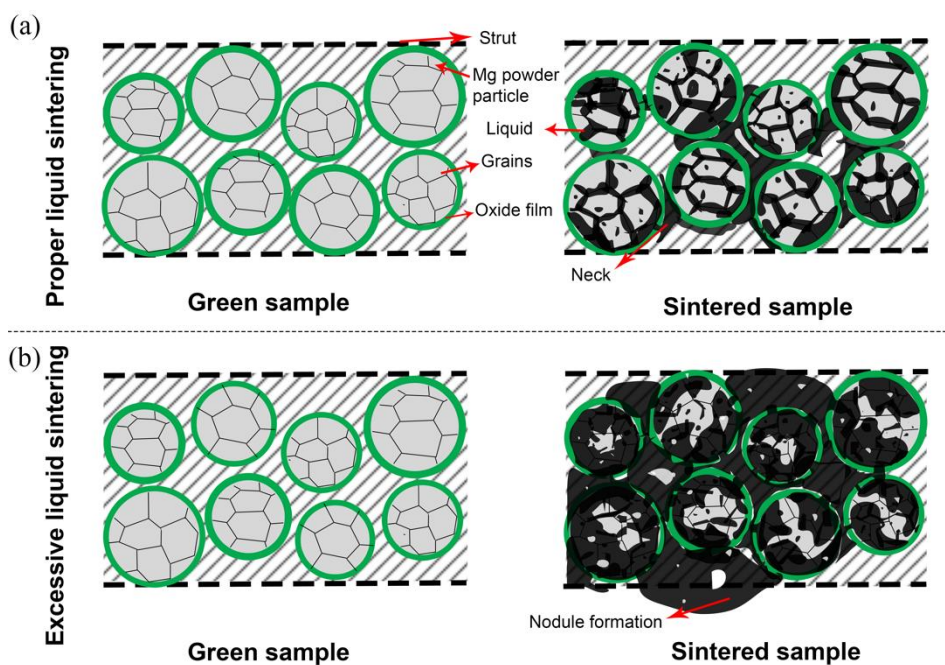


Figure 2.9 A schematic illustration of liquid-phase sintering of the Mg 3D scaffolds: (a) proper liquid-phase sintering and (b) excessive liquid-phase sintering.

The fidelity of Mg scaffolds or dimensional precision is of paramount importance. A proper sintering scheme (*i.e.*, 650 °C for 5 min) allowed for the fabrication of the Mg scaffolds with high fidelity (Figure 2.8), a high relative density of struts, and suitable macro porosity. The sintered scaffolds did not shrink much, as compared to the printed ones, since voids derived from the evaporation of the binder were still visible (Figure 2.7c4). In other words, the retention of micropores in the struts resulted in insignificant shrinkage. Although a longer holding time and a higher temperature increased the relative

density of struts (Table 2.2), they led to excessive liquid-phase sintering, which caused the formation of nodules and affected the strut fidelity (Figure 2.7a3-e3). A longer holding time caused the melting of more Mg and, thus, the formation of excessive Mg liquid. Apart from more liquid formation, higher sintering temperature also enhanced the flowability of Mg liquid through the cracked MgO envelope due to a decrease in its viscosity [34]. The main reason for the formation of nodules that occupied the designed macropores between struts was a lack of wetting of the molten Mg on powder particle surfaces. When the volume fraction of the liquid went beyond the capability of the capillary force to draw the whole liquid into the bridges formed in the sintered neck regions between powder particles, the excessive liquid reached the exterior of the struts (Figure 2.9b), tending to minimize its surface area by forming ball-shaped nodules (Figure 2.7). This phenomenon was also reported in another liquid-phase sintering study [35] and similarly, the balling effect occurred during SLM to fabricate Mg scaffolds [36].

2.4.4. Hierarchical pore structure

The binder removal and the subsequent formation of necks between Mg powder particles enabled the creation of a micropore structure inside the struts. At the same time, accurate 3D printing and high fidelity achieved in the process of debinding and sintering maintained the designed macro pores between the struts (Figure 2.8c). Therefore, the fabricated Mg scaffolds possessed an interconnected and hierarchical pore structure, including macropores (between struts) with sizes of 400 - 500 μm and micropores with sizes of 20 - 100 μm (inside struts). In comparison with the SLM technique that can only produce scaffolds with dense struts, the SC-3DP technique developed in the present study, is more attractive, given that both macropores and micropores play important roles in bone regeneration. Macropores provide spaces and tunnels for cell adhesion, new blood vessel formation and bone ingrowth. It has been found that implants have better osteogenesis when pore sizes are $> 300 \mu\text{m}$ [37, 38]. Other studies have found that pore sizes down to 50 μm are efficient in supporting bone ingrowth [39, 40]. Furthermore, the interconnected porous structure allows for cell growth and the transport of nutrients and metabolic waste [38]. Therefore, the porous Mg scaffolds fabricated in this study may have great potential to be used as bone substituting biomaterials that enable the regeneration of bone defects. Considering the structural features of the 3D printed scaffolds, it is worth taking further steps to investigate their mechanical properties, degradation behavior, *in vitro* cell response, and *in vivo* bone regeneration performance.

2.5. Conclusions

Biodegradable porous Mg scaffolds with interconnected pore structures were successfully fabricated using the SC-3DP approach. Ink characteristics were determined and the

parameters for 3D printing, debinding and sintering were optimized. All the prepared inks with 54, 58, and 62 vol% Mg powder loading exhibited viscoelastic behavior with adequate elastic moduli for the fabrication of self-supporting structures and were printable with optimized printing parameters (*i.e.*, applied pressure and printing speed). The 58 vol% Mg powder loaded ink possessed a wide printability window for printing 3D periodic lattice structures on a millimeter scale. The binder composed of polymer and additives could be removed from the green body and a highly limited amount of carbon residue was left over after debinding. Sintering at the melting point of pure Mg within a short time was found to be suitable for neck formation and for the final Mg scaffolds with good fidelity and considerable densification. As a result, Mg scaffolds with high porosity and a hierarchical pore structure could be obtained, presenting the possibilities for bone ingrowth. The results obtained from this study provided a new way of fabricating biodegradable Mg scaffolds for orthopedic applications.

References

- [1] C. Xu, A. Bouchemit, G. L'esperance, L. L. Lebel, D. Therriault, Solvent-cast based metal 3D printing and secondary metallic infiltration, *J. Mater. Chem. C* 5 (2017) 10448-10455.
- [2] C. Xu, Q. Wu, G. L'esperance, L. L. Lebel, D. Therriault, Environment-friendly and reusable ink for 3D printing of metallic structures, *Mater. Des.* 160 (2018) 262-269.
- [3] C. Yang, Z. G. Huan, X. Y. Wang, C. T. Wu, J. Chang, 3D printed Fe scaffolds with HA nanocoating for bone regeneration, *ACS Biomater. Sci. Eng.* 4 (2018) 608-616.
- [4] S. L. Taylor, A. E. Jakus, R. N. Shah, D. C. Dunand, Iron and nickel cellular structures by sintering of 3D-printed oxide or metallic particle inks, *Adv. Eng. Mater.* 19 (2017) 8.
- [5] J. P. Li, J. R. De Wijn, C. A. Van Blitterswijk, K. De Groot, The effect of scaffold architecture on properties of direct 3D fiber deposition of porous Ti6Al4V for orthopedic implants, *J. Biomed. Mater. Res. Part A*. 92A (2010) 33-42.
- [6] S. L. Taylor, A. J. Lbeh, A. E. Jakus, R. N. Shah, D. C. Dunand, NiTi-Nb micro-trusses fabricated via extrusion-based 3D-printing of powders and transient-liquid-phase sintering, *Acta Biomater.* 76 (2018) 359-370.
- [7] S. L. Taylor, R. N. Shah, D. C. Dunand, Ni-Mn-Ga micro-trusses via sintering of 3D-printed inks containing elemental powders, *Acta Mater.* 143 (2018) 20-29.
- [8] J. C. James E. Smay, And Jennifer A. Lewis, Colloidal Inks for directed assembly of 3-D Periodic Structures, *Langmuir*. 18 (2002) 5429-5437.
- [9] M. Doube, M. M. Klosowski, I. Arganda-Carreras, F. P. Cordelieres, R. P. Dougherty, J. S. Jackson, B. Schmid, J. R. Hutchinson, S. J. Shefelbine, BoneJ: Free and extensible bone image analysis in ImageJ, *Bone*. 47 (2010) 1076-1079.
- [10] M. Calvo, A. E. Jakus, R. N. Shah, R. Spolenak, D. C. Dunand, Microstructure and processing of 3D printed tungsten microlattices and infiltrated W-Cu composites, *Adv. Eng. Mater.* 20 (2018) 9.
- [11] A. E. Jakus, E. B. Secor, A. L. Rutz, S. W. Jordan, M. C. Hersam, R. N. Shah, Three-dimensional printing of high-content graphene scaffolds for electronic and biomedical applications, *ACS Nano*. 9 (2015) 4636-4648.
- [12] A. E. Jakus, A. L. Rutz, S. W. Jordan, A. Kannan, S. M. Mitchell, C. Yun, K. D. Koube, S. C. Yoo, H. E. Whiteley, C. P. Richter, R. D. Galiano, W. K. Hsu, S. R. Stock, E. L. Hsu, R. N. Shah, Hyperelastic "bone": A highly versatile, growth factor-free, osteoregenerative, scalable, and surgically friendly biomaterial, *Sci. Transl. Med.* 8 (2016) 15.
- [13] W. E. R. Richard J. Higgins, Michael J. Cima, and H. Kent Bowen, Ceramic surface reactions and carbon retention during non-oxidative binder removal: Al₂O₃/Poly(methyl methacrylate) at 20°-700°C, *J. Am. Ceram. Soc.* 77 (1994) 2243-2253.
- [14] W. E. R. Keigo Hirakata, Michael J. Cima, Surface chemistry of lead titanate and its impact on binder removal, *J. Am. Ceram. Soc.* 79 (1996) 1002-1008.
- [15] N. Paxton, W. Smolan, T. Bock, F. Melchels, J. Groll, T. Jungst, Proposal to assess printability of bioinks for extrusion-based bioprinting and evaluation of rheological properties governing bioprintability, *Biofabrication*. 9 (2017) 044107.
- [16] S. Hong, C. Sanchez, H. Du, N. Kim, Fabrication of 3D printed metal structures by use of high-viscosity Cu paste and a screw extruder, *J. Electron. Mater.* 44 (2015) 836-841.

- [17] U. Scheithauer, E. Schwarzer, H.-J. Richter, T. Moritz, Thermoplastic 3D printing-An additive manufacturing method for producing dense ceramics, *Int. J. Appl. Ceram. Technol.* 12 (2015) 26-31.
- [18] J. M. Lee, W. Y. Yeong, Design and printing strategies in 3D bioprinting of cell-hydrogels: A review, *Adv. Healthc. Mater.* 5 (2016) 2856-2865.
- [19] M. Mooney, The viscosity of a concentrated suspension of spherical particles *J. Colloid Sci.* 6 (1950) 162-170.
- [20] M. M. Rueda, M. C. Auscher, R. Fulchiron, T. Perie, G. Martin, P. Sonntag, P. Cassagnau, Rheology and applications of highly filled polymers: A review of current understanding, *Prog. Polym. Sci.* 66 (2017) 22-53.
- [21] Y. Z. Guangqiang Xie, And Wenshu Lin A, Plasticizer combinations and performance of wood flour–poly(lactic acid) 3D printing filaments, *BioResources.* 12 (2017) 6736-6748.
- [22] C. R. Tubio, F. Guitian, A. Gil, Fabrication of ZnO periodic structures by 3D printing, *J. Eur. Ceram. Soc.* 36 (2016) 3409-3415.
- [23] J. A. Lewis, Direct-write assembly of ceramics from colloidal inks, *Curr. Opin. Solid State Mat. Sci.* 6 (2002) 245-250.
- [24] R. B. Rao, K. L. Krafcik, A. M. Morales, J. A. Lewis, Microfabricated deposition nozzles for direct-write assembly of three-dimensional periodic structures, *Adv. Mater.* 17 (2005) 289-293.
- [25] A. J. Poslinski, M. E. Ryan, R. K. Gupta, S. G. Seshadri, F. J. Frechette, Rheological behavior of filled polymeric systems I. Yield stress and shear-Thinning effects, *J. Rheol.* 32 (1988) 703-735.
- [26] W. Z. Edidiong Nseowo Udofia, Microextrusion Based 3D Printing – A Review, in *The 29th Annual International Solid Freeform Fabrication Symposium*, TMS, Texas, USA, 2018.
- [27] M. Li, X. Tian, D. J. Schreyer, X. Chen, Effect of needle geometry on flow rate and cell damage in the dispensing-based biofabrication process, *Biotechnol. Prog.* 27 (2011) 1777-1784.
- [28] N. H. L. Z.Y. Liu, S.B. Tor, K.A. Khor, Y. Murakoshi, R. Maeda, Binder system for micropowder injection molding, *Mater. Lett.* 48 (2001) 31-38.
- [29] J. A. Lewis, Binder removal from ceramics, *Annu. Rev. Mater. Sci.* 27 (1997) 147-173.
- [30] M. Salehi, S. Maleksaeedi, H. Farnoush, N. M. L. Sharon, G. K. Meenashisundaram, M. Gupta, An investigation into interaction between magnesium powder and Ar gas: Implications for selective laser melting of magnesium, *Powder Technol.* 333 (2018) 252-261.
- [31] Z. A. Munir, Analytical treatment of the role of surface oxide layers in the sintering of metals, *J. Mater. Sci.* 14 (1979).
- [32] M. Salehi, S. Maleksaeedi, M. a. B. Sapari, M. L. S. Nai, G. K. Meenashisundaram, M. Gupta, Additive manufacturing of magnesium–zinc–zirconium (ZK) alloys via capillary-mediated binderless three-dimensional printing, *Mater. Des.* 169 (2019) 107683.
- [33] M. Beghi, G. Caglioti, V. Carvelli, C. Poggi, Liquid hot isostatic pressing of QE22A magnesium alloy: A preliminary test, *Metal. Sci. Technol.* 21 (2003).
- [34] H. L. Mi Guangbao, Li Peijie, P.S.Popel, I.S.Abaturrov, Viscosity of AZ91D magnesium alloy melt with small additions of calcium, *Chin. J. Nonferrous Met.* 19 (2009) 1372-1378.

- [35] M. Salehi, S. Maleksaeedi, M. L. S. Nai, M. Gupta, Towards additive manufacturing of magnesium alloys through integration of binderless 3D printing and rapid microwave sintering, *Addit. Manuf.* 29 (2019) 100790.
- [36] V. Manakari, G. Parande, M. Gupta, Selective laser melting of magnesium and magnesium alloy powders: A review, *Metals.* 7 (2016) 2-35.
- [37] V. Karageorgiou, D. Kaplan, Porosity of 3D biomaterial scaffolds and osteogenesis, *Biomaterials.* 26 (2005) 5474-5491.
- [38] X. J. Wang, S. Q. Xu, S. W. Zhou, W. Xu, M. Leary, P. Choong, M. Qian, M. Brandt, Y. M. Xie, Topological design and additive manufacturing of porous metals for bone scaffolds and orthopaedic implants: A review, *Biomaterials.* 83 (2016) 127-141.
- [39] C.-K. L. Bong-Soon Chang, Choon-Ki Lee, Osteoconduction at porous hydroxyapatite with various pore configurations, *Biomaterials.* 21 (2000) 1291-1298.
- [40] F. He, G. Qian, W. Ren, J. Li, P. Fan, H. Shi, X. Shi, X. Deng, S. Wu, J. Ye, Fabrication of β phosphate composite ceramic sphere-based scaffolds with hierarchical pore structure for bone regeneration, *Biofabrication.* 9 (2017) 025005.

Supplementary material



Figure S2.1 Liquid phase fraction of the Mg-Zn scaffolds as a function of temperature for defining the working window of liquid-phase sintering.

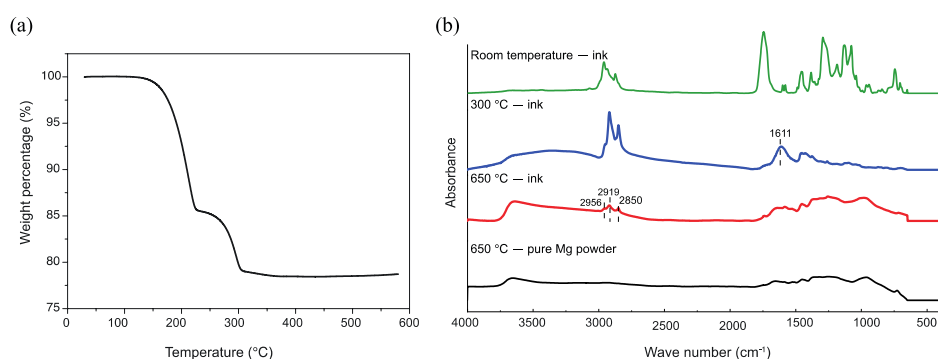


Figure S2.2 Characteristics of the interactions between the PLGA binder and Mg powder during debinding: (a) TGA performed at 10 °C/min with argon flow, showing the decomposition of plasticizers at 125 - 225 °C and PLGA polymer at 260 - 303 °C, (b) FTIR analysis results showing that a new peak at 1611 cm⁻¹ appeared after the material

was heated to 300 °C and it disappeared after the material was heated to 650 °C. The band could be identified as metal carboxylate asymmetric stretching absorbance [S1]. The spectra of pure Mg powder and the ink after heating to 650 °C were similar to each other, indicating that most of the binder were decomposed. The only difference lay in the three bands at 2850 - 2960 cm^{-1} in the spectrum of the ink, which corresponded to the stretching vibration of the C-H group. This demonstrated that the interactions between PLGA and Mg powder during debinding led to the production of nonvolatile char.

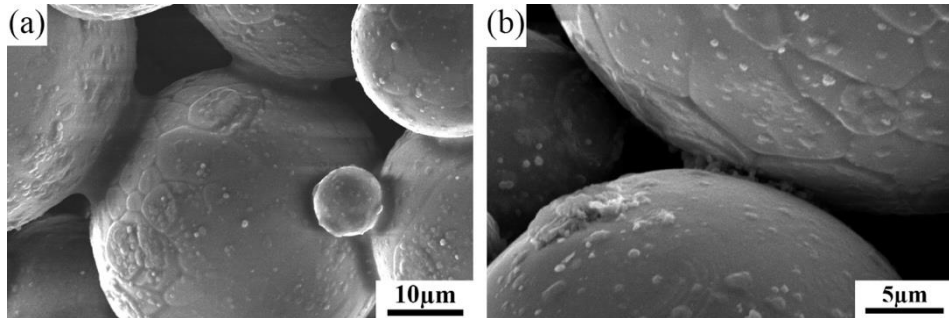


Figure S2.3 Interactions between the PLGA binder and Mg powder during debinding: (a) binder bonded Mg powder particles before debinding and (b) residues anchoring on Mg powder particle surfaces after debinding at 300, 450 or 630 °C.

Reference

[S1] R. J. Higgins, W. E. Rhine, M. J. Cima, H. K. Bowen, Ceramic surface reactions and carbon retention during non-oxidative binder removal: Al_2O_3 /poly(methyl methacrylate) at 20-700°C, *J. Am. Ceram. Soc.* 77 (1994) 2243-2253.

3

Ink extrusion-based additive manufacturing of pure Mg scaffolds

Here, we present a new generation of extrusion-based 3D printed porous Mg scaffolds that are coated with MgF_2 and MgF_2 -CaP to improve their corrosion resistance and biocompatibility, thereby bringing the AM scaffolds closer to meeting the clinical requirements for bone substitution. The mechanical properties, in vitro biodegradation behavior, electrochemical response, and biocompatibility of the 3D printed Mg scaffolds with a macroporosity of 55% and a strut density of 92% were evaluated. Furthermore, comparisons were made between the bare scaffolds and the scaffolds with the coatings. The coating not only covered the struts but also infiltrated the struts through micropores, resulting in decreases in both macro- and micro-porosity. The bare Mg scaffolds exhibited poor corrosion resistance due to highly interconnected porous structure, while the MgF_2 -CaP coatings remarkably improved the corrosion resistance, lowering the biodegradation rate of the scaffolds down to 0.2 mm/y. The compressive mechanical properties of the bare and coated Mg scaffolds before and during in vitro immersion tests up to 7 days were both in the range of the values reported for the trabecular bone. Moreover, direct culture of MC3T3-E1 preosteoblasts on the coated Mg scaffolds confirmed their good biocompatibility.¹

¹ The chapter is based on a scientific paper: J. Dong, N. Tümer, N.E. Putra, J. Zhu, Y. Li, M.A. Leeftang, P. Taheri, L.E. Fratila-Apachitei, J.M.C. Mol, A.A. Zadpoor, J. Zhou, Extrusion-based 3D printed magnesium scaffolds with multifunctional MgF_2 and MgF_2 -CaP coatings, *Biomater. Sci.* 9 (2021), 7159-7182.

3.1. Introduction

Extrusion-based AM technique has been successfully applied to fabricate porous Mg scaffolds [1]. With this technique, Mg scaffolds can be printed at room temperature by extruding a Mg powder loaded ink into a designed porous structure, followed by debinding and sintering to decompose the binder present in the ink and consolidate the remaining Mg powder. This technique can, indeed, avoid the difficulties that have been encountered in applying powder bed fusion AM for fabricating Mg scaffolds. Moreover, unlike powder bed fusion AM, extrusion-based AM is capable of delivering hierarchically interconnected porous Mg scaffolds that can only be achieved through template-replicating method [2, 3] and facilitate cell adhesion, proliferation, migration and differentiation [4].

Pure Mg was chosen in our first attempt to make the material system simple [1]. However, in general, pure Mg exhibits a relatively high biodegradation rate [5-7], which can cause premature implant failure and the generation of a large amount of hydrogen gas, triggering acute and unfavorable inflammatory responses. The large surface area of porous Mg exposed to physiological media accelerates the biodegradation further. The high rate of biodegradation also leads to a high rate of ion release, which negatively affects the cytocompatibility of porous Mg. Slowing down the biodegradation process is therefore of paramount importance and thus the focus of the present research. Surface modification is a well-known technology to improve the corrosion resistance of Mg [8], *i.e.*, to reduce its biodegradation rate. To date, various surface modification methods have been developed for Mg [9]. However, ensuring the consistent quality of coating on the strut surfaces with micropores in a 3D porous structure remains a challenge due to the geometric complexities of the surfaces and the porous structure as a whole [10]. The highly porous structure of the fabricated scaffolds must be taken into consideration, when it comes to the choice of the methods suitable for surface modification. For porous structures, the chemical conversion method is usually preferred, since the chemical reaction between the Mg substrate and chemical conversion solution during the coating procedure allows any exposed Mg surfaces to be uniformly coated. Among various conversion coatings, fluoride conversion coating is one of the most effective methods for porous Mg-based materials, since it has been found that a MgF_2 coating layer can, indeed, form on the entire surface of the struts of porous Mg [3, 11, 12], although the pore sizes of the scaffolds used in those studies (150-400 μm) are much larger than the sizes of the micropores that were present in the struts of the scaffolds fabricated earlier (10-100 μm) [1]. In addition to improving the corrosion resistance, MgF_2 coating has the other advantages of strongly adhering to the Mg substrate and demonstrating good biocompatibility [13, 14]. However, MgF_2 coating has a limited osteogenic ability [3]. To overcome this limitation, an additional coating consisting of calcium phosphate (CaP)

compounds may be superimposed, considering their osteoconductive ability that is essential for bone regeneration and maturation through promoting osteoblast proliferation [15, 16]. The combination of both fluoride and CaP coatings with MgF₂ as an interlayer on bulk Mg-based materials has, indeed, turned out to be advantageous for orthopedic applications [17, 18]. However, there is yet no information available in the literature regarding the applicability of MgF₂-CaP coatings to geometrically ordered and hierarchical porous Mg scaffolds, although such coatings have been applied to solid magnesium and Mg alloy samples and demonstrated the expected benefits.

Here, we fabricated porous Mg scaffolds using the extrusion-based AM technique and applied MgF₂ single-layer coating and MgF₂-CaP double-layer coatings to the scaffolds. We evaluated the mechanical properties, biodegradation behavior, and biocompatibility of the bare and coated Mg scaffolds. By proving the feasibility of applying multifunctional coatings on the Mg scaffolds and the resultant enhanced corrosion resistance and surface biocompatibility, we intended to bring the AM Mg scaffolds closer to their application as a qualified bone substitute.

3.2. Material and methods

3.2.1. Scaffold manufacturing

Pure Mg powder (impurity < 0.01%) with a median particle size of 44.96 μm (Tangshan Weihao Magnesium Powder Co. Ltd., China) was used as the starting material. A Mg powder loaded ink was prepared by manually mixing 50 vol% Mg powder particles with a binder system composed of hexane and polyisobutylene polymer (Mw ~ 500,000, Sigma Aldrich, Germany). The ink was loaded into a syringe (EFD, Nordson, Germany) mounted on a 3D Bioscaffolder printer (BS 3.2, GeSim, Germany).

A cylindrical porous architecture with a lay-down pattern of 0°/90°/0° was designed using the GeSim custom software (Figure 3.1a). A linear infill pattern with a strut size of 580 μm and a spacing distance of 360 μm were adopted (Figure 3.1b), resulting in a density of 62.2% (calculated by SolidWorks) or a macro-porosity of 37.8%.

The Mg scaffolds were then printed using the Bioscaffolder printer by extruding the prepared ink under an applied pressure of 140-160 kPa and at a printing speed of 5 mm/s. The printed scaffolds were then subjected to debinding and sintering, which was conducted in a tube furnace (Carbolite Gero, Germany) under a controlled atmosphere of argon (purity ≥ 99.9999%). The printed scaffolds were heated at a rate of 5 °C/min from room temperature to 640 °C with a dwelling time of 1 h, followed by furnace cooling to room temperature. These fabricated scaffolds are hereafter referred to as “bare Mg”.

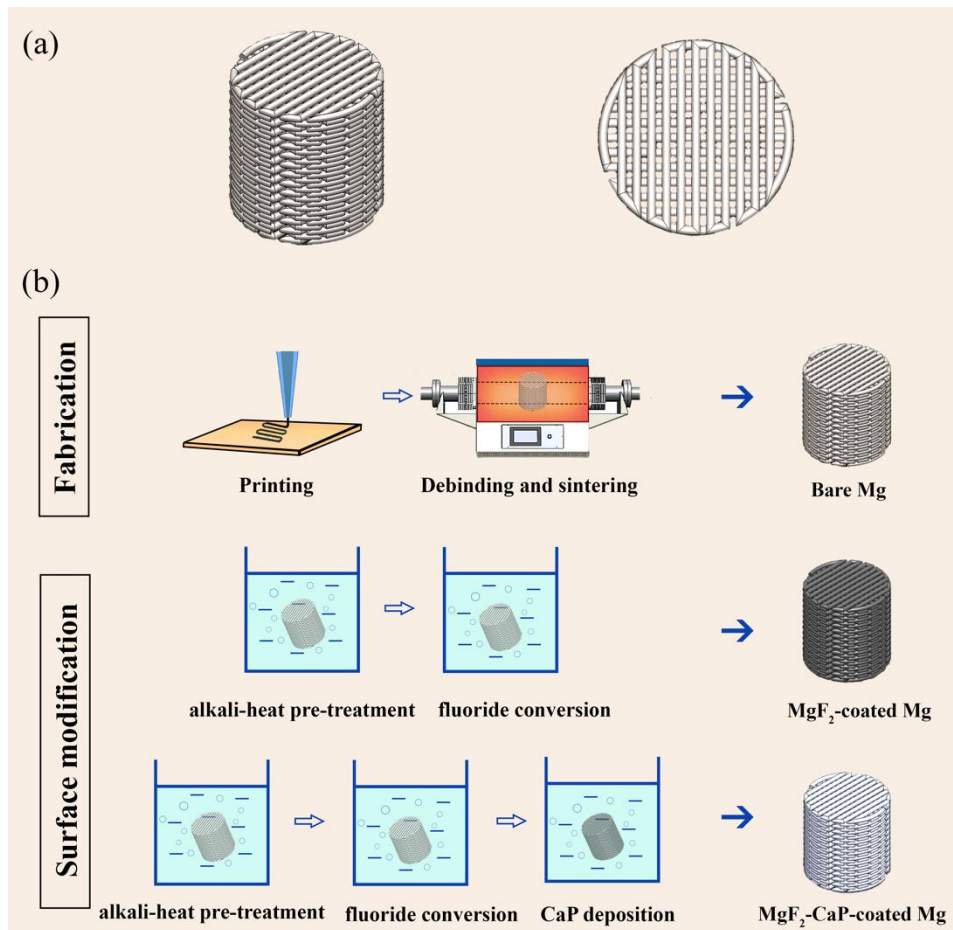


Figure 3.1 Design of porous Mg scaffold (a, b) and the schematic illustrations of the steps of scaffold fabrication and then surface modification (c).

3.2.2. Surface modification

3.2.2.1. Fluoride conversion

Prior to the fluoride conversion treatment, an alkali-heat pre-treatment was performed. The bare Mg scaffolds were boiled in a 5 mol NaOH solution at 80 °C for 24 h. Then, they were cleaned with distilled water and isopropanol for 5 min, respectively, followed by air drying. For the fluoride conversion treatment, the alkali-heat pre-treated scaffolds were then immersed in 40% hydrofluoric acid (HF) at room temperature for 66 h [18]. The fluoride-treated scaffolds were then rinsed with distilled water and isopropanol, and

followed by air drying. The fluoride-treated scaffolds are hereafter referred to as “MgF₂-coated Mg” (Figure 3.1c).

3.2.2.2. CaP coating deposition on the MgF₂ interlayer

The hydrothermal deposition method was used for CaP coating deposition. The MgF₂-coated Mg scaffolds were immersed in a mixture of Na₂HPO₄·12H₂O (9.41 g/L) and Ca(NO₃)₂ (26.20 g/L) at 70 °C for 24 h, followed by washing with distilled water and air drying [19]. The coated scaffolds are hereafter denoted as “MgF₂-CaP-coated Mg” (Figure 3.1c).

3.2.3. Microstructural characterization

The Mg powder embedded in an epoxy resin and fabricated Mg scaffold struts were ground, polished, and etched in a solution composed of nitric acid, acetic acid, water, and ethanol at a volume ratio of 1:3:4:12. After etching, the microstructure of the Mg powder was observed using an optical microscope (OM, VH-Z250R, Keyence Corp., USA), while that of the fabricated Mg scaffold struts was observed under a scanning electron microscope (SEM, JSM-IT100, JEOL, Japan). The average grain size was determined by using the line intercept method.

3.2.4. Porosity characterization

The porosity of the as-printed Mg scaffolds was calculated using the weighing method, based on the equation:

$$\text{Absolute porosity} = 1 - \left(\frac{m_{p-Mg}}{V_{bulk}} \right) / \rho_{p-Mg} \quad (1)$$

where m_{p-Mg} is the weight of the as-printed Mg scaffolds, V_{bulk} the bulk volume of the as-printed Mg scaffolds and ρ_{p-Mg} the density of printed Mg scaffolds (*i.e.*, 1.61 g/cm³, calculated from the Mg ink after solvent evaporation).

The porosities of the bare, MgF₂-coated, and MgF₂-CaP-coated Mg scaffolds were determined in three ways. First, a simple weighing method was adopted, based on the following equation:

$$\text{Absolute porosity} = 1 - \left(\frac{m_{Mg}}{V_{bulk}} \right) / \rho_{Mg} \quad (2)$$

where m_{Mg} is the weight of the sample, V_{bulk} the bulk volume of the scaffold sample, and ρ_{Mg} the theoretical density of pure Mg (*i.e.*, 1.74 g/cm³).

Second, X-ray micro-computed tomography (μ CT, Nanotom 180 NF, GE Phoenix) with a resolution of 6 μm was used to scan the Mg scaffolds. Dicom images of the scanned samples were exported to Dragonfly (Object Research Systems, Canada) after reconstruction. Suitable thresholding was applied to segment each sample. The “Bone volume” corresponding to the volume of the scaffold sample and “Total volume” corresponding to the bulk volume of the scaffold sample were measured by using the plugin “bone analysis” in the same software. The absolute porosity was obtained according to the equation:

$$\text{Absolute porosity} = 1 - \frac{V_{Mg}}{V_{bulk}} \quad (3)$$

where V_{Mg} is the volume of the sample and V_{bulk} the bulk volume.

Third, the interconnected porosity and pore size distribution were measured by means of mercury intrusion porosimetry (MIP, Micromeritics Autopore IV 9500) at pressures over the range of 0 to 210 MPa. Pore interconnectivity was quantified using the following equation:

$$\text{Interconnectivity} = \frac{\text{interconnected porosity}}{\text{absolute porosity}} \quad (4)$$

where the absolute porosity was obtained from the weighing method, as described above.

3.2.5. Characterization of surface-modified scaffold struts

The morphologies and the cross-section microstructures of the bare, MgF_2 -coated, and MgF_2 -CaP-coated Mg scaffolds at the periphery and at the center were examined using a scanning electron microscope (SEM, JSM-IT100, JEOL, Japan) equipped with energy-dispersive X-ray spectroscopy (EDS). The microporosities of the bare and coated Mg scaffolds, the layer thicknesses of MgF_2 and MgF_2 -CaP coatings, and the volume fractions of the Mg matrix, the coatings, and the compounds formed inside micropores were measured from the SEM images of the polished cross sections using the ImageJ software (National Institutes of Health, USA). The phase identification of the scaffolds was performed using an X-ray diffractometer (XRD, Bruker D8 Advance diffractometer in the Bragg-Brentano geometry). The diffractometer was equipped with a Lynxeye position sensitive detector and was operated at 45 kV and 40 mA over a scan range of 20–100° and at a step size of 0.030° using Cu K α radiation. In addition, Fourier-transform infrared spectroscopy (FTIR) spectra were obtained using a Thermo-Nicolet Nexus FTIR apparatus equipped with a liquid-nitrogen cooled MCT-A (mercury-cadmium-telluride) detector and a smart apertured grazing angle (SAGA) accessory at an incident angle of 80°. An infrared background was collected on the bare Mg scaffolds for collecting the

final spectra of the MgF₂-coated and MgF₂-CaP-coated Mg scaffolds with the setting of 128 scans at a resolution of 2 cm⁻¹.

3.2.6. *In vitro* degradation behavior

3.2.6.1. Immersion tests

In vitro immersion tests of the bare, MgF₂-coated, and MgF₂-CaP-coated Mg scaffolds (12.38 mm in diameter and 12.64 mm in height) were conducted in the revised simulated body fluid (r-SBF) [20] for 7 days. The height and diameter of the scaffolds were chosen to be both larger than 10 mm in order to perform the mechanical tests of the as-fabricated scaffolds and those that were retrieved after the immersion tests at selected time points according to the ISO 13314 standard [21] which specifies that all spatial dimensions of specimen for compression test (*i.e.*, diameter and height) should not be less than 10 mm with a specimen height to diameter ratio between 1 and 2. The temperature of the thermal bath was maintained at 37 °C. 450 mL r-SBF solution was used for the immersion test of each specimen. The solution volume-to-surface area ratio was 7 mL/cm² [22]. The tests were performed in triplicate. Two micro pH-meter electrodes (inlabNMR, METTLER TOLEDO) were used to monitor the changes of the local (*i.e.*, close to the outer surface of the specimen) and distant (*i.e.*, further away from the specimen) pH values. Mg, Ca, and P ion concentrations in the r-SBF solution after the immersion tests of the bare and coated Mg scaffolds up to 7 days were analyzed using an inductively coupled plasma optical emission spectroscope (ICP-OES, iCAP 6500 Duo Thermo Fisher Scientific). The bare, MgF₂-coated, and MgF₂-CaP-coated Mg scaffolds after the immersion tests were imaged using the same μ CT scanner and same scanning protocol as it was done previously and the images were exported after reconstruction. After segmenting the coating(s) and degradation products separately using the Dragonfly software, the volumes of the Mg substrate were calculated using the plugin “bone analysis” and the volume loss was calculated using the following equation:

$$\text{Volume loss} = \frac{V_{Mg \text{ before degradation}} - V_{Mg \text{ after degradation}}}{V_{Mg \text{ before degradation}}} \quad (5)$$

where $V_{Mg \text{ before degradation}}$ and $V_{Mg \text{ after degradation}}$ are the volumes of the scaffolds before and after immersion, respectively.

The morphologies and cross-section microstructures of the Mg scaffolds at the periphery and at the center after the immersion tests at selected time points were observed under the SEM (JSM-IT100, JEOL, Japan). The compositions of the degradation products formed on the scaffolds were analyzed using EDS, while the phase identification was examined by XRD (Bruker D8 Advance diffractometer in the Bragg-Brentano geometry).

The FTIR spectra of the degraded bare, MgF₂-coated, and MgF₂-CaP-coated porous Mg specimens were obtained with those before the biodegradation as the background.

3.2.6.2. Electrochemical tests

Copper foil tapes were attached to the bare, MgF₂-coated, and MgF₂-CaP-coated Mg samples for connecting to copper wires, before the samples were partially mounted in an epoxy resin. The scaffold sample with a surface area of 12.37 cm² was exposed to the electrolyte. Electrochemical tests were performed in triplicate using a Bio-Logic SP-200 potentiostat (Bio-Logic Science Instruments, France) in r-SBF at 37 °C. A three-electrode electrochemical cell was set up with graphite as the counter electrode, Ag/AgCl as the reference electrode, and bare or coated Mg scaffold sample as the working electrode. Potentiodynamic polarization (PDP) and linear polarization resistance (LPR) tests were carried out. The samples were first allowed to stabilize at the open circuit potential (OCP) for 1 h. Then, the polarization started at an initial potential of -0.3 V *versus* OCP and increased to +0.5 V *versus* OCP at a scan rate of 0.5 mV/s. The corrosion potentials E_{corr} and corrosion current density i_{corr} were determined by the Tafel method through linear extrapolation using the EC-lab software. From the PDP results, the corrosion rates (CR) were calculated according to the ASTM standard G102-89 and using:

$$CR_{\text{electrochemical}}[mm/y] = 3.27 \times 10^{-3} \times EW \times \frac{i_{\text{corr}}}{\rho} \quad (6)$$

where EW is the equivalent weight of Mg (valence 2), i_{corr} the current density [$\mu\text{A}/\text{cm}^2$], and ρ the theoretical density of Mg [g/cm^3].

The LPR tests were conducted at different times of exposure up to 3 days from -25 mV to +25 mV *versus* OCP at a scan rate of 0.167 mV/s. (After 3 days, the electrolyte penetrated into the trench between the resin and embedded Mg scaffolds due to the degradation of the scaffolds, resulting in unreliable results.)

3.2.7. Mechanical properties

Uniaxial compression tests of the as-fabricated bare Mg, MgF₂-coated Mg and MgF₂-CaP-coated Mg scaffolds, as well as the MgF₂-coated and MgF₂-CaP-coated scaffold specimens retrieved after 1, 3, and 7 days of *in vitro* immersion, were performed using a Lloyd machine (LR5K, 5 kN load cell) at a crosshead speed of 2 mm/min. The Young's moduli and yield strengths of the tested specimens were determined according to ISO 13314: 2011. The Young's modulus was determined from the slope of the initial linear region of the obtained stress-strain curve and the yield strength was determined from the intersection between the curve and the parallel line at 0.2% offset to the linear region. Beyond this point, permanent deformation occurred, as well as work hardening and more

importantly the densification of the porous structure, leading to increases in stress. Considering the requirement for bone implants to provide mechanical support while maintaining an interconnected porous structure, the stresses beyond the yield stress were considered of less interest.

3.2.8. Biocompatibility evaluation

3.2.8.1. Cell preculture and extract preparation

Preosteoblast MC3T3-E1 cells (Sigma-Aldrich, Germany) were pre-cultured in α -minimal essential medium (α -MEM, Thermo Fisher Scientific, USA) without ascorbic acid, but supplemented with 10% fetal bovine serum (FBS, Thermo Fisher Scientific, USA) and 1% penicillin/streptomycin (p/s, Thermo Fisher Scientific, USA) for 7 days under physiological conditions (5% CO₂ and 37 °C). The medium was refreshed every 2-3 days.

The extract culture media were prepared by immersing bare, MgF₂-coated, and MgF₂-CaP-coated Mg scaffold samples (9.54 mm in diameter and 4.85 mm in height) in the α -MEM (without ascorbic acid, but with 10% FBS, 1% p/s) under the abovementioned physiological conditions for 72 h [23]. The ratio of surface area of the sample to the volume of the medium was 1.25 cm²/mL, according to the EN ISO standards 10993-12 [24]. The supernatant was then collected, filtered, and diluted into 100, 50 and 10% with the α -MEM. The pH of these extracts was measured by using a pH-meter (METTLER TOLEDO) and the Mg ion concentrations in those extracts were measured using ICP-OES (iCAP 6500 Duo Thermo Fisher Scientific).

3.2.8.2. Indirect cytocompatibility tests

MC3T3-E1 cells (1×10^4 cells) were seeded in a 24 well plate and cultured in the α -MEM for 24 h. Thereafter, the α -MEM was exchanged with the 100, 50 and 10% extracts of the bare, MgF₂-coated Mg, and MgF₂-CaP-coated porous Mg samples. The original α -MEM (without ascorbic acid, but with 10% FBS, 1% p/s) served as the negative control. After 1, 3, and 7 days of cell culture, the extracts were replaced with fresh α -MEM (without ascorbic acid, but with 10% FBS, 1% p/s) to prevent any interference between the extract and the assay. At the indicated time points, 50 μ L Prestoblue reagent was added per well, prior to incubation at 37 °C for 1 h. Absorbance values were measured using a Victor X3 microplate reader (Perkin Elmer, The Netherlands) over a wavelength range of 530 to 590 nm. The tests were performed in triplicate. The average metabolic activity of the cells was calculated using:

$$\text{Metabolic activity} = \frac{\text{Absorbance (Mg specimen)}}{\text{Absorbance (negative control)}} \times 100\% \quad (7)$$

Furthermore, actin staining was performed to observe the morphology of the cells cultured with the extracts. The MC3T3-E1 cells (5×10^3 cells) were cultured for 7 days on 48-well glass disks in 200 μ L of the extracts. The samples were washed with phosphate buffered saline (PBS, Sigma-Aldrich, Germany), fixed using 4% formaldehyde/PBS (Sigma-Aldrich, Germany) for 15 min at room temperature, and permeabilized with 0.5% Triton/PBS at 4 °C for 5 min. Afterwards, 1% bovine serum albumin (BSA)/PBS (Sigma-Aldrich, Germany) was added per well, followed by 5 min of incubation, the addition of rhodamine phalloidin (1:1000 in 1% BSA/PBS, Life Technologies Corp., USA), and incubation at 37 °C for 1 h. The samples were then washed by 0.5% Tween/PBS (Sigma-Aldrich, Germany) three times prior to being mounted on glass slides with Prolong gold (containing 4',6-diamidino-2-phenylindole (DAPI), Life Technologies, USA). The cytoskeleton and cell nuclei were examined using a fluorescence microscope (ZOE fluorescent cell imager, Bio-Rad Laboratories Inc., USA).

3.2.8.3. Direct cytocompatibility tests

To observe the morphology of the cells seeded on the bare, MgF₂-coated, and MgF₂-CaP-coated Mg scaffolds, a live/dead staining assay was performed. The MC3T3-E1 preosteoblasts (4×10^5 cells per samples) were dropwise seeded on the scaffolds (9.54 mm in diameter and 2.26 mm in height) and were cultured in 8 mL α -MEM (without ascorbic acid, but with 10% FBS, 1% p/s). Compared to the other tests, smaller scaffolds with smaller surface area (883.95 mm²) were used here to ensure the ratio of surface area to medium volume at 1.25 cm²/mL, as each well in 6 well plate cannot accommodate more than 8 mL medium. Powder bed fusion AM fabricated titanium (Ti-6Al-4V) scaffolds with a similar design served as the reference material. After 1 day and 3 days of cell culture, the scaffolds were taken out of the medium and the medium was stored. The samples were then washed with PBS and incubated in PBS containing 2 μ L/mL of calcein and 1.5 μ L/mL of ethidium homodimer-1 (LIVE/DEAD Viability/Cytotoxicity Kit, Life Technologies Corp., USA) for 15 min in the dark at room temperature. Afterwards, the PBS solution was replaced with the previously stored medium to prevent further reaction between the PBS and scaffolds during the imaging process, prior to the observation of live and dead cells on the scaffolds under the fluorescence microscope. Furthermore, the morphology of the cells residing on the surface of the specimens was inspected with SEM. After 1 day and 3 days of cell culture, the samples were washed with PBS, fixed with 4% formaldehyde for 15 min, followed by a dehydration step in 50, 70, and 100% ethanol for 10 min each. Hexamethyldisilazane was further used for 30 min. The samples were dried for at least 2 h and then gold sputtered prior to SEM imaging.

3.2.9. Statistical analysis

All the experimental values are expressed as mean \pm standard deviation. The statistical analysis of the metabolic activity results obtained from the indirect cytotoxicity tests was performed using ANOVA, followed by the Tukey *post hoc* test ($\alpha = 0.05$) with $p < .0001$, ****; $p < .001$, ***; $p < .01$, and **; $p < .05$, *; *n.s.* = not significant.

3.3. Results

3.3.1. Geometrical characteristics of the as-sintered and as-coated scaffolds

The as-printed pure Mg scaffolds showed a geometrically ordered porous structure with accurate stacks of layers of struts, as designed, with an average strut width of $587.6 \pm 11.7 \mu\text{m}$ and a strut spacing of $351.4 \pm 18.5 \mu\text{m}$ (Figure 3.2a). During subsequent sintering, the overall dimensions of the scaffolds shrank by $9.5 \pm 0.2\%$. As a result, the as-sintered scaffolds had a reduced strut width of $528.1 \pm 12.6 \mu\text{m}$ and a strut spacing of $298.4 \pm 16.6 \mu\text{m}$ (Table 3.1). After the fluoride conversion treatment, the MgF_2 -coated Mg scaffolds showed a brown surface with dimensions similar to the as-sintered ones, while the MgF_2 -CaP-coated Mg scaffolds had a rough, white surface with an increased average strut width of $562.1 \pm 38.0 \mu\text{m}$ and a reduced strut spacing of $246.9 \pm 21.7 \mu\text{m}$ (Figure 3.2a and Table 3.1).

The porosities measured using the weight-volume and μCT methods showed the same trend. As compared to the bare Mg scaffolds (around 55%), the absolute porosity of the MgF_2 -coated Mg scaffolds decreased (around 50%). After coating with MgF_2 -CaP, the absolute porosity of the scaffolds further decreased to around 45% (Figure 3.2b). MIP was used to measure the interconnected porosities of the scaffolds. The coated scaffolds possessed less interconnected pores, as compared with the bare Mg scaffolds. However, each of the three groups of the Mg scaffolds still possessed a pore interconnectivity of above 80%. In addition, the pore size distribution determined by MIP showed a bimodal distribution of pore sizes in the bare and coated Mg scaffolds. The pores with sizes ranging between 100 and 400 μm corresponded to the macropores between the struts, defined in the scaffold design. The second peak of the pore diameter of the MgF_2 -CaP-coated Mg scaffolds decreased to around 200 μm , from those in the bare and MgF_2 -coated Mg scaffolds (around 300 μm) (Figure 3.2c). The pores with sizes below 50 μm corresponded to micropores in the struts, which were the residual micropores after the debinding and sintering processes, and the volume of micropores, as indicated by the first pore size peak, decreased significantly after the application of the surface modification (Figure 3.2c).

The as-sintered Mg scaffolds had equiaxed grains and the grain size increased from $8.6 \pm 1.7 \mu\text{m}$ in the Mg powder to $26.9 \pm 2.0 \mu\text{m}$ (Figure 3.2d and e).

Table 3.1 Characteristics of the bare and coated Mg scaffolds fabricated by means of extrusion-based AM, following by MgF_2 single-layer coating or MgF_2 -CaP double-layer coatings.

Sample group	Height (mm)	Diameter (mm)	Strut width (μm)	Strut spacing (μm)	Absolute porosity (weight-volume)
Design	12.64	12.38	580	360	37.8%
As-printed	12.57 ± 0.05	12.13 ± 0.1	587.6 ± 11.7	351.4 ± 18.5	$60.0 \pm 1.9\%$
As-sintered bare Mg	11.31 ± 0.27	10.92 ± 0.25	528.1 ± 12.6	298.4 ± 16.6	$54.5 \pm 2.4\%$
MgF_2 -coated Mg	11.32 ± 0.42	10.97 ± 0.23	529.2 ± 15.7	294.2 ± 18.3	$50.2 \pm 1.3\%$
MgF_2 -CaP-coated Mg	11.61 ± 0.33	11.24 ± 0.31	562.1 ± 38.0	246.9 ± 21.7	$45.7 \pm 1.2\%$

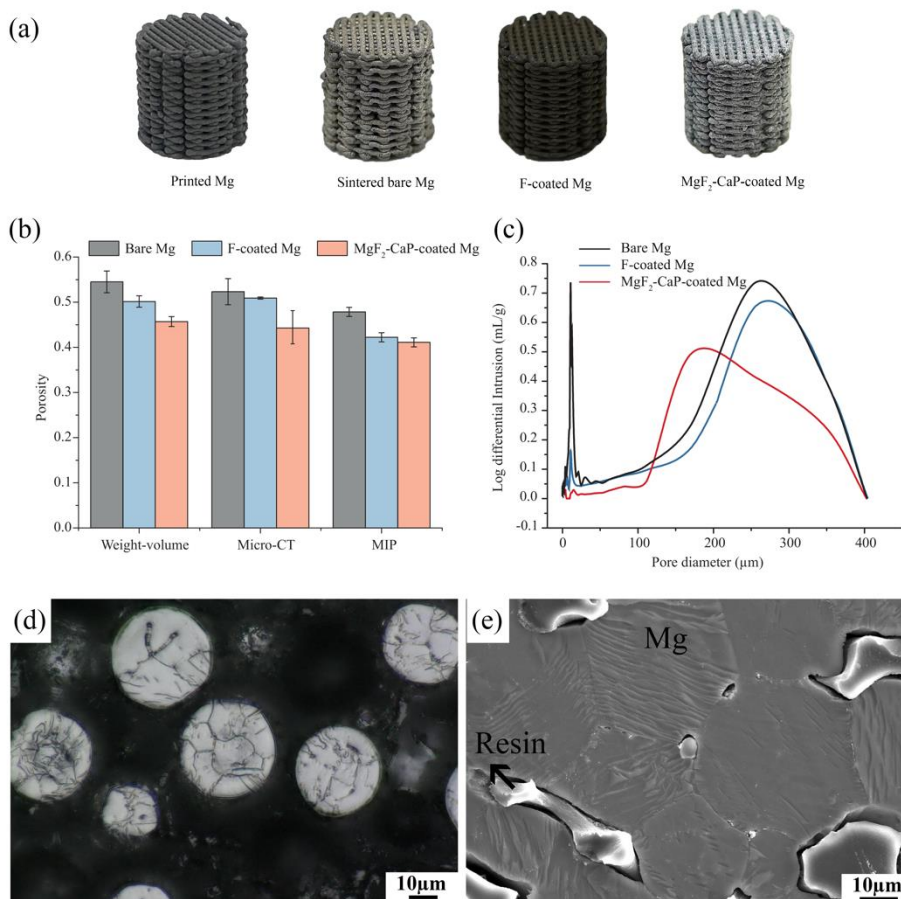


Figure 3.2 Characteristics of the bare and coated Mg scaffolds: (a) macrographs, (b) porosities (weight-volume, Micro-CT and MIP analysis), (c) pore size distributions (MIP analysis), (d) microstructure of the Mg powder, and (e) microstructure of the as-sintered Mg scaffolds.

3.3.2. Morphological and structural characteristics of the as-sintered and as-coated scaffolds

3.3.2.1. Surface characteristics

The surface morphologies of the bare and coated Mg scaffolds are shown in Figure 3.3a, d and g. The partially consolidated Mg powder particles in the bare Mg scaffolds had relatively clean and smooth surfaces, and the necks between neighboring powder particles, as well as the micropores in powder particle junctions, were formed during sintering (Figure 3.3b). Most of the micropores and necks were retained in the MgF₂-coated Mg

scaffolds (Figure 3.3e). However, those were difficult to discern in the MgF₂-CaP-coated scaffolds (Figure 3.3h). From the SEM images at a high magnification, as compared to the surface of the bare Mg scaffolds, the MgF₂-coated Mg scaffolds exhibited a riverbed-like morphology on struts and Mg, F and O were detected by EDS (Figure 3.3f). Crystal aggregates could be observed on the surface of struts in the MgF₂-CaP-coated Mg scaffolds (Figure 3.3h) and, at a high magnification, dandelion-like crystals with a rod-shaped micro/nanostructure were visible on the aggregates, which consisted of Ca, P, C, O, Na, and Mg (Figure 3.3i).

XRD analysis confirmed the formation of MgF₂ on MgF₂-coated Mg scaffold struts. The detected CaP compound on MgF₂-CaP-coated Mg scaffold struts was identified to be hydroxyapatite (HA) (Figure 3.3j). In addition to the Mg matrix and HA, Mg(OH)₂ was also detected in the MgF₂-CaP-coated porous Mg. In the FTIR spectra of the MgF₂-coated Mg specimens, the bands at 1641 cm⁻¹ and 3420 cm⁻¹ were attributed to the presence of residual water in the samples [25]. However, the absorbance band of MgF₂ could not be detected, since its vibration is around 431 cm⁻¹, which is beyond the range of the measurements [26]. The bands at 1000-1200 cm⁻¹ in the spectra of the MgF₂-CaP-coated porous Mg corresponded to the asymmetric stretching bending vibrations of the PO₄³⁻ group in HA [27] (Figure 3.3k).

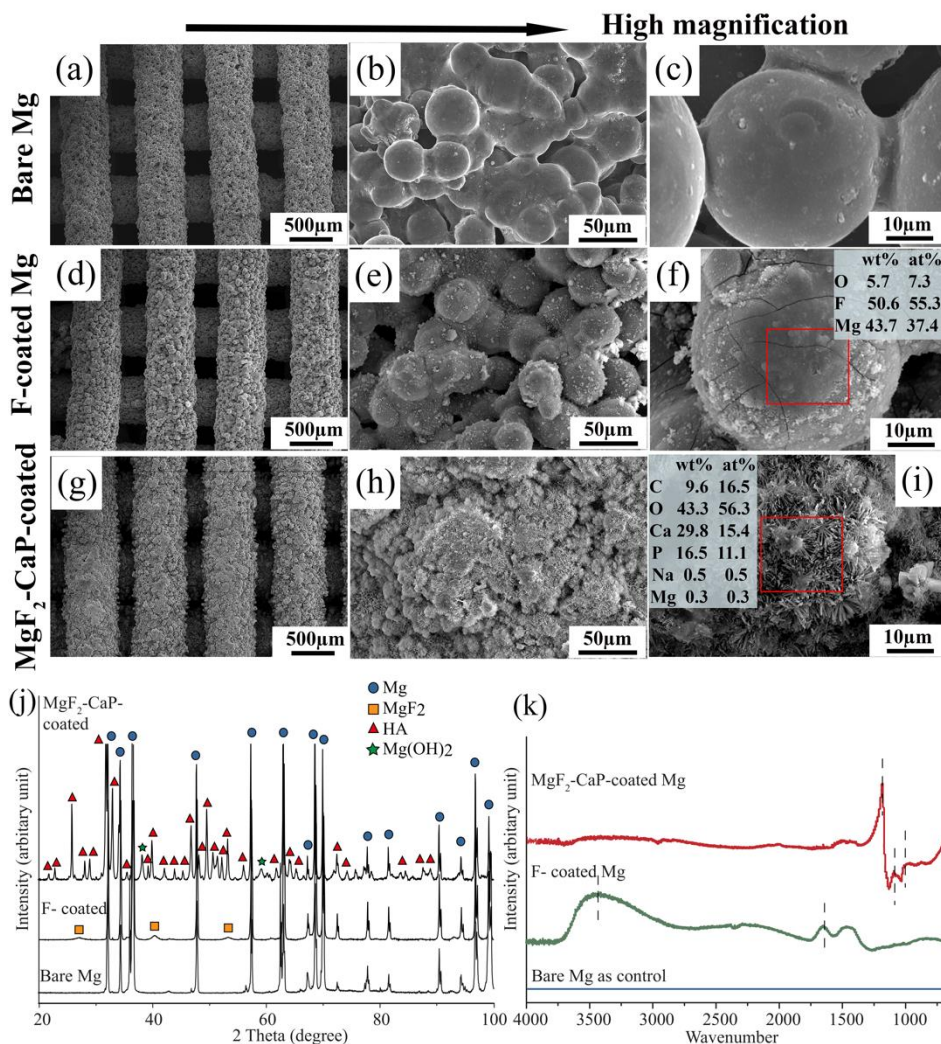


Figure 3.3 Characteristics of the MgF₂ single-layer coating and MgF₂-CaP double-layer coatings on the strut surfaces of the Mg scaffolds: (a-c) bare Mg scaffolds, (d-f) MgF₂-coated Mg scaffolds, (g-i) MgF₂-CaP-coated Mg scaffolds, (j) XRD patterns, and (k) FTIR spectra.

3.3.2.2. Cross-section microstructures of struts

The cross-section of the struts of the bare Mg scaffolds showed fully interconnected networks with micropores (Figure 3.4a). The strut surfaces of both the MgF₂-coated and MgF₂-CaP-coated Mg scaffolds at the periphery and at the center initially with micropores were covered and the micropores were partially filled (Figure 3.4b-e). At the

periphery of the MgF₂-Ca-P coated Mg scaffolds, the outer surface of the struts was covered by a thick layer, which tended to flatten the uneven surfaces through the formation of layers with different thicknesses at different locations (see the boxed areas in Figure 3.4d). However, the thick CaP coating could not be observed on the surfaces of the struts at the center of the MgF₂-CaP-coated scaffolds (Figure 3.4e). EDS mapping was performed on the peripheral struts at a high magnification (Figure 3.4f-i), which revealed that O and F were densely present on the surfaces of the Mg powder particle networks (*i.e.*, the micropores of the struts) in both MgF₂-coated and MgF₂-CaP-coated Mg struts, indicating the formation of a Mg (OH)₂ film during the alkali-heat pre-treatment and the MgF₂ coating. Some O present at the top of the MgF₂ coating likely resulted from the formation of MgO and/or Mg(OH)₂ during the fluoride and hydrothermal CaP deposition treatments (Figure 3.4h and i). The outermost layer on the MgF₂-CaP-coated Mg struts was predominantly composed of Ca and P with a small amount of O (Figure 3.4g and i), indicating the formation of a CaP layer on the pre-existing MgF₂ coating during the hydrothermal CaP deposition treatment. The magnified image (*i.e.*, the inset in Figure 3.4f) shows the cross-section microstructure of the fluoride coating and its depth profile. The MgF₂ coating contained cracks and had a relatively uniform thickness of 1.37 ± 0.42 μm on average, while the CaP coating was dense and had thicknesses ranging from between 1.85 and 39.90 μm . The microporosity of the struts decreased significantly after the surface modification and, at the same time, the volume fraction of the Mg substrate in the struts decreased from $91.5\% \pm 0.4\%$ to $77.0\% \pm 3.5\%$ after the fluoride conversion, followed by CaP deposition (Table 3.2).

Table 3.2 Volume fractions of microporosity, the Mg matrix and coatings in the struts.

Sample	Microporosity	Mg matrix	Compounds	
			inside micropores	Ca-P coating
Bare Mg	$8.5\% \pm 0.4\%$	$91.5\% \pm 0.4\%$	--	--
MgF ₂ -coated Mg	$1.9\% \pm 0.2\%$	$86.3\% \pm 0.3\%$	$11.8\% \pm 0.2\%$	--
MgF ₂ -CaP-coated Mg	$0.8\% \pm 0.6\%$	$77.0\% \pm 3.5\%$	$21.6\% \pm 3.8\%$	$0.6\% \pm 0.5\%$

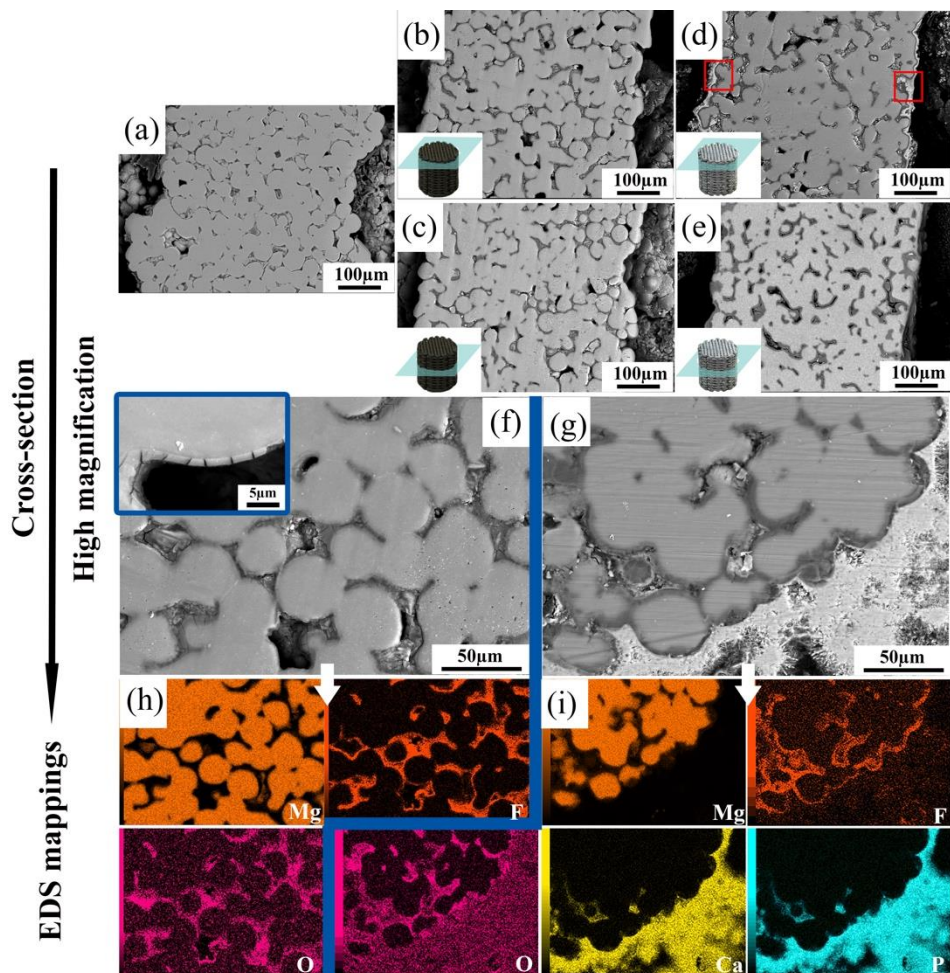


Figure 3.4 SEM images (backscatter mode) of the cross-section of the struts of the bare and coated Mg scaffolds: (a) bare Mg, (b) MgF_2 -coated Mg at the periphery, (c) MgF_2 -coated Mg at the center, (d) MgF_2 -CaP-coated Mg at the periphery (the boxed areas show the formation of CaP coating tended to flatten the uneven surfaces of the scaffolds), (e) MgF_2 -CaP-coated Mg at the center, (f and h) MgF_2 -coated Mg at the periphery at a high magnification and corresponding EDS analysis (f-inset image: MgF_2 coating on the surface at a high magnification), and (g and i) MgF_2 -CaP-coated Mg at the periphery at a high magnification and corresponding EDS analysis.

3.3.3. *In vitro* degradation behavior

3.3.3.1. Material loss during immersion tests

The bare Mg scaffolds lost their structural integrity after 1 day of immersion in r-SBF, while the MgF₂-coated and MgF₂-CaP-coated Mg scaffolds maintained their structural integrity and were covered by the corrosion products when inspected at day 7 of the immersion test (Figure 3.5a). During the first 24 h of immersion, both the local and distant pH values of all the three groups kept increasing, with the local pH being higher than the distant pH (Figure 3.5b). However, the slopes of the curves and the differences between the local and distant pH values were very different between the three groups. As compared with the bare Mg specimens, the local pH value associated with the MgF₂-coated porous Mg specimens were lower (8.3) after 1 day of immersion, while the values associated with the MgF₂-CaP-coated porous Mg were even lower (7.7). Over the period from day 1 to day 7, the local and distant pH values associated with the MgF₂-CaP-coated porous Mg sample remained low, as compared with those associated with the MgF₂-coated Mg specimens, indicating the better protection afforded by the additional CaP coating (Figure 3.5b). In terms of the volume loss, the bare Mg scaffolds lost more than 35% of their volume after only 1 day of immersion. Over the same period of time, the Mg samples coated with MgF₂ lost around 10% of their volume. The volume loss decreased to < 5% after the application of the MgF₂-CaP coatings (Figure 3.5c). At all the time points, the Mg scaffolds with the MgF₂-CaP coatings showed lower volume losses than those with the MgF₂ coating only (Figure 3.5c). Moreover, until day 7, the concentrations of the Mg ions released from the MgF₂-CaP-coated porous Mg scaffolds increased the least, while the most significant Mg ion release was observed for the bare Mg specimens within one day. Ca and P ion concentrations in the r-SBF exhibited a decreasing trend over the 7 day period, except for slight increases in Ca and P ion concentrations during the first 6 h in the case of the MgF₂-CaP coated Mg scaffolds, likely caused by the release of some Ca and P ions from the CaP coating present on the scaffolds (Figure 3.5d).

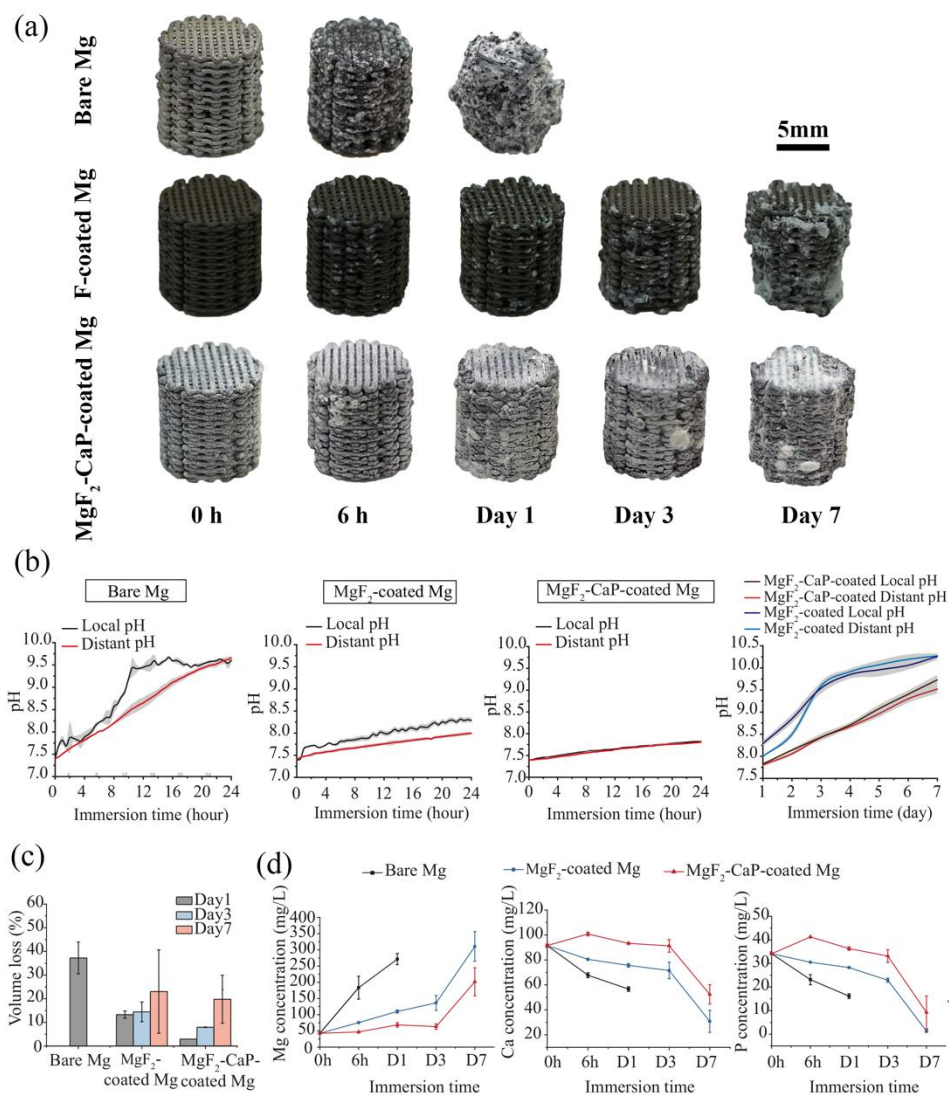
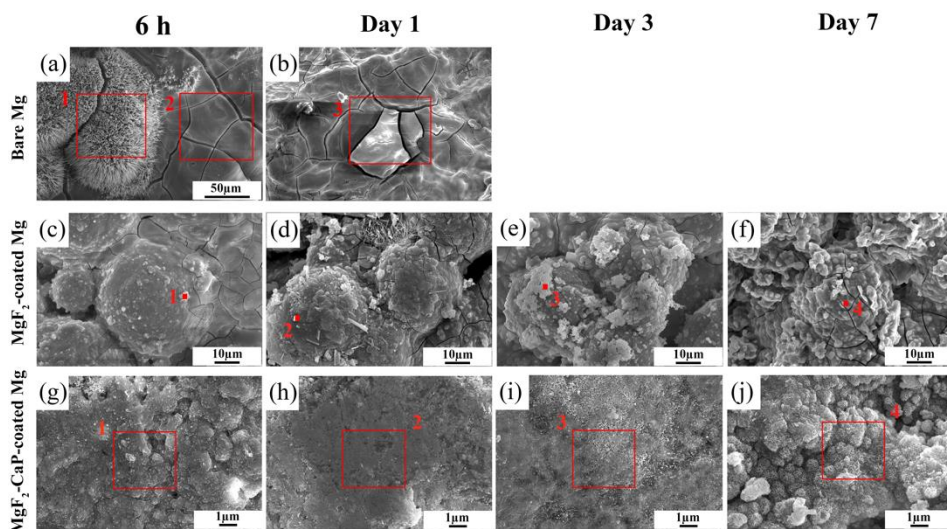


Figure 3.5 *In vitro* degradation behaviors of the three groups of the bare and coated Mg scaffolds: (a) visual inspection of degraded scaffolds, (b) pH variations with time, (c) volume losses at different time points, and (d) changes of the concentrations of ions in r-SBF with time.

3.3.3.2. Characteristics of degradation products

On struts

Four time points (*i.e.*, 6 h and 1, 3 and 7 days) were selected as those for the examination of the biodegradation products formed on the struts of the coated Mg scaffolds, while only 6 h and 1 day for the bare Mg scaffolds (Figure 3.6). Two kinds of biodegradation products were formed on the strut surfaces of the bare Mg scaffolds after 6 h immersion. The needle-shaped products contained Mg, O, C, and Cl (Figure 3.6a, box 1), while the cracked flake-shaped compounds only contained Mg, O, and C (Figure 3.6a, box2). After 1 day of immersion, the flake-shaped compounds containing Mg and O (Figure 3.6b, box 3) seemed to be loose. Regarding the MgF₂-coated Mg scaffolds after *in vitro* biodegradation, the Mg powder particles were still clearly recognizable, with increased amounts of white deposited compounds from 6 h to 7 days of immersion (Figure 3.6c-f). Interestingly, Ca was found after immersion only for 6 h, while P was detected for the first time at day 3 (Figure 3.6d and e). Furthermore, the amount of F decreased with immersion time and it could not be detected any more at day 7 (Figure 3.6f, box 4). After immersion, the MgF₂-CaP coated Mg scaffolds were covered by a layer of dense corrosion products that contained O, C, Ca, and P without Mg until day 3 (Figure 3.6g-i, box 1-3). At day 7, rose-like biodegradation products were formed on the surface of the MgF₂-CaP-coated scaffolds with the presence of Mg, O, and C, as well as small amounts of Ca and P (Figure 3.6j, box 4).



EDS results

Wt%	Bare Mg			MgF ₂ -coated Mg				MgF ₂ -CaP-coated Mg			
Area	1	2	3	1	2	3	4	1	2	3	4
Mg	29.1	41.1	47.1	43.3	40.2	24.7	21.6				30.0
O	47.2	33.5	52.9	17.1	23.2	43.3	55.2	12.7	27.8	30.5	49.2
C	15.7	25.4		20.0	24.2	18.8		68.0	33.9	45.6	19.7
Cl	8.1										
F				17.6	10.9	4.9					
Ca				2.0	1.43	6.1	13.9	12.4	23.2	13.6	0.3
P						2.1	9.4	6.9	15.1	10.4	0.8

Figure 3.6 Surface morphologies and EDS analyses of the biodegradation products on the struts at different time points: (a-b) bare Mg, (c-f) MgF₂-coated Mg, and (g-j) MgF₂-CaP-coated Mg.

To identify the composition of the corrosion products, XRD and FTIR were used to examine the surfaces of the biodegraded Mg scaffolds (Figure 3.7). In addition to the α -Mg phase in the substrate, the XRD results revealed the presence of Mg₃(OH)₅Cl·4H₂O and Mg(OH)₂ on the surface of the bare Mg scaffolds after 6 h immersion, while only Mg(OH)₂ was found at day 1 (Figure 3.7a). The appearance of the peaks at 3700 cm⁻¹ in the FTIR spectrum (Figure 3.7b) could be attributed to the O-H stretching vibration in the crystal structure of Mg(OH)₂ [25]. Furthermore, the bands between 750-900 cm⁻¹ and 1440-1550 cm⁻¹ likely resulted from CO₃²⁻ [28, 29] (Figure 3.7b). Regarding MgF₂-coated Mg, only the α -Mg and MgF₂ phases were found after 6 h of immersion, while Mg(OH)₂ started to appear at day 1 and onwards (Figure 3.7c). Similar to bare Mg, FTIR revealed the possible presence of Mg(OH)₂ and carbonates on the surface of biodegraded MgF₂-coated Mg and the intensities of these biodegradation products increased with immersion

time (Figure 3.7d). $\text{Mg}(\text{OH})_2$ and HA were found on the strut surfaces of the MgF_2 -CaP-coated Mg scaffolds after 6 h immersion and dicalcium phosphate (DCP, CaHPO_4) was first found at day 3 (Figure 3.7e). The intensity of the peak corresponding to $\text{Mg}(\text{OH})_2$ suddenly increased at day 7, which was consistent with the result that the peak of OH^- was stronger at day 7 in the FTIR spectrum of the MgF_2 -CaP-coated Mg scaffolds (Figure 3.7f). The clearly visible absorption bands at 1160 and 1040 cm^{-1} that corresponded to phosphates appeared at all the time points. Similarly, carbonate (1440-1550 cm^{-1}) was found at all the time points (Figure 3.7f).

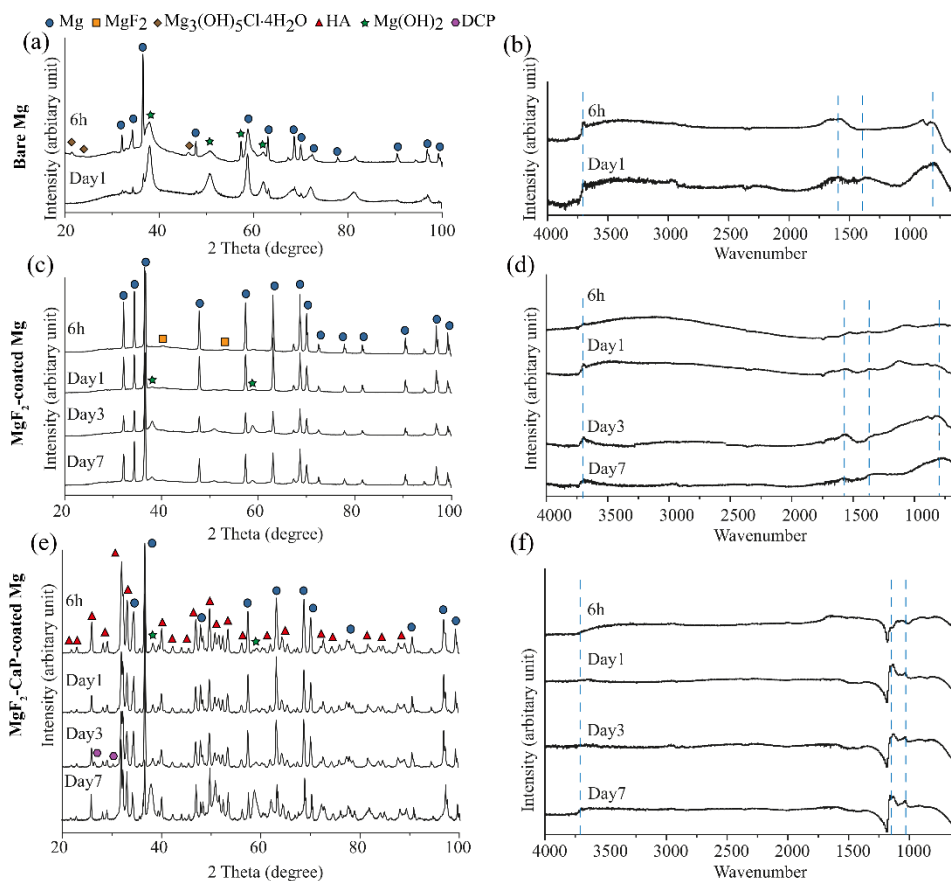


Figure 3.7 Characteristics of the corrosion products formed on the struts at different time points during *in vitro* immersion: (a, c and e) XRD patterns, and (b, d and f) FTIR spectra.

Inside struts

Apart from the characterization of the strut surfaces of the biodegraded Mg scaffolds, the corrosion behavior and formed biodegradation products were characterized through

examining the cross-sections of the struts under SEM in the backscatter mode (Figure 3.8). In the case of the bare Mg scaffolds (day 1), the struts in the peripheral region were examined. The subsurface of the Mg struts (light grey) was mostly replaced by biodegradation products (dark grey), while the initial micropores in the struts were fully filled with the biodegradation products (Figure 3.8a1). The struts in the central region of the scaffolds showed a similar cross section (not shown in the figure). EDS mapping revealed the presence of oxide and/or hydroxide in the biodegradation products (Figure 3.8a2). The peripheral struts of the scaffolds subjected to the fluoride conversion treatment were still integrated without obvious corrosion into the subsurface after 1 day of immersion (Figure 3.8b1). However, when observing the struts at a high magnification, corrosion underneath the MgF_2 coating could be found and the corrosive medium penetrated through this layer, attacking the Mg substrate, with the evidence of the presence of O not only filling the micropores that were surrounded by F, but also appearing underneath F, as shown in the EDS mappings (the arrows in Figure 3.8b2). After immersion for 7 days, some of the peripheral struts were still integrated (Figure 3.8c1), while the others were partially damaged with the features of replacing the Mg substrate with the biodegradation products and disintegration from the sintered Mg powder particle boundaries (*i.e.*, the area of the necks formed during the sintering process) (see the inset in Figure 3.8c1). At this time point, the fluoride conversion coating still survived in most of the micropores with the deposition of Ca (Figure 3.8c2). However, the struts at the center of the MgF_2 -coated scaffolds showed that a larger area of Mg was replaced by the corrosion products (Figure 3.8d), as compared with those at the periphery of the scaffolds. In comparison to the degraded MgF_2 -coated Mg scaffolds, in the struts at the periphery of the MgF_2 -CaP-coated Mg scaffolds at day 1, there was no obvious corrosion penetrating through the MgF_2 coating that covered the inner surface of micropores (Figure 3.8e1). At day 7, on the cross section of the peripheral struts of the MgF_2 -CaP-coated scaffolds, a thick layer of biodegradation products containing O was found just underneath the HA compound, while the outer CaP coating remained dense and intact (Figure 3.8f1 and f2). The struts at the center of the MgF_2 -CaP coated Mg scaffolds had denser infill of the corrosion products than those at the periphery (Figure 3.8g).

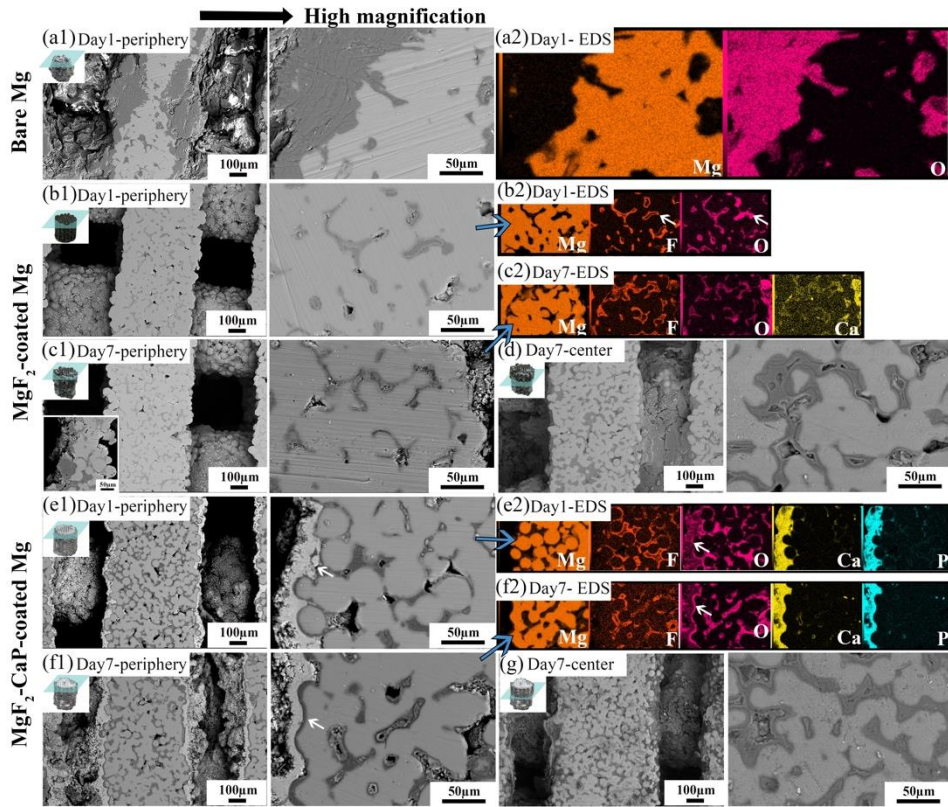


Figure 3.8 SEM images (backscatter mode) of the cross section of the degraded struts: (a1 and a2) the strut cross section of the bare Mg scaffold at the periphery after 1 day immersion and corresponding EDS analysis, (b1 and b2) the strut cross section of the MgF₂-coated Mg scaffold at the periphery after 1 day immersion and corresponding EDS analysis, (c1 and c2) the strut cross section of the MgF₂-coated Mg scaffold at the periphery after 7 day immersion and corresponding EDS analysis, (d) the strut cross section of the MgF₂-coated Mg scaffold at the center after 7 day immersion, (e1 and e2) the strut cross section of the MgF₂-CaP-coated Mg scaffold at the periphery after 1 day immersion and corresponding EDS analysis, (f1 and f2) the strut cross section of the MgF₂-CaP-coated Mg scaffold at the periphery after 7 day immersion and (g) the strut cross section of the MgF₂-CaP-coated scaffold at the center after 7 day immersion.

(In all the EDS mappings, carbon was present on the samples and uniformly distributed on the polished cross-sectional surfaces of the biodegraded scaffolds. However, the carbon that originated from the corrosion products might be interfered with that generated from the grinding or polishing media used. Therefore, the element mappings of carbon are not shown in the figure.)

3.3.4. Electrochemical behavior

PDP results showed a significant reduction in anodic current density of the MgF_2 -coated Mg as compared to the bare Mg (Figure 3.9a). The MgF_2 -CaP Mg showed an even higher reduction in both the anodic as well as cathodic current density as compared to the bare Mg and MgF_2 -coated Mg, indicating enhanced passivation and hence corrosion protection by the MgF_2 -CaP coating. The bare Mg exhibits the most negative corrosion potential (E_{corr}) and the highest corrosion current density (i_{corr}). The MgF_2 -coated and MgF_2 -CaP coated Mg specimens presented more positive E_{corr} and lower i_{corr} . The corrosion rates of the bare, MgF_2 -coated, and MgF_2 -CaP coated porous Mg, calculated from the PDP results, were 2.2 ± 0.0 , 1.4 ± 0.4 , and 0.2 ± 0.0 mm/y, respectively, assuming uniform corrosion. Moreover, the initial LPR value of the bare Mg scaffolds was 0.5 ± 0.1 $\text{k}\Omega\cdot\text{cm}^2$, while the initial LPR values of the MgF_2 -coated Mg and MgF_2 -CaP-coated Mg scaffolds were 1.3 ± 0.1 and 4.0 ± 1.3 $\text{k}\Omega\cdot\text{cm}^2$, respectively. The polarization resistance of both the bare and MgF_2 -coated Mg scaffolds exhibited a gentle decreasing trend with immersion time, while that of the MgF_2 -CaP-coated Mg scaffolds increased sharply to 18.3 ± 5.4 $\text{k}\Omega\cdot\text{cm}^2$ after 1 day of immersion and then decreased to 4.0 ± 1.2 $\text{k}\Omega\cdot\text{cm}^2$ after 3 days (Figure 3.9b).

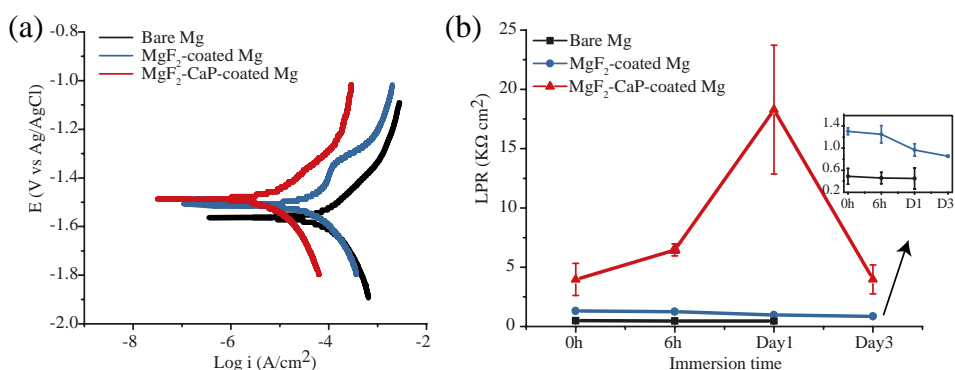


Figure 3.9 (a) Potentiodynamic polarization after 1 h of exposure and (b) linear polarization resistance over a period of 3 days of exposure for the bare Mg, MgF_2 -coated Mg and MgF_2 -CaP coated Mg scaffolds.

3.3.5. Mechanical properties before and during *in vitro* degradation

The compressive stress-strain curves of the as-fabricated bare Mg and coated scaffolds all began with an elastic region, followed by a densification stage where permanent deformation occurred (Figure 3.10a). The slopes of the linear elastic region were distinct.

The Young's moduli of the coated Mg scaffolds were much higher than that of the bare Mg scaffolds (Figure 3.10b). However, the coated Mg scaffolds started fracturing at a lower strain, as compared to the bare Mg scaffolds. As compared with the MgF₂-coated porous Mg, the MgF₂-CaP-coated porous Mg had an even lower strain to failure and, thus, a lower ductility. The as-sintered bare Mg scaffolds exhibited a yield strength of 4.7 ± 0.7 MPa and a Young's modulus of 184.4 ± 37.3 MPa (Figure 3.10b). After the surface modification, the yield strengths of the MgF₂-coated Mg and MgF₂-CaP-coated Mg increased to 10.0 ± 1.2 MPa and 16.4 ± 0.5 MPa, respectively, while their Young's moduli increased to 346.7 ± 124.83 MPa and 499.5 ± 33.9 MPa, respectively.

Over the *in vitro* immersion period, the yield strength of the MgF₂-coated scaffolds maintained at a level around 10 MPa until day 3 and then decreased to 6.6 ± 0.4 MPa at day 7, while the Young's modulus of those scaffolds was quite stable at around 350 MPa until day 7 (Figure 3.10c and d). During the same period, both yield strength and Young's modulus of the MgF₂-CaP-coated Mg scaffolds increased until day 3 and then decreased after 7 days of immersion (Figure 3.10c and d).

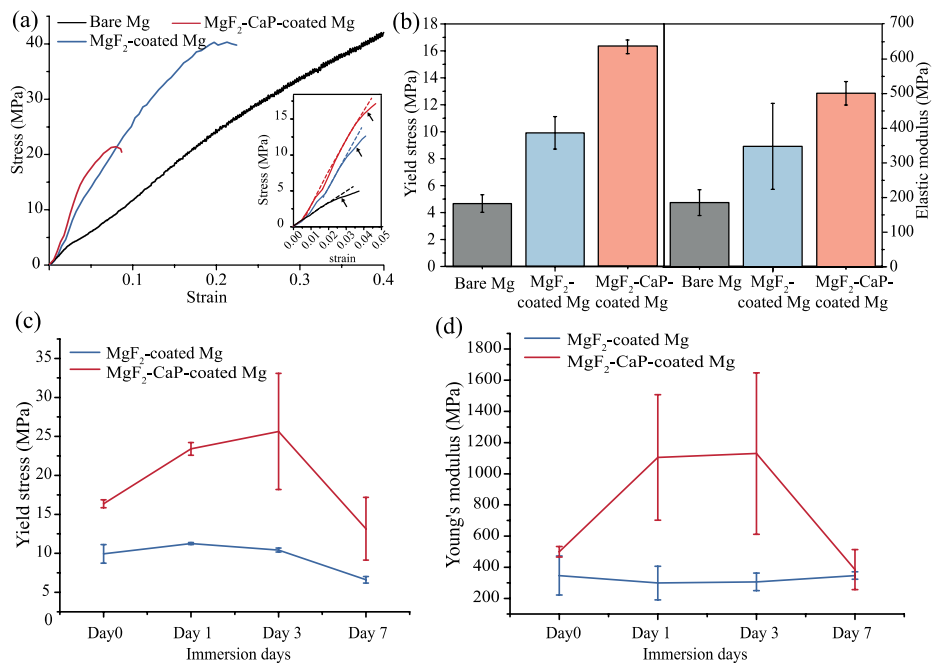


Figure 3.10 Compressive mechanical properties of the bare and coated Mg scaffolds: (a) stress-strain curves, (b) Young's moduli and yield strengths, (c) variation of yield strength with immersion time, and (d) variation of Young's modulus with immersion time. Dash lines in the inset indicate the linear region and arrows indicate the yield stresses.

3.3.6. *In vitro* biocompatibility

3.3.6.1. Responses of cells in indirect cell culture assays

The exposure of cells to the 100% extract medium of the bare Mg scaffolds resulted in cytotoxicity after 1 day of cell culture (Figure 3.11a). However, high levels of metabolic activity (>80%) were observed when cells were cultured in the 50 and 10% extracts (Figure 3.11a). With the surface modification applied, the metabolic activity was significantly improved, especially for the 100% extracts. After 7 days of culture, the growth of the preosteoblasts in the extract of MgF₂-CaP-coated Mg at all the concentrations was promoted, as evidenced by the metabolic activities above 100% (Figure 3.11a). The pH values of the extract media of the bare Mg, MgF₂-coated, and MgF₂-CaP-coated porous Mg were around 8 for all the groups (Figure 3.11b). The concentration of the Mg ion found in these extracts showed an inverse trend, as compared with the results of the metabolic activity (Figure 3.11b). The release of Mg ions into the extract media significantly decreased after the application of the fluoride conversion and CaP deposition treatments, and the extracts of MgF₂-CaP-coated porous Mg specimens contained the lowest concentration of Mg ion (< 200 ppm).

The results of actin staining showed that the cells cultured in the 10 and 50% extracts of all the three groups fully covered the wells after 7 days of culture (Figure 3.11c). However, there were obvious differences among the 100% extracts of the bare Mg, MgF₂-coated, and MgF₂-CaP-coated porous Mg specimens. Only a few cells were viable when cultured in the 100% extract of the bare Mg. However, cells grew and spread healthily in the 100% extract of MgF₂-CaP-coated Mg (Figure 3.11c), which is consistent with the results of the cell metabolic activity (Figure 3.11a).

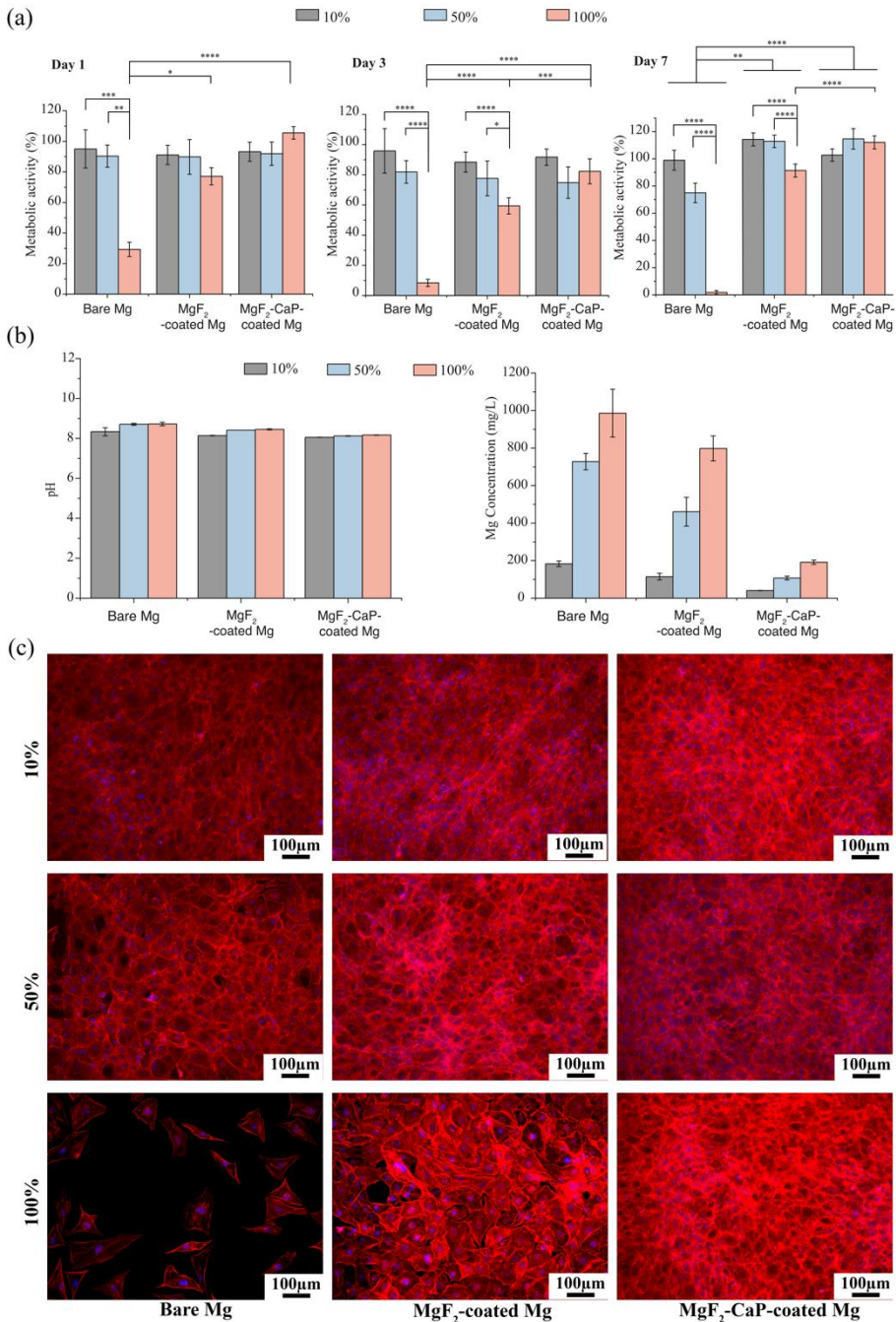


Figure 3.11 Indirect biological evaluation of the bare and coated Mg scaffolds: (a) metabolic activities of preosteoblasts cultured in the 10, 50 and 100% extracts, (b) pH and Mg ion concentrations of the extract media of different concentrations and (c)

rhodamine phalloidin (red) and DAPI (blue) stained preosteoblasts after 7 days of culture in the extracts of different concentrations.

3.3.6.2. Responses of cells in direct cell culture assays

Due to a too high degradation rate, the bare Mg scaffolds lost structural integrity and partially collapsed, when cultured with cells in the α -MEM for 1 day. It was thus meaningless for direct seeding of preosteoblasts on the scaffolds. Therefore, direct cell culture assays were performed on the MgF₂-coated and MgF₂-CaP-coated Mg scaffolds with Ti-6Al-4V scaffolds as the reference (Figure 3.12). After 1 and 3 days of cell culture, most of the cells on the MgF₂-coated Mg scaffolds were not adherent. Therefore, only a few viable (green) cells could be observed on the scaffolds (Figure 3.12a and d). However, the cells attached onto the MgF₂-CaP-coated Mg scaffolds were much larger in number than those on the MgF₂-coated Mg scaffolds and the cells showed a spread morphology with cell-cell contacts after 3 days (Figure 3.12b, e, h, k and n). By comparison, the cells residing on the MgF₂-coated Mg scaffolds were fewer and more polarized (Figure 3.12m). On the surface of the reference AM Ti-6Al-4V scaffolds, the cells developed far-stretching filopodia between the original powder particles (Figure 3.12o).

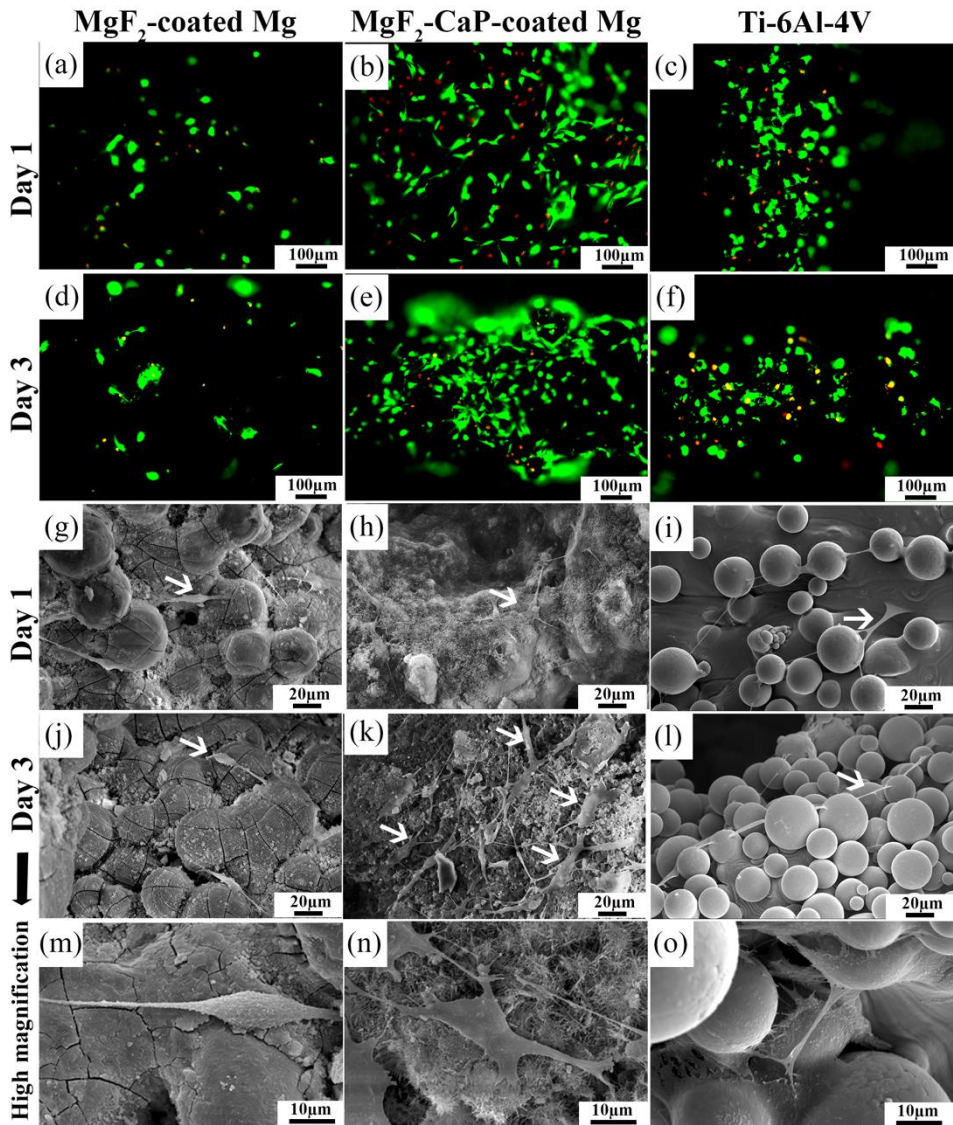


Figure 3.12 Direct biological evaluation of the coated Mg scaffolds (with Ti-6Al-4V as the reference): (a-f) calcein acetoxymethyl (green, indicating living cells) and ethidium homodimer-1 (red, indicating dead cells) stained preosteoblasts on the coated Mg scaffolds and (g-o) the morphologies of cells on the coated Mg scaffolds and cells at a high magnification.

3.4. Discussion

We fabricated biodegradable porous Mg scaffolds using extrusion-based 3D printing, followed by debinding and sintering as well as the application of MgF₂ and CaP coatings. While pure Mg with a highly porous structure rapidly degraded in simulated physiological environments, the applied surface modifications slowed down the biodegradation and enhanced the surface biocompatibility to bring the 3D printed Mg scaffolds closer to meeting the requirements for bone substitution. This study presents the first ever demonstration of extrusion-based 3D printed highly porous Mg with satisfactory mechanical properties and biocompatibility.

3.4.1. Scaffold fabrication technology

The developed extrusion-based 3D printing process yielded pure Mg scaffolds with a geometrically ordered structure, similar to the initial design. The 3D printing strategy applied can be found in Chapter 2 [1]. Considering the fast degradation rate of porous Mg, relatively thicker struts should be adopted to allow the observation of the degradation behavior of the scaffolds after a long immersion period. However, too thick struts would lead to narrow diffusion paths for pyrolysis products to move to the green body surfaces where the decomposed binder under argon gas flow could quickly escape [30]. This would negatively influence the debinding process, resulting in carbon residues in the sintered scaffolds. Therefore, a medium strut size of 580 μm was adopted in the design of the scaffolds. A pore size of 360 μm was chosen, since it has been found that implants with pores larger than 300 μm favor direct osteogenesis in connection with vascularization and high oxygenation [31].

With regard to post-processing, a single-step scheme combining debinding and sintering was employed, based on our previous work presented in Chapter 2 [1]. In this study, however, the sintering condition was further optimized to obtain struts with a higher relative density. It should be mentioned that a higher relative density of struts is of great importance for achieving the desired properties of Mg scaffolds, such as a sufficiently high strength and enhanced corrosion resistance. Based on the results obtained from differential scanning calorimetry (DSC) (Figure S3.1) for pure Mg powder, the powder started melting at around 643 $^{\circ}\text{C}$, slightly below the theoretical melting point of pure Mg (650 $^{\circ}\text{C}$), probably due to the presence of impurities in the powder [32]. Therefore, sintering at 640 $^{\circ}\text{C}$ for 1 h was adopted in our study to generate a small amount of liquid Mg for powder particle bonding. As compared to the relative density of the struts (54% \pm 6%) obtained from the previous study, the optimized sintering parameters (640 $^{\circ}\text{C}$ /1 h) resulted in a relative density above 90% in the struts of the pure Mg scaffolds (Figure 3.2b) and Mg powder particles were mostly bonded through neck formation (Figure 3.3b). As a result, the fabricated Mg scaffolds possessed a pore interconnectivity

of 88%, which is expected to offer enhanced osteogenesis by favoring the attachment, growth, and differentiation of cells [33].

Unlike the typical columnar grain structure formed during laser AM [34], the microstructure of the extrusion-based 3D printed and sintered Mg scaffolds was featured by fully equiaxed grains (Figure 3.2e). However, the average grain size of the fabricated Mg scaffolds was larger than that of laser AM Mg [35] due to rapid cooling involved in the latter.

3.4.2. Surface modification

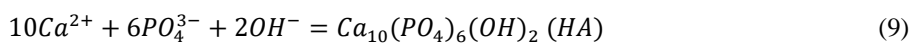
Surface modification has been used as an effective means for Mg-based implants to reach the performance required for orthopedic implants [36]. The merits of chemical conversion coating to protect magnesium are well recognized, including high protectiveness, high adhesion strength, the ease of operation, and high cost-effectiveness [36]. However, it was never demonstrated in the case of porous magnesium with micropores having sizes smaller than 50 μm . By using the chemical conversion method, MgF_2 coating was successfully applied to the porous Mg scaffolds in the present study (Figure 3.3). It should be mentioned that prior to the fluoride conversion treatment, an alkali-heat pre-treatment was performed to provide an underneath film for better protection of the substrate. We found that without this pre-treatment, MgF_2 coating could not significantly improve the corrosion resistance of Mg. That is because alkali-heat pre-treatment removes inclusions and impurities at the surface [37], such as oxides or carbon residue, and forms a homogenous, dense, and well-bonded $\text{Mg}(\text{OH})_2$ film (even on the struts of the Mg scaffolds, Figure S3.2), which is helpful to form a more protective MgF_2 coating layer on the top [13]. This coating strategy has been also employed by other researchers to achieve effective protection for Mg alloys [14, 18, 38, 39]. The alkali-heat pre-treatment and fluoride conversion treatment were optimized, based on the preliminary results obtained from the evaluation of the corrosion behavior of the MgF_2 -coated Mg scaffolds in the r-SBF (Figure S3.3). Microcracks could be observed across the MgF_2 coating (Figure 3.3f and Figure 3.4f), as also observed by other researchers [56, 57], which was probably caused by the large differences in the physical and mechanical properties between the $\text{Mg}(\text{OH})_2$ film and MgF_2 [17] as well as the evolution of hydrogen during the fluoride conversion treatment.

The hydrothermal deposition method was employed in this study to prepare CaP coating, which is the simplest and the least expensive way of preparing CaP-containing coating, as compared with other techniques [40-43]. With this method, HA was successfully formed on the struts of the MgF_2 -coated porous Mg scaffolds in this study (Figure 3.3), which was not demonstrated before. On the cross section of MgF_2 -CaP coated struts, the subsurface was composed of dense HA (Figure 3.3h) and the outer

surface contained loose and dandelion-like crystals (Figure 3.3i). During the hydrothermal deposition process, the treatment solution with a pH of 3.9 penetrated through the MgF₂ coating present on the struts, leading to slight corrosion of the underneath Mg substrate. As a result, the percentage of the Mg substrate in the struts decreased (Table 3.2), and the local pH increased rapidly during the initial stage of the treatment, which has been observed in other studies too [44, 45]. Afterwards, OH⁻ interacted with the phosphate anions [46]:



The rapid adsorption of PO₄³⁻ on the strut surface resulted in the initial nucleation of HA on the surface. The preferential nucleation on the surface led to the formation of a dense HA layer, which can be expressed as [46]:



Then, the formed dense HA layer acted as a protective layer to separate the MgF₂-coated Mg substrate from the environment, which moderated the successive corrosion of Mg, and thus, suppressed the local pH increase [46]. However, the dense layer was not very compact and the corrosive medium could still penetrate into the coating layers through some defect areas. Therefore, the OH⁻ generated at the defect sites and then HA crystals formed and grew from the defects, based on the above equation. That is why the outer HA was featured with fine rods. The complex structures of the HA crystals formed on the magnesium substrate have also been observed in other studies [44, 47].

The formation of protective layers on the struts at the center of the porous scaffolds should be considered, since it is as important as that on the struts at the periphery. However, no previous studies regarding the spatial variations of the coatings could be found in the literature. In the present study, both the periphery and center of the coated scaffolds were examined. Clearly, MgF₂ was able to form both at the periphery and at the center (Figure 3.4b and c). However, the CaP coating could not be found at the center of the MgF₂-CaP-coated scaffolds (Figure 3.4d and e), although the hydrothermal deposition method is, in principle, capable of coating the entire surface of porous structures. This lack of coating at the center of the scaffolds may be due to the limited ability of the flocculent-shaped CaP compounds in the prepared CaP solution to diffuse through the macropores into the scaffold center, especially after an HA layer had already been formed at the entrance of the macropores at the periphery of the scaffolds.

Nevertheless, thanks to the high pore interconnectivity of the Mg scaffolds, Mg(OH)₂ film (from alkali-heat pre-treatment) and MgF₂ coating were successfully formed on the inner walls of micropores (with sizes below 50 μm) in the struts (Figure 3.4f and g) and

infiltrated the struts through micropores, resulting in a decreased micro-porosity in the struts (Table 3.2).

3.4.3. Biodegradation behavior

To determine the *in vitro* biodegradation rates of Mg and its alloy, researchers have applied various methods, including weight loss measurement, hydrogen evolution measurement, μ CT, and electrochemical methods. Although weight loss measurement is the most widely used method, the chemical solution used for removing the corrosion products from the struts may also attack the prepared coatings in our study, which would lead to untrustworthy results. Hydrogen evolution measurements may be influenced by possible leakage and the entrapment of hydrogen bubbles inside the scaffolds [48]. μ CT is a non-destructive method and has been employed for determining the biodegradation rates of AM Mg scaffolds [48]. Based on these considerations, in the present study, the last two methods (*i.e.*, μ CT and electrochemical methods) were chosen to determine the biodegradation rates of the Mg scaffolds.

The *in vitro* biodegradation rate of the Mg scaffolds (2.2 mm/y) was higher than the rates of the solid counterparts in the form of cast and rolled pure Mg (*i.e.*, 0.84 and 1.94 mm/y, respectively) [5]. The volume loss of the scaffolds after 1 day of immersion (*i.e.*, $37\% \pm 7\%$) was higher than that of pure Mg foam fabricated through powder metallurgy (around 25%) [49, 50]. The higher biodegradation rate of the fabricated pure Mg scaffolds could be attributed to the high pore interconnectivity of the scaffolds, which led to the exposure of all Mg scaffold surfaces to the r-SBF solution, allowing corrosion to occur at multiple intricate sites. In addition, the pressureless liquid-phase sintering strategy adopted in our study could only create vulnerable necks connecting Mg powder particles, instead of forming a flattened inter-particle area at a compaction step to impose plastic deformation in the route of conventional powder metallurgy [49, 51]. Therefore, it was no surprise that the biodegradation rate of the fabricated Mg scaffolds was high. Actually, the reported biodegradation rates of porous pure Mg foam or scaffolds (7.4 – 11.4 mm/y) fabricated by using other methods [51-53] are all much higher than the expected biodegradation rate of an ideal bone substitute (0.2 – 0.5 mm/y) due to the presence of pore networks [54]. Therefore, surface modification has been frequently performed on porous Mg foams to restrain rapid biodegradation [18, 50, 51, 55].

Both the MgF_2 -coated and MgF_2 -CaP-coated Mg scaffolds exhibited much lower degradation rates (1.4 ± 0.4 and 0.2 ± 0.0 mm/y, respectively) than the bare Mg scaffolds, indicating the effectiveness of the MgF_2 coating and MgF_2 -CaP coatings to protect the porous Mg substrate from rapid corrosion (Figure 3.5). In addition to the corrosion-protecting effect, the presence of MgF_2 and HA compounds inside the micropores of the

peripheral struts (Figure 3.4f and g) greatly inhibited the localized corrosion of the struts at micropores as the early preferential sites.

At both the macro and micro level, the present investigations revealed different corrosion behaviors of the bare Mg, MgF₂-coated, and MgF₂-CaP-coated Mg scaffolds. Without any coating, the bare Mg substrate rapidly dissolved once in contact with r-SBF, resulting in sharp increases in the local pH and distant pH values within a short period of time at the start of the immersion tests (Figure 3.5b). The needle-shaped (Mg₃(OH)₅Cl·4H₂O) and flake-shaped corrosion products (Mg(OH)₂) were formed and fully covered the surfaces of the scaffolds only after 6 h of immersion (Figure 3.6a). However, the protective nature of the corrosion product is limited, in particular in the presence of Cl⁻ in the r-SBF solution and, therefore, a relatively loose corrosion layer was observed after 1 day of immersion (Figure 3.6b), leading to a high volume loss for the bare Mg scaffolds.

In the case of the MgF₂-coated Mg scaffolds, however, MgF₂ could effectively protect the Mg substrate from rapid corrosion at the beginning of *in vitro* immersion, as evidenced by less sharply increased pH values, a smaller amount of Mg ion release, a smaller volume loss at day 1 (Figure 3.5b-d), the passivation stage of PDP and a slightly higher LPR value (Figure 3.9b), as compared to the bare Mg scaffolds. Nevertheless, the samples degraded continuously along with steady increases in pH value, Mg ion release, and volume loss, and gradual decreases in LPR value during 7 days of immersion in the r-SBF solution, which may be because the thin, cracked MgF₂ coating gradually lost its protective capacity for prolonged immersion times. Localized corrosion noticeably occurred during 7 days of immersion (Figure 3.8c1), which might be due to the cracks across the MgF₂ coating. With the presence of the defect, the r-SBF solution could penetrate through the MgF₂ coating and reach the Mg substrate, thereby initiating corrosion underneath the MgF₂ coating (Figure 3.8b1). Regarding the corrosion products, Mg(OH)₂ and small amounts of carbonate and phosphate might have formed on the strut surface of the scaffolds on day 1 (Figure 3.6 and 3.8). The anodic region of the potentiodynamic curve of MgF₂-coated Mg, showing lower current densities, also indicates the formation of an initially effective protective layer (Figure 3.9a). The passivation behavior of MgF₂ coating on Mg was also found in another study [56]. However, breakdown of the passivation occurred upon slightly increasing the anodic overpotential during polarization, indicating an imperfect protective layer, not sufficiently compact to prevent the further attack by the corrosive solution for prolonged exposure times. On the cross sections of the struts, although the corrosion products formed could largely block the micropores (Figure 3.8b), Cl⁻ ions could still be absorbed by the porous corrosion products, leading to further corrosion into the struts and increases in local pH [57]. Consequently, calcium-containing precipitation not only formed on the

strut surface of the scaffolds, but also in the micro-pores of the struts at day 7 (Figure 3.8c1 and c2).

The MgF₂-CaP-coated Mg scaffolds possessed an HA outer layer and a MgF₂ interlayer at the periphery of the scaffolds. The minor changes of the pH values and the small amount of the Mg ion release after 3 days of immersion indicated that the HA layer provided effective protection at the beginning of the immersion tests (Figure 3.5b-d). Mg(OH)₂ and carbonate started to form on the surface after 6 h, which partially covered the outer layer of HA (Figure 3.6g and 3.8). The morphology of the surface changed from fine rods to a relatively flat surface after 6 h and day 1 (Figure 3.6h), which provided a better barrier to corrosion, due to the effective coverage on the loose HA layer. This can explain why the LPR value of the MgF₂-CaP-coated scaffolds increased after 1 day of immersion (Figure 3.9b). However, the LPR value decreased after 3 days of immersion (Figure 3.9b). At day 7, Mg(OH)₂ dominated the surface of the scaffolds (Figure 3.6j and EDS results) and the release of Mg²⁺ ions sharply increased, indicating that the MgF₂-HA coatings were penetrated through and the underneath Mg substrate was attacked. This explanation could be supported by the observed cross-section microstructures (Figure 3.8e1, e2, f1 and f2): a thicker O-containing layer was found underneath the HA/MgF₂ layers at day 7, as compared with the microstructure at day 1 (Figure 3.8e2 and f2, white arrows in the O element maps). In the struts, the corrosion behavior was similar to that of the struts of the MgF₂-coated Mg scaffolds (Figure 3.8e1 and f1).

Interestingly, for both the MgF₂-coated Mg and MgF₂-CaP-coated Mg scaffolds, the struts at the center showed more severe corrosion than those at the periphery (Figure 3.8c1, d, f1 and g), which may be the case because the relatively narrow space at the center area may cause crevice-like corrosion to occur. The diffusion of Mg²⁺ ions from and oxidizing agents towards the center of the scaffolds was more difficult than that at the periphery, leading to an ion concentration gradient. As a result, negatively charged Cl⁻ ions might have migrated into the narrow space under the attraction of positively charged Mg²⁺ ions [48]. Therefore, a high Cl⁻ concentration might have induced a high corrosion rate of Mg at the center of the scaffolds.

3.4.4. Mechanical properties before and during *in vitro* degradation

The compressive mechanical properties of the bare and coated Mg scaffolds fabricated by using extrusion-based 3D printing were in the range of those of the trabecular bone (*i.e.*, yield strength = 0.2 - 80 MPa; Young's modulus = 10 - 2,000 MPa) [58]. The yield strength (4.7 ± 0.7 MPa) and Young's modulus (184.4 ± 37.3 MPa) of the bare Mg

scaffolds also fell into the range of those of Mg foams with similar porosities fabricated by using the conventional powder metallurgy methods (*i.e.*, yield strength = 2 - 6 MPa, Young's modulus = 0.11 - 0.4 GPa) [51, 59], although a compaction step prior to sintering was employed in the conventional methods, in contrast to the pressureless sintering performed in this study.

The stress-strain curve of the bare Mg scaffolds did not show a plateau stage (Figure 3.10a), which is usually observed for most geometrically ordered 3D printed porous metallic scaffolds [48]. That is because the design of the 0/90/0° pattern (without vertical struts) for the scaffolds and the inherent ductility of Mg struts led to densification beyond the yield point and the decreases in the volume fraction of the pores in the compressed specimens, resulting in further increases in stress with the applied strain. In another study, a similar curve of extrusion-based 3D printed scaffolds was observed [60]. As compared to the bare Mg scaffolds, the coated Mg scaffolds possessed higher yield strengths and Young's moduli, but exhibited a shorter densification stage and failed at a lower strain (Figure 3.10a and b). This resulted from the infill of micropores in the struts during the surface modification and the lower overall porosities of the coated Mg scaffolds (Figure 3.1b and 3.3), which allowed the scaffolds to withstand higher loads before densification occurred. With the formation of the Mg(OH)₂, MgF₂ and MgF₂-CaP film/coatings on the scaffolds, the MgF₂-coated and MgF₂-CaP-coated Mg scaffolds could be considered similar to Mg-matrix composite scaffolds. In addition to the formation of inorganic compounds (Mg(OH)₂, MgF₂, and HA) during the surface modification, the volume fraction of the Mg substrate decreased. Therefore, the decreased ductile phase (*i.e.*, the Mg substrate) and increased brittle phases (coatings) resulted in a less ductile characteristic of the coated Mg scaffolds, as compared with the bare Mg scaffolds.

During the period of *in vitro* degradation, the mechanical properties of the MgF₂-coated and MgF₂-CaP-coated Mg scaffolds remained within the range of those of trabecular bone (Figure 3.10c and d). When the scaffolds still maintained the structural integrity at the beginning of the immersion tests, the corrosion products deposited and formed on the scaffolds and inside the struts acted as reinforcing phases, providing a strengthening effect and thus improving the mechanical properties of the coated scaffolds (Figure 3.10 c and d). However, later on, the coatings were penetrated through by the corrosive medium and more Mg substrate became degraded, as the corrosion progressed (Figure 3.8). Both the dissolution of the Mg scaffolds and localized corrosion resulted in the decreased mechanical properties of the coated scaffolds after 7 days of immersion (Figure 3.10c and d).

3.4.5. Biocompatibility

It was clearly observable that the level of cell viability strongly depended on the Mg extract concentration (Figure 3.11a). After 7 days of cell culture, only the MgF₂-CaP-coated Mg extracts (all dilution ratios) fulfilled the Level 0 cytotoxicity requirement, while the 100% MgF₂-coated Mg extracts showed slight cytotoxicity (Level 1), and the 100 and 50% bare Mg extracts were categorized as materials exhibiting severe (Level 4) and mild cytotoxicities (Level 2), respectively, according to the ISO 10993-5 standard [61]. The rhodamine-phalloidin and DAPI staining showed similar results concerning the effect of extract concentration on the growth of preosteoblasts (Figure 3.11c). The pH values of all the extracts were below 8.5, because of the buffering effect of the medium. The tolerance threshold of the pH value for MC3T3-E1 cells is 8.8 [5]. Therefore, instead of the increased pH value, the Mg²⁺ ions release was the dominant factor for cytotoxicity. The amount of Mg²⁺ ion release in the cell culture medium had the same trend as that in r-SBF during the immersion tests, which corresponded to the biodegradation rates of the scaffolds (Figure 3.5). A safe Mg concentration for MC3T3-E1 cells has been reported to be around 400 mg/L [23]. Therefore, it is understandable that the 100% MgF₂-coated Mg extracts (798 ± 66 mg/L Mg), 100% bare Mg extracts (985 ± 127 mg/L Mg) and 50% bare Mg extracts (728 ± 44 mg/L Mg) caused cytotoxicity (Figure 3.11b). Although Mg ion plays an important role in bone regeneration, locally high Mg²⁺ concentration may have an adverse effect on the attachment and proliferation of cells [5]. Moreover, F ion was not detected in the extracts of the coated samples, which might be because MgF₂ was stable in the cell culture medium.

In the direct cell tests, only a few cells were found to attach and poorly spread on the surface of the MgF₂-coated Mg struts (Figure 3.12a and d), although the MgF₂ coating on Mg alloy was previously found to be biocompatible and able to promote cell attachment and proliferation [62]. This might be due to the rapid degradation of the MgF₂-coated Mg scaffolds, which was accompanied by the generation of hydrogen bubbles and excessive Mg ion release, thereby producing a hazardous environment for the cells to attach. By contrast, numerous cells attached to the surfaces of MgF₂-CaP-coated Mg struts, exhibiting a relatively spread morphology (Figure 3.12b and e). The good cytocompatibility of the MgF₂-CaP-coated Mg scaffolds could be attributed to the following factors: (i) improvement in the corrosion resistance and (ii) good chemical biocompatibility and favorable morphology of the HA layer, which enlarged the bioactive surface area for cell attachment and released a favorable signal [63]. Furthermore, the HA formed in the CaP coating has the potential to promote the osteogenic differentiation of cells [64], which needs to be verified for the extrusion-based 3D printing Mg scaffolds in future studies.

3.5. Conclusions

We developed 3D printed biodegradable porous Mg scaffolds with multi-functional coatings. The fabricated porous structure of the scaffolds was highly interconnected. With the MgF₂ single-layer coating and MgF₂-CaP double-layer coatings, the scaffolds showed lower corrosion rates of 1.4 and 0.2 mm/y in the r-SBF solution, respectively, as compared to the bare Mg corroding at 2.2 mm/y. Owing to the infill of the coating materials in the micropores of the struts, the Young's moduli and yield strengths of the coated Mg scaffolds were enhanced, but their ductility decreased. In addition, the mechanical properties of the coated Mg scaffolds and those during *in vitro* immersion tests up to 7 days were in the range of those of the trabecular bone. Moreover, the indirect and direct culture assays with preosteoblasts on the scaffolds with a combination of MgF₂ and CaP coatings revealed good cytocompatibility, due to an acceptable amount of Mg ion release and the formation of HA on the struts of the scaffolds. Such biocompatible extrusion-based 3D printed Mg scaffolds with MgF₂ and CaP coatings are promising biomaterials to be studied further as a new generation of bone substitutes.

References

- [1] J. Dong, Y. Li, P. Lin, M. A. Leeflang, S. Van Asperen, K. Yu, N. Tumer, B. Norder, A. A. Zadpoor, J. Zhou, Solvent-cast 3D printing of magnesium scaffolds, *Acta Biomater.* 114 (2020) 497-514.
- [2] G. Jia, Y. Hou, C. Chen, J. Niu, H. Zhang, H. Huang, M. Xiong, G. Yuan, Precise fabrication of open porous Mg scaffolds using NaCl templates: Relationship between space holder particles, pore characteristics and mechanical behavior, *Mater. Des.* 140 (2018) 106-113.
- [3] W. Wang, G. Jia, Q. Wang, H. Huang, X. Li, H. Zeng, W. Ding, F. Witte, C. Zhang, W. Jia, G. Yuan, The in vitro and in vivo biological effects and osteogenic activity of novel biodegradable porous Mg alloy scaffolds, *Mater. Des.* 189 (2020) 108514.
- [4] T. Yang, Y. Hu, C. Wang, B. P. Binks, Fabrication of hierarchical macroporous biocompatible scaffolds by combining pickering high internal phase emulsion templates with three-dimensional printing, *ACS Appl. Mater. Interfaces.* 9 (2017) 22950-22958.
- [5] X. Gu, Y. Zheng, Y. Cheng, S. Zhong, T. Xi, In vitro corrosion and biocompatibility of binary magnesium alloys, *Biomaterials.* 30 (2009) 484-498.
- [6] M. Esmaily, J. E. Svensson, S. Fajardo, N. Birbilis, G. S. Frankel, S. Virtanen, R. Arrabal, S. Thomas, L. G. Johansson, Fundamentals and advances in magnesium alloy corrosion, *Prog. Mater. Sci.* 89 (2017) 92-193.
- [7] D. Mei, S. V. Lamaka, X. Lu, M. L. Zheludkevich, Selecting medium for corrosion testing of bioabsorbable magnesium and other metals – A critical review, *Corros. Sci.* 171 (2020) 108722.
- [8] G. Song, Control of biodegradation of biocompatible magnesium alloys, *Corros. Sci.* 49 (2007) 1696-1701.
- [9] Z. Yin, W. Qi, R. Zeng, X. Chen, C. Gu, S. Guan, Y. Zheng, Advances in coatings on biodegradable magnesium alloys, *J. Magnes. Alloy.* 8 (2020) 42-65.
- [10] Q. Zhang, Y. Leng, R. Xin, A comparative study of electrochemical deposition and biomimetic deposition of calcium phosphate on porous titanium, *Biomaterials.* 26 (2005) 2857-2865.
- [11] M. Lalk, J. Reifenrath, N. Angrisani, A. Bondarenko, J. M. Seitz, P. P. Mueller, A. Meyer-Lindenberg, Fluoride and calcium-phosphate coated sponges of the magnesium alloy AX30 as bone grafts: a comparative study in rabbits, *J. Mater. Sci. Mater. Med.* 24 (2013) 417-436.
- [12] M. Q. Cheng, T. Wahafu, G. F. Jiang, W. Liu, Y. Q. Qiao, X. C. Peng, T. Cheng, X. L. Zhang, G. He, X. Y. Liu, A novel open-porous magnesium scaffold with controllable microstructures and properties for bone regeneration, *Sci. Rep.* 6 (2016) 24134.
- [13] T. F. D. Conceição, N. Scharnagl, Fluoride conversion coatings for magnesium and its alloys for the biological environment, in *Surface Modification of Magnesium and its Alloys for Biomedical Applications, Volume II: Modification and Coating Techniques*, edited by T. S. N. Sankara Narayanan, Il-Song Park and Min-Ho Lee, Woodhead Publishing Series in Biomaterials 2015, pp. 3-21.
- [14] F. Witte, J. Fischer, J. Nellesen, C. Vogt, J. Vogt, T. Donath, F. Beckmann, In vivo corrosion and corrosion protection of magnesium alloy LAE442, *Acta Biomater.* 6 (2010) 1792-1799.

- [15] L. Zhang, J. Pei, H. Wang, Y. Shi, J. Niu, F. Yuan, H. Huang, H. Zhang, G. Yuan, Facile preparation of poly(lactic acid)/brushite bilayer coating on biodegradable magnesium alloys with multiple functionalities for orthopedic application, *ACS Appl. Mater. Interfaces*. 9 (2017) 9437-9448.
- [16] Y. Su, I. Cockerill, Y. Zheng, L. Tang, Y. X. Qin, D. Zhu, Biofunctionalization of metallic implants by calcium phosphate coatings, *Bioact. Mater.* 4 (2019) 196-206.
- [17] J. H. Jo, B. G. Kang, K. S. Shin, H. E. Kim, B. D. Hahn, D. S. Park, Y. H. Koh, Hydroxyapatite coating on magnesium with MgF₂ interlayer for enhanced corrosion resistance and biocompatibility, *J. Mater. Sci. Mater. Med.* 22 (2011) 2437-2447.
- [18] S. Julmi, A. K. Kruger, A. C. Waselau, A. Meyer-Lindenberg, P. Wriggers, C. Klose, H. J. Maier, Processing and coating of open-pored absorbable magnesium-based bone implants, *Mater. Sci. Eng. C-Mater. Biol. Appl.* 98 (2019) 1073-1086.
- [19] Z. T. Chen, X. L. Mao, L. L. Tan, T. Friis, C. T. Wu, R. Crawford, Y. Xiao, Osteoimmunomodulatory properties of magnesium scaffolds coated with beta-tricalcium phosphate, *Biomaterials*. 35 (2014) 8553-8565.
- [20] A. Oyane, Hyun. Kim, T. Furuya, T. Kokubo, T. Miyazaki, T. Nakamura, Preparation and assessment of revised simulated body fluids, *J. Biomed. Mater. Res. Part A*. 65A (2003) 188-195.
- [21] Mechanical testing of metals— Ductility testing—Compression test for porous and cellular metals, *ISO 13314* (2011).
- [22] Y. Xin, T. Hu, P. K. Chu, In vitro studies of biomedical magnesium alloys in a simulated physiological environment: A review, *Acta Biomater.* 7 (2011) 1452-1459.
- [23] J. L. Wang, F. Witte, T. F. Xi, Y. F. Zheng, K. Yang, Y. S. Yang, D. W. Zhao, J. Meng, Y. D. Li, W. R. Li, K. M. Chan, L. Qin, Recommendation for modifying current cytotoxicity testing standards for biodegradable magnesium-based materials, *Acta Biomater.* 21 (2015) 237-249.
- [24] Biological evaluation of medical devices —Part 12: Sample preparation and reference materials, *ISO 10993-12:2012* (2012).
- [25] Y. Zhu, G. Wu, Y.-H. Zhang, Q. Zhao, Growth and characterization of Mg(OH)₂ film on magnesium alloy AZ31, *Appl. Surf. Sci.* 257 (2011) 6129-6137.
- [26] R. Rojaee, M. Fathi, K. Raeissi, Electrophoretic deposition of nanostructured hydroxyapatite coating on AZ91 magnesium alloy implants with different surface treatments, *Appl. Surf. Sci.* 285 (2013) 664-673.
- [27] C. Dehghanian, N. Aboudzadeh, M. A. Shokrgozar, Characterization of silicon-substituted nano hydroxyapatite coating on magnesium alloy for biomaterial application, *Mater. Chem. Phys.* 203 (2018) 27-33.
- [28] Y. Xin, C. Liu, X. Zhang, G. Tang, X. Tian, P. K. Chu, Corrosion behavior of biomedical AZ91 magnesium alloy in simulated body fluids, *J. Mater. Res.* 22 (2011) 2004-2011.
- [29] M.M. Figueiredo, J. a. F. Gamelas, A. G. Martins, Characterization of bone and bone-based graft materials using FTIR spectroscopy in *Infrared Spectroscopy – Life and Biomedical Sciences*, edited by Theophanides Theophile, InTechOpen, London, 2012, pp. 315-337.
- [30] J. A. Lewis, Binder removal from ceramics, *Annu. Rev. Mater. Sci.* 27 (1997) 147-173.
- [31] V. Karageorgiou, D. Kaplan, Porosity of 3D biomaterial scaffolds and osteogenesis, *Biomaterials*. 26 (2005) 5474-5491.

- [32] [https://chem.libretexts.org/Bookshelves/Organic_Chemistry/Book%3A_Organic_Chemistry_Lab_Techniques_\(Nichols\)/06%3A_Miscellaneous_Techniques/6.01%3A_Melting_Point/6.1C%3A__Melting_Point_Theory](https://chem.libretexts.org/Bookshelves/Organic_Chemistry/Book%3A_Organic_Chemistry_Lab_Techniques_(Nichols)/06%3A_Miscellaneous_Techniques/6.01%3A_Melting_Point/6.1C%3A__Melting_Point_Theory)
- [33] X. J. Wang, S. Q. Xu, S. W. Zhou, W. Xu, M. Leary, P. Choong, M. Qian, M. Brandt, Y. M. Xie, Topological design and additive manufacturing of porous metals for bone scaffolds and orthopaedic implants: A review, *Biomaterials*. 83 (2016) 127-141.
- [34] F. Bar, L. Berger, L. Jauer, G. Kurtuldu, R. Schaublin, J. H. Schleifenbaum, J. F. Loffler, Laser additive manufacturing of biodegradable magnesium alloy WE43: A detailed microstructure analysis, *Acta Biomater*. 98 (2019) 36-49.
- [35] B. Xie, M. Zhao, Y. Zhao, Y. Tian, D. Yin, C. Gao, C. Shuai, A. Atrens, Effect of alloying Mn by selective laser melting on the microstructure and biodegradation properties of pure Mg, *Metals*. 10 (2020) 1527.
- [36] M. Song, R. Zeng, Y. Ding, R. W. Li, M. Easton, I. Cole, N. Birbilis, X. Chen, Recent advances in biodegradation controls over Mg alloys for bone fracture management: A review, *J. Mater. Sci. Technol*. 35 (2019) 535-544.
- [37] W. Q. Z. Yin, R. Zeng, X. Chen, C. Gu, S. Guan, Y. Zheng, Advances in coatings on biodegradable magnesium alloys, *J. Magnes. Alloy*. 8 (2020) 42-65.
- [38] P. Xiong, J. Yan, P. Wang, Z. Jia, W. Zhou, W. Yuan, Y. Li, Y. Liu, Y. Cheng, D. Chen, Y. Zheng, A pH-sensitive self-healing coating for biodegradable magnesium implants, *Acta Biomater*. 98 (2019) 160-173.
- [39] A. Drynda, T. Hassel, R. Hoehn, A. Perz, F. W. Bach, M. Peuster, Development and biocompatibility of a novel corrodible fluoride-coated magnesium-calcium alloy with improved degradation kinetics and adequate mechanical properties for cardiovascular applications, *J. Biomed. Mater. Res. A*. 93 (2010) 763-775.
- [40] S. Shadanbaz, G. J. Dias, Calcium phosphate coatings on magnesium alloys for biomedical applications: A review, *Acta Biomater*. 8 (2012) 20-30.
- [41] J. Yang, F.-Z. Cui, I. S. Lee, X. Wang, Plasma surface modification of magnesium alloy for biomedical application, *Surf. Coat. Tech*. 205 (2010) S182-S187.
- [42] H. Tang, Y. Gao, Preparation and characterization of hydroxyapatite containing coating on AZ31 magnesium alloy by micro-arc oxidation, *J. Alloys Compd*. 688 (2016) 699-708.
- [43] M. B. Kannan, Electrochemical deposition of calcium phosphates on magnesium and its alloys for improved biodegradation performance: A review, *Surf. Coat. Tech*. 301 (2016) 36-41.
- [44] C. Zhang, M. Yanlong, L. Chenglong, hydroxyapatite coating on fluorine-treated magnesium alloy by hydrothermal method and Its electrochemical corrosion behaviour in Hank's solution, *Prot. Met. Phys. Chem*. 55 (2019) 127-135.
- [45] M. Tomozawa, S. Hiromoto, Growth mechanism of hydroxyapatite-coatings formed on pure magnesium and corrosion behavior of the coated magnesium, *Appl. Surf. Sci*. 257 (2011) 8253-8257.
- [46] Z. Chunyan, Z. Shiyu, L. Xinpeng, H. Hongchuan, Microstructure and corrosion properties of calcium phosphate coating on magnesium alloy prepared by hydrothermal treatment at various pH values, *Rare Metal Mat. Eng*. 47 (2018) 2993-2999.

- [47] M. Tomozawa, S. Hiromoto, Microstructure of hydroxyapatite- and octacalcium phosphate-coatings formed on magnesium by a hydrothermal treatment at various pH values, *Acta Mater.* 59 (2011) 355-363.
- [48] Y. Li, J. Zhou, P. Pavanram, M. A. Leeflang, L. I. Fockaert, B. Pouran, N. Tumer, K. U. Schroder, J. M. C. Mol, H. Weinans, H. Jahr, A. A. Zadpoor, Additively manufactured biodegradable porous magnesium, *Acta Biomater.* 67 (2018) 378-392.
- [49] E. Dayaghi, H. R. Bakhsheshi-Rad, E. Hamzah, A. Akhavan-Farid, A. F. Ismail, M. Aziz, E. Abdolahi, Magnesium-zinc scaffold loaded with tetracycline for tissue engineering application: *In vitro* cell biology and antibacterial activity assessment, *Mater. Sci. Eng. C-Mater. Biol. Appl.* 102 (2019) 53-65.
- [50] M. Yazdimamaghani, M. Razavi, D. Vashae, L. Tayebi, Surface modification of biodegradable porous Mg bone scaffold using polycaprolactone/bioactive glass composite, *Mater. Sci. Eng. C-Mater. Biol. Appl.* 49 (2015) 436-444.
- [51] M. H. Kang, H. Lee, T. S. Jang, Y. J. Seong, H. E. Kim, Y. H. Koh, J. Song, H. D. Jung, Biomimetic porous Mg with tunable mechanical properties and biodegradation rates for bone regeneration, *Acta Biomater.* 84 (2019) 453-467.
- [52] E. Aghion, Y. Perez, Effects of porosity on corrosion resistance of Mg alloy foam produced by powder metallurgy technology, *Mater. Charact.* 96 (2014) 78-83.
- [53] H. Y. Zhuang, Y. Han, A. L. Feng, Preparation, mechanical properties and *in vitro* biodegradation of porous magnesium scaffolds, *Mater. Sci. Eng. C-Mater. Biol. Appl.* 28 (2008) 1462-1466.
- [54] C. Shuai, S. Li, S. Peng, P. Feng, Y. Lai, C. Gao, Biodegradable metallic bone implants, *Mater. Chem. Front.* 3 (2019) 544-562.
- [55] S. Toghyani, M. Khodaei, M. Razavi, Magnesium scaffolds with two novel biomimetic designs and MgF₂ coating for bone tissue engineering, *Surf. Coat. Tech.* 395 (2020) 125929.
- [56] U. Riaz, Z. U. Rahman, H. Asgar, U. Shah, I. Shabib, W. Haider, An insight into the effect of buffer layer on the electrochemical performance of MgF₂ coated magnesium alloy ZK60, *Surf. Coat. Tech.* 344 (2018) 514-521.
- [57] H. Wu, C. Zhang, T. Lou, B. Chen, R. Yi, W. Wang, R. Zhang, M. Zuo, H. Xu, P. Han, S. Zhang, J. Ni, X. Zhang, Crevice corrosion - A newly observed mechanism of degradation in biomedical magnesium, *Acta Biomater.* 98 (2019) 152-159.
- [58] M. Yazdimamaghani, M. Razavi, D. Vashae, K. Moharamzadeh, A. R. Boccaccini, L. Tayebi, Porous magnesium-based scaffolds for tissue engineering, *Mater. Sci. Eng. C-Mater. Biol. Appl.* 71 (2017) 1253-1266.
- [59] M. K. Saeid Toghyani, Modified spacer removal and optimum sintering temperature for porous magnesium scaffold fabrication, *J. Tissue Eng.* 2 (2019) 48-57.
- [60] N. E. Putra, M. A. Leeflang, M. Minneboo, P. Taheri, L. E. Fratila-Apachitei, J. M. C. Mol, J. Zhou, A. A. Zadpoor, Extrusion-based 3D printed biodegradable porous iron, *Acta Biomater.* (2020) 741-756.
- [61] Biological evaluation of medical devices—Part 5: Tests for *in vitro* cytotoxicity, ISO 10993-5:2009 (2009).
- [62] W. Yu, H. Zhao, Z. Ding, Z. Zhang, B. Sun, J. Shen, S. Chen, B. Zhang, K. Yang, M. Liu, D. Chen, Y. He, *In vitro* and *in vivo* evaluation of MgF₂ coated AZ31 magnesium alloy

porous scaffolds for bone regeneration, *Colloids Surf. B: Biointerfaces*. 149 (2017) 330-340.

[63] Sae Kim, Ji Jo, Sung Lee, Min Kang, Hyoun Kim, Yuri Estrin, Jong Lee, Jung Lee, Y. Koh, Hydroxyapatite-coated magnesium implants with improved in vitro and in vivo biocorrosion, biocompatibility, and bone response, *J. Biomed. Mater. Res. A*. 102A (2013) 429-441.

[64] C. Yang, Z. G. Huan, X. Y. Wang, C. T. Wu, J. Chang, 3D printed Fe scaffolds with HA nanocoating for bone regeneration, *ACS Biomater. Sci. Eng.* 4 (2018) 608-616.

Supplementary material

Methods

Differential Scanning Calorimetry (DSC) analysis of the pure magnesium (Mg) powder was carried out using a DSC instrument (Netzsch DSC 404, Germany). The sample was undergone a heating process from 25 to 590 °C at a heating rate of 20 °C/min and from 590 to 700 °C at a lower heating rate of 5 °C/min.

The surface and cross-section of the coated scaffolds with different conditions were observed using SEM (JSM-IT100, JEOL, Japan). The back-scatter mode was applied for the observation of the cross section of the scaffolds.

In vitro immersion tests of the samples coated under different conditions were conducted in revised simulated body fluid (r-SBF) in a thermal bath at 37 °C for 6 h. The samples after *in vitro* degradation at different time points were imaged.

Results

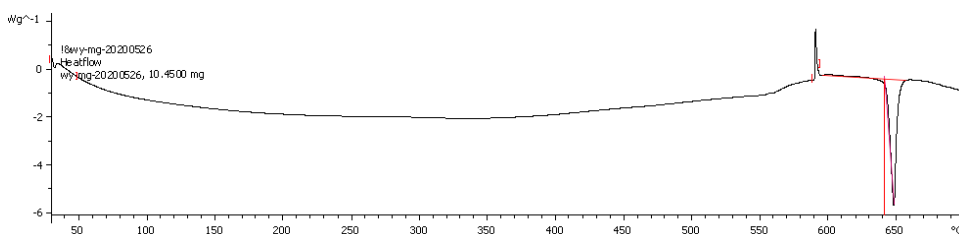


Figure S3.1 DSC result of pure Mg powder

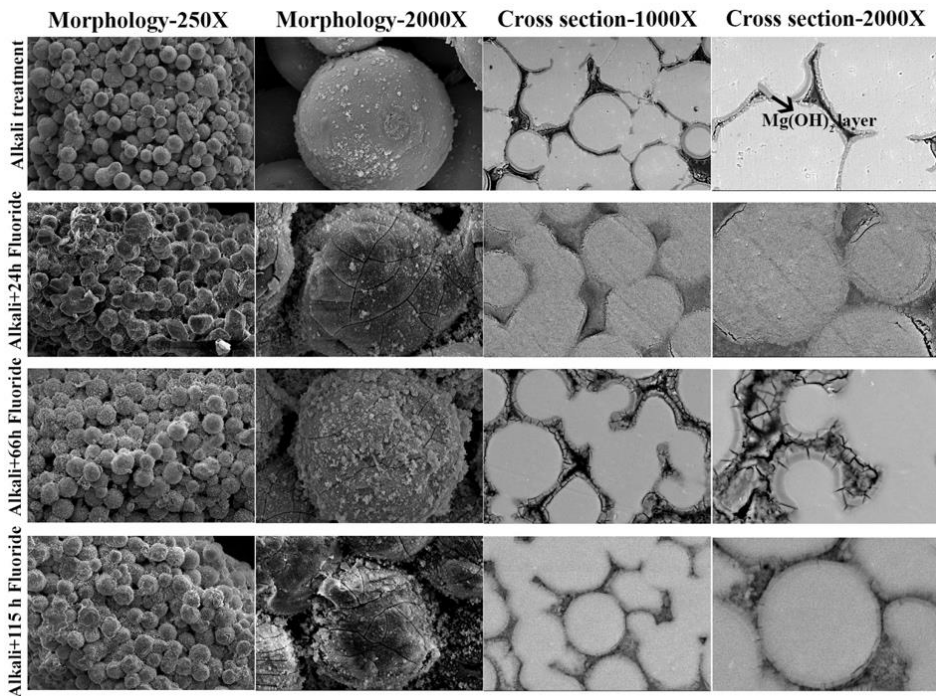


Figure S3.2 Surface and cross-section morphologies of the coatings obtained under different conditions.

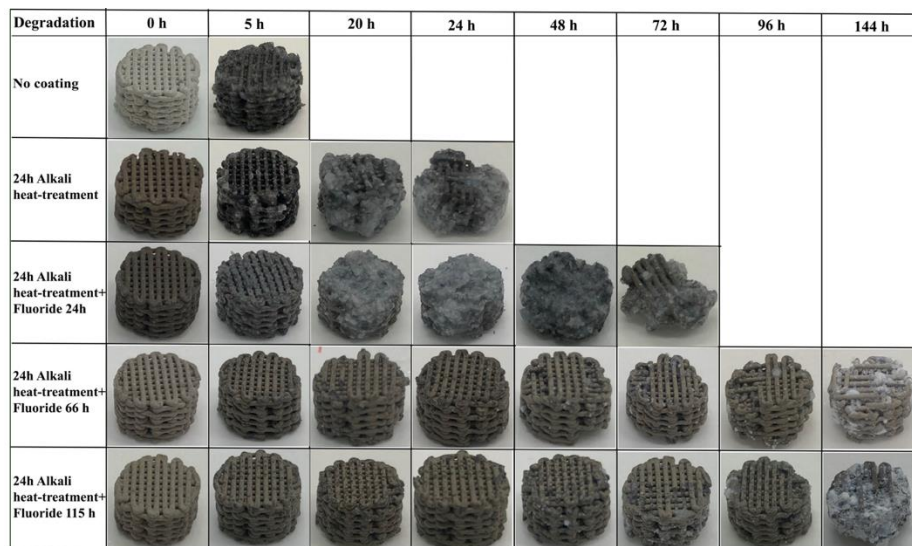


Figure S3.3 Degradation behavior of the scaffolds with the coatings obtained under different conditions.

4

Ink extrusion-based additive manufacturing of Mg-Zn scaffolds

Here, alloying Mg with Zn was used as a strategy to enhance the corrosion resistance and mechanical properties of AM geometrically ordered Mg-Zn scaffolds simultaneously. The Mg-Zn scaffolds with a porosity of 50.3% and strut density of 93.1% were composed of the Mg matrix and MgZn₂ second phase particles. The in vitro biodegradation rate of the Mg-Zn scaffolds decreased by 81% at day 1, as compared to pure Mg scaffolds. Over 28 days of static immersion in modified simulated body fluid, the corrosion rate of the Mg-Zn scaffolds decreased from 2.3 ± 0.9 mm/y to 0.7 ± 0.1 mm/y. The yield strength and Young's modulus of the Mg-Zn scaffolds were about three times as high as those of pure Mg scaffolds and remained within the range of those of trabecular bone throughout the biodegradation tests. Indirect culture of MC3T3-E1 preosteoblasts in Mg-Zn extracts indicated favorable cytocompatibility. In direct cell culture, some cells could spread and form filopodia on the surface of the Mg-Zn scaffolds. Overall, this study demonstrates the great potential of the extrusion-based AM Mg-Zn scaffolds to be further developed as biodegradable bone-substituting biomaterials.¹

¹The chapter is based on a scientific paper: J. Dong, N. Tümer, M. A. Leeﬂang, P. Taheri, L. E. Fratila-Apachitei, J. M. C. Mol, A. A. Zadpoor, J. Zhou, Extrusion-based additive manufacturing of Mg-Zn alloy scaffolds, J. Magnes. Alloy, 10 (2021), 2491-2509.

4.1. Introduction

Pure Mg scaffolds fabricated by using extrusion-based AM have been extensively studied in terms of their mechanical, biodegradation, and biological properties [1]. It has been shown that the pure Mg scaffolds with a highly interconnected pore structure degrade too fast, although their mechanical properties are acceptable. While surface modification can be used for improving the corrosion resistance of such scaffolds, coatings can only provide effective protection at the beginning of biodegradation. After the coating is degraded or penetrated through, the exposed Mg substrate will dominate the overall biodegradation process [1]. To address this challenge, the corrosion resistance of the Mg substrate must be improved.

Alloying is one of the strategies that can effectively slow down the biodegradation of Mg by an order of magnitude or more [2]. Zinc has been extensively studied as a common alloying element for Mg. It has been shown to enhance both the corrosion resistance and mechanical properties of Mg [2-7]. According to the literature [8, 9], adding < 6 wt% of Zn to Mg leads to a balanced combination of mechanical, corrosion, and biological properties, while 4 wt% of Zn results in optimal grain refinement and improved mechanical properties. Moreover, unlike other frequently used alloying elements (*e.g.*, Al or rare earth elements), Zn is one of the most abundant, essential elements in the human body and plays an important role in bone formation, mineralization, and preservation [10]. Indeed, *in vivo* studies have confirmed that Mg-Zn binary alloys have a great potential to serve as orthopedic implants [5, 11, 12]. To date, porous Mg-Zn foams have been developed through the conventional powder metallurgy methods [3, 13, 14]. However, no reports on geometrically ordered porous Mg-Zn scaffolds have appeared in the literature.

In this study, a pre-alloyed Mg-Zn (4 wt% Zn) powder was chosen as the starting material and Mg-Zn binary alloy scaffolds with a geometrically ordered and fully interconnected porous structure were fabricated using extrusion-based AM. The biodegradation, mechanical properties, and biological behavior of these scaffolds were then characterized. Pure Mg scaffolds fabricated using a similar approach served as a reference group to study the effects of Zn addition on the properties of the resulting biomaterials.

4.2. Material and methods

4.2.1. Scaffold manufacturing

A cylindrical porous scaffold with a diameter of 12.38 mm and a height of 12.64 mm was designed (Figure 4.1a). A lay-down pattern of $0^{\circ}/90^{\circ}/0^{\circ}$ was adopted (Figure 4.1b) for

the scaffold and the scaffold was designed, using a custom software package associated with the 3D BioScaffolder printer (BS 3.2, GeSim, Germany). Pure Mg powder (impurity < 0.01 wt%) and Mg-Zn powder (95.6 wt% Mg, 4.1 wt% Zn and 0.3 wt% impurities, Figure 4.1c) with a spherical particle shape and median particle sizes of 44.96 μm and 37.7 μm , respectively, were used as the starting materials (Tangshan Weihao Magnesium Powder Co., China). The mean grain size of the Mg-Zn powder was $2.8 \pm 0.1 \mu\text{m}$ (Figure 4.1d), while that of the pure Mg powder was $8.6 \pm 1.7 \mu\text{m}$ [1], which was determined by using the line intercept method after etching the powder particle cross section in a solution composed of nitric acid, acetic acid, water, and ethanol at a volume ratio of 1:3:4:12.

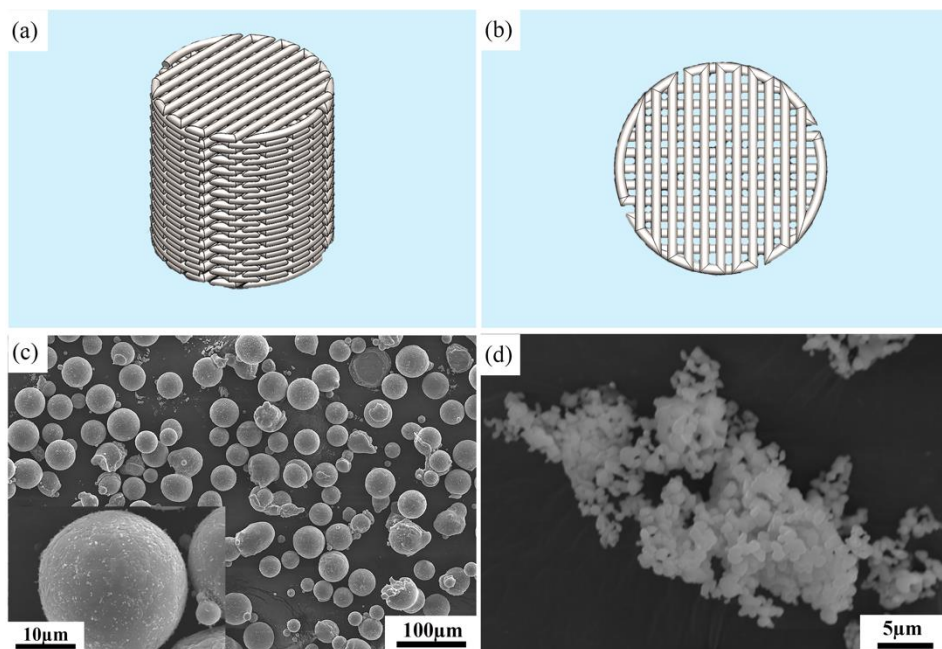


Figure 4.1 The design of scaffolds and the Mg-Zn powder using for scaffold manufacturing: (a) CAD design, (b) lay-down pattern of the scaffold design, (c) pre-alloyed Mg-Zn powder particle morphology and (d) microstructure of the etched pre-alloyed Mg-Zn powder.

Powder loaded inks were prepared by mixing the Mg powder with a binder system composed of hexane and polyisobutylene polymer ($M_w \sim 500,000$, Sigma Aldrich, Germany). The ink was loaded into a syringe (Nordson EFD, Germany) and was then extruded into 3D porous scaffolds through a 580 μm tapered nozzle tip using the 3D BioScaffolder printer. The deposition angles were of 0° and 90° , which were interchanged every layer. A printing pressure of 140-160 kPa and a speed of 5 mm/s were used for 3D printing. After 3D printing, the as-printed Mg-Zn and pure Mg scaffolds were

loaded into a tube furnace (STF16/180, Carbolite Gero Ltd., UK) under a controlled argon atmosphere (purity $\geq 99.9999\%$; inlet pressure: 1 bar) for debinding and sintering. The as-printed Mg-Zn scaffolds and pure Mg scaffolds were respectively heated to 580 °C and 640 °C at 5 °C/min with a dwelling time of 1 h, followed by furnace cooling. The as-sintered Mg-Zn and pure Mg scaffolds were ultrasonically cleaned in isopropyl alcohol for 10 min prior to the subsequent characterization steps.

4.2.2. Characterization of the fabricated scaffolds

The morphology of the as-printed Mg-Zn scaffolds as well as the morphologies and the cross-section microstructures of the as-sintered Mg-Zn and pure Mg scaffolds were examined using a scanning electron microscope (SEM, JSM-IT100, JEOL, Japan). The micro-porosity of the struts was measured from the SEM images taken on the polished cross sections using ImageJ (National Institutes of Health, USA). The polished Mg-Zn and pure Mg scaffold struts were etched using the same method as for the Mg-Zn powder. The etched specimens were then observed using the same SEM. The absolute porosities of the as-printed and as-sintered scaffolds were calculated using the following equations, based on the weighing method:

$$\varphi_p = \left(1 - \frac{\frac{m_p}{\rho_p}}{V_{bulk}} \right) \times 100\% \quad (1)$$

$$\varphi_s = \left(1 - \frac{\frac{m_s}{\rho_{Mg}}}{V_{bulk}} \right) \times 100\% \quad (2)$$

where φ_p and φ_s are, respectively, the absolute porosities of the as-printed and the as-sintered Mg-Zn and pure Mg scaffolds [%], m_p and m_s are, respectively, the masses of the as-printed and as-sintered Mg-Zn scaffolds or those of the pure Mg scaffold [g], V_{bulk} is the bulk volume of the scaffolds [cm³], ρ_p is the density of the as-printed scaffolds, and ρ_{Mg} is the theoretical density of Mg (*i.e.*, 1.74 g/cm³). The pore size distribution and the corresponding differential and cumulative intrusion volumes of the Mg-Zn and pure Mg scaffolds were measured using a mercury intrusion porosimeter (MIP, Micromeritics Autopore IV 9500) at pressures over the range of 0 to 210 MPa.

The phases present in the Mg-Zn scaffolds were identified using an X-ray diffractometer (XRD, Bruker D8 Advance diffractometer in Bragg-Brentano geometry). The X-ray diffractometer was equipped with a graphite monochromator and a Vantec position-sensitive detector that was set to work at 45 kV and 40 mA. A scan range of 20–100° and a step size of 0.030° using the Cu $K\alpha$ radiation were employed.

4.2.3. *In vitro* immersion tests

In vitro immersion tests of the Mg-Zn scaffolds were performed in revised simulated body fluid (r-SBF) [15] for up to 28 days in a thermal bath maintained at 37 °C. The same tests of the pure Mg scaffolds were performed only for 1 day. 450 mL of the r-SBF solution was used for the immersion tests of each specimen with a solution volume-to-surface area ratio of 7 mL/cm² (the surface area was calculated based on the CAD design) [16]. The changes of the pH values measured close to the outer surface of the specimens and further away from it were monitored using two pH micro electrodes (inlabNMR, METTLER TOLEDO). An inductively coupled plasma optical emission spectroscope (ICP-OES, iCAP 6500 Duo Thermo Fisher) was used to determine the concentrations of Mg, calcium (Ca), phosphate (PO₄³⁻), and Zn ions in the r-SBF solution after the immersion tests of Mg-Zn and pure Mg scaffold samples at different time points.

X-ray micro-computed tomography (μCT, Nanotom 180 NF, GE Phoenix) scans of the Mg-Zn and pure Mg scaffolds before and after the immersion tests were acquired with a resolution of 6 μm. DICOM images of the scanned samples were imported into Dragonfly (Object Research Systems, Canada). After segmenting the corrosion products using Dragonfly, the volumes of the pure Mg and Mg-Zn specimens before and after the immersion tests were calculated by using the plugin “bone analysis”. The volume loss was calculated according to the following equation:

$$\text{Volume loss [\%]} = \frac{(V_{\text{Mg before degradation}} - V_{\text{Mg after degradation}})}{V_{\text{Mg before degradation}}} \times 100\% \quad (3)$$

where $V_{\text{Mg before degradation}}$ and $V_{\text{Mg after degradation}}$ are the volumes of the specimens before and after the immersion test, respectively.

The average corrosion rates of Mg-Zn and pure Mg scaffolds were determined using the following equation according to ASTM G1-03:

$$\text{Corrosion rate [mm/y]} = 8.76 \times 10^4 \times \frac{V}{A \times t} \quad (4)$$

where V is the loss of volume [g] (*i.e.*, $V_{\text{Mg before degradation}} - V_{\text{Mg after degradation}}$), A the surface area of scaffold sample [cm²], and t the duration of *in vitro* immersion test [h].

In addition, the spacing between the struts of the Mg-Zn scaffolds that were retrieved after immersion for various durations (*i.e.*, 1, 3, 7, 14 and 28 days) was determined using the plugin “bone analysis” in Drangonfly. Furthermore, the volumes and porosities of the retrieved Mg-Zn scaffolds (including the corrosion products) were determined.

4.2.4. Characterization of *in vitro* corrosion products

Fourier-transform infrared spectroscopy (FTIR) spectra of the biodegraded Mg-Zn and pure Mg scaffolds were obtained by using a FTIR apparatus (Thermo-Nicolet Nexus, USA) equipped with a liquid-nitrogen cooled MCT-A (mercury-cadmium-telluride) detector and a SAGA accessory at an incident angle of 80° with the setting of 128 scans at a resolution of 2 cm⁻¹. The Mg-Zn and pure Mg scaffolds before *in vitro* biodegradation were used for collecting the infrared background with the same settings. In addition, X-ray photoelectron spectroscopy (XPS, Thermo Fisher Scientific, K-Alpha Model, USA) was used to characterize the surface chemical states of the biodegraded Mg-Zn scaffolds after 1, 3, 7, 14, and 28 days of immersion. The measurements were performed under normal emission at a spot size of 400 μm and a base pressure of 10⁻⁷ mbar using a monochromatic Al Kα X-ray source. The Thermo Scientific Avantage v5.903 software (Thermo Fisher Scientific, USA) was used for processing and peak fitting. The surface morphologies and cross-section microstructures of the biodegraded Mg-Zn and pure Mg scaffolds at the selected time points were examined using the same SEM as detailed earlier, equipped with an energy-dispersive X-ray spectroscope (EDS).

4.2.5. Electrochemical tests

The specimens (Mg-Zn or pure Mg) were connected to a copper wire using copper foil tape and were then mounted into epoxy resin. The surface area of the specimens exposed to the electrolyte was 12.37 cm². Electrochemical tests were performed in triplicate using a Bio-Logic SP-200 potentiostat (Bio-Logic Science Instruments, France) in the r-SBF solution at 37 °C. A three-electrode electrochemical cell was set up with graphite as the counter electrode, Ag/AgCl as the reference electrode, and Mg-Zn or pure Mg scaffold sample as the working electrode.

Potentiodynamic polarization (PDP) measurements were performed after stabilization of open circuit potential (OCP) at 1 h of exposure. Then, the specimen was polarized from -0.3 V to +0.5 V *versus* OCP at a scan rate of 0.5 mV/s. The Tafel extrapolation method was used for determining the corrosion potential E_{corr} and corrosion current density i_{corr} . The corrosion rates (CR) were calculated according to the obtained i_{corr} , based on the ASTM standard G102-89:

$$CR_{\text{electrochemical}}[\text{mm/y}] = 3.27 \times 10^{-3} \times EW \times \frac{i_{\text{corr}}}{\rho} \quad (5)$$

where EW is the equivalent weight of Mg (valence 2), i_{corr} the current density [$\mu\text{A}/\text{cm}^2$], and ρ the theoretical density of Mg [g/cm^3].

The linear polarization resistance (LPR) of the scaffold sample was measured consecutively at distinct exposure times up to 21 days at ± 25 mV *versus* OCP at a potential sweep rate of 0.167 mV s⁻¹.

4.2.6. Mechanical properties

Uniaxial compression tests of the as-fabricated Mg-Zn scaffold specimens as well as the Mg-Zn scaffold specimens retrieved after 1, 3, 7 and 14 days of *in vitro* immersion were performed using an Instron universal mechanical testing machine (ElectroPuls E10000, Germany) with a 10 kN load cell at a crosshead speed of 2 mm/min (corresponding to an initial strain rate of 0.003 s^{-1}). The mechanical properties of the scaffolds, including their elastic modulus and yield strength were obtained according to the ISO 13314: 2011 standard. The slope of the initial linear region of the stress-strain curve was defined as the elastic modulus. An 0.2% strain offset line parallel to the initial linear elastic region was drawn and the stress value at the intersection with the stress-strain curve was defined as the yield stress.

4.2.7. Cytocompatibility evaluation

4.2.7.1. Preculture of cells and preparation of extracts

Preosteoblasts MC3T3-E1 (Sigma Aldrich, Germany) were pre-cultured for 7 days in α -minimum essential medium (α -MEM, Thermo Fisher Scientific, USA) without ascorbic acid, but supplemented with 10% fetal bovine serum (FBS, Thermo Fisher Scientific, USA) and 1% penicillin/streptomycin (p/s, Thermo Fisher Scientific, USA) under physiological conditions (5% CO₂ and 37 °C). The medium was refreshed once every 2-3 days.

The extracts of the Mg-Zn and pure Mg scaffolds were prepared by immersing the sterilized Mg-Zn and pure Mg scaffolds with a diameter of 10 mm and a height of 5 mm in the α -MEM (without ascorbic acid but with 10% FBS and 1% p/s) under the abovementioned physiological conditions for 72 h. The specimen-to-medium ratio was 1.25 cm²/mL [17]. Afterwards, 100, 50, and 10% extracts of Mg-Zn and pure Mg were obtained by collecting, filtering, and diluting the corresponding supernatants. The pH values of these extracts were measured by using a pH meter (METTLER TOLEDO). The concentrations of the released Mg and Zn ions in those extracts were measured using ICP-OES (iCAP 6500 Duo Thermo Fisher, USA).

4.2.7.2. Indirect cytotoxicity tests

PrestoBlue assay (Thermo Fisher Scientific, USA) was used to evaluate the indirect cytocompatibility of the Mg-Zn and pure Mg scaffolds. First, 1×10^4 MC3T3-E1 preosteoblast cells were cultured in the α -MEM (without ascorbic acid but with 10% FBS and 1% p/s) for 24 h, prior to exchanging the α -MEM with the 100%, 50%, and 10% Mg-Zn or pure Mg extracts (n=4/group). The same number of cells was cultured in the original α -MEM (without ascorbic acid but with 10% FBS and 1% p/s) as the negative control.

After 1, 3, and 7 days of culture, the Mg-Zn and pure Mg extract media were replaced with the α -MEM (without ascorbic acid but with 10% FBS and 1% p/s) to prevent any interference between the extract and the tetrazolium salt [18], prior to adding the PrestoBlue reagent. Thereafter, the specimens were incubated with 50 μ L of the PrestoBlue reagent at 37 °C for 1 h. The absorbance values were then measured using a Victor X3 microplate reader (Perkin Elmer, The Netherlands) over a wavelength range of 530 - 590 nm. The average metabolic activity of the cells was calculated according to the following equation:

$$\text{Metabolic activity [\%]} = \frac{\text{Absorbance (Mg specimen)}}{\text{Absorbance (negative control)}} \times 100\% \quad (6)$$

Furthermore, rhodamine phalloidin and 4',6-diamidino-2-phenylindole (DAPI) dyes were used to stain the cytoskeleton and nucleus of the cells in order to observe the morphology of the cells grown in the extracts. Therefore, MC3T3-E1 cells (number = 5×10^3) were cultured on 48-well glass disks in 200 μ L extracts ($n=2$). After 3 days of cell culture, the specimens were washed with phosphate buffered saline (PBS, Sigma-Aldrich, Germany) and were then fixed using 4% formaldehyde/PBS (Sigma-Aldrich, Germany) for 15 min at room temperature. Afterwards, the specimens were permeabilized with 0.5% Triton/PBS at 4 °C for 5 min. Then, 1% bovine serum albumin (BSA)/PBS (Sigma-Aldrich, Germany) was added per well, followed by incubation for 5 min. Consecutively, 1:1000 rhodamine phalloidin (Thermo Fisher Scientific, USA) in 1% BSA/PBS was added per well, followed by incubation for 1 h at 37 °C and three times wash with 0.5% Tween/PBS (Sigma-Aldrich, Germany). Then, the glass disk specimens were taken out of the wells and were mounted on glass slides with Prolong gold (containing 4',6-diamidino-2-phenylindole (DAPI), Life Technologies, USA). A fluorescence microscope (ZOE fluorescent cell imager, Bio-Rad, USA) was then employed to observe the cytoskeleton and nuclei of the cells.

4.2.7.3. Direct cytotoxicity tests

To observe the distribution and morphology of the MC3T3-E1 cells seeded on the Mg-Zn scaffolds, a live/dead staining assay was performed. A total of 4×10^5 cells were seeded on the scaffolds (height = 2.4 mm, diameter = 9.3 mm, $n=2$) in 48-well plates, which were then cultured in 1 mL of the α -MEM (without ascorbic acid but with 10% FBS and 1% p/s). After 2.5 h (to allow for the attachment of the cells to the specimens), the scaffolds together with 1 mL α -MEM were transferred to 6-well plates. Additional α -MEM (7 mL) was added to the wells to reach a specimen-to-medium ratio of 1.25 cm²/mL. After 3 days of cell culture, the specimens were taken out of the cultured medium and the medium was stored. Afterwards, the specimens were washed with PBS and were incubated in a PBS solution containing 0.5 μ L/mL of calcein and 1.5 μ L/mL of ethidium

homodimer-1 (LIVE/DEAD Viability/Cytotoxicity Kit, Life Technologies Corp., USA) for 15 min in the dark at room temperature. The PBS solution was then replaced by the previously stored medium to prevent further reaction between the PBS solution and Mg-Zn scaffolds during the imaging process. Thereafter, the live and dead cells on the scaffolds were observed with a fluorescence microscope (ZOE cell imager, Bio-Rad, USA). Furthermore, the morphology of cells on the Mg-Zn scaffolds was observed under the same SEM. After 3 days of cell culture, the specimens ($n=2$) were washed with PBS and were fixed with 4% formaldehyde (Sigma Aldrich, Germany) for 15 min, followed by dehydration stages in 50, 70, and 100% ethanol for 10 min each. They were further preserved by immersion in hexamethyldisilazane (Sigma Aldrich, Germany) for 30 min. The specimens were then dried overnight prior to SEM imaging.

4.2.8. Statistical analysis

Statistical analyses of the concentrations of Mg ion release and the metabolic activity results obtained from the indirect cytotoxicity tests were performed with ANOVA, followed by the Tukey *post hoc* test ($\alpha = 0.05$) with $p < .0001$, ****; $p < .001$, ***; $p < .01$ and **; $p < .05$, *.

4.3. Results

4.3.1. Structural characteristic of the scaffolds

The as-printed Mg-Zn and pure Mg scaffolds with freestanding characteristics were similar in their exterior appearance to the design. After sintering, the dimensions of the Mg-Zn and pure Mg scaffolds were reduced by $10.7 \pm 0.1\%$ and $9.5 \pm 0.2\%$, respectively (Figure 4.2a). The struts of the top layer of the printed Mg-Zn scaffolds perpendicularly bridged the struts of the underlying layer, precisely as designed (Figure 4.2b). The powder particles were evenly embedded in the binder (Figure 4.2c). Sufficient powder loading in the ink allowed the scaffolds with a high aspect ratio to be built with almost no distortions. The as-printed Mg-Zn and pure Mg scaffolds had similar micro-porosities, and the strut width and spacing values were quite close to the design values (Table 4.1). After sintering (Figure 4.2d1 and e1), the width shrinkages of the struts of the Mg-Zn and pure Mg scaffolds were measured to be $11.2 \pm 3.2\%$ and $10.2 \pm 2.3\%$, respectively (Table 4.1). The total porosity of the sintered Mg-Zn scaffolds ($50.3 \pm 3.4\%$ from the weighing method and $49.4 \pm 5.7\%$ from the μ CT analysis) was lower than that of the sintered pure Mg scaffolds ($54.5 \pm 2.4\%$ from the weighing method and $52.3 \pm 2.9\%$ from the μ CT analysis). In the close-up views of the struts, sintering necks and open micropores could be observed between Mg-Zn or pure Mg powder particles (Figure 4.2d2 and e2). The micropores inside the struts were more clearly visible when examining the cross-section

microstructure (Figure 4.2d3 and e3). From the MIP analysis, the micropores were found to be mostly in a size range of 2 - 10 μm , centered at around 5 μm (Figure 4.2f). The lower cumulative intrusion volume of the Mg-Zn scaffolds (the inset in Figure 4.2f) indicated fewer micropores in their struts, as compared to those of the pure Mg scaffolds, which is consistent with the calculated micro-porosities based on the cross-section microstructures of the struts (Table 4.1).

Table 4.1 Morphological characteristics of the Mg-Zn and pure Mg scaffolds fabricated by using the extrusion-based AM technique.

Sample group	Strut width (μm)	Strut spacing (μm)	Porosity in the struts after sintering	Absolute Porosity
Design	580	360	--	37.8%
As-printed Mg-Zn	581.2 ± 14.9	343.9 ± 18.5	--	$58.3 \pm 1.6\%$
As-printed Mg	587.6 ± 11.7	351.4 ± 18.5	--	$60.0 \pm 1.9\%$
As-sintered Mg-Zn	516.1 ± 15.3	331.7 ± 39.5	$6.9 \pm 1.0\%$	$50.3 \pm 3.4\%$ (W) $49.4 \pm 5.7\%$ (μCT)
As-sintered Mg	528.1 ± 12.6	298.4 ± 16.6	$8.5 \pm 0.4\%$	$54.5 \pm 2.4\%$ (W) $52.3 \pm 2.9\%$ (μCT)

The etched Mg-Zn specimen showed a grain size of $26.5 \pm 3.5 \mu\text{m}$ with second phase particles dispersing at grain boundaries (Figure 4.2d4), while the etched pure Mg specimen exhibited a grain size of $28.3 \pm 1.2 \mu\text{m}$ with clean grain boundaries (Figure 4.2e4). Based on the XRD analysis, the as-sintered Mg-Zn scaffolds consisted of the α -Mg phase and MgZn_2 second phase, while only the α -Mg phase was detected in the as-sintered pure Mg scaffolds (Figure 4.2g).

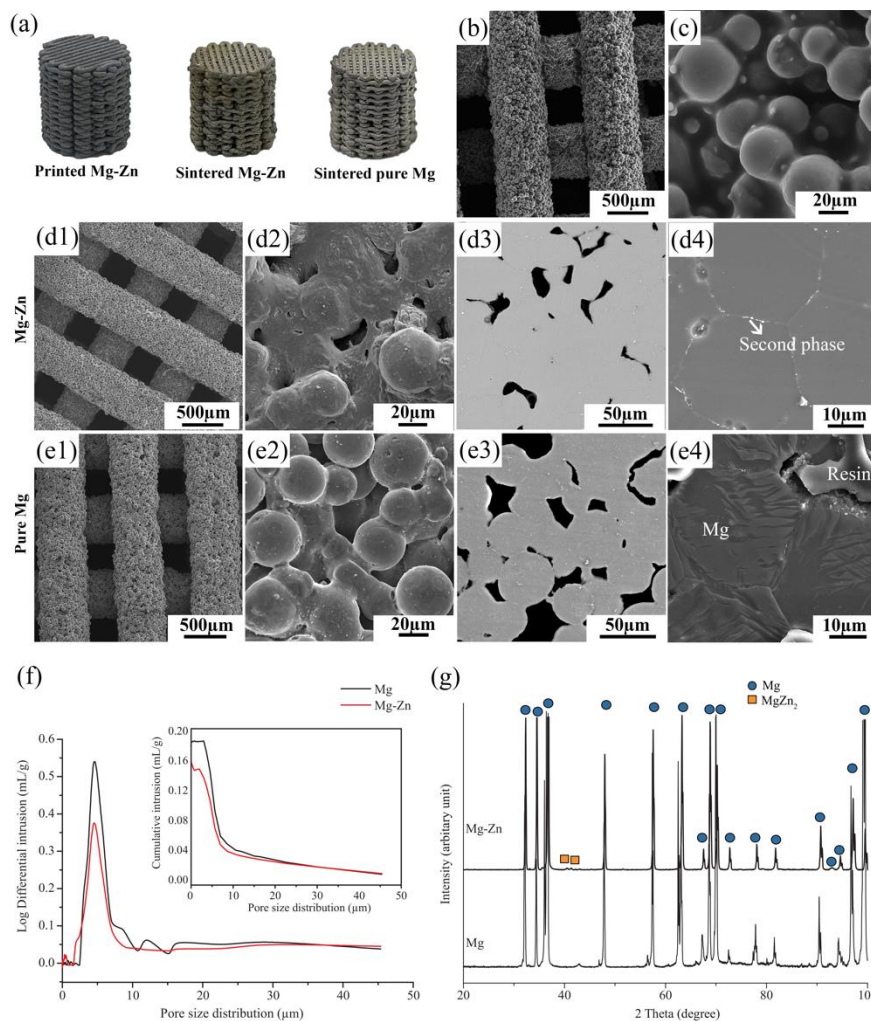


Figure 4.2 Characteristics of the fabricated Mg-Zn scaffolds in comparison with those of the pure Mg scaffolds: (a) macrographs, (b and c) the morphologies of the as-printed Mg-Zn scaffold struts at different magnifications, (d1-d4) the morphology, cross section and microstructure of the as-sintered Mg-Zn scaffolds, (e1-e4) the morphology, cross section and microstructure of the as-sintered pure Mg scaffolds, (f) micropore size distributions in the struts (the plot of pure Mg cited from [18]), and (g) XRD patterns (the pattern of pure Mg cited from [18]).

4.3.2. *In vitro* biodegradation behavior

The Mg-Zn scaffolds maintained their structural integrity for the entire 28 days of immersion in the r-SBF solution with white biodegradation products gradually forming on their surface, while the pure Mg scaffolds lost most of their peripheral parts after 1 day of immersion (Figure 4.3a). The pH changes in the proximity of the scaffold sample (*i.e.*, local pH) and further away (*i.e.*, distant pH) were measured (Figure 4.3b). At the initial stage of the immersion, the local pH of both Mg-Zn and pure Mg exhibited fluctuations (see the arrows in Figure 4.3b), while the distant pH increased steadily. During the first 24 h of immersion, the pH values associated with the pure Mg increased from 7.4 to around 9.5 with the local pH being higher than the distant one most of the time. The local pH value associated with the pure Mg specimens sharply increased to 9.3 during the first 10 h of immersion and tended to stabilize thereafter (Figure 4.3b). By comparison, the pH values associated with the Mg-Zn specimens remained lower than 8.0 during the first 24 h of immersion, with the local pH being only slightly higher than the distant one (Figure 4.3b). The increase of the pH value associated with the Mg-Zn specimens slowed down after 10 days of immersion (Figure 4.3c). The release of Mg ions from pure Mg was about twice as much as that from Mg-Zn during the first 24 h of immersion, while higher amounts of Ca and P ions were detected in the r-SBF solution of the Mg-Zn group (Figure 4.3d). Throughout 28 days of immersion, the amount of Mg ions released from the Mg-Zn scaffolds increased from 141.3 ± 13.0 mg/L at day 1 to 359.3 ± 54.8 mg/L at day 28 (Figure 4.3e). Over this period, the amounts of remaining Ca and P ions decreased. According to the μ CT analysis, up to 28 days of immersion, the interspacing between the struts of the Mg-Zn scaffolds exhibited a gradual ascending trend (Figure 4.3f). After segmenting the images of the Mg-Zn scaffolds (excluding the corrosion products), the volume loss of the Mg-Zn scaffolds was found to have increased from $7.1 \pm 2.0\%$ after 1 day of immersion to $64.6 \pm 2.8\%$ after 28 days of immersion (Figure 4.3g). The volume loss of the pure Mg scaffolds has been found to be $37.3 \pm 6.7\%$ after 1 day of immersion [1], which is close to that of Mg-Zn after 7 days of immersion (the dash line in Figure 4.3g). The average *in vitro* corrosion rate of the Mg-Zn scaffolds decreased from 2.3 ± 0.9 mm/y after 1 day of immersion to 0.7 ± 0.1 mm/y after 28 days of immersion (Figure 4.3h). In the case of the pure Mg scaffolds, the corrosion rate reached 12.1 ± 0.2 mm/y after 1 day. When including the corrosion products during the segmentation of the Mg-Zn scaffolds, the volume of the specimens was found to increase until day 7, and subsequently decreased (Figure 4.3i). Once the corrosion products were segmented apart from the Mg-Zn substrate, the porosity of the Mg-Zn scaffolds gradually increased from an initial value of $49.4 \pm 5.7\%$ to $80.0 \pm 0.6\%$ after 28 days of immersion. By comparison, the porosity of the Mg-Zn scaffolds with the corrosion products decreased to $33.4 \pm 7.1\%$ at day 1 and further decreased to $24.0 \pm 3.5\%$ at day 3 (Figure 4.3j). Then, the porosity remained stable until day 14 and subsequently increased at day 28 (Figure 4.3j).

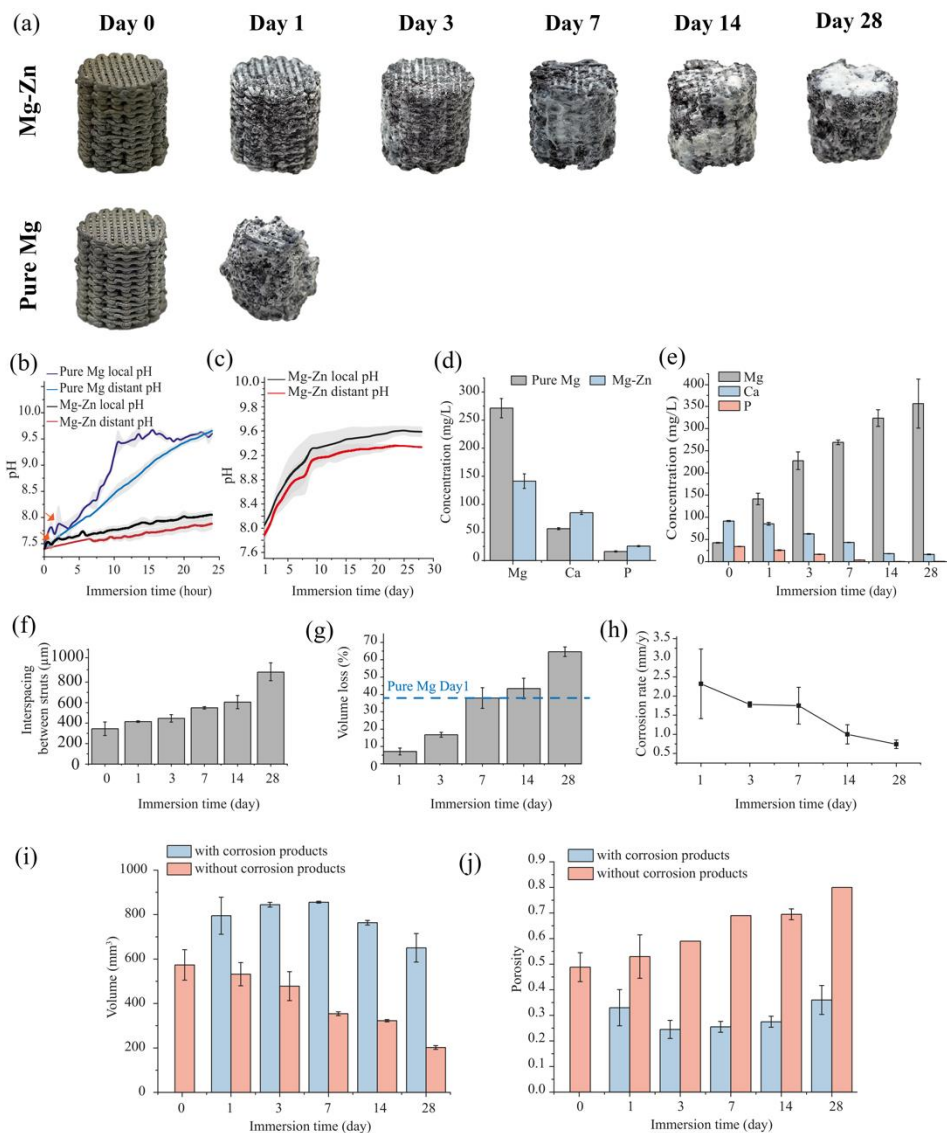


Figure 4.3 *In vitro* biodegradation characteristics of the Mg-Zn scaffolds in comparison with those of the pure Mg scaffolds: (a) visual inspection of degraded scaffolds over immersion time, (b) pH variations during the first day of immersion, (c) pH variations up to 28 days of immersion, (d) changes of the concentrations of ions in r-SBF during the first day of immersion, (e) changes of the concentrations of ions in r-SBF up to 28 days of immersion, (f) changes of the interspacing between the struts of the degraded Mg-Zn scaffolds with immersion time, (g) volume loss over time, (h) calculated corrosion rates of the Mg-Zn scaffolds over time, (i and j) changes of the volume and porosity of the

degraded Mg-Zn scaffolds with and without the corrosion products with immersion time. The results of pure Mg are cited from [18].

4.3.3. Characteristics of biodegradation products on the scaffolds

4.3.3.1. Chemical characteristics of the scaffold surface

FTIR revealed the presence of hydroxide (OH^-) and carbonates (CO_3^{2-}) on the surface of the biodegraded pure Mg scaffolds with the following characteristics: OH^- absorption band at 3700 cm^{-1} [19] and CO_3^{2-} bands between $750\text{-}900\text{ cm}^{-1}$ and $1400\text{-}1550\text{ cm}^{-1}$ [20, 21]. By comparison, during the first day of immersion, the phosphates (PO_4^{3-}) with the absorption peak at around 1100 cm^{-1} emerged on the degraded Mg-Zn scaffolds with the appearance of CO_3^{2-} (Figure 4.4a). However, the absorption peak of PO_4^{3-} decreased with the immersion time and disappeared after 28 days of immersion (Figure 4.4a). XPS further revealed the compositional changes of the biodegradation products on the surface of the Mg-Zn scaffolds with the immersion time (Figure 4.4b). The total XPS spectrum showed that the biodegradation products were composed of C, Mg, Zn, P, Ca, and O after 1 day of immersion. The percentage of Mg decreased until 14 days and sharply increased at day 28, while the percentages of Zn, P, and Ca increased first, started to decrease from day 14, and became too low to be detected at the end of the immersion period (Figure 4.4b). Furthermore, the high-resolution XPS spectra of C1s, Mg1s, Zn2p_{3/2}, Ca2p, and P2p were collected from the surfaces of the specimens (after *in vitro* biodegradation for 1, 7, and 28 days) and were then fitted (Figure 4.4c-g). The peaks located at 285 and 290 eV may be due to hydrocarbon contamination and CO_3^{2-} , respectively (Figure 4.4c) [22]. The peaks at 1303, 1304, and 1305 eV corresponded to $\text{Mg}(\text{OH})_2$, MgO, and MgCO_3 , respectively (Figure 4.4d) [23], while the peak located at 1022 eV was attributed to ZnO (Figure 4.4e) [24]. The Ca 2p peak consisted of Ca 2p_{1/2} at 348 eV and Ca 2p_{2/3} at 347 eV, and a Mg Auger peak at 351 eV was also present in this region (Figure 4.4f) [25]. The P2p peaks observed at about 133 and 134 eV (Figure 4.4g) could be assigned to PO_4^{3-} . ZnO, Ca^{2+} , and PO_4^{3-} were observed on the surfaces of the specimens after 1 day and 7 days of immersion, but they could not be detected any more after 28 days of immersion (Figure 4.4e-g).

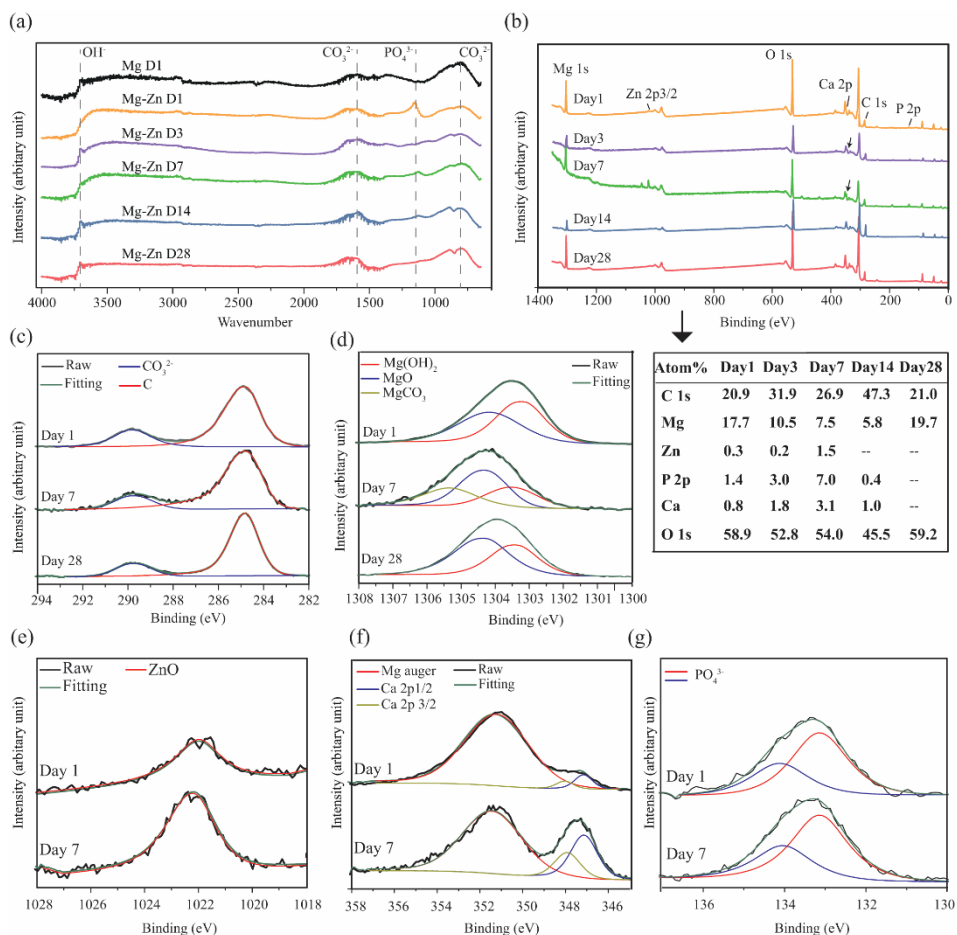


Figure 4.4 Characteristics of the biodegradation products on the surface of Mg-Zn scaffold struts: (a) FTIR spectra (the spectrum of pure Mg after the first day of immersion cited from [18]), and (b-g) XPS spectra.

4.3.3.2. Morphological characteristics

The original struts of the pure Mg scaffolds could not be recognized after only 1 day of immersion and their surfaces became completely covered by the biodegradation products (Figure 4.5a1). The corrosion product layer with cracks consisted of C, O, Mg, and a minor amount of Ca (Figure 4.5a2). At the center of the scaffolds, the space between the struts was filled with the biodegradation products (Figure 4.5a3). The pure Mg struts were mostly replaced by the biodegradation products (Figure 4.5a4) composed of Mg and O [1]. By comparison, the struts of the Mg-Zn scaffolds were still clearly visible after 1 day of immersion (Figure 4.5b1) with a biodegradation product layer composed of C, O, Na,

Mg, Zn, P, and Ca deposited on the struts (Figure 4.5b2). The cross-section microstructure of the Mg-Zn scaffolds after 1 day of immersion showed the structural integrity of the struts and the interspacing between the struts were still well maintained (Figure 4.5b3). The biodegradation products were formed within the initial interconnected pore network of the porous structure (Figure 4.5b4). At day 3, both the struts and the space between the struts were covered by a thick deposition layer (Figure 4.5c1). Flake-shaped products were formed on the surface, which contained C, O, Mg, Zn, and Ca (Figure 4.5c2), while the space between the struts at the center of scaffolds were partially filled with the biodegradation products (Figure 4.5c3). It was also observed that the struts corroded locally and the corroded areas were replaced by the biodegradation products (Figure 4.5c3 and c4). At day 7, the biodegradation products on the surface were loose and porous (Figure 4.5d1). Some needle-shaped crystals had also formed on the surface, in which Mg, O, Ca, and Cl were detected (Figure 4.5d2). At the center of the scaffolds, after 7 days of immersion, the struts were further corroded, and dense biodegradation products had formed and fully filled the space between the struts (Figure 4.5d3), closely surrounding the remaining struts (Figure 4.5d4). At day 14, the surface of the scaffolds showed a bumpy morphology, instead of the original porous features (Figure 4.5e1), and many bump-shaped corrosion products, containing C, O, Mg, and Ca, had appeared on the top of the former deposition layer (Figure 4.5e2). At this time point, most of the struts were corroded with a few struts retaining their integrity (Figure 4.5e3 and e4). After 28 days, a relatively dense and compact layer with a fish-scale-like structure was formed (Figure 4.5f1), in which Ca had disappeared, while C, O, Mg, and a trace amount of Na were detected (Figure 4.5f2). The biodegradation products at the center of the scaffolds were more porous (Figure 4.5f3 and f4). In order to reveal the compositions of the biodegradation products formed at the center of the scaffolds, EDS mapping analysis was performed on the scaffolds after 14 days of immersion, showing that Mg and O were the main elements with some trace amounts of Ca, P, C and Zn.

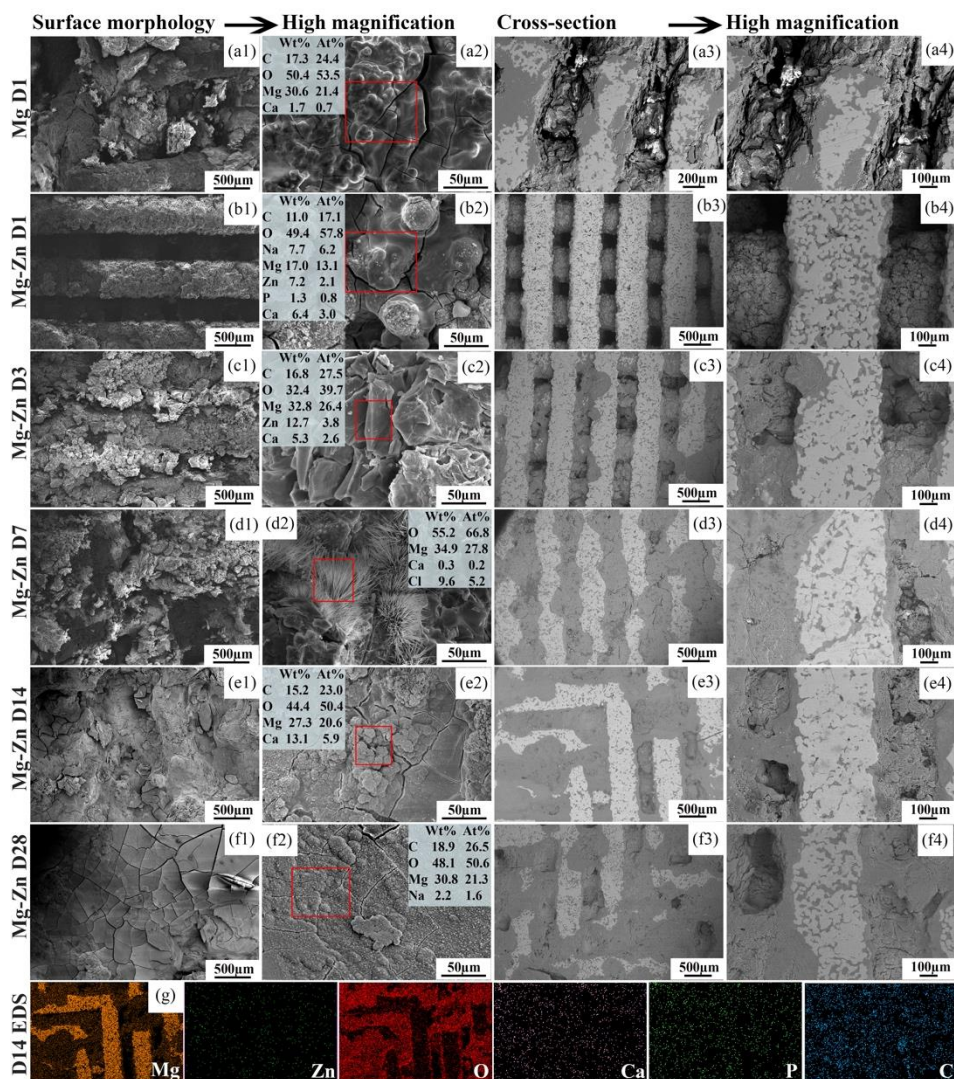


Figure 4.5 SEM images of the biodegradation products on the scaffold outer surfaces and in the center of the Mg-Zn scaffold in comparison with those of the pure Mg scaffolds: (a1-a4) pure Mg scaffolds after 1 day of immersion, (b1-b4) Mg-Zn scaffolds after 1 day of immersion, (c1-c4) Mg-Zn scaffolds after 3 days of immersion, (d1-d4) Mg-Zn scaffolds after 7 days of immersion, (e1-e4) Mg-Zn scaffolds after 14 days of immersion, (f1-f4) Mg-Zn scaffolds after 28 days of immersion, and (g) EDS analysis of the Mg-Zn scaffolds after 14 days of immersion. The boxed area and values indicate the spots where the EDS analyses were performed and the corresponding elemental compositions, respectively.

4.3.4. Electrochemical response

The Mg-Zn and pure Mg scaffolds exhibited similar anodic and cathodic polarization behaviors. However, Mg-Zn exhibited a nobler corrosion potential (E_{corr}) and a lower current density (i_{corr}) than those of pure Mg (Figure 4.6a). The current density values of Mg-Zn and pure Mg were respectively $4.3 \cdot 10^{-5} \pm 0.9 \cdot 10^{-5}$ and $9.6 \cdot 10^{-5} \pm 1.7 \cdot 10^{-5} \text{ A} \cdot \text{cm}^{-2}$, corresponding to corrosion rates of 1.1 ± 0.8 and $2.2 \pm 0.0 \text{ mm/y}$. The LPR values of the Mg-Zn scaffolds decreased from $2.1 \pm 0.4 \text{ K}\Omega \cdot \text{cm}^2$ to $1.1 \pm 0.2 \text{ K}\Omega \cdot \text{cm}^2$ during the first 3 days of immersion, and then increased to $2.2 \pm 0.1 \text{ K}\Omega \cdot \text{cm}^2$ until day 14, followed by a decrease at day 21 (Figure 4.6b). As compared with Mg-Zn, the LPR values of the pure Mg scaffolds remained at a very low level during the first day of immersion (around $0.5 \text{ K}\Omega \cdot \text{cm}^2$).

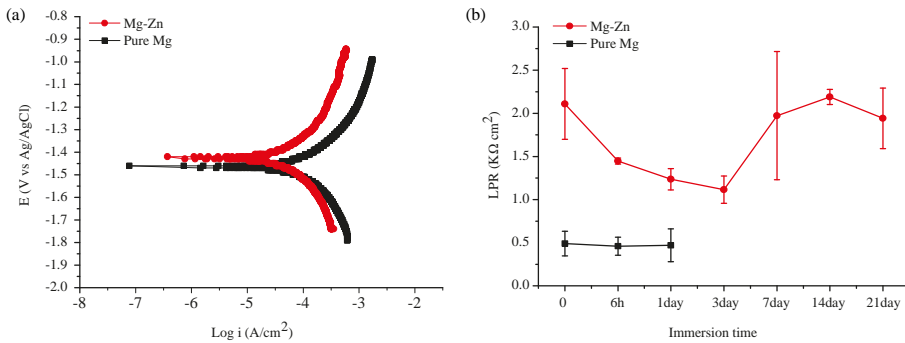


Figure 4.6 Electrochemical test results: (a) Potentiodynamic polarization after 1 h of exposure, and (b) linear polarization resistance over a period of 21 days of exposure for the bare Mg and Mg-Zn scaffolds. The results of pure Mg are cited from [18].

4.3.5. Mechanical properties

The uniaxial compressive stress-strain curves of the Mg-Zn and pure Mg scaffolds both began with a linear elastic region, followed by densification during the plastic deformation stage until failure (Figure 4.7a). The yield strength and elastic modulus of the Mg-Zn scaffolds ($14.5 \pm 3.0 \text{ MPa}$ and $448.8 \pm 42.4 \text{ MPa}$, respectively) were much higher than those of the pure Mg scaffolds ($4.7 \pm 0.7 \text{ MPa}$ and $184.4 \pm 37.3 \text{ MPa}$, respectively). The biodegraded specimens showed a notable decline in strain to failure from $30 \pm 8\%$ prior to the *in vitro* immersion to $16 \pm 1\%$ after 14 days of immersion (Figure 4.7b). Over the *in vitro* immersion period, the yield strength of the scaffolds markedly increased from $14.5 \pm 3.0 \text{ MPa}$ before degradation to $34.9 \pm 7.3 \text{ MPa}$ after 3 days of immersion and then declined to $24.6 \pm 7.6 \text{ MPa}$ at day 14 (Figure 4.7c). Likewise,

the elastic modulus increased from 448.8 ± 42.4 MPa to 735.9 ± 220.6 MPa at day 3 and then decreased to 282.9 ± 83.6 MPa after 14 days of immersion (Figure 4.7d).

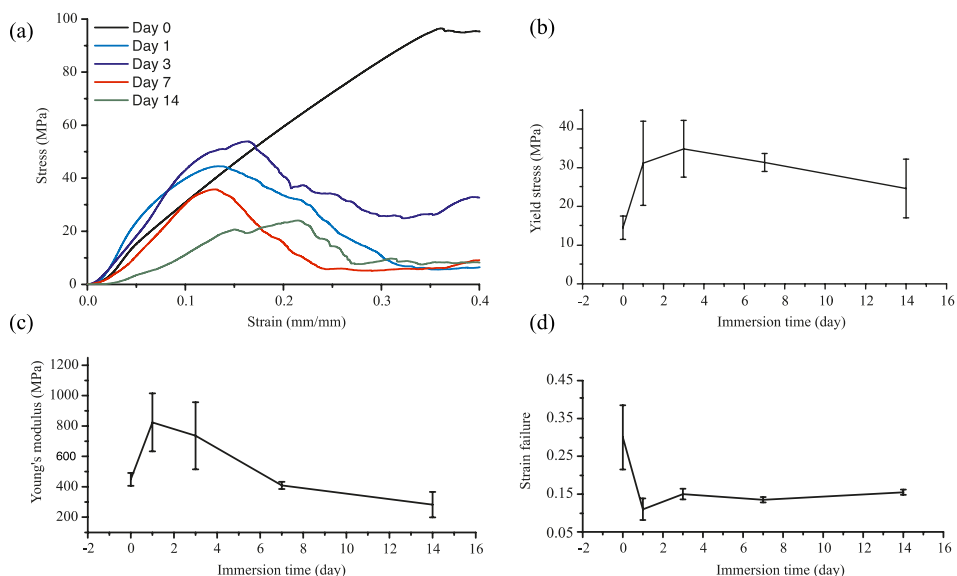


Figure 4.7 Compressive mechanical properties of the Mg-Zn scaffolds in comparison with those of the pure Mg scaffolds: (a) stress-strain curves of the scaffolds before *in vitro* biodegradation (the curve of pure Mg cited from [18]), (b) stress-strain curves of the degraded Mg-Zn scaffolds, (c) variation of yield strength with immersion time, and (d) variation of Young's modulus with immersion time. Dash lines in the insets indicate the linear regions; arrows and crosses indicate the yield strengths.

4.3.6. *In vitro* biological evaluation of the scaffolds

The exposure of MC3T3-E1 cells to the 100% extracts of the Mg-Zn and pure Mg scaffolds led to instant cytotoxicity (Figure 4.8a). When the extracts were diluted to 50%, a low metabolic activity of $24.0 \pm 6.6\%$ was detected for the Mg-Zn group, which decreased until day 7, while the pure Mg group showed a higher metabolic activity of $84.8 \pm 12.8\%$ after 1 day of culture, which was maintained until 7 days of cell culture. When the extracts were further diluted to 10%, however, the metabolic activity of the Mg-Zn and pure Mg groups stayed at high levels ($> 90\%$) until 7 days of cell culture (Figure 4.8a). The pH values of the 10% extracts of the Mg-Zn and pure Mg scaffolds were only marginally lower than those of the corresponding 50 and 100% extracts (Figure 4.8b). However, lower concentrations of Mg ions were found in the diluted extracts of

both Mg-Zn and pure Mg (Figure 4.8c). In addition, the concentrations of Mg ions in the 50% and 100% Mg-Zn extracts were lower than those in the 50 and 100% pure Mg extracts (Figure 4.8c). The concentration of Zn ions released from the Mg-Zn scaffolds decreased with increasing dilution ratio of the extracts (17.0 ± 2.4 mg/L in the 100% extract and 2.1 ± 0.1 mg/L in the 10% extract) (Figure 4.8c). When cultured in the 10% Mg-Zn extracts for 3 days, the cells formed a confluent layer and showed a spread morphology with well-developed stress fibers (Figure 4.8e), similar to the control group (0% extract, *i.e.*, the α -MEM medium) (Figure 4.8d). However, only a few cells could be observed in the 50% Mg-Zn extracts (Figure 4.8f) and they presented a less spread morphology. In the 100% Mg-Zn extracts, there were hardly any cells (Figure 4.8g).

In the direct cell culture, the preosteoblasts showed a homogenous distribution over the struts of the Mg-Zn scaffolds after 3 days with the presence of both viable and unhealthy/dead preosteoblasts (Figure 4.8i). The cells were also less spread as compared to the cells grown on the reference Ti6Al4V scaffolds (Figure 4.8h). SEM imaging of the Mg-Zn scaffolds after 3 days of culture revealed that some cells could spread between the cluster of particles (the arrows Figure 4.8j), whereas others settled on such clusters adopting a round morphology (the arrows in Figure 4.8k).

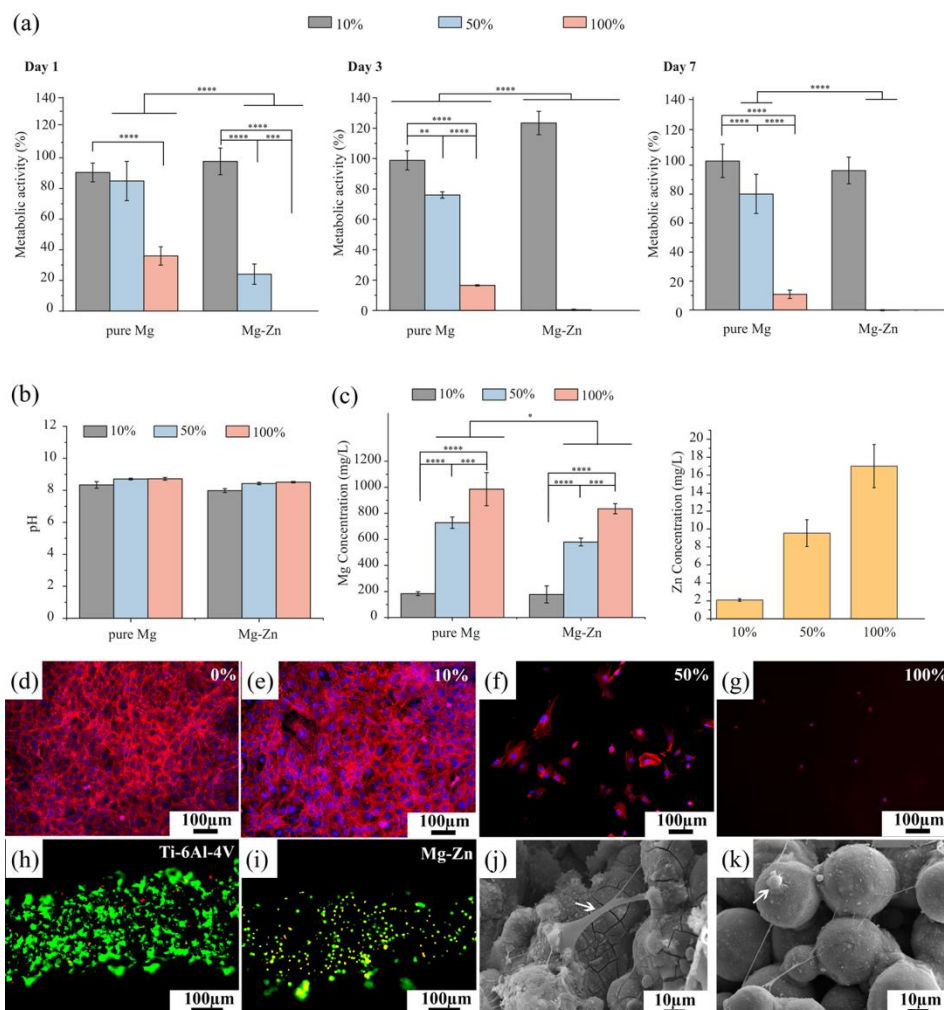


Figure 4.8 *In vitro* biological evaluation of the scaffolds: (a) indirect metabolic activity values of preosteoblasts cultured in the 10, 50 and 100% extracts of the Mg-Zn and pure Mg scaffolds [18], (b-c) pH and ion concentrations of the Mg-Zn and pure Mg [18] extract media of different concentrations, (d-g) rhodamine phalloidin (red) and DAPI (blue) stained preosteoblasts after 3 days of culture in the 0, 10, 50 and 100% extracts of the Mg-Zn scaffolds, (h-i) calcein acetoxyethyl (green, indicating living cells) and ethidium homodimer-1 (red, indicating dead cells) stained preosteoblasts on the Mg-Zn scaffolds (with Ti-6Al-4V as the reference), and (j-k) the morphologies of cells on the Mg-Zn scaffolds after 3 days of direct cell culture.

4.4. Discussion

For the first time, extrusion-based AM was employed to fabricate geometrically ordered pre-alloyed Mg-Zn scaffolds. Upon heating, the Mg-Zn binary alloy was brought into the solid-liquid two-phase region between the solidus and liquidus [26], thus having a broader sinterability window than pure Mg. Therefore, a specific sintering scheme was first developed for the fabrication of the Mg-Zn scaffolds. The fabricated Mg-Zn scaffolds with denser struts and the dispersed second phase contributed to the improved mechanical properties and corrosion resistance, as compared to those of the pure Mg scaffolds. In addition, the indirect culture of preosteoblasts in the Mg-Zn extracts with the recommended dilution ratio (6-10 times [27]) revealed good biocompatibility.

4.4.1. Fabrication of the Mg-Zn scaffolds

The extrusion-based AM technique enabled precise printing of the Mg-Zn and pure Mg scaffolds with strut sizes and strut spacing values close to the design values (Table 4.1). A single-step debinding and sintering process was applied to the as-printed Mg-Zn scaffolds. The sintering step of the Mg-Zn scaffolds was, however, different from the one applied to pure Mg in our previous study [28]. The existence of the liquid-solid two-phase region for the Mg-Zn alloy allowed for the variation of the density of the struts by controlling the volume fraction of the liquid phase formed during sintering, which was infeasible for pure Mg due to the absence of such a liquid-solid two-phase region. To determine a suitable range of the sintering temperatures, the dependence of liquid phase fraction on temperature was calculated, based on the thermodynamic equilibrium (Figure S4.1). In conventional powder metallurgy, an optimum fraction of the liquid phase for liquid-phase sintering is reportedly between 5 and 15 vol% and the higher fraction of the liquid phase, the higher density of struts could be achieved within a shorter sintering time [29]. Therefore, a sintering temperature range of 570 to 590 °C was selected, corresponding to a liquid fraction range of 10-15 vol% for the Mg-Zn alloy with 4 wt% Zn. The optimization of the sintering scheme was based on the measured density of the struts and the fidelity of the Mg-Zn scaffolds (Figure S4.2). Although a higher temperature (590 °C/1 h) was beneficial for the densification of Mg-Zn scaffold struts (Figure S4.2a), the fidelity of the scaffolds was diminished due to the formation of nodules at the peripheral struts (the arrow in Figure S4.2d). This was also observed during the optimization of the sintering scheme for pure Mg [28]. To ensure that a similar level of porosity could be achieved and to avoid an unexpected increase in grain size, sintering with a dwelling time of 1 h was selected for the Mg-Zn scaffolds (the same as for the pure Mg). Based on the preceding studies, the optimized sintering parameters of 580 °C/1 h and 640 °C/1 h [1] were used for the sintering of the Mg-Zn and Mg scaffolds, respectively. After the post-processing, both the Mg-Zn and pure Mg scaffolds possessed

a hierarchical porous structure with macropore sizes of about 300 μm and micropore sizes of $< 100 \mu\text{m}$ in the struts (Table 4.1 and Figure 4.2), which could be favorable for the adhesion, proliferation, and differentiation of cells [30]. Under the premise of guaranteeing fidelity, the fabricated Mg-Zn scaffolds exhibited a slightly higher density in the struts and, thus, lower porosity of the whole structure than the pure Mg scaffolds (Figure 4.2f and Table 4.1).

The precipitated MgZn_2 second phase was found in the Mg-Zn scaffolds (Figure 4.2d4) due to the low solubility of Zn (1.6 wt%) in the α -Mg phase at room temperature [26], which has been also reported in some other studies on Mg-Zn alloys [3, 31]. The mean grain size of the original Mg-Zn powder ($2.8 \pm 0.1 \mu\text{m}$) was smaller than that of the pure Mg powder ($8.6 \pm 1.7 \mu\text{m}$), which could be attributed to the grain-refining effect of Zn [9, 32]. However, this effect was not clearly visible any more after sintering, as evidenced by the similar grain sizes of the sintered Mg-Zn and pure Mg scaffolds (about 30 μm).

4.4.2. *In vitro* biodegradation behavior

The static *in vitro* corrosion resistance of the Mg-Zn scaffolds was significantly better than that of the pure Mg scaffolds (Table 4.2). Comparisons in pH value, the concentration of Mg ion, and volume loss after 1 day of immersion all clearly showed that the fabricated Mg-Zn scaffolds had much improved corrosion resistance (Figure 4.3). Similar remarkable improvements in the corrosion resistance have been observed in other studies on the cast and powder metallurgy Mg-Zn binary alloys [3, 4]. The improved corrosion resistance of the Mg-Zn scaffolds could be attributed to the addition of Zn, which elevates the corrosion potential of Mg (Figure 4.6a) [4, 5]. Although the presence of second phase particles could cause micro-galvanic corrosion, the corrosion of our Mg-Zn alloy with $< 5 \text{ wt\% Zn}$ was not dominated by micro-galvanic corrosion, since with a low Zn content, second phase particles are dispersed in the α -Mg matrix (Figure 4.2d4) instead of forming a continuous network structure that could lead to widespread and distinct anode-cathode sites [4]. In addition, Zn can increase the tolerance limits of impurities, thereby reducing the corrosion rate of Mg [33]. Moreover, many other researchers [5, 34-37] have found that the addition of Zn to Mg can accommodate the formation of a compact corrosion product film. When a Mg-Zn alloy is exposed to the r-SBF solution, the alloy surface is oxidized to generate Mg^{2+} and Zn^{2+} ions and, at the same time, OH^- and H_2 are produced by the reduction of H_2O . The Mg^{2+} and Zn^{2+} ions react with OH^- to form $\text{Mg}(\text{OH})_2$ and $\text{Zn}(\text{OH})_2$ as a layer of precipitates on the alloy surface. It is well known that, in the r-SBF solution, $\text{Mg}(\text{OH})_2$ is vulnerable to Cl^- attack, leading to the formation of soluble MgCl_2 . However, $\text{Zn}(\text{OH})_2$ is known to be transformed into stable ZnO at the very early stage of immersion (within 300 s), contributing to the

formation of a protective corrosion film on the surface of the Mg-Zn alloy [35]. Therefore, during the first day of immersion, ZnO compounds appeared on the surface of the Mg-Zn scaffolds (Figure 4.4e), providing a more stable film than the one present on the surface of the pure Mg, which was preferable for the deposition of calcium phosphate products. This could explain why after 1 day of immersion, PO_4^{3-} was formed on the Mg-Zn scaffolds but not on the pure Mg scaffolds (Figure 4.4a). The calcium phosphate phase that is similar in composition to the inorganic phase of the bone can be utilized by osteoblasts to form new bone [38].

The static *in vitro* biodegradation rate of the Mg-Zn scaffolds presented here was compared with those of the bulk and foam Mg-Zn alloys fabricated by conventional techniques (Table 4.2) [36, 39-41] and with the desired rates of biodegradation. We found that the biodegradation rate of the Mg-Zn scaffolds (0.7 ± 0.1 mm/y at day 28) developed here is quite close to the biodegradation rate of an ideal bone substitute (0.2 - 0.5 mm/y) [42]. In addition, the corrosion rate (1.7 ± 0.5 mm/y at day 7) of our Mg-Zn scaffolds is similar to cast and extruded Mg-Zn alloys (with 4 wt% Zn) (1.9 - 4.3 mm/y at day 7, Table 4.2). The fabricated Mg-Zn scaffolds with a porosity of around 50% had an initial biodegradation rate of 2.3 ± 0.9 mm/y, which is similar to the biodegradation rate of the Mg-Zn alloy (4 wt% Zn, grain size = $23.2 \mu\text{m}$) with 1% porosity fabricated through conventional powder metallurgy (Table 4.2). One of the reasons for such a remarkable corrosion resistance is the finer grains in our Mg-Zn scaffolds ($26.5 \pm 3.5 \mu\text{m}$), especially when compared with that of the bulk alloys in the as-cast condition (Table 4.2). Another important reason could be that the interconnected porous structure of our Mg-Zn scaffolds allowed stable ZnO to participate in the formation of the corrosion products everywhere, which helps in maintaining the integrity of the structure and effectively retards the progress of the corrosion process.

Table 4.2 Comparisons between the *in vitro* biodegradation rates of the Mg-Zn scaffolds and those of the same alloy in other studies.

Material	Fabrication technique	Porosity	Grain size (μm)	<i>In vitro</i> degradation rate (mm/y)	Medium	Ref.
Mg-4Zn	cast	0%	--	day 6: 2.1	c-SBF	[36]
Mg-4Zn	cast	0%	100	day 7: 4.3 day 14: 3.4	c-SBF	[39]
Mg-4Zn	cast + extrusion	0%	11.2	day 7: 1.9	PBS	[40]
Mg-4Zn	cast + extrusion	0%	14.5	day 10: 3.7	PBS	[41]
Mg-4Zn	powder metallurgy	0.9%	23.2	day 1: 2.5	3.5% NaCl	[3]
Mg-4Zn	extrusion-based AM	$50.3 \pm 3.4\%$	26.5	day 1: 2.3 ± 0.9 day 7: 1.7 ± 0.5 day 14: 1.0 ± 0.3 day 28: 0.7 ± 0.1	r-SBF	this study
Pure Mg	extrusion-based AM	$54.5 \pm 2.4\%$	28.3	day 1: 12.1 ± 0.2	r-SBF	this study
Ideal bone substitute	--	--	--	0.2 – 0.5	--	[42]

At the early stage of *in vitro* immersion, ZnO could be found on the surface of the Mg-Zn scaffolds accompanied by Mg(OH)₂, MgO, MgCO₃, and calcium and phosphate-containing precipitates (Figure 4.4a and b). At the later stages of *in vitro* immersion (*i.e.*, day 14 and day 28), however, ZnO could not be detected any more on the surface of the specimens (Figure 4.4b). This is likely because Zn is less chemically active, as compared to Mg. Mg is, therefore, preferentially oxidized and Mg-containing degradation products are formed on the surface first [36]. With time, thus, more and more Mg(OH)₂ or MgO are found in the outer layers of the biodegradation products, while ZnO is found in the inner layers. This trend has been also reported in other studies [36, 43]. In addition, the formed ZnO could facilitate the further formation of Mg(OH)₂ [37], leading to an increasingly dense degradation layer on the surface of the Mg-Zn scaffolds (Figure 4.5b1-f1).

After 1 day of immersion, corrosion was found to have occurred to the struts both at the periphery and in the center of the scaffolds. The biodegradation products formed on the peripheral struts and inside the initial micropores in the struts (Figure 4.5b3-b4) led to a sharp increase in the total volume of the scaffolds (including the volume of the biodegradation products), but a decrease in porosity (Figure 4.3i and j). With corrosion further progressing over time, the struts gradually became incomplete and stable degradation products continuously formed on the struts until the space between the struts was fully occupied (Figure 4.5c3, d3 and e3). As a result, the porosity of the scaffolds (including the biodegradation products) was maintained at around 25% (Figure 4.3j), and the volume of the scaffolds (including the biodegradation products) was higher than that of the initial scaffolds between days 3 and 14 (Figure 4.3i). The biodegradation products present at the center of the scaffolds had a similar composition to those on the surface (Figure 4.5g).

The compact and dense biodegradation products present on the surface and in the space between the struts generally hindered the further corrosion of the Mg-Zn scaffolds, hence reducing the corrosion rate from 2.3 ± 0.9 mm/y to 0.7 ± 0.1 mm/y over 28 days of immersion (Figure 4.3h). The reduced corrosion rate was also reflected in the gradually stable pH values from day 7 (Figure 4.3c), the minor changes of the volume and porosity of the Mg-Zn scaffolds (excluding the biodegradation products) between days 7 and 14 of immersion (Figure 4.3i and j), and the increased LPR values at days 7 and 14 (Figure 4.6b). It has been found that thanks to the formation of a stable degradation product layer on Mg-Zn alloy implants, the further *in vivo* corrosion is retarded, which makes the micro-environment more favorable for the establishment of osteointegration [12].

4.4.3. Bone-mimicking mechanical properties

The uniaxial compressive stress-strain curves of both the Mg-Zn and pure Mg scaffolds exhibited two stages: (i) an initial elastic stage and (ii) a densification stage (Figure 4.7a). Unlike other geometrically ordered 3D printed porous metallic scaffolds [44], the strain-stress curves of the Mg-Zn and pure Mg scaffolds studied here did not exhibit a plateau stage, which would normally be expected of a porous structure with a 0° to 90° lay-down pattern or 90° interconnection between struts [45]. In addition to the pattern, both macropores and micropores in the scaffolds contribute to the strain-hardening behavior observed during the plastic deformation stage [46].

The yield strength and elastic modulus of the Mg-Zn scaffolds were about three times as high as those of the pure Mg scaffolds (Figure 4.7a). The significantly enhanced mechanical properties of the Mg-Zn scaffolds could be attributed to the combined effects of the material and the structure. From a material perspective, the compressive yield strength of the bulk Mg-Zn alloy (4 wt% Zn, 110 MPa [47]) is much higher than that of

bulk pure Mg (21 MPa [48]). The maximum solubility of Zn in Mg is 1.6 wt% at room temperature in the equilibrium state. Part of Zn in the Mg-Zn alloy is, therefore, dissolved in the α -Mg matrix, generating solid-solution strengthening. The rest of Zn precipitates from the α -Mg matrix during cooling from the sintering temperature and constitutes the second phase dispersed along the grain boundaries, thereby strengthening the Mg-Zn alloy through a dispersion-strengthening mechanism [4]. In other words, both the solid-solution strengthening and dispersion strengthening mechanisms contributed to the improved mechanical properties of the Mg-Zn scaffolds.

For application as biodegradable metallic bone implants, the mechanical properties of Mg-Zn porous biomaterials should be maintained until the newly formed bone can take over the mechanical function from the implants and provide enough mechanical support. Therefore, understanding the evolution of the mechanical properties of scaffolds with biodegradation time is of great importance to avoid sudden premature failure. During the 28 days of *in vitro* biodegradation, the mechanical properties of our Mg-Zn scaffolds remained in the range of those of trabecular bone (*i.e.*, yield strength = 0.2 – 80 MPa; elastic modulus = 10 – 2000 MPa) [49]. The yield strength and elastic modulus of the Mg-Zn scaffolds were indeed influenced by *in vitro* biodegradation. The formation of the corrosion products, resulting in increased mechanical properties, and the dissolution of the Mg-Zn scaffolds, resulting in decreased mechanical properties, nicely balanced each other out (Figure 4.3 and Figure 4.5) [50]. Throughout the initial immersion period, the structure of the Mg-Zn scaffolds maintained its general integrity, suggesting that the corrosion products likely played an important role in increasing the mechanical properties of the scaffolds. The yield strength and elastic modulus were measured at an initial deformation stage, when interfacial bonding between the Mg-Zn scaffolds and corrosion products was still good and the applied load could easily be transferred between the Mg-Zn scaffold and the corrosion products [50]. Moreover, the formation of the corrosion products filling the micropores inside the struts and covering the struts led to a sharp decrease in the porosity of the entire scaffolds (including the corrosion products, Figure 4.3j), enabling them to withstand higher loads. Therefore, the corrosion products (*i.e.*, the inorganic compounds) effectively acted like a reinforcing phase in the Mg-Zn scaffolds, providing a strengthening effect [51], which explains why the yield strength and elastic modulus of the Mg-Zn scaffolds increased after 1 day of immersion (Figure 4.7c and d). After 3 days of immersion, localized corrosion occurred (Figure 4.5c3), which could lead to the generation of stress concentrations. In addition, the Mg-Zn scaffolds themselves could bear less loading, as the corrosion progressed. As a result, declining trends of the yield strength and elastic modulus were observed (Figure 4.7c and d).

4.4.4. Characteristic responses of preosteoblasts

For both the Mg-Zn and pure Mg scaffolds, different dilution ratios of the extracts led to different levels of preosteoblast viability. According to the ISO 10993-5 standard [52], the 100% extracts of both Mg-Zn and pure Mg were severely toxic (Level 4) after 7 days of cell culture. The 50% extract of Mg-Zn was also categorized as severely toxic (Level 4), while the 50% extract of pure Mg showed slight toxicity (Level 1). When the extracts of Mg-Zn and pure Mg were further diluted to 10%, about 100% metabolic cell activity was detected, showing no toxicity (Level 0). The effect of the dilution ratio of the extract on the growth of preosteoblasts was supported by the rhodamine-phalloidin and DAPI stainings (Figure 4.8d-g).

The pH values of the extracts of the Mg-Zn and pure Mg scaffolds were all below 8.5, being lower than the pH tolerance threshold of MC3T3-E1 cells (pH = 8.8) [6]. Therefore, the release of ions was the primary factor determining the cytocompatibility of the scaffolds. It is well known that Mg ion promotes bone regeneration [53]. However, an excessively high Mg ion concentration can adversely affect cell proliferation [27]. A safe Mg ion concentration for MC3T3-E1 cells is less than 360 mg/L [27], which can explain the cytotoxic effects of the 50 and 100% extracts of Mg-Zn and pure Mg (Figure 4.8a and c). As compared to the 50 and 100% extracts of pure Mg, the extracts of Mg-Zn had significantly less Mg²⁺ release (Figure 4.8c), due to a lower biodegradation rate of the Mg-Zn scaffolds (Figure 4.3). The cells cultured in these extracts, however, exhibited more severe toxicity than the pure Mg counterparts (Figure 4.8a). This inhibitory effect on the growth of preosteoblasts could be attributed to the high Zn²⁺ concentration in the Mg-Zn extracts. Since the human body has a much greater demand for Mg than for Zn, Zn exhibits a more significant dose-dependent effect on cytocompatibility than Mg. A low concentration of Zn²⁺ has been found to promote the viability, proliferation, and migration of osteoblast cells, while a high concentration of Zn²⁺ has been shown to cause adverse effects [38]. The IC₅₀ of Zn²⁺ (*i.e.*, the half maximal inhibitory concentration) is reported to be about 5.9 mg/L for MC3T3-E1 cells [54] with a safe limit of 3 mg/L [55, 56], which explains why the 50% (9.6 ± 1.5 mg/L) and 100% extracts (17.0 ± 2.4 mg/L) of Mg-Zn exhibited severe toxicity, while the 10% Mg-Zn extract was cytocompatible (2.1 ± 0.1 mg/L).

The *in vitro* biosafety evaluation of biodegradable Mg does not reflect the *in vivo* situation where the circulating body fluid tends to decrease the local concentrations of Mg and Zn ions. In addition, the concentrations of detected Mg and Zn ions in the blood serum (*in vivo*) are reported to be much lower than those in the extracts (*in vitro*), and the cells in tissue (*in vivo*) and culture medium (*in vitro*) have different maximum tolerated doses of Mg and Zn ions [27, 38]. Considering these factors, 6-10 times dilution of the original extracts has been strongly recommended for the *in vitro* cytotoxicity tests of Mg to be developed as potential orthopedic implants [27]. Such a dilution ratio corresponds

to the biocompatible Mg-Zn extracts (*i.e.*, 10% extracts) in the indirect assays performed here (Figure 4.8a).

While our direct cell culture tests demonstrated a certain level of cytotoxicity for the Mg-Zn scaffolds (Figure 4.8i) including unhealthy cells (Figure 4.8k), a number of stretched cells with developed filopodia adhering well to the corrosion layer of the Mg-Zn scaffolds were also observed (Figure 4.8j). Both the spreading and non-spreading morphologies of the MC3T3-E1 cells have also been observed on extruded Mg-Zn alloys (6 wt% Zn) [7]. Furthermore, it has been reported that such extruded Mg-Zn implants exhibit good *in vivo* biocompatibility [5, 57, 58], superior osseointegration due to a stable corrosion layer, and improved osteogenic differentiation of rat bone mesenchymal stem cells (rBMCs) [12]. In addition, the *in vivo* biodegradation of the extruded Mg-Zn implants (degradation rate: 2.32 mm/y) has not been found to be harmful to the adjacent bone tissues because the excess Mg^{2+} can be excreted by the kidney, while Zn^{2+} can be absorbed by the surrounding tissues and excreted through the gastrointestinal route and the kidney [5]. Therefore, it is important to realize that *in vitro* cytocompatibility assessment cannot completely mimic the *in vivo* conditions and comprehensive *in vitro* and *in vivo* studies are required to better understand the biological responses of cells to our scaffolds.

4.5. Conclusions

In this study, for the first time, biodegradable Mg-Zn alloy scaffolds were successfully fabricated through the extrusion-based AM technique and subsequent debinding and sintering. With the pure Mg scaffolds as the reference, the Mg-Zn scaffolds were comprehensively studied for their intended application as a biodegradable bone substitute.

1. The porous structure of the fabricated Mg-Zn scaffolds was interconnected, owing to the presence of macropores from the pattern design and the micropores formed in the struts.
2. The μCT results showed that, as compared to the pure Mg scaffolds, the corrosion rate of the Mg-Zn scaffolds at day 1 was reduced by 81%. Over 28 days of static immersion in r-SBF, the *in vitro* corrosion rate of the Mg-Zn scaffolds decreased from 2.3 ± 0.9 mm/y after 1 day to 0.7 ± 0.1 mm/y after 28 days.
3. The yield strength and elastic modulus of the Mg-Zn scaffolds were 14.5 ± 3.0 and 448.8 ± 42.4 MPa, respectively, which are about three times higher than those of the pure Mg scaffolds. During 28 days of *in vitro* biodegradation, the mechanical properties of the Mg-Zn scaffolds remained within the range of those of trabecular bone.

4. The indirect culture of preosteoblasts in the 10% Mg-Zn extracts revealed good cytocompatibility. Although direct cell culture on the Mg-Zn scaffolds showed cytotoxicity, an *in vivo* study needs to be performed to evaluate the biocompatibility of the Mg-Zn scaffolds under real physiological conditions.

5. Preparing coatings on the scaffolds or introducing bioactive components inside the scaffold to form composites may be explored to further improve the biocompatibility of such 3D printed Mg-Zn scaffolds.

References

- [1] J. Dong, N. Tümer, N.E. Putra, J. Zhu, Y. Li, M.A. Leeflang, P. Taheri, L.E. Fratila-Apachitei, J.M.C. Mol, A.A. Zadpoor, J. Zhou, Extrusion-based 3D printed magnesium scaffolds with multifunctional MgF₂ and MgF₂-CaP coatings, *Biomater. Sci.* 9 (2021) 7159-7182.
- [2] N. T. Kirkland, J. Lespagnol, N. Birbilis, M. P. Staiger, A survey of bio-corrosion rates of magnesium alloys, *Corros. Sci.* 52 (2010) 287-291.
- [3] J. Yu, J. Wang, Q. Li, J. Shang, J. Cao, X. Sun, Effect of Zn on microstructures and properties of Mg-Zn alloys prepared by powder metallurgy method, *Rare Metal Mat. Eng.* 45 (2016) 2757-2762.
- [4] S. Cai, T. Lei, N. Li, F. Feng, Effects of Zn on microstructure, mechanical properties and corrosion behavior of Mg-Zn alloys, *Mater. Sci. Eng. C.* 32 (2012) 2570-2577.
- [5] S. Zhang, X. Zhang, C. Zhao, J. Li, Y. Song, C. Xie, H. Tao, Y. Zhang, Y. He, Y. Jiang, Y. Bian, Research on an Mg-Zn alloy as a degradable biomaterial, *Acta Biomater.* 6 (2010) 626-640.
- [6] X. Gu, Y. Zheng, Y. Cheng, S. Zhong, T. Xi, In vitro corrosion and biocompatibility of binary magnesium alloys, *Biomaterials.* 30 (2009) 484-498.
- [7] S. Zhang, J. Li, Y. Song, C. Zhao, X. Zhang, C. Xie, Y. Zhang, H. Tao, Y. He, Y. Jiang, Y. Bian, In vitro degradation, hemolysis and MC3T3-E1 cell adhesion of biodegradable Mg-Zn alloy, *Mater. Sci. Eng. C-Mater. Biol. Appl.* 29 (2009) 1907-1912.
- [8] D. B. Prabhu, P. Gopalakrishnan, K. R. Ravi, Morphological studies on the development of chemical conversion coating on surface of Mg-4Zn alloy and its corrosion and bio mineralisation behaviour in simulated body fluid, *J. Alloys Compd.* 812 (2020) 152146.
- [9] C. J. Boehlert, K. Knittel, The microstructure, tensile properties, and creep behavior of Mg-Zn alloys containing 0-4.4wt.% Zn, *Mater. Sci. Eng. A-Struct. Mater. Prop. Microstruct. Process.* 417 (2006) 315-321.
- [10] H. Tapiero, K. D. Tew, Trace elements in human physiology and pathology: zinc and metallothioneins, *Biomed. Pharmacother.* 57 (2003) 399-411.
- [11] J. Li, P. Han, W. Ji, Y. Song, S. Zhang, Y. Chen, C. Zhao, F. Zhang, X. Zhang, Y. Jiang, The in vitro indirect cytotoxicity test and in vivo interface bioactivity evaluation of biodegradable FHA coated Mg-Zn alloys, *Mater. Sci. Eng. B-Adv. Funct. Solid-State Mater.* 176 (2011) 1785-1788.
- [12] W. Yu, D. Chen, Z. Ding, M. Qiu, Z. Zhang, J. Shen, X. Zhang, S. Zhang, Y. He, Z. Shi, Synergistic effect of a biodegradable Mg-Zn alloy on osteogenic activity and anti-biofilm ability: an *in vitro* and *in vivo* study, *RSC Adv.* 6 (2016) 45219-45230.
- [13] Z. S. Seyedraoufi, S. Mirdamadi, Synthesis, microstructure and mechanical properties of porous Mg-Zn scaffolds, *J. Mech. Behav. Biomed. Mater.* 21 (2013) 1-8.
- [14] Y. Yan, Y. Kang, D. Li, K. Yu, T. Xiao, Q. Wang, Y. Deng, H. Fang, D. Jiang, Y. Zhang, Microstructure, mechanical properties and corrosion behavior of porous Mg-6 wt.% Zn scaffolds for bone tissue engineering, *J. Mater. Eng. Perform.* 27 (2018) 970-984.
- [15] A. Oyane, Hyun. Kim, T. Furuya, T. Kokubo, T. Miyazaki, T. Nakamura, Preparation and assessment of revised simulated body fluids, *J. Biomed. Mater. Res. Part A.* 65A (2003) 188-195.

- [16] Y. Xin, T. Hu, P. K. Chu, In vitro studies of biomedical magnesium alloys in a simulated physiological environment: A review, *Acta Biomater.* 7 (2011) 1452-1459.
- [17] Biological evaluation of medical devices —Part 12: Sample preparation and reference materials, ISO 10993-12:2012 (2012).
- [18] J. Fischer, M. H. Prosenec, M. Wolff, N. Hort, R. Willumeit, F. Feyerabend, Interference of magnesium corrosion with tetrazolium-based cytotoxicity assays, *Acta Biomater.* 6 (2010) 1813-1823.
- [19] Y. Zhu, G. Wu, Y.-H. Zhang, Q. Zhao, Growth and characterization of Mg(OH)₂ film on magnesium alloy AZ31, *Appl. Surf. Sci.* 257 (2011) 6129-6137.
- [20] Y. Xin, C. Liu, X. Zhang, G. Tang, X. Tian, P. K. Chu, Corrosion behavior of biomedical AZ91 magnesium alloy in simulated body fluids, *J. Mater. Res.* 22 (2011) 2004-2011.
- [21] M.M. Figueiredo, J. a. F. Gamelas, A. G. Martins, Characterization of bone and bone-based graft materials using FTIR spectroscopy in *Infrared Spectroscopy – Life and Biomedical Sciences*, edited by Theophanides Theophile, InTechOpen, London, 2012, pp. 315-337.
- [22] F. Khairallah, A. Glisenti, XPS study of MgO nanopowders obtained by different preparation procedures, *Surf. Sci. Spectra.* 13 (2006) 58-71.
- [23] J. E. Qu, M. Ascencio, L. M. Jiang, S. Omanovic, L. X. Yang, Improvement in corrosion resistance of WE43 magnesium alloy by the electrophoretic formation of a ZnO surface coating, *J. Coat. Technol. Res.* 16 (2019) 1559-1570.
- [24] Y. Li, P. Pavanram, J. Zhou, K. Lietaert, P. Taheri, W. Li, H. San, M. A. Leeflang, J. M. C. Mol, H. Jahr, A. A. Zadpoor, Additively manufactured biodegradable porous zinc, *Acta Biomater.* 101 (2020) 609-623.
- [25] J. E. Gray-Munro, M. Strong, The mechanism of deposition of calcium phosphate coatings from solution onto magnesium alloy AZ31, *J. Biomed. Mater. Res. Part A.* 90 (2009) 339-350.
- [26] D. Kapinos, B. Augustyn, M. Szymanek, Methods of introducing alloying elements into liquid magnesium, *Metall. Foundry Eng.* 40 (2014) 141.
- [27] J. L. Wang, F. Witte, T. F. Xi, Y. F. Zheng, K. Yang, Y. S. Yang, D. W. Zhao, J. Meng, Y. D. Li, W. R. Li, K. M. Chan, L. Qin, Recommendation for modifying current cytotoxicity testing standards for biodegradable magnesium-based materials, *Acta Biomater.* 21 (2015) 237-249.
- [28] J. Dong, Y. Li, P. Lin, M. A. Leeflang, S. Van Asperen, K. Yu, N. Tumer, B. Norder, A. A. Zadpoor, J. Zhou, Solvent-cast 3D printing of magnesium scaffolds, *Acta Biomater.* 114 (2020) 497-514.
- [29] R. M. German, Sintering with a liquid phase, in *Sintering: from Empirical Observations to Scientific Principles*, edited by Randall M. German, Elsevier, 2014, pp. 247-303.
- [30] J. M. Seok, T. Rajangam, J. E. Jeong, S. Cheong, S. M. Joo, S. J. Oh, H. Shin, S. H. Kim, S. A. Park, Fabrication of 3D plotted scaffold with microporous strands for bone tissue engineering, *J. Mat. Chem. B.* 8 (2020) 951-960.
- [31] Y. Yan, H. Cao, Y. Kang, K. Yu, T. Xiao, J. Luo, Y. Deng, H. Fang, H. Xiong, Y. Dai, Effects of Zn concentration and heat treatment on the microstructure, mechanical properties and corrosion behavior of as-extruded Mg-Zn alloys produced by powder metallurgy, *J. Alloys Compd.* 693 (2017) 1277-1289.

- [32] E. Koç, M. B. Kannan, M. Ünal, E. Candan, Influence of zinc on the microstructure, mechanical properties and in vitro corrosion behavior of magnesium–zinc binary alloys, *J. Alloys Compd.* 648 (2015) 291-296.
- [33] G. Song, A. Atrens, Corrosion mechanisms of magnesium alloys, *Adv. Eng. Mater.* 1 (1999) 11-33.
- [34] D. Yin, E. Zhang, S. Zeng, Effect of Zn on mechanical property and corrosion property of extruded Mg-Zn-Mn alloy, *Trans. Nonferrous Met. Soc. China.* 18 (2008) 763-768.
- [35] H.-Y. Ha, J.-Y. Kang, J. Yang, C. D. Yim, B. S. You, Limitations in the use of the potentiodynamic polarisation curves to investigate the effect of Zn on the corrosion behaviour of as-extruded Mg–Zn binary alloy, *Corros. Sci.* 75 (2013) 426-433.
- [36] H. R. Bakhsheshi-Rad, E. Hamzah, A. Fereidouni-Lotfabadi, M. Daroonparvar, M. a. M. Yajid, M. Mezbahul-Islam, M. Kasiri-Asgarani, M. Medraj, Microstructure and bio-corrosion behavior of Mg-Zn and Mg-Zn-Ca alloys for biomedical applications, *Mater. Corros.* 65 (2014) 1178-1187.
- [37] E. Dayaghi, H. R. Bakhsheshi-Rad, E. Hamzah, A. Akhavan-Farid, A. F. Ismail, M. Aziz, E. Abdolahi, Magnesium-zinc scaffold loaded with tetracycline for tissue engineering application: *In vitro* cell biology and antibacterial activity assessment, *Mater. Sci. Eng. C-Mater. Biol. Appl.* 102 (2019) 53-65.
- [38] H. Yang, B. Jia, Z. Zhang, X. Qu, G. Li, W. Lin, D. Zhu, K. Dai, Y. Zheng, Alloying design of biodegradable zinc as promising bone implants for load-bearing applications, *Nat. Commun.* 11 (2020) 401.
- [39] M. E. Moussa, H. I. Mohamed, M. A. Waly, G. S. Al-Ganainy, A. B. Ahmed, M. S. Talaat, Comparison study of Sn and Bi addition on microstructure and bio-degradation rate of as-cast Mg-4wt% Zn alloy without and with Ca-P coating, *J. Alloys Compd.* 792 (2019) 1239-1247.
- [40] W. Jiang, J. Wang, W. Zhao, Q. Liu, D. Jiang, S. Guo, Effect of Sn addition on the mechanical properties and bio-corrosion behavior of cytocompatible Mg–4Zn based alloys, *J. Magnes. Alloy.* 7 (2019) 15-26.
- [41] M. Sabbaghian, R. Mahmudi, K. S. Shin, Microstructure, texture, mechanical properties and biodegradability of extruded Mg–4Zn–xMn alloys, *Mater. Sci. Eng. A-Struct. Mater. Prop. Microstruct. Process.* 792 (2020) 139828.
- [42] C. Gao, M. Yao, S. Li, P. Feng, S. Peng, C. Shuai, Highly biodegradable and bioactive Fe-Pd-bredigite biocomposites prepared by selective laser melting, *J. Adv. Res.* 20 (2019) 91-104.
- [43] Y. Song, E.-H. Han, D. Shan, C. D. Yim, B. S. You, The effect of Zn concentration on the corrosion behavior of Mg–xZn alloys, *Corros. Sci.* 65 (2012) 322-330.
- [44] S. M. Ahmadi, S. A. Yavari, R. Wauthle, B. Pouran, J. Schrooten, H. Weinans, A. A. Zadpoor, Additively manufactured open-cell porous biomaterials made from six different space-filling unit cells: the mechanical and morphological properties, *Materials (Basel).* 8 (2015) 1871-1896.
- [45] F. S. L. Bobbert, K. Lietaert, A. A. Eftekhari, B. Pouran, S. M. Ahmadi, H. Weinans, A. A. Zadpoor, Additively manufactured metallic porous biomaterials based on minimal surfaces: A unique combination of topological, mechanical, and mass transport properties, *Acta Biomater.* 53 (2017) 572-584.

- [46] Yu. N. Podrezov, L. G. Shtyka, A. D. G. Verbylo, Strain-hardening of porous iron under uniaxial compression, *Powder Metall. Met. Ceram.* 39 (2000) 92-96.
- [47] M. Hradilová, D. Vojtěch, J. Kubásek, J. Čapek, M. Vlach, Structural and mechanical characteristics of Mg–4Zn and Mg–4Zn–0.4Ca alloys after different thermal and mechanical processing routes, *Mater. Sci. Eng. A-Struct. Mater. Prop. Microstruct. Process.* 586 (2013) 284-291.
- [48] D. Zhao, F. Witte, F. Lu, J. Wang, J. Li, L. Qin, Current status on clinical applications of magnesium-based orthopaedic implants: A review from clinical translational perspective, *Biomaterials.* 112 (2017) 287-302.
- [49] M. Yazdimamaghani, M. Razavi, D. Vashaei, K. Moharamzadeh, A. R. Boccaccini, L. Tayebi, Porous magnesium-based scaffolds for tissue engineering, *Mater. Sci. Eng. C-Mater. Biol. Appl.* 71 (2017) 1253-1266.
- [50] R. Hedayati, S. M. Ahmadi, K. Lietaert, N. Tumer, Y. Li, S. Amin Yavari, A. A. Zadpoor, Fatigue and quasi-static mechanical behavior of bio-degradable porous biomaterials based on magnesium alloys, *J. Biomed. Mater. Res. Part A.* 106 (2018) 1798-1811.
- [51] Y. Li, J. Zhou, P. Pavanram, M. A. Leeftang, L. I. Fockaert, B. Pouran, N. Tumer, K. U. Schroder, J. M. C. Mol, H. Weinans, H. Jahr, A. A. Zadpoor, Additively manufactured biodegradable porous magnesium, *Acta Biomater.* 67 (2018) 378-392.
- [52] Biological evaluation of medical devices—Part 5: Tests for in vitro cytotoxicity, ISO 10993-5:2009 (2009).
- [53] Y. Zhang, J. Xu, Y. C. Ruan, M. K. Yu, M. O'laughlin, H. Wise, D. Chen, L. Tian, D. Shi, J. Wang, S. Chen, J. Q. Feng, D. H. Chow, X. Xie, L. Zheng, L. Huang, S. Huang, K. Leung, N. Lu, L. Zhao, H. Li, D. Zhao, X. Guo, K. Chan, F. Witte, H. C. Chan, Y. Zheng, L. Qin, Implant-derived magnesium induces local neuronal production of CGRP to improve bone-fracture healing in rats, *Nat. Med.* 22 (2016) 1160-1169.
- [54] A. Yamamoto, R. Honma, M. Sumita, Cytotoxicity evaluation of 43 metal salts using murine fibroblasts and osteoblastic cells, *J. Biomed. Mater. Res.* 39 (1998) 331-340.
- [55] Atsuo Ito, Haruo Kawamura, Makoto Otsuka, Masako Ikeuchi, Hajime Ohgushi, Kunio Ishikawa, Kazuo Onuma, Noriko Kanzaki, Yu Sogo, N. Ichinose, Zinc-releasing calcium phosphate for stimulating bone formation, *Mater. Sci. Eng. C-Mater. Biol. Appl.* 22 (2002) 21-25.
- [56] G. Jin, H. Cao, Y. Qiao, F. Meng, H. Zhu, X. Liu, Osteogenic activity and antibacterial effect of zinc ion implanted titanium, *Colloids Surf. B: Biointerfaces.* 117 (2014) 158-165.
- [57] D. Chen, Y. He, H. Tao, Y. Zhang, Y. Jiang, X. Zhang, S. Zhang, Biocompatibility of magnesium-zinc alloy in biodegradable orthopedic implants, *Int. J. Mol. Med.* 28 (2011) 343-348.
- [58] Y. He, H. Tao, Y. Zhang, Y. Jiang, S. Zhang, C. Zhao, J. Li, B. Zhang, Y. Song, X. Zhang, Biocompatibility of bio-Mg-Zn alloy within bone with heart, liver, kidney and spleen, *Sci. Bull.* 54 (2009) 484-491.

Supplementary file

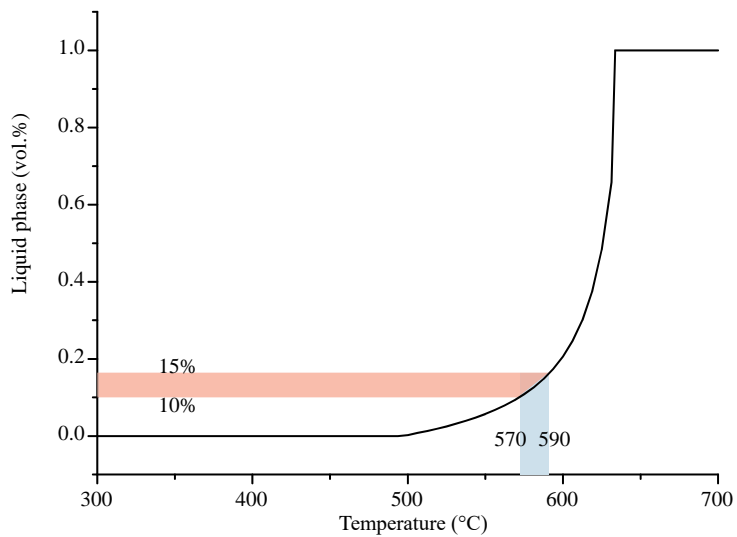


Figure S4.1 Liquid phase fraction of the Mg-Zn scaffolds as a function of sintering temperature for defining the working window of liquid-phase sintering.

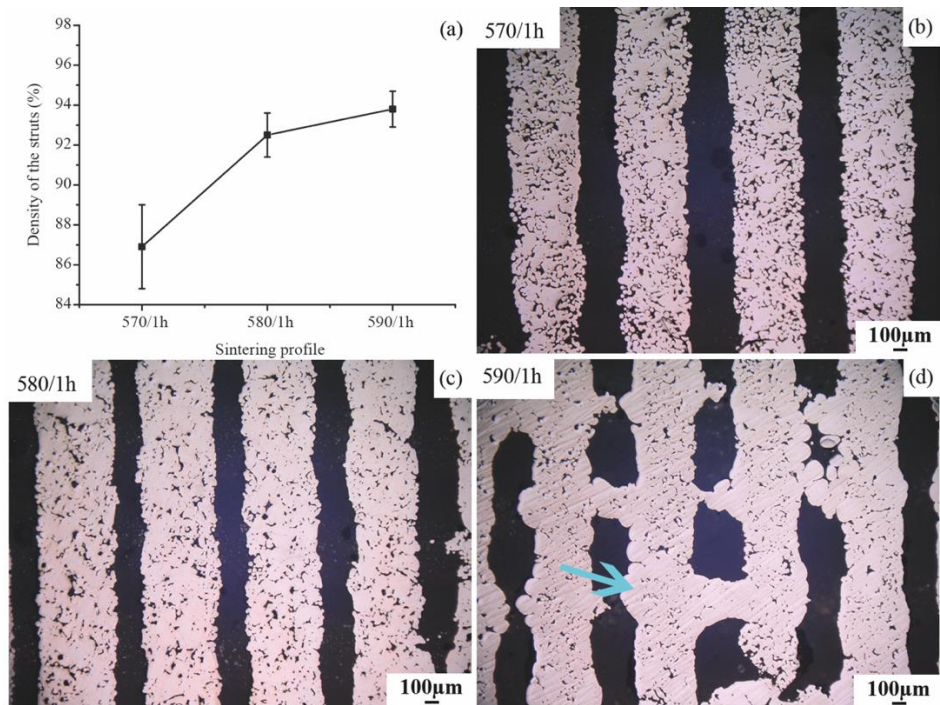


Figure S4.2 The densities of the struts of the Mg-Zn scaffolds sintered under different conditions (a), and the cross-section microstructures of the Mg-Zn scaffolds sintered at 570 (b), 580 (c) and 590 °C (d), with a dwelling time of 1 h.

5

Ink extrusion-based additive manufacturing of Mg-Zn/bioceramic scaffolds

Here, we developed an extrusion-based additive manufacturing technique to fabricate biodegradable Mg-Zn/bioceramic composite scaffolds ex-situ. Inks carrying a Mg-Zn powder and 5, 10 and 15% β -tricalcium phosphate (TCP) powder particles were investigated regarding the dispersion of β -TCP particles in the inks and viscoelastic properties. Optimally formulated inks were then employed for subsequent 3D printing of porous composite scaffolds. The in vitro biodegradation rate of the scaffolds containing 5% β -TCP decreased to 0.5 mm/y, which falls within the range desired for critical-sized bone substitution. As compared to the monolithic Mg-Zn scaffolds, the mechanical properties of the composite scaffolds were much enhanced, which remained in the range of the cancellous bone properties even after 28 d of in vitro degradation. The Mg-Zn/5TCP and Mg-Zn/10TCP scaffolds also exhibited improved biocompatibility when cultured with preosteoblasts, as compared to Mg-Zn scaffolds. In addition, the ALP activity and mineralization level of the composite scaffolds were much enhanced in the extracts of the composite scaffolds. Taken together, this research marks a great breakthrough in fabricating porous Mg-matrix composite scaffolds that meet several design criteria in terms of appropriate biodegradation rate, mechanical properties, and bioactivity.¹

¹The chapter is based on a scientific paper: J. Dong, P. Lin, N.E. Putra, N. Tümer, M. A. Leeﬂang, Z. Huan, L. E. Fratila-Apachitei, J. Chang, A. A. Zadpoor, J. Zhou, Extrusion-based additive manufacturing of Mg-Zn/bioceramic scaffolds, Acta Biomaterialia, 151 (2022), 628-646.

5.1. Introduction

The treatment of post-traumatic femoral nonunion with large segmental bone defect remains a great challenge in orthopedics [1]. Current therapeutic approaches to such bone defect repair include the implantation of autologous, allogeneic, or synthetic grafts, as well as the use of distraction osteogenesis techniques. However, all the approaches mentioned above have their own disadvantages and limitations [2]. Magnesium and its alloys have been considered promising implant materials to be used for the regeneration of such critical-sized bone defects, because of their biodegradability, favorable mechanical properties, and osteogenic potential [3]. However, the application of Mg and its alloys in orthopedics is still limited because of their high corrosion rates, resulting in the generation of a large amount of hydrogen gas that could trigger acute inflammatory responses and formation of gas voids [4]. The release of potentially toxic ions from the alloying elements along with fast biodegradation can also occur. Numerous studies have indicated the strong need for developing Mg-based materials with adjustable biodegradation rates and desirable biocompatibility to meet the requirements for bone repair [5-8]. Although surface modification can potentially solve these problems, it only helps to delay the start of corrosion. Indeed, the acceleration of corrosion often occurs when the coating breaks down [9]. Another promising approach is to form Mg-based composites through the addition of bioceramic particles to Mg [10]. Bioceramics based on calcium phosphate, such as hydroxyapatite (HA) and β -tricalcium phosphate (β -TCP), are particularly interesting for bone repair applications due to their similarity to natural bone in composition, and their osteoinductive and osteoconductive properties [10]. Unlike HA that has a very low solubility in the physiological environment, β -TCP exhibits a suitable biodegradation profile with a proper match with the rate of bone tissue regeneration [5]. It has been found that the addition of β -TCP to Mg alloys is, indeed, effective in enhancing their strength, stabilizing their corrosion rate, and improving their cytocompatibility [11-13]. With these findings in mind, researchers have made great efforts to fabricate Mg/ β -TCP composites with various techniques. Both liquid-state processing techniques, such as stir casting [14, 15] and liquid infiltration [13], and solid-state processing methods, such as powder metallurgy [11, 16] and friction stir processing [17], have been applied for the fabrication of such composites. However, none of these techniques is capable of fabricating complex 3D architectures with fully interconnected porous networks that are of great importance for bone substitutes [18]. Indeed, an interconnected porous structure affords the bone substitute with favorable permeability and large surface area, thereby facilitating cell proliferation and differentiation [19, 20].

In recent years, additive manufacturing (AM) has emerged as a powerful technique for the precise, free-form fabrication of orthopedic implants with complex internal and external macro- and micro-architectures [21]. The recent advances in AM techniques

have also enabled the production of Mg-based composite bone substitutes [22]. However, the available studies are limited both in number and scope. Only a few research groups have succeeded in employing powder bed fusion (PBF) AM techniques for the fabrication of Mg-bioceramic composites [23-26]. These studies are still in their infancy and are limited to bulk Mg-based composites, instead of porous scaffolds that are preferable for bone regeneration. High-level porosity and the agglomeration of ceramic particles, corresponding to undesirable defects and compositional variations, respectively, are common observations in these studies due to the sharp differences between the magnesium and bioceramic in the whole range of physical and chemical properties, such as melting and evaporation temperatures, crystal structure, wettability, reflectivity, thermal expansion coefficient, and chemical reactivity [22]. In addition, concerns have been raised about operating PBF AM to fabricate Mg-based alloys or composites, considering the high flammability of Mg powder [27]. Most laboratories try to avoid this risk. A laser-free AM technique would be a safer and more promising alternative.

Extrusion-based AM of such composites is a room temperature technique that works by continuously pushing a viscoelastic ink, composed of a metal powder, a ceramic powder, and a binder system through a nozzle to build a 3D structure based on CAD design, followed by debinding and sintering [28]. This technique effectively avoids the problems associated with PBF AM techniques. Another advantage of the ink extrusion-based AM is that various components can be flexibly added into the ink to create multi-functional bone-substituting materials [29, 30]. Even though this production technique has been explored to fabricate porous Mg and Mg alloy bone substitutes [28, 31, 32], no reports have appeared in the literature reporting the fabrication of Mg-bioceramic composite scaffolds.

Here, we used an ink extrusion-based AM technique to fabricate Mg-Zn/ β -TCP composite scaffolds. As the scaffolds made of a Mg-Zn alloy exhibited a very promising biodegradation rate, despite their cytotoxicity [32], the Mg-Zn alloy was chosen as the matrix. We hypothesized that the addition of β -TCP into the scaffolds would improve both the cytocompatibility and bioactivity of the Mg-Zn scaffolds. The main challenge lies in achieving uniform dispersion of micro-sized bioceramic particles in the metal matrix, considering their large surface areas and the strong van der Waals forces between dispersed particles [6]. The agglomeration of incorporated bioceramic particles has, indeed, been found to cause the formation of pores and defects, deteriorating the corrosion behavior and mechanical properties of the resulting composite [33]. To minimize such effects, two fabrication processes may be combined. For example, conventional powder metallurgy may be followed by hot extrusion [34-39] while high-shear solidification may be combined with equal channel angular extrusion [40, 41] or with high-pressure die casting [15]. In the present research, we tried to overcome this challenge by developing

an optimized binder system for preparing inks with well-dispersed particles, which could greatly reduce the processing complexity of the composites, as compared with the other solutions mentioned above. At the same time, rheological properties of the inks should be finely tuned in order to guarantee printability. In other words, it was critical to develop inks with well-dispersed solid particles (both metal and ceramic) and also with viscoelastic behavior necessary for the printability of these inks.

Herein, we report, for the first time, the successful fabrication of Mg-based composite scaffolds with 5, 10, and 15 wt% of β -TCP particles using ink extrusion-based AM. First, we present the results of our study regarding ink development. Then, we characterize the 3D printed composite scaffolds in terms of microstructure, *in vitro* biodegradation, biodegradation-dependent mechanical properties. Finally, we use preosteoblasts to assess the cytocompatibility and bioactivity (*i.e.*, cell viability and osteogenic response) of the developed specimens. The successful employment of ink extrusion-based 3D printing to fabricate porous Mg alloy/bioceramic composites marks the emergence of a new category of porous Mg biomaterials potentially to be used in orthopedics and it also devises another strategy for achieving uniform dispersion of micro-sized reinforcing particles in porous composites.

5.2. Material and methods

A schematic illustration of the composite fabrication steps, including ink preparation, structural design, 3D printing, debinding, and sintering is presented in Figure 5.1.

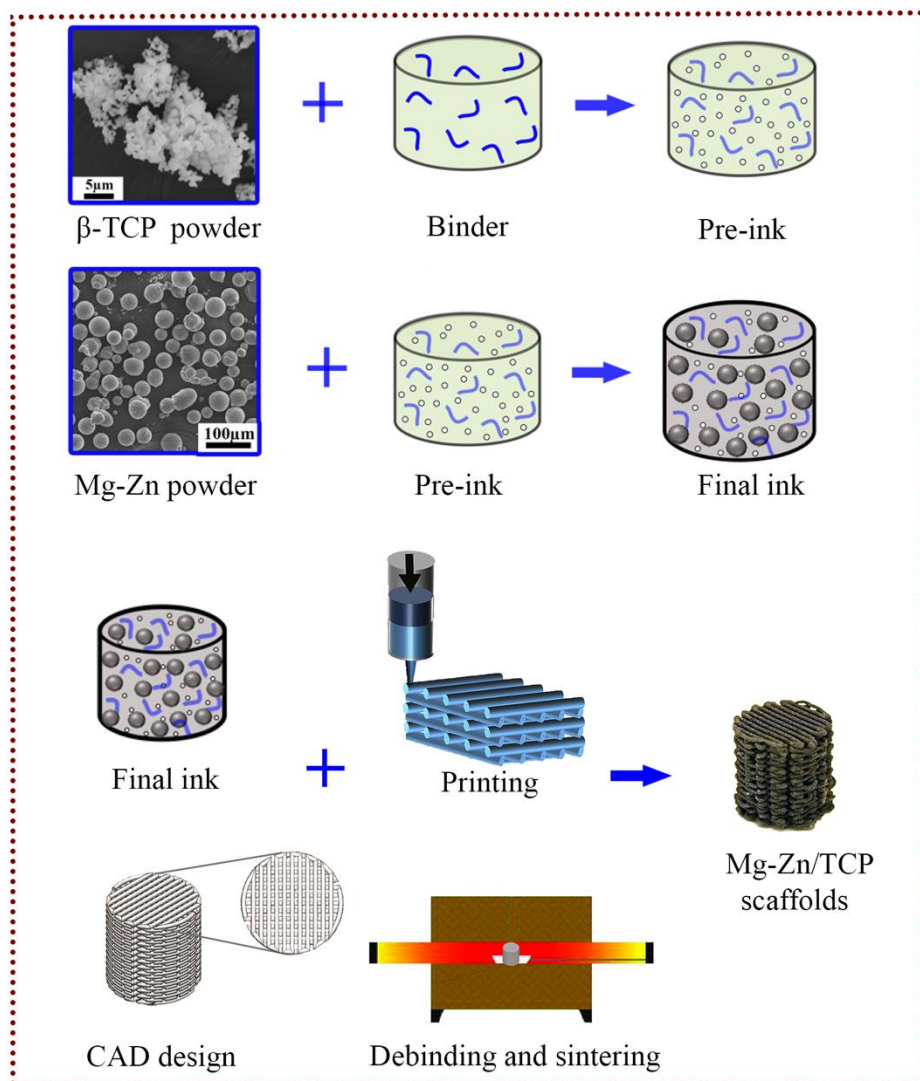


Figure 5.1 A schematic illustration of the fabrication steps of the composite scaffolds.

5.2.1. Ink preparation and characterization

5.2.1.1. Ink preparation

A pre-alloyed spherical Mg-Zn alloy powder (95.6 wt% Mg, 4.1 wt% Zn and 0.3 wt% impurities: Al and Ca, Tangshan Weihao Magnesium Powder Co., China) with a median particle size of 37.7 μm (standard deviation of 6.6 μm , Figure 5.1), and a β -TCP powder

with an average particle size of 5.3 μm (standard deviation of 8.9 μm , Figure 5.1) were used as the starting materials for the preparation of inks. A binder system with the polyisobutylene polymer ($M_w \sim 500,000$, Sigma Aldrich, Germany) in hexane was chosen.

Prior to the addition of the Mg-Zn powder, the β -TCP powder particles were mixed with 93, 95, and 97 vol% binders (denoted as 93, 95, and 97% pre-inks) to evaluate the homogeneity of the dispersions with a scanning electron microscope (SEM, JSM-IT100, JEOL). The pre-inks were mixed for 2 h at room temperature using a magnetic stirrer at a speed of 100-150 rpm. The quadrat method was used for the quantification of the distribution of β -TCP particles in the binder solution [42]. The obtained SEM images were divided into 35 contiguous quadrats. To minimize the edge effects, only the particles that were inside and in contact with the left and bottom sides of each quadrat were counted. The number of β -TCP particles, N_q , in each quadrat was counted using ImageJ (National Institutes of Health, USA) and was then manually checked. The degree of the asymmetry of a statistical distribution around the mean number was quantified by its skewness, β , as [43]:

$$\beta = \frac{q}{(q-1)(q-2)} \sum \left(\frac{N_{qi} - N_q^{mean}}{\sigma} \right)^3 \quad (1)$$

where q is the total number of the quadrats, N_{qi} the number of the β -TCP particles in the i th quadrat ($i = 1, 2, \dots, q$), N_q^{mean} the mean number of the β -TCP particles per quadrat, and σ the standard deviation of the N_q distribution. An increase in the β value indicates an increased degree of agglomeration of β -TCP particles.

Different groups of inks were then prepared by adding the Mg-Zn powder to the prepared 93, 95, and 97% pre-inks, with mass ratios of 95:5, 90:10, and 85:15 (*i.e.*, volume ratios of 97:3, 94:6, and 91:9) between the Mg-Zn powder and β -TCP powder, respectively. The mixing process for these inks was the same as that for the pre-inks, as described above. The inks were further optimized, based on their rheological properties (as described below) for printing Mg-Zn/5 wt% β -TCP, Mg-Zn/10 wt% β -TCP, and Mg-Zn/15 wt% β -TCP composite scaffolds, hereafter denoted as Mg-Zn/5TCP, Mg-Zn/10TCP, and Mg-Zn/15TCP, respectively. Mixing was performed in a glove box to prevent the oxidation of Mg-Zn powder particles.

5.2.1.2. Rheological characterization

The rheological properties of the prepared inks were determined using a rheometer. The rheological properties of the prepared inks were determined using a rheometer (Physica MCR 301, Anton Paar, Germany). The inks were loaded onto a pair of parallel plates (diameter = 25 mm, distance = 1 mm). Shear stress-viscosity measurements were performed with stresses ranging between 1 and 10,000 Pa and a linear viscoelastic range

was defined. Rotational shear rate ramps varying between 0.1 and 1000 s⁻¹ were applied to the inks and the shear rate-viscosity curves were obtained. In addition, creep-recovery tests were performed to evaluate the viscoelastic properties of the inks. A constant shear stress ($\tau = 10$ Pa) selected within the linear viscoelastic range was applied for 60 s and the resulting strain was recorded. The stress was then removed, and the strain was measured for another 180 s. The compliance J was defined from the ratio of the measured strain to the applied stress. The recovery ability of the inks could then be determined as:

$$R = \frac{J_{max} - J_{\infty}}{J_{max}} \quad (2)$$

where R is the degree of recovery of the ink, and J_{max} and J_{∞} are the compliances at the end of the creep and the recovery tests, respectively.

5.2.2. Composite scaffold fabrication

A porous cylindrical structure (having a diameter of 12.38 mm and a height of 12.64 mm, designed for compressive tests, according to the ISO 13314 standard) with a lay-down pattern of 0°/90°/0° was designed using the GeSim custom software (Figure 5.1). The structure had the following characteristics: struts size = 580 μ m, strut spacing = 360 μ m, and relative density = 62.2%, and layer number = 27. The adoption of the strut size was based on the considerations of the biodegradation of the scaffolds and the ability of the binder to escape during thermal debinding [31]. A pore size of 360 μ m was chosen because it was found earlier that implants with pores larger than 300 μ m were favorable for bone ingrowth [44]. The prepared inks were loaded into syringes (EFD, Nordson, Germany) with a 580 μ m tapered nozzle (art. No. 500890, EFD, Vieweg, Germany) and were then extruded at room temperature using a 3D Bioscaffolder 3.2 printer (GeSiM Bio-instruments, Germany) under an applied pressure of 140-160 kPa and at a printing speed of 10 mm/s. The 3D printing strategy regarding the adoption of printing pressure and speed can be found in our previous publication [28].

To investigate the effect of the β -TCP dispersion in the binder on the quality of the 3D printed composite materials, Mg-Zn/10 wt% β -TCP-containing inks with 93, 95, and 97% pre-inks were prepared and extruded through the printer nozzle. The printed struts and the cross section of the used nozzles were imaged with SEM. In addition, to check the printability of the inks, Mg-Zn/5TCP, Mg-Zn/10TCP, and Mg-Zn/15TCP composite scaffolds printed with 93, 95, and 97% pre-inks were imaged using an optical microscope (OM, VH-Z250R, Keyence Corp., USA). After optimization based on the homogeneity of β -TCP dispersion and the printability, Mg-Zn/5TCP, Mg-Zn/10TCP, and Mg-Zn/15TCP composite scaffolds were printed with the optimized inks, using the Bioscaffolder. The powder loading volume fractions of the optimized inks were 48 vol%

for the Mg-Zn/5TCP ink, 47 vol% for the Mg-Zn/10TCP ink, and 46 vol% for the Mg-Zn/15TCP ink.

The as-printed Mg-Zn/ β -TCP composite scaffolds were dried overnight, followed by debinding and sintering in a tube furnace (STF16/180, Carbolite Gero Ltd., UK) under highly pure argon flow (purity=99.9999%; inlet pressure = 1 bar). The printed Mg-Zn/5TCP samples were heated from room temperature to 600 °C at a heating rate of 2 °C/min and the printed Mg-Zn/10TCP and Mg-Zn/15TCP samples were heated to 620 and 640 °C, respectively, at a heating rate of 1 °C/min. The dwelling time of all the samples was 1 h, followed by furnace cooling. The as-sintered composite scaffolds were ultrasonically cleaned in acetone and isopropyl alcohol sequentially for 10 min each, prior to subsequent investigations.

5.2.3. Characterization of the composite scaffolds

The porous structures of the Mg-Zn/TCP composite scaffolds were observed using SEM, and the width and spacing of the struts were measured. The absolute porosities of the as-sintered composite scaffolds were calculated using the dry weighing method as:

$$\varphi = \left(1 - \frac{m}{\rho_{Mg-Zn/TCP} V_{bulk}} \right) \times 100\% \quad (3)$$

where φ is the absolute porosity of the as-sintered composite scaffold [%], m the mass of the as-sintered composite scaffold [g], V_{bulk} the bulk volume [cm³], and $\rho_{Mg-Zn/TCP}$ the theoretical density of the Mg-Zn/TCP composite material (*i.e.*, 1.78 g/cm³ for Mg-Zn/5TCP, 1.82 g/cm³ for Mg-Zn/10TCP, and 1.86 g/cm³ for Mg-Zn/15TCP).

The cross sections of the as-sintered porous Mg-Zn/TCP struts were observed using SEM and the elemental compositions were detected or mapped using a SEM equipped with X-ray energy dispersive spectroscopy (EDS, JEOL JSM-IT100, Japan). A counting area size of 81.9 μ m by 65.0 μ m, a counting time of 15 min, a live-time correction of 3% on average, and an acceleration voltage of 15 kV were used for EDS mapping. The micro-porosities and the phase fractions in the struts were measured from the SEM images using ImageJ. The distribution of the β -TCP particles in the Mg-Zn/TCP composites was quantified by the β value that was obtained from the quadrat method described above.

The phases in the Mg-Zn/TCP composite scaffolds were identified using an X-ray diffractometer (XRD, D8 Advance, Bruker, USA) equipped with a graphite monochromator and a Lynxeye position-sensitive detector. A scan range of 20 -100° and a step size of 0.030° using Co $K\alpha$ radiation were employed.

Nanoindentation tests were conducted on a polished Mg-Zn/5TCP specimen using a nanoindenter (G200, KLA, California) equipped with a standard Berkovich tip. A total number of 400 indentations were performed on the struts of the scaffolds with a minimum distance of 40 μm between every two indentations. The indented specimens were then examined with SEM.

The surface roughness of the scaffolds was measured using a digital optical microscope (Keyence, VH-6000). The function of “Roughness” was used and the linear average surface roughness (R_a) was acquired. Roughness values of three struts on each sample were measured.

5.2.4. *In vitro* immersion tests

The *in vitro* immersion tests of the Mg-Zn/5TCP and Mg-Zn/10TCP composite scaffolds were performed using a revised simulated body fluid (r-SBF) [45] for up to 28 d. Since the Mg-Zn/15TCP composite scaffolds collapsed after 8 d of immersion, the results are displayed only until day 7. The test conditions were as follows: immersion for 1, 3, 7, 14, and 28 d; temperature = 37 ± 0.5 °C; pH (r-SBF) = 7.40; 7 mL medium per 1 cm^2 of the scaffold surface area. During the *in vitro* degradation tests, the pH values of the media were recorded using a pH electrode (InlabNMR, METTLER TOLEDO).

To determine the *in vitro* corrosion rates of the composite scaffolds, X-ray micro-computed tomography (μCT , Nanotom 180 NF, GE Phoenix) with a resolution of 6 μm was used to scan the composite scaffolds before and after *in vitro* degradation. The obtained μCT images were reconstructed and exported into Dragonfly (Object Research Systems, Canada). After segmenting the corrosion products from the degraded composite scaffolds in the Dragonfly software, the volumes of the Mg-Zn/TCP composite scaffolds before and after degradation were calculated by using the function “bone analysis”. The volume loss and the corresponded average corrosion rate were determined as:

$$\text{Volume loss [\%]} = \frac{(V_{Mg \text{ before degradation}} - V_{Mg \text{ after degradation}})}{V_{Mg \text{ before degradation}}} \times 100\% \quad (4)$$

$$\text{Corrosion rate [mm/y]} = 8.76 \times 10^4 \times \frac{V}{A \times t} \quad (5)$$

where $V_{Mg \text{ before degradation}}$ and $V_{Mg \text{ after degradation}}$ are the volumes of the composite scaffold before immersion and after immersion [cm^3], respectively, V is the loss of volume [cm^3] (*i.e.*, $V_{Mg \text{ before degradation}} - V_{Mg \text{ after degradation}}$), A the surface area of the composite scaffold [cm^2], and t the duration of *in vitro* immersion [h].

By incorporating the corrosion products into Dragonfly, the volumes and porosities of the Mg-Zn/TCP composite scaffolds after immersion for different durations were calculated using the “bone analysis” function.

5.2.5. Characterization of the biodegradation products

Following uninterrupted immersion until the selected time points (*i.e.*, 1, 3, 7, 14, and 28 d), the morphological characteristics of the biodegradation products on the periphery and at the center of the Mg-Zn/TCP composite scaffolds were observed under SEM (JEOL JSM-IT100, Japan). The chemical elements present in the degradation products and their compositions were analyzed using EDS, while the phase identification was carried out by using XRD (Bruker D8 Advance diffractometer in the Bragg-Brentano geometry).

From the CT images of Mg-Zn/5TCP, Mg-Zn/10TCP and Mg-Zn/15TCP composite scaffold samples, the peripheral (the 100th slice from the top) and central slices (the 500th slice from the top) were selected to reveal the deposition of the corrosion products inside the composite scaffolds.

5.2.6. Uniaxial compression tests

The compressive mechanical properties of the Mg-Zn/TCP composite scaffolds, as well as the specimens retrieved at the selected time points of the *in vitro* immersion tests, were determined using a mechanical testing machine (Zwick Z100, Germany) with a 10 kN load cell. The tests were performed using a crosshead speed of 2 mm/min. The quasi-elastic gradient (hereafter referred to as Young’s modulus), yield strengths and compressive strength of the specimens were determined according to ISO 13314: 2011. The slope of the initial linear line in the stress-strain curve was taken as the Young’s modulus. A 0.2% offset line, parallel to the linear region, was defined and the intersection with the curve was taken as the yield strength. Compressive stress was determined by the first local maximum stress in the stress-strain curve.

5.2.7. Cytocompatibility of the composite scaffolds

5.2.7.1. Cell culture

Mouse preosteoblast cells (MC3T3-E1, Sigma Aldrich, Germany) were pre-cultured for 7 d in α -minimum essential medium (α -MEM, Thermo Fisher Scientific, USA), supplemented with 10% fetal bovine serum (FBS, Thermo Fisher Scientific, USA) and 1% penicillin/streptomycin (p/s, Thermo Fisher Scientific, USA). The medium was refreshed every 2-3 d.

5.2.7.2. Cell viability and cell adhesion

Prior to cell seeding, the scaffolds were sterilized by heating to 120 °C for 2 h. The samples were incubated for 3 days with the α -minimum essential medium (α -MEM). The MC3T3-E1 preosteoblasts (1×10^4 cells per sample) were seeded onto the Mg-Zn/TCP specimens (2.4 mm in height and 9.25 mm in diameter) in 8 mL α -MEM (without ascorbic acid, but with 10% FBS, 1% p/s) in 6-well plates. The porous Mg-Zn scaffolds were used as the control group. The viability of the preosteoblasts was examined using a live/dead assay (LIVE/DEAD Viability/Cytotoxicity Kit, Life Technologies Corp., USA) in duplicate. After 3 d of cell culture, the specimens with the cells were stained using calcein and ethidium homodimer-1 (Thermo Fisher Scientific, USA). Thereafter, the live and dead cells on the scaffolds were observed with a fluorescence microscope (ZOE cell imager, Bio-Rad, USA). In addition, the trypan blue assay (Bio-Rad, USA) was used for the quantification of cell viability on the scaffolds in triplicate. For each group, the scaffolds without cells were used as the background control. After 1, 3, 7 and 14 d of cell culture, the cells were trypsinized from the specimens and the well plates. After centrifuging, the cell suspensions were obtained. 10 μ L of trypan blue dye was used to mix with 10 μ L of each cell suspension which was subsequently pipetted into a dual-chamber cell counting slide. The living cells were counted using an automated cell counter (TC20, Bio-Rad, USA). After subtracting the number obtained from the background control, the mean and standard deviation of the number of the living cells of each group were obtained. To examine the cell adhesion and morphology on the scaffolds, the specimens were fixed and dehydrated, after the preosteoblasts were cultured on them for 3 d. Then, the specimens were sputtered with gold and were observed by SEM.

5.2.7.3. Osteogenic ability

To evaluate the bioactivity of the developed composites, the extracts of the Mg-Zn/TCP composite scaffolds were prepared through immersing the sterilized composite scaffolds in the α -MEM under the above physiological conditions for 72 h. The extracts were supplemented with ascorbic acid and β -glycerophosphate. For both alkaline phosphate (ALP) tests and Alizarin Red S staining, the supplementary medium only was used as the control group. Both the ALP tests and Alizarin Red S staining were performed in triplicate for each group. The ALP tests were performed after 14 d of cell culture in the extracts using an alkaline phosphatase assay kit (ab83371, Abcam, USA). For the ALP tests, the culture medium was supplemented with 50 μ g mL⁻¹ ascorbic acid (1:1000) and 4 mM β -glycerophosphate (1:500) (both from Sigma Aldrich, Germany). The ALP tests followed the product manufacturer's protocol (ab83371, Abcam, USA).

In addition, Alizarin Red S staining was performed after 21 days to assess calcium in the matrix of cells. Cells were cultured in the prepared extracts supplemented with ascorbic acid and β -glycerophosphate, as described above. After 21 d of cell culture, the specimens were fixed using a 4% (v/v) formaldehyde solution (Sigma Aldrich,

Germany). The specimens were then incubated in a 2% (w/v) Alizarin Red S solution (Sigma Aldrich, Germany) for 30 min in the dark. The specimens were then rinsed five times with distilled water before being imaged by a ZOE fluorescent cell imager (Bio-Rad, The Netherlands). Quantification was performed by exposing the stained specimens to a solution of 20% methanol and 10% acetic acid. After 15 min, the absorbance of Alizarin Red was read on a Victor X3 plate reader (Perkin Elmer, The Netherlands) at a wavelength of 450 nm.

5.2.8. Statistical analysis

The results of the viable cell count, ALP activity, and Alizarin Red S absorption tests were statistically analyzed using two-way ANOVA, followed by a Tukey multiple comparison *post hoc* test (**** = $p < 0.0001$, *** = $p < 0.001$, ** = $p < 0.01$, and * = $p < 0.05$, *n.s.* = not significant). The SPSS Statistics 20 software (IBM, USA) was used for the statistical analysis.

5.3. Results

5.3.1. Ink characteristics

The dispersions of β -TCP particles in the binder with the β -TCP/binder volume ratios of 7:93, 5:95, and 3:97 are shown in Figure 5.2A-(a-c), respectively. Some agglomerates of β -TCP particles were clearly visible in the 93% pre-ink group (Figure 5.2A-a), while in the 95% (Figure 5.2A-b) and 97% pre-ink groups (Figure 5.2A-c), the dispersions of β -TCP particles were more uniform. The β value, indicating the degree of inhomogeneity, was 1.2 ± 0.2 for the 93% pre-ink group, 0.6 ± 0.3 for the 95% pre-ink group, and 0.4 ± 0.2 for the 97% pre-ink group.

The Mg-Zn powder particles were further mixed with the pre-inks (*i.e.*, the mixtures of the binder and β -TCP) to prepare the inks for 3D printing. The dispersions of the β -TCP particles in the printed specimens (Mg-Zn/10TCP as an example here) exhibited the same trend (Figure 5.2A-(d-f)) as for the pre-inks. Large clusters of β -TCP particles were still visible in the specimens that were 3D printed using the 93% pre-ink (Figure 5.2A-d), which sometimes even resulted in clogging the nozzle during 3D printing (Figure S5.1a). The β -TCP particles were most uniformly distributed on the surfaces of Mg-Zn powder particles, when using the 97% pre-ink for 3D printing, with more binder covering the powder particles (Figure 5.2A-f).

The 97% pre-ink allowed a highly uniform distribution of β -TCP particles in the printed specimens. Therefore, it was first used for preparing the Mg-Zn/5TCP, Mg-Zn/10TCP, and Mg-Zn/15TCP inks to check their printability. All the three groups of the

prepared inks using the 97% pre-ink exhibited shear-thinning (Figure 5.2B-a and b, denoted as Mg-Zn/5TCP_97%, Mg-Zn/10TCP_97% and Mg-Zn/15TCP_97%, respectively). However, the Mg-Zn/10TCP_97% and Mg-Zn/15TCP_97% inks did not show quick recovery when the applied shear stress was removed (Figure 5.2A-c and d), with recovery degrees of -6% and -1%, respectively (Table 5.1). These two inks were, thus, not suitable for the extrusion-based 3D printing [28]. This was further evidenced by the non-freeform characteristics of the specimens printed with the Mg-Zn/10TCP_97% or Mg-Zn/15TCP_97% (Figure 5.2C-a). The 95% pre-ink was, therefore, used to prepare the Mg-Zn/10TCP and Mg-Zn/15TCP inks (denoted as Mg-Zn/10TCP_95% and Mg-Zn/15TCP_95%, respectively). Similar to the Mg-Zn/5TCP_97% ink, the Mg-Zn/10TCP_95% ink exhibited shear-thinning (Figure 5.2B-a), while the deformation did recover when the applied stress was removed (Figure 5.2B-c), which allowed for the realization of freestanding 3D structures without any deflection of the spanning struts (Figure 5.2C-c). The Mg-Zn/15TCP_95% inks showed a much lower recovery degree, as compared to the printable inks (Table 5.1) and the resulting structure showed a large degree of the deflection of the strut layer (Figure 5.2C-b). Eventually, the Mg-Zn/15TCP_93% ink (prepared using 93% pre-ink) with a recovery degree of 29% was chosen, as it enabled the successful printing of Mg-Zn/15TCP 3D structures. Based on the above rheological results and the quality of the resulting composite scaffolds, the 97% pre-ink was chosen for printing the Mg-Zn/5TCP composite scaffolds, while the 95% and 93% pre-inks were used for printing the Mg-Zn/10TCP and Mg-Zn/15TCP composite scaffolds, respectively.

Table 5.1 The recovery degrees of the inks as determined by the creep-recovery tests.

Sample group	97% pre-inks	95% pre-inks	93% pre-inks
Mg-Zn/5TCP	26% ± 12%	--	--
Mg-Zn/10TCP	-6% ± 5%	19% ± 2%	--
Mg-Zn/15TCP	-1% ± 1%	9% ± 3%	29% ± 8%

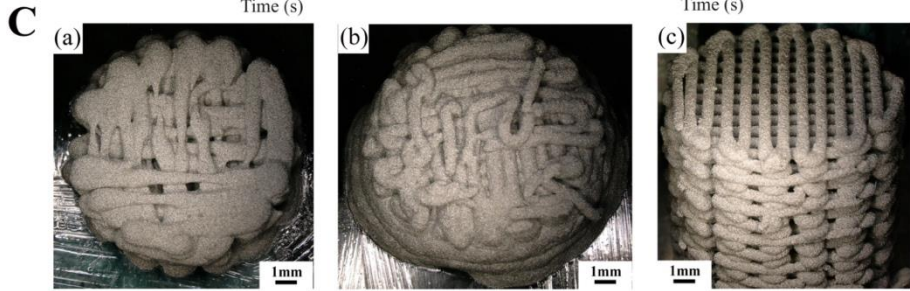
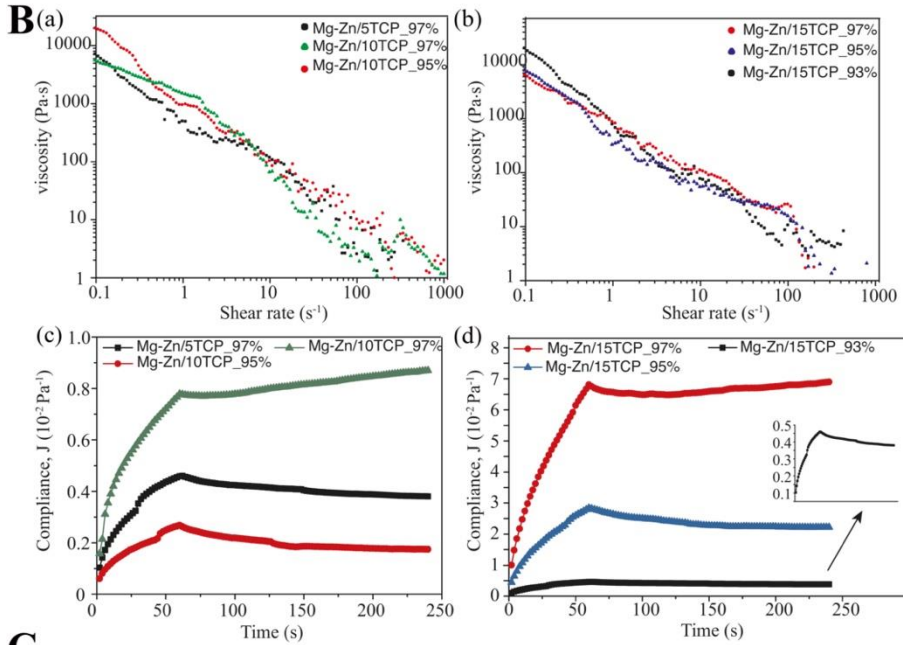
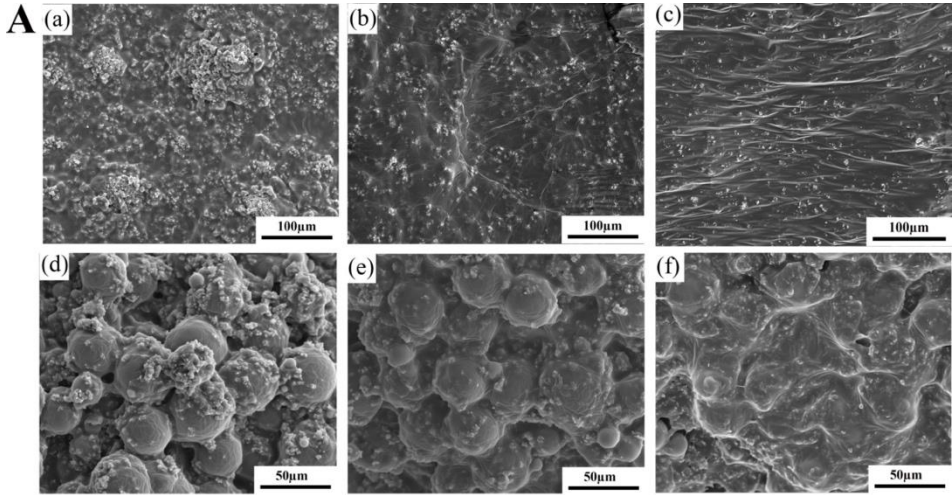


Figure 5.2 (A) The dispersion of β -TCP particles in the 93% pre-ink (a), 95% pre-ink (b), and 97% pre-ink (c) (SEM, JEOL, $\times 250$), and the distribution of the β -TCP particles in the Mg-Zn/10TCP specimens printed using the 93% pre-ink (d), 95% pre-ink (e), and 97% pre-ink (f), (SEM, JEOL, $\times 500$) (B) the rheological characteristics of the prepared inks: results obtained from the shear rate sweep tests (a)-(b) and the results obtained from the creep-recovery tests (c)-(d); (C) the macrographs of representative samples printed using the prepared inks (optical microscope, Keyence, $\times 50$): Mg-Zn/15TCP_97% or Mg-Zn/10TCP_97% inks (a), Mg-Zn/15TCP_95% ink (b), and Mg-Zn/5TCP_97%, Mg-Zn/10TCP_95%, or Mg-Zn/15TCP_93% (c).

5.3.2. Characteristics of the porous Mg-Zn/TCP composite scaffolds

Using the optimally formulated inks, the Mg-Zn/5TCP, Mg-Zn/10TCP, and Mg-Zn/15TCP composite scaffolds could be successfully printed. All the three groups of the printed Mg-Zn/TCP composite scaffolds showed a geometrically ordered porous structure with a $0^\circ/90^\circ/0^\circ$ pattern (Figure S5.2a-c), as designed. The struts aligned accurately without any deflection over the spanning space and the adjacent layers adhered to each other (Figure S5.2a-c). From the close-up views of the struts in the composite scaffolds, the β -TCP particles and the binder uniformly covered the Mg-Zn powder particles in the Mg-Zn/5TCP (Figure S5.2d) and Mg-Zn/10TCP scaffolds (Figure 5.2A-e). However, the β -TCP particles agglomerated on the surface of the Mg-Zn powder particles in the Mg-Zn/15TCP specimens (Figure S5.2e).

After sintering, the porosities of the struts were $0.1 \pm 0.11\%$ for Mg-Zn/5TCP, $0.3 \pm 0.23\%$ for Mg-Zn/10TCP, and $13.9 \pm 4.7\%$ for Mg-Zn/15TCP. The other detailed structural characteristics of the composite scaffolds are presented in Table 5.2. The as-sintered Mg-Zn/5TCP and Mg-Zn/10TCP composite scaffolds showed highly densified struts with almost no apparent pores (Figure 5.3A-a1 and b1), while the Mg-Zn/15TCP composite scaffolds had porous struts (Figure 5.3A-c1). The edges of the original Mg-Zn powder particles disappeared due to liquid-phase sintering. The Mg-Zn alloy matrix with dispersed β -TCP particles was observed on the surfaces of all the three groups of the Mg-Zn/TCP composite scaffolds (Figure 5.3A-(a2-c2)). The cross-sectional images of the Mg-Zn/5TCP and Mg-Zn/10TCP composite scaffolds revealed almost uniform distributions of the bioceramic phase (Figure 5.3A-a3 and b3), while clustering was predominately observed in the Mg-Zn/15TCP composite scaffolds (Figure 5.3A-c3). The degrees of the inhomogeneity of the bioceramic phase in the three groups of the composite scaffolds were quantified (Table 5.4). The Mg-Zn/15TCP group had a higher β value than the Mg-Zn/5TCP and Mg-Zn/10TCP groups, confirming the presence of more agglomerates in the Mg-Zn/15TCP composite scaffolds.

In addition to the Mg-Zn matrix phase, another two phases, namely an integrated grey phase (arrow 1 in Figure 5.3A-a4 and b4) and an isolated particle-shaped phase (arrow 2 in Figure 5.3A-b4), were present in all the three Mg-Zn/TCP composite scaffold groups, as shown in the amplified cross-sectional images (Figure 5.3A-(a4-c4)). XRD revealed that besides the Mg-Zn matrix phase and the MgO phase, inevitably present in the Mg samples due to the sintering process, there were two new phases, *i.e.*, the $\text{Ca}_2\text{Mg}_6\text{Zn}_3$ and $\text{Ca}_4\text{P}_2\text{O}$ phases, but no β -TCP phase was detected (Figure 5.3B), indicating that diffusion between the Mg-Zn matrix and β -TCP occurred during sintering.

Table 5.2 The morphological characteristics of the extrusion-based 3D printed Mg-Zn/ β -TCP composite scaffolds.

Sample group	Strut width (μm)	Strut spacing (μm)	Porosity in the struts after sintering	Absolute porosity of the scaffolds
Design	580	360	--	37.8%
Mg-Zn	516.1 ± 15.3	331.7 ± 39.5	$6.9 \pm 1.0 \%$	$50.3 \pm 3.4\%$
Mg-Zn/5TCP	456.3 ± 13.9	310.8 ± 18.8	$0.1 \pm 0.1\%$	$47.6 \pm 10.6\%$
Mg-Zn/10TCP	429.2 ± 17.6	316.6 ± 23.0	$0.3 \pm 0.2\%$	$48.5 \pm 4.0\%$
Mg-Zn/15TCP	451.7 ± 14.8	362.3 ± 27.2	$13.9 \pm 4.7\%$	$55.2 \pm 17.9\%$

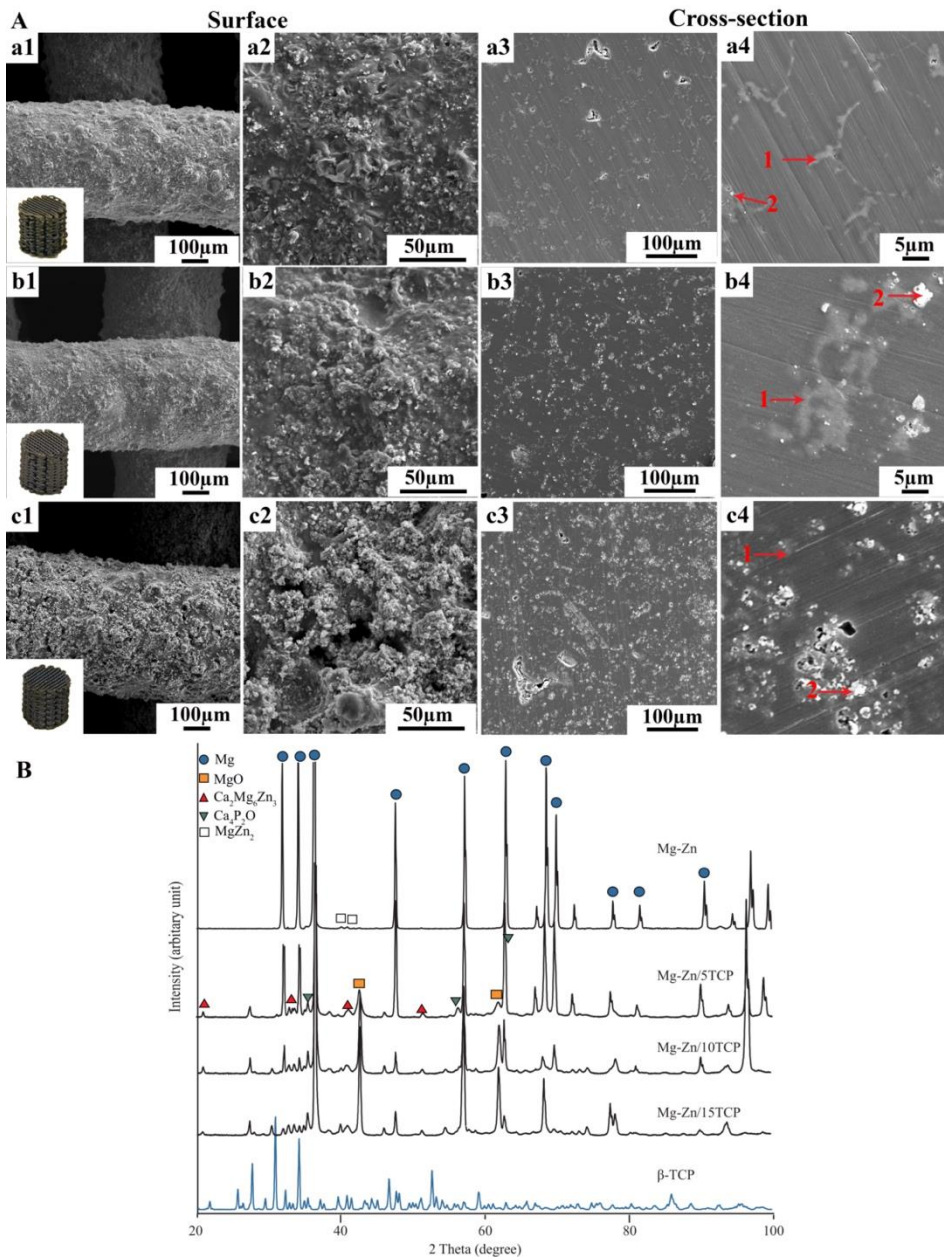


Figure 5.3 The characteristics of the fabricated Mg-Zn/TCP composite scaffolds (SEM, JEOL): (A) microstructures: (a1-a4) Mg-Zn/5TCP, (b1-b4) Mg-Zn/10TCP, (c1-c4) Mg-Zn/15TCP; (B) XRD patterns (Bruker, ICDD card number: Mg, 04-019-3684; MgO, 04-010-4039; $\text{Ca}_2\text{Mg}_6\text{Zn}_3$, 00-012-0266; $\text{Ca}_4\text{P}_2\text{O}$, 04-010-2306; β -TCP, 00-055-0898).

To identify the two new phases in the composite scaffolds, EDS mapping was used to examine the elemental compositions. The integrated grey phase was found to be mainly composed of Ca, Zn and Mg, which suggests the presence of $\text{Ca}_2\text{Mg}_6\text{Zn}_3$ (Figure 5.4A). The isolated particle-shaped phase was mostly attached to the integrated grey phase, which could be readily observed in the scaffolds with higher β -TCP concentrations (*i.e.*, Mg-Zn/10TCP and Mg-Zn/15TCP, Figure 5.4B, and Figure S5.3). EDS mapping could, therefore, not distinguish these two phases. EDS point analysis was consequently used to identify each phase. Compared with points 1 and 2, points 3 and 4 had more O and P but less Zn (Figure 5.4B and Table 5.3). Combined with the XRD results, the isolated particles could be identified as $\text{Ca}_4\text{P}_2\text{O}$. The volume fractions of $\text{Ca}_2\text{Mg}_6\text{Zn}_3$ and $\text{Ca}_4\text{P}_2\text{O}$ in the composite scaffolds are listed in Table 5.4.

Table 5.3 The EDS analysis of the Mg-Zn/ β -TCP specimens shown in Figure 5.4B.

Weight%	C	O	Mg	P	Ca	Zn
#1	2.5	6.4	52.2	0.4	10.8	27.7
#2	2.4	3.2	47.7	0.5	13.6	32.5
#3	4.7	12.6	55.7	1.2	12.7	13.1
#4	5.1	17.6	50.0	1.2	12.9	13.3

Table 5.4 The β values of the bioceramic particles and the volume fractions of the new phases in the Mg-Zn/ β -TCP specimens.

Sample group	β	$\text{Ca}_4\text{P}_2\text{O}$	$\text{Ca}_2\text{Mg}_6\text{Zn}_3$
Mg-Zn/5TCP	0.51 ± 0.1	$0.20\% \pm 0.10\%$	$6.70\% \pm 1.32\%$
MgZn/10TCP	0.63 ± 0.2	$0.93\% \pm 0.51\%$	$10.07\% \pm 2.50\%$
MgZn/15TCP	1.52 ± 0.2	$2.39\% \pm 1.16\%$	$15.32\% \pm 2.97\%$

The nanohardness of the Mg-Zn matrix was 43.0 ± 3.0 GPa, while that of the $\text{Ca}_2\text{Mg}_6\text{Zn}_3$ and $\text{Ca}_4\text{P}_2\text{O}$ phase combination was 55.1 ± 8.0 GPa (Figure 5.4C and D). In addition, the surface roughness values of Mg-Zn/5TCP, Mg-Zn/10TCP, and Mg-Zn/15TCP, Ra, were 5.9 ± 1.5 μm , 8.8 ± 5.6 μm , and 9.1 ± 1.2 μm , respectively.

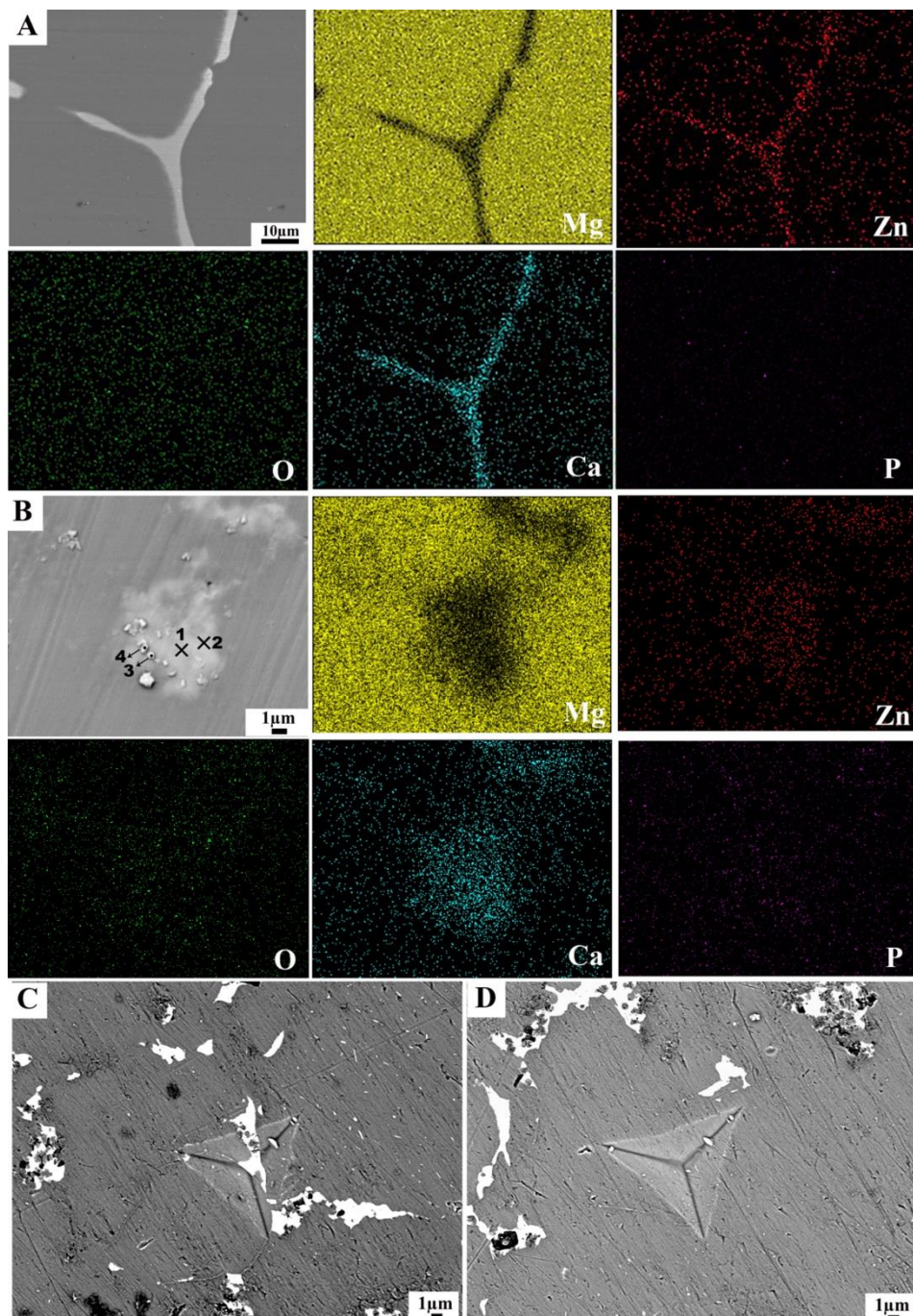


Figure 5.4 The characteristics of the phases in the Mg-Zn/TCP composite scaffolds (SEM, JEOL, $\times 1500$): (A) the phases in Mg-Zn/5TCP and the corresponding EDS mapping, (B)

the phases in Mg-Zn/10TCP and the corresponding EDS mapping, (C) nano-indentation (G200, Berkovich tip, maximum indentation depth of 2000 nm) on the $\text{Ca}_2\text{Mg}_6\text{Zn}_3$ and $\text{Ca}_4\text{P}_2\text{O}$ combined phases, and (D) nano-indentation on the Mg-Zn matrix.

5.3.3. *In vitro* degradation performance of the composite scaffolds

During the *in vitro* immersion tests in r-SBF, white corrosion products gradually deposited on the composite scaffolds (Figure 5.5a, Figure S5.4a, and Figure S5.5a). The biodegradation behavior of both the peripheral and central layers in the composite scaffolds could be observed on the 2D slices of the μCT reconstructions (Figure 5.5a, Figure S5.4a, and Figure S5.5a). The struts (white part) on the peripheries and at the centers of the composite scaffolds gradually biodegraded and were replaced by the biodegradation products (grey part). The struts at the central layers degraded more than those on the periphery for all the three Mg-Zn/TCP groups (Figure 5.5a, Figure S5.4a, and Figure S5.5a). During the *in vitro* biodegradation, the biodegradation products stayed in the composite scaffolds. With increasing immersion time, more and more biodegradation products replaced the struts and occupied the spaces between the struts (*i.e.*, filling in the macropores of the composite scaffolds, Figure 5.5a, Figure S5.4a, and Figure S5.5a). The degradation products entrapped in the composite scaffolds increased the volumes of the composite scaffolds at the beginning of the *in vitro* immersion, when the degradation products were included during the segmentation of the composite scaffolds (Figure 5.5b, Figure S5.4b, and Figure S5.5b). The relative densities of the Mg-Zn/5TCP and Mg-Zn/10TCP composite scaffolds also showed an increasing trend (corresponding to the decreasing porosities of the composite scaffolds) until day 14 (Figure 5.5c, Figure S5.4c). However, when the biodegradation products were segmented apart from the scaffold substrates, the volumes and relative densities showed a decreasing trend with immersion time for all the three Mg-Zn/TCP groups (Figure 5.5b and c, Figure S5.4b and c, and Figure S5.5b and c). At the beginning of the *in vitro* immersion, the *in vitro* biodegradation rates of the scaffolds were 1.0 ± 0.4 mm/y for Mg-Zn/5TCP, 1.6 ± 0.7 mm/y for Mg-Zn/10TCP, and 4.1 ± 3.4 mm/y for Mg-Zn/15TCP, respectively (Figure 5.5d). After 28 d, the biodegradation rates of Mg-Zn/5TCP and Mg-Zn/10TCP decreased to 0.5 mm/y and 0.7 mm/y, respectively. The biodegradation rate of Mg-Zn/15TCP decreased to 2.3 ± 0.4 mm/y after 7 d of immersion (Figure 5.5d). During the *in vitro* degradation, Mg ions gradually released to r-SBF. Mg-Zn/15TCP released the most at day 7 (Figure 5.5e) and had the highest pH level (Figure S5.6), which is consistent with this high rate.

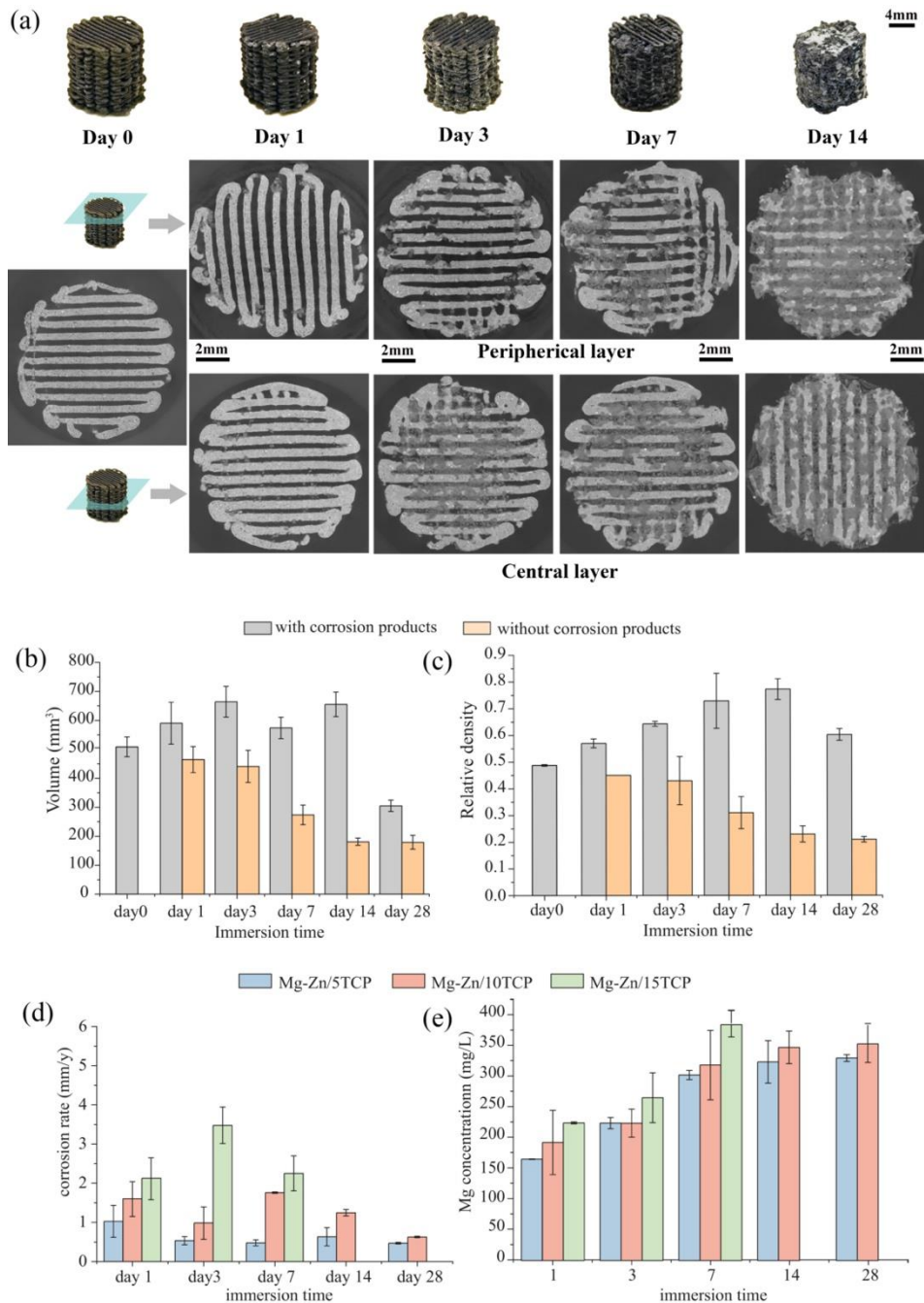


Figure 5.5 *In vitro* degradation behavior: (a) the macrographs and 2D μ CT slices of the degraded Mg-Zn/10TCP specimens, (b-c) the changes in the volumes and relative

densities of the degraded Mg-Zn/10TCP specimens with and without corrosion products, (d) corrosion rates, and (e) changes of Mg ion concentrations in r-SBF up to 28 days.

5.3.4. Characteristics of the biodegradation products

A layer of biodegradation products formed and covered the struts of the Mg-Zn/10TCP specimens after 24 h of immersion (Figure 5.6a). The biodegradation products grew with the immersion time and almost filled the spaces (*i.e.*, macropores) between the struts after day 14 (Figure 5.6b-c). The Mg-Zn/5TCP specimens showed a similar biodegradation behavior (Figure S5.7a-c). As for the Mg-Zn/15TCP specimens, the degradation of the struts was notable only after 3 d of immersion and the formed biodegradation products showed a rather bumpy morphology (Figure S5.8b-c). The magnified images of biodegraded Mg-Zn/10TCP showed the appearance of riverbed-like biodegradation products (Figure 5.6d) which were followed by the gradual formation of cauliflower-like biodegradation products that almost fully covered the surface at day 14 (Figure 5.6e-f). The major elements present in the peripheral biodegradation products were C, O, Mg, Ca, and Zn. Similar observations were made for the Mg-Zn/5TCP and Mg-Zn/15TCP specimens (Figure S5.7 and Figure S5.8). At the center of the specimens, the biodegradation products contained MgO, replacing the original struts, as biodegradation progressed (grey area), while CaP-containing compounds (white area) were deposited between the struts (Figure 5.6g, Figure S5.7g, Figure S5.8g, and the corresponding EDS mappings).

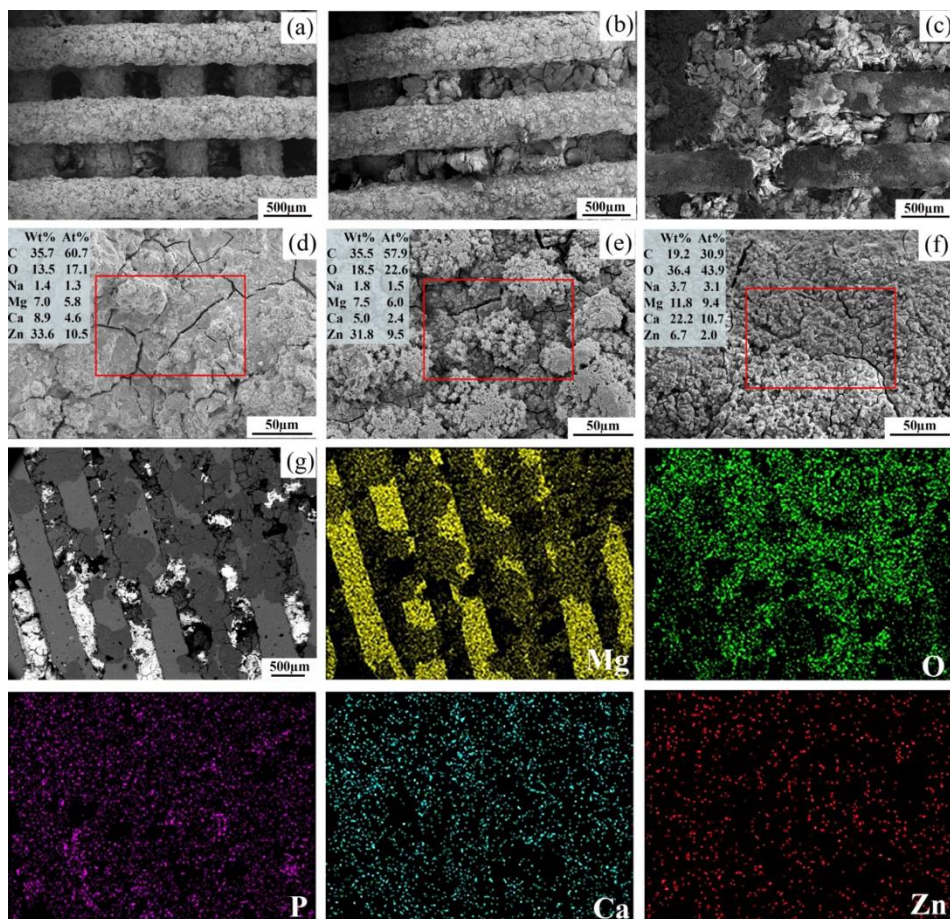


Figure 5.6 The morphologies and chemical compositions of *in vitro* biodegradation products on the Mg-Zn/10TCP scaffolds (SEM, JEOL, $\times 40$ and $\times 500$): on the periphery after 1 (a and d), 7 (b and e), 14 d (c and f) of biodegradation, and (g) at the center of the scaffolds after 14 d of biodegradation and the corresponding EDS mapping. The boxed areas and values indicate where the EDS analyses were performed and the corresponding elemental compositions, respectively.

In addition, XRD was used to examine the phases in the biodegraded scaffolds. In addition to the Mg matrix phase, $\text{Ca}_2\text{Mg}_6\text{Zn}_3$, and $\text{Ca}_4\text{P}_2\text{O}$ that were present in the as-sintered scaffolds, the following phases were identified in the biodegraded Mg-Zn/TCP specimens: MgO, $\text{Mg}(\text{OH})_2$, ZnO, brushite ($\text{CaHPO}_4 \cdot 2\text{H}_2\text{O}$), and $\text{CaCO}_3 \cdot \text{H}_2\text{O}$ (Figure 5.7 and Figure S5.9). The intensities of the Mg peaks clearly decreased with the immersion time (lines 1 in Figure 5.7 and Figure S5.9), while the peaks corresponding to

Mg(OH)₂ intensified (lines 2 in Figure 5.7 and Figure S5.9). The brushite peaks disappeared after 14 d of immersion (lines 3 in Figure 5.7).

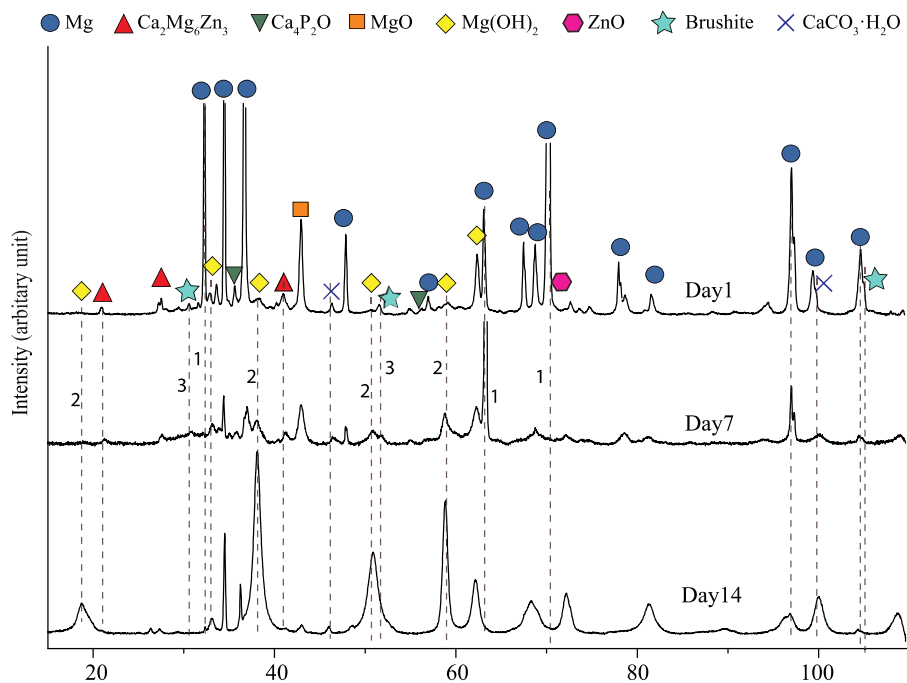


Figure 5.7 The XRD (Bruker) patterns of the Mg-Zn/10TCP scaffolds after 1, 7, and 14 d of biodegradation.

5.3.5. Mechanical properties along with *in vitro* degradation

Under uniaxial compression, all the Mg-Zn/TCP composite scaffolds exhibited smooth stress-strain curves that started with a linear elastic region, followed by a plastic deformation region (Figure 5.8a). The yield strengths of the as-sintered composite scaffolds were 24.4 ± 13.4 MPa for Mg-Zn/5TCP, 31.3 ± 1.9 MPa for Mg-Zn/10TCP, and 23.5 ± 0.6 MPa for Mg-Zn/15TCP. The elastic moduli of the three groups of the as-sintered composite scaffolds were 431.6 ± 102.9 MPa, 585.3 ± 117.6 MPa, and 455.7 ± 53.7 MPa, respectively. The compressive strengths were 40.9 ± 17.5 MPa for Mg-Zn/5TCP, 39.1 ± 22.7 MPa for Mg-Zn/10TCP, and 29.9 ± 2.5 MPa for Mg-Zn/15TCP. A decline in strain at failure from $19 \pm 7\%$ for Mg-Zn/5TCP to $11 \pm 3\%$ for Mg-Zn/15TCP was observed, indicating that the scaffolds became less ductile with increasing β -TCP percentage. After *in vitro* biodegradation, the yield strengths and elastic moduli of the Mg-Zn/5TCP and Mg-Zn/10TCP specimens remained unchanged or even increased until

day 3, followed by a decreasing trend. The same properties of Mg-Zn/15TCP gradually decreased with time (Figure 5.8b and c).

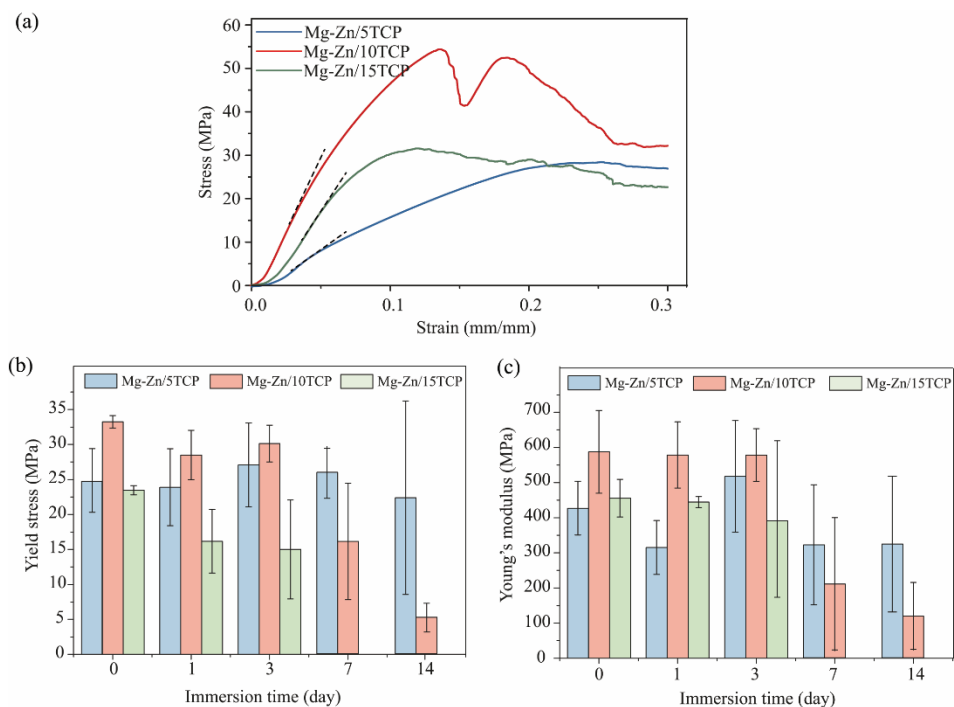


Figure 5.8 The compressive properties of the Mg-Zn/10TCP specimens (Zwick, 10kN load cell, crosshead speed: 2mm/s): (a) the stress-strain curves of the scaffolds before degradation (the dashed line indicates the linear elastic region), (b) the variations of the yield strength with the immersion time, and (c) the variations of the Young's modulus with the immersion time.

5.3.6. *In vitro* biocompatibility

High levels of metabolic activity were observed, when cells were cultured with the extracts of the Mg-Zn/5TCP and Mg-Zn/10TCP scaffolds (Figure S5.10). However, the metabolic activity of the extract of Mg-Zn/15TCP at day 7 was below 20%, indicating its cytotoxicity. Therefore, for direct cell culture assay, only porous Mg-Zn/5TCP and Mg-Zn/10TCP were further tested, with Mg-Zn specimens for comparison purposes. The live/dead staining after 3 d of culture showed homogeneous cell distributions on the struts of all the groups (Figure 5.9a-c). Preosteoblasts with a stretching shape were observed on both the Mg-Zn/5TCP (Figure 5.9b) and Mg-Zn/10TCP specimens (Figure 5.9a). In contrast, the cells on the Mg-Zn scaffolds were mostly red and rounded (Figure 5.9c).

The SEM imaging confirmed that the cells attached to the Mg-Zn/5TCP and Mg-Zn/10TCP surfaces developed many filopodia and showed spreading morphologies with cell-cell contacts after 3 d of culture (Figure 5.9d and e). The viable cells on the Mg-Zn/5TCP and Mg-Zn/10TCP specimens increased until day 7, and their numbers were significantly higher than the number of the cells on the Mg-Zn scaffolds (Figure 5.9f). After 14 d of culture, the viable cells on Mg-Zn/5TCP were at the same level as day 7, but those on the Mg-Zn/10TCP specimens decreased.

Both the Mg-Zn/5TCP and Mg-Zn/10TCP specimens showed enhanced levels of ALP activity, as compared to the control group (Figure 5.9i). To study the mineralization level of the specimens, Alizarin Red S staining was conducted at day 21. The stained calcified nodules indicated that mineralization had occurred both in the Mg-Zn/5TCP and Mg-Zn/10TCP extracts (Figure 5.9g and h). Both of those mineralization levels were higher than that of the control group, but there was no statistically significant difference between Mg-Zn/5TCP and Mg-Zn/10TCP (Figure 5.9i).

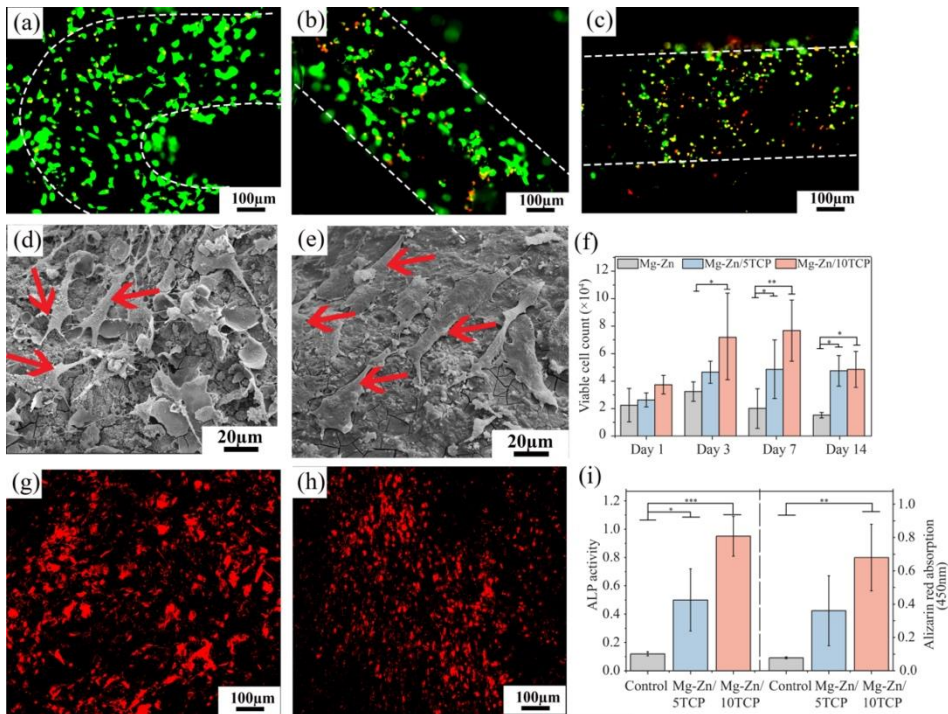


Figure 5.9 The *in vitro* biological evaluation of the Mg-Zn/5TCP and Mg-Zn/10TCP specimens: calcein acetoxyethyl (green, showing viable cells) and ethidium homodimer-1 (red, showing damaged cells) fluorescence staining of MC3T3-E1 preosteoblasts after 3 d of culture on Mg-Zn/10TCP (a), Mg-Zn/5TCP (b), and Mg-Zn

(c), respectively (the white dashed lines indicate the rough edge of the scaffold struts); the morphologies of the preosteoblasts after 3 d of culture on Mg-Zn/10TCP (d) and Mg-Zn/5TCP (e), and the number of viable preosteoblasts (f); the Alizarin Red S staining of the cells cultured in the extracts of Mg-Zn/10TCP (g) and Mg-Zn/5TCP (h) scaffolds after 21 d of culture; (i) the quantification of ALP (after 14 d of culture) and Alizarin Red S staining (after 21 d of culture).

5.4. Discussion

5.4.1. Fabrication of the composite scaffolds

5.4.1.1. Ink preparation

The key to successful extrusion-based 3D printing of Mg scaffolds is the design and preparation of a printable ink with suitable viscoelastic properties. In the case of Mg-based composite scaffolds, the dispersion of micro-sized bioceramic particles in the ink is another critical factor that needs to be carefully considered. We observed that the agglomeration of bioceramic particles greatly affects the flowability of the inks, making the nozzle clog during the printing process (Figure S5.1a). Uniform dispersion of bioceramic particles was beneficial both for printing and for improving the final properties of the fabricated composite scaffolds. To obtain inks with an optimal β -TCP dispersion, we first studied the dispersion of β -TCP in the binder. The β -TCP distribution was more homogenous for higher percentages of the binder (Figure 5.2A-(a-c)), indicating that the binder itself could act as a dispersant. Polyisobutylene with hexane is reported to stabilize dispersed particles through steric stabilization [46, 47]. In this scenario, an organic layer forms on the surface of the particles, acting as a steric barrier and preventing the particles from coming into direct surface contact [48]. Therefore, to achieve good dispersion of β -TCP, the binder should ideally be capable of forming a steric layer on each β -TCP particle. This is why a higher percentage of the binder corresponded to more uniform dispersion of the bioceramic particles.

Furthermore, we found that the dispersion of β -TCP particles in the inks was largely dependent on that of β -TCP in the binder (i.e., pre-inks, Figure 5.2A). At a given ratio of β -TCP to binder (e.g., 97% that reached the best dispersion degree), loading a larger amount of β -TCP in the ink resulted in a larger amount of binder in the prepared ink (i.e., mixtures of β -TCP, binder, and the Mg-Zn powder). For reaching the best dispersion degree, 52 vol% binder is needed for the Mg-Zn/5TCP ink, 70 vol% for the Mg-Zn/10TCP ink and 77 vol% for the Mg-Zn/15TCP ink. On the other hand, too much binder resulted in inks losing their viscoelastic properties, because of the low level of powder loading (e.g., Mg-Zn/10TCP_97% and Mg-Zn/15TCP_97%, Figure 5.2B). Therefore, the homogeneity and viscoelasticity of the inks need to be simultaneously

considered. Binder is needed for uniform dispersion in the ink, but too much binder makes the ink unprintable. For being able to print, the dispersion of β -TCP in the Mg-Zn/10TCP and Mg-Zn/15TCP inks had to be compromised in the present study. Because of a lower percentage of β -TCP loading, the Mg-Zn/5TCP ink showed the best dispersion, while being also printable (Figure S5.2d).

In summary, extrusion-based 3D printing has demonstrated significant advantages for the fabrication of composite scaffolds over other AM techniques, because it allows for the fine-tuning of printable inks to optimize the dispersion of micro-sized particles. The binder system should, therefore, be judiciously designed to both possess suitable viscoelastic characteristics and exhibit favorable dispersion behavior. Additional dispersants may be added into the binder system to further improve its dispersion function.

5.4.1.2. Interfacial bonding between Mg and bioceramic in the composite scaffolds

For the as-sintered composite scaffolds, having sufficiently strong interfacial bonding between the Mg-based matrix and bioceramic reinforcement is crucial both for realizing a strengthening effect and to improve their integrity during biodegradation [49]. An effective way to enhance interfacial bonding is to form an interlayer at the Mg/bioceramic interface so as to chemically interlock the constituents [50]. To form an interlayer, two criteria must be met: (i) a thermochemical reaction needs to take place at the Mg/bioceramic interface to form an intermediate layer as a reaction product, and (ii) either the bioceramic elemental atoms diffuse across the Mg oxide layer into Mg or the elemental atoms in the Mg matrix diffuse across the Mg oxide layer out of Mg. It has been found that Mg can react with β -TCP through a solid-state reaction [49, 51]. Mg^{2+} and Zn^{2+} have the energetically preferential Ca-5 site in the β -TCP structure for substitution [52]. We could, therefore, take advantage of the reaction between the Mg matrix and the added β -TCP during sintering to enhance the interfacial bonding. However, the original MgO layer on the surfaces of Mg powder particles is quite stable and the diffusion coefficient of the Mg atoms (*i.e.*, 5.25×10^{-24} at 650 °C) through the oxide layer is relatively low [53]. Some other studies have used spark plasma sintering to fabricate Mg/ β -TCP composites while applying external pressure during the sintering process to disrupt the oxide layer, thereby increasing diffusion [49, 51]. However, the specific design of our porous scaffolds with a complex 3D structure restricted us from applying external mechanical pressure. Instead, we tried to apply a liquid-phase sintering strategy to facilitate effective diffusion. In this approach, a small volume fraction of liquid phase is formed during sintering, thereby facilitating the disruption of the oxide layer present on the surface of the powder particles [28]. Because of the faster diffusion of atoms during liquid-state sintering as compared to solid-state sintering and the high diffusivity of Ca in Mg [54], a $\text{Ca}_2\text{Mg}_6\text{Zn}_3$ intermediate layer quickly formed during sintering (Figure 5.4A,

B and Table 5.4). It has been found that $\text{Ca}_2\text{Mg}_6\text{Zn}_3$ can form when the Zn/Ca atomic ratio exceeds 1.2 [55]. MgO could form at the interface between the $\text{Ca}_2\text{Mg}_6\text{Zn}_3$ phase and Mg-Zn matrix as a thin layer (Figure 5.3B, but not observable in the microstructure under SEM), because of the high affinity of Mg with the O atoms from β -TCP, which also helped enhance the interfacial bonding due to the high stability of MgO.

The diffusion or the reaction stopped when it reached an equilibrium. At the area of local agglomerates of β -TCP, the β -TCP particles could not completely react with the surrounding Mg-Zn matrix and, therefore, a small amount of the $\text{Ca}_4\text{P}_2\text{O}$ phase that derived from $\text{Ca}_3(\text{PO}_4)_2$ was left beside the $\text{Ca}_2\text{Mg}_6\text{Zn}_3$ phase (Figure 5.3 and Figure 5.4). However, the particle-shaped $\text{Ca}_4\text{P}_2\text{O}$ phase had poorer interfacial bonding with the Mg-Zn matrix as compared to the integrated $\text{Ca}_2\text{Mg}_6\text{Zn}_3$ phase, as confirmed by the detachment of the $\text{Ca}_4\text{P}_2\text{O}$ phase during sanding (Figure 5.3A-c4).

The addition of a larger amount of β -TCP into the Mg-Zn scaffolds resulted in higher fractions of the $\text{Ca}_2\text{Mg}_6\text{Zn}_3$ and $\text{Ca}_4\text{P}_2\text{O}$ phases. The total volume fractions of these two new phases (i.e., 6.90% for Mg-Zn/5TCP, 11.0% for Mg-Zn/10TCP, and 17.7% for Mg-Zn/15TCP; Table 5.4) were higher than the design values (i.e., 2.8%, 5.8% and 8.9% β -TCP in volume percentage) because of the diffusion between the Mg-Zn matrix and β -TCP. This was confirmed by EDS mapping (Figure 5.4A and B), which also detected the presence of Ca in the Mg matrix.

5.4.1.3. The fabricated Mg-Zn/TCP composite scaffolds

Previous studies showed that excessive flow of liquid Mg and poor wettability between molten Mg and solid Mg powder particles caused nodules to form on the struts [28, 32]. β -TCP has a better wettability with liquid Mg than other bioceramics, such as HA [10]. In this study, the reaction that occurred between the liquid Mg-Zn and β -TCP further promoted the wettability. More liquid Mg-Zn could, therefore, be accommodated in the porous structure, when the scaffolds with a higher β -TCP volume fraction were sintered in the liquid state. This means that a higher temperature could be chosen for sintering the scaffolds with a higher β -TCP percentage to achieve higher densification, while maintaining the fidelity of the struts. For sintering the Mg-Zn/TCP scaffolds, 600 °C could be used for 5% β -TCP, 620 °C for 10% β -TCP, and 640 °C for 15% β -TCP to reach maximum densification. Under the optimized sintering conditions, the relative densities of struts reached 99.9% for the Mg-Zn/5TCP and 99.5% for the Mg-Zn/10TCP composite scaffolds, which were much higher than that of the Mg-Zn scaffolds (Table 5.2). This confirms that the density of the composite scaffolds in extrusion-based 3D printing can reach and even exceed the levels observed in high laser power PBF AM and in external pressure-assisted powder metallurgy approaches (Table S5.1). This marks a big step forward in the AM of Mg-based scaffolds, because high laser power and the risk of

explosion can be avoided altogether without having to compromise in terms of the relative density of the struts. This study also sheds light on the design of Mg/bioceramic composite scaffolds with adjusted densification.

The porosity of the struts of Mg-Zn/15TCP specimens was quite high (*i.e.*, $13.9 \pm 4.7\%$). This was because the severe agglomeration of β -TCP particles not only resulted in the generation of a great number of voids during 3D printing (Figure S5.1a) but also decreased the flowability of the liquid phase formed during liquid-phase sintering.

5.4.2. Biodegradation behavior

The degradation rate of the Mg-Zn/5TCP composite scaffold (*i.e.*, 0.5 mm/y at day 28) was lower than that of the porous Mg-Zn scaffold without any addition of β -TCP, fabricated by using the same 3D printing technique [32]. This value reached the ideal range of biodegradation rates suggested for bone substitutes (*i.e.*, 0.2–0.5 mm/y) [56]. The biodegradation rate of the Mg-Zn/10TCP specimens (*i.e.*, 0.7 mm/y at day 28) was similar (*i.e.*, 0.7 mm/y and 1.7 mm/y at day 28 and day 7, respectively) to that of the Mg-Zn scaffolds, while the Mg-Zn/15TCP specimens exhibited the highest rate (*i.e.*, 2.3 mm/y at day 7). This means that the addition of a certain amount of β -TCP could help the extrusion-based 3D printed Mg scaffolds reach a desired degradation rate, but adding too much β -TCP would adversely affect the corrosion resistance of the scaffolds.

The highly densified Mg-Zn/5TCP struts with fewer open micropores, as compared to the Mg-Zn struts (Table 5.2), significantly decreased the surface area of the struts for the initiation of biodegradation. This was one of the main reasons for the decreased biodegradation rate of the Mg-Zn/5TCP scaffolds. Moreover, the new phases formed in the Mg-Zn/TCP scaffolds must have influenced the corrosion behavior and corrosion mechanism, since the Mg-Zn/10TCP specimens that possessed highly densified struts (Table 5.2) consistently showed higher corrosion rates during the *in vitro* immersion period, as compared to Mg-Zn/5TCP (Figure 5d).

To reveal the effects of the new phases on the corrosion mechanism of the Mg-Zn/TCP specimens, the degraded specimens (Figure S5.11a) were observed under SEM. During the *in vitro* immersion, the corrosion of these specimens was found to have been initiated at the grain boundaries or in the surrounding area of the formed interfacial phases, predominately the $\text{Ca}_2\text{Mg}_6\text{Zn}_3$ phase. The $\text{Ca}_2\text{Mg}_6\text{Zn}_3$ phase has a higher standard electrode potential than the Mg matrix [57]. The Mg-Zn matrix, therefore, degraded in the r-SBF as the anode, while the $\text{Ca}_2\text{Mg}_6\text{Zn}_3$ phase was protected. The $\text{Ca}_2\text{Mg}_6\text{Zn}_3$ phase was quite stable and remained largely unaffected, as the Mg-Zn matrix became corroded (Figure S5.11a). It was also observed that the corrosion pathway diverted when it met the $\text{Ca}_2\text{Mg}_6\text{Zn}_3$ phase (see the arrows in Figure S5.11b), indicating that the $\text{Ca}_2\text{Mg}_6\text{Zn}_3$ phase

acted as a temporary local corrosion barrier, blocking the pitting pathway and limiting intense corrosion propagation [58]. Although the generation of the $\text{Ca}_2\text{Mg}_6\text{Zn}_3$ phase was not designed intentionally at the start, its presence in the scaffolds decreased the corrosion rate, while the original β -TCP particles quickly dissolved in the electrolyte, accelerating the corrosion of the specimens [11]. The micro-galvanic corrosion and the blocking effect of the $\text{Ca}_2\text{Mg}_6\text{Zn}_3$ phase compete as the Mg-Zn/TCP specimens corrode. In the Mg-Zn/5TCP group, the $\text{Ca}_2\text{Mg}_6\text{Zn}_3$ phase was mainly distributed in a strip-shaped network along the grain boundaries (Figure 5.3Aa3 and a4). The associated blocking effect of this phase, thus, dominated the corrosion behavior [55, 58], which contributed to the desired biodegradation rate of these specimens. However, the irregular shape of the $\text{Ca}_2\text{Mg}_6\text{Zn}_3$ phase with larger surface areas in the Mg-Zn/10TCP and Mg-Zn/15TCP groups resulted in galvanic corrosion dominating the corrosion response. In addition, the $\text{Ca}_2\text{Mg}_6\text{Zn}_3$ phase, having strong interfacial bonding with the Mg-Zn matrix, could inhibit the electrolyte (*i.e.*, r-SBF) from seeping into the struts, while the poor interfacial bonding between the $\text{Ca}_4\text{P}_2\text{O}$ phase and the Mg-Zn matrix increased the available surface area that directly contacted the electrolyte. Mg-Zn/10TCP and Mg-Zn/15TCP with higher volume fractions of the $\text{Ca}_4\text{P}_2\text{O}$ phase, therefore, had more initiation sites for corrosion in the struts, as compared to Mg-Zn/5TCP at the beginning of *in vitro* immersion.

During *in vitro* degradation, hydrogen was produced through a cathodic reaction, resulting in a local alkaline environment. The alkalinity of the local solution induced the precipitation of the corrosion products. The formation of magnesium hydroxide ($\text{Mg}(\text{OH})_2$) on the surface may act as a protective layer against further corrosion. Although the formation of the stable ZnO phase (Figure 5.7 and Figure S5.11) might stabilize this corrosion layer [32], $\text{Mg}(\text{OH})_2$ could react with Cl^- in r-SBF, resulting in its dissolution and the generation of cracks in the layer (Figure S5.11a). Nevertheless, it was interesting to find out that the stable $\text{Ca}_2\text{Mg}_6\text{Zn}_3$ phase in the corrosion layer could inhibit crack propagation and maintain the integrity of the corrosion layer, thereby providing prolonged protection for the scaffold substrates (arrow in Figure S5.11a). Therefore, the corrosion rates of the Mg-Zn/5TCP and Mg-Zn/10TCP groups decreased at the beginning of the *in vitro* degradation and then increased at days 14 and 7 (Figure 5.5d), respectively, when the $\text{Ca}_2\text{Mg}_6\text{Zn}_3$ phase fell off. The formed protective layer provided favorable sites for the nucleation and deposition of Ca- and P-containing compounds.

A higher Ca ion concentration was, indeed, detected in the medium collected after the *in vitro* immersion tests of the scaffolds with a higher β -TCP content (Figure S5.12), indicating an intensified rate of release of Ca ions from the composite scaffolds. We speculated that Ca ions might be released from the Mg-Zn matrix during the dissolution of the composite scaffolds, since it was found that Ca atoms diffused into the Mg-Zn matrix during sintering and were uniformly distributed there (Figure 5.4A and B). During

in vitro degradation, with Ca being saturated locally and in the alkaline microenvironment, carbonate and apatite could form and continuously grow on the previously formed protective layer, as mentioned above. The presence of a notable number of Mg ions could inhibit the HA formation, but it could also stabilize more acidic hydrated apatite compounds, such as brushite [59, 60]. That is why brushite was detected on the biodegraded scaffolds during degradation. After 14 d of biodegradation, brushite was difficult to be detected and the corrosion products were mainly $\text{Mg}(\text{OH})_2$ (Figure 5.7 and S9). This could be because the $\text{PO}_4^{2-}/\text{HPO}_4^-$ ions in the surrounding solution had been exhausted by forming apatite compounds, while $\text{Mg}(\text{OH})_2$ and CaCO_3 continued to be deposited.

Having discussed the biodegradation behavior of the composite scaffolds at the micro level, it is important to consider the macro-scale mechanisms as well. Despite the benefits of a porous structure in allowing bone ingrowth, it remains a major challenge to introduce porosity into a Mg-based material, given that it increases its corrosion rate as compared to a bulk Mg counterpart [61-67] due to the increase in surface area. In this study, however, the *in vitro* biodegradation rates of the all three groups of Mg-Zn/TCP (*i.e.*, 0.5-2.3 mm/y, porosity: 48%-55%) were lower than or similar to those of near-bulk materials with similar compositions (*i.e.*, 0.6-15 mm/y [68-72]). Unlike other traditional manufacturing techniques [68-72] and the recently reported binder jet AM technique [62], extrusion-based 3D printing technique allows for the fabrication of geometrically ordered porous Mg structures, which could then be used to adjust the biodegradation behavior of the scaffolds. The structures featured in this study were furnished with struts that had an angle of 90° at their intersections, which limited the diffusion of Mg^{2+} and OH^- ions, especially in the central region of the scaffolds. The corrosion products, including $\text{Mg}(\text{OH})_2$, ZnO and brushite, formed immediately between the struts in the local alkaline environment (Figure 5.6, S5 and S7). Given the stability of the corrosion products, as mentioned above, and the limited flowability of the electrolyte, the formed corrosion products were entrapped inside the scaffolds (Figure 5.5a, S3a and S4a), leading to an increase in the total volume of the scaffolds (including the volume of biodegradation products) and a decrease in porosity (Figure 5.5, S3 and S4) during most of the *in vitro* degradation period. The entrapped corrosion products in the pores of the scaffolds acted as a highly protective barrier, and also helped maintain the integrity of the scaffolds, thereby inhibiting the further progress of the corrosion process. Therefore, the scaffolds showed a relatively low rate of biodegradation and a decreasing trend with the immersion time (Figure 5.5d). On the other hand, the accumulation of the corrosion products between the struts created narrow spaces where crevice-like corrosion might occur, accelerating the corrosion at the center of the scaffolds. Therefore, more severe corrosion was found in the central area as compared to the periphery (Figure 5.5a, S4a and S5a). These results indicate that the

design of open porous structures is of great importance in tailoring the biodegradation behavior of Mg-based materials.

5.4.3. Mechanical behavior

When choosing the strain rate for compression test, the effect of strain rate on the mechanical responses should be considered. The strain-hardening effect has indeed been found in some metallic materials, such as Ti [73, 74] and Mg [75]. At a standardized strain rate, the strain-hardening effect can be minimized in highly porous structure [76]. According to the standard ISO 13314: 2011, the initial compression strain rate should be between 10^{-3} and 10^{-2} s^{-1} . Therefore, for the highly porous Mg-Zn/TCP scaffold specimens with a height of 12 mm, a crosshead speed of 2 mm/min (corresponding to an initial strain rate of 0.003 s^{-1}) was chosen.

The uniaxial compressive stress-strain curves of the Mg-Zn/TCP specimens were similar to those of the extrusion-based 3D printed Mg-Zn scaffolds [32], starting with an initial elastic stage and followed by a strain-hardening stage (Figure 5.8). The yield strengths and Young's moduli of all the three groups of the Mg-Zn/TCP composite scaffolds were higher than those of the previously reported Mg-Zn scaffolds [32]. Remarkably, the yield strengths of the Mg-Zn/5TCP and Mg-Zn/10TCP composite scaffolds were about two times as high as the yield strength of the Mg-Zn scaffolds. First, the significant enhancements in strength could be attributed to the strong interfacial bonding between the Mg-Zn matrix and $Ca_2Mg_6Zn_3$ phase, and the higher nanohardness of the newly formed phases (55.1 GPa) as compared with the nanohardness of the Mg-Zn matrix (43.0 GPa). The load could, therefore, be effectively transferred from the Mg-based matrix to the second phase [77]. Second, the presence of the well-dispersed, micro-sized Ca_4P_2O phase in the Mg-Zn matrix may act as obstacles to dislocation movement, thereby strengthening the scaffolds [78]. On the other hand, the Ca_4P_2O phase with an irregular shape may also act as a crack initiation site when the specimens are (dynamically) loaded. Third, almost fully dense struts of Mg-Zn/5TCP and Mg-Zn/10TCP could withstand higher loads during the mechanical tests while largely avoiding the stress concentrations that resulted from micropores in the struts. In Mg-Zn/15TCP, the presence of large clusters of Ca_4P_2O as well as voids adversely affected its mechanical properties, leading to a lower yield strength and lower toughness (Supplementary material).

Bone substitutes should continue to provide sufficient mechanical support as *in vivo* biodegradation progresses and before the newly formed bone can take over the mechanical role of the scaffolds. Understanding the time-dependent evolution of the mechanical properties of biodegradable biomaterials is, therefore, of great importance. The Mg-Zn/TCP specimens developed here exhibited bone-mimicking mechanical properties during the *in vitro* degradation process, reaching the range of the trabecular

bone (*i.e.*, yield strength = 0.2 – 80 MPa; Young's modulus = 10 – 2,000 MPa) [64]. After 14 d of *in vitro* degradation, the Mg-Zn/5TCP scaffolds could still match the strength of the femoral cancellous bone (15 MPa) [79, 80], indicating that these scaffolds could provide enough mechanical support for treating femoral nonunion. The mechanical properties of Mg-Zn/5TCP and Mg-Zn/10TCP fluctuated during the *in vitro* degradation (Figure 5.8b and c), which is likely due to the competition between the dissolution of the scaffolds which leads to a decreased strength value and the formation of corrosion products that increases the strength value [32]. The corrosion products could be considered as an additional reinforcing phase at the beginning of the immersion in r-SBF (*i.e.*, the first 7 days) when the interfacial bonding between the substrate and corrosion products is still strong. Our results show that the corrosion products could not be disintegrated, when they formed in the center area of the composite scaffolds, and therefore, most of the $\text{Ca}_2\text{Mg}_6\text{Zn}_2$ phase still stayed in the original area of the struts surrounded by the corrosion products (Figure S5.11a), further contributing to strengthening the composite scaffolds. Furthermore, the formation of the corrosion products filling the micropores and the space between the struts led to a decrease in the porosity of the specimens (Figure 5.5), which contributed to higher mechanical properties. After 14 d of biodegradation, the Mg-Zn/10TCP specimens showed a lower yield strength and Young's modulus than the Mg-Zn/5TCP specimens, because the higher corrosion rate of the former resulted in a larger loss of Mg, as the *in vitro* degradation processes progressed (Figure 5.5b).

5.4.4. Biological response

Cellular adhesion is a prerequisite for cell proliferation and osteogenic differentiation [77]. The cell adhesion assay was performed by seeding preosteoblasts directly on the fabricated scaffolds. The well-spread morphology of the cells and the increased number of viable cells during the first week of culture demonstrated that the Mg-Zn/5TCP and Mg-Zn/10TCP scaffolds supported the adhesion and proliferation of the cells, as compared to the Mg-Zn scaffolds. Although the original β -TCP phase was not found in the as-sintered Mg-Zn/TCP composite scaffolds anymore, the addition of β -TCP into the Mg-Zn scaffolds was still effective in improving the early cell response. First, the Mg-Zn/TCP composite scaffolds released less zinc ions, when they were immersed in the cell culture medium (Figure S5.12). It has been shown that a too high concentration of Zn^{2+} inhibits the growth of preosteoblast, while a low concentration promotes the viability, proliferation, and migration of osteoblasts [81]. Part of the zinc originally present in the Mg matrix or in the MgZn_2 secondary phase of the Mg-Zn scaffolds was consumed for generating a more stable phase (*i.e.*, $\text{Ca}_2\text{Mg}_6\text{Zn}_3$) in the Mg-Zn/TCP composite scaffolds. As discussed above, the $\text{Ca}_2\text{Mg}_6\text{Zn}_3$ phase did not degrade or dissolve during the immersion tests, meaning that a limited number of zinc ions were released from this phase.

Consequently, while the degradation rates of Mg-Zn/5TCP and Mg-Zn/10TCP were similar to that of Mg-Zn, a smaller number of Zn^{2+} ions were released from those groups. Second, the formation of brushite on the scaffolds during initial biodegradation could stimulate cell proliferation and differentiation *in vitro* and promote the regeneration of vascularized bone *in vivo* [82]. After 14 d, however, both Mg-Zn/5TCP and Mg-Zn/10TCP showed cell growth inhibition (Figure 5.9f). This is likely because the increasing numbers of Mg, Ca_4P_2O , and $Ca_2Mg_6Zn_3$ particles that became disintegrated from the scaffolds could affect the cell response. Such submicron-sized particles are known to induce cytotoxicity in various cell lines [83]. In addition, the brushite layer was found to be covered by a $Mg(OH)_2$ layer at the later time points, which could reduce the bioactivity on the surfaces of the specimens. In an earlier *in vivo* study [11], a dense Mg-Zn/10wt% β -TCP composite material (*in vitro* biodegradation rate: 15.9 mm/y) was implanted into rabbits to evaluate its biocompatibility. It was found that the Mg^{2+} , Zn^{2+} , and Ca^{2+} ions could be metabolized in the blood with no adverse effects on the kidney, liver, or heart. As compared to the dense Mg-Zn/10 wt% β -TCP material mentioned above, the Mg-Zn/TCP specimens developed in this research had much lower biodegradation rates, which would undoubtedly be also safe for the visceral organs, if being implanted in animals.

The influences of the extracts from the Mg-Zn/5TCP and Mg-Zn/10TCP composite scaffolds on the osteogenic differentiation and mineralization of preosteoblasts were evaluated by ALP and Alizarin Red S assays, respectively (Figure 5.9g-i). Both extracts exhibited a clear effect on promoting the osteogenic differentiation and matrix mineralization, which could be because the appropriate concentrations of the released Mg, Zn, and Ca ions activated specific signaling pathways, stimulating mineralization [84-86]. The human body can regulate ion concentrations in the local environment through active transport processes, and both the degradation rate and surface condition of the scaffolds may change in a more complex microenvironment *in vivo*. *In vivo* studies should, therefore, be performed on the extrusion-based 3D printed Mg-Zn/TCP specimens to better understand their biological responses.

5.5. Conclusions

We fabricated porous Mg-Zn/ β -TCP composite scaffolds using the extrusion-based 3D printing technique for the first time and characterized their *in vitro* properties for potential use as bone substitutes. Three groups of the porous composite scaffolds, *i.e.*, Mg-Zn/5TCP, Mg-Zn/10TCP, and Mg-Zn/15TCP, were successfully fabricated. The ink formulations were optimized to balance the homogeneity of bioceramic particles with appropriate viscoelastic properties and, thus, printability. The dispersion of β -TCP in the Mg-Zn/5TCP inks and the resulting scaffolds were the most uniform. The fabricated Mg-

Zn/TCP scaffolds presented interconnected pore networks with accurately controlled macropores. The relative densities of the materials making up the struts were higher than 99% in the Mg-Zn/5TCP and Mg-Zn/10TCP specimens, reaching the level usually only achieved through PBF AM. During sintering, the added β -TCP reacted with the Mg-Zn matrix, producing two new phases, namely $\text{Ca}_2\text{Mg}_6\text{Zn}_3$ and $\text{Ca}_4\text{P}_2\text{O}$, that greatly affected the properties and biodegradation behavior of the composites. The Mg-Zn/5TCP specimens showed a decreased *in vitro* rate of biodegradation (*i.e.*, 0.5 mm/y) as compared with Mg-Zn. This rate falls within the desired range of biodegradation for ideal bone substitutes. As for the Mg-Zn/15TCP specimens, the inhomogeneous dispersion of β -TCP deteriorated their biodegradation behavior. The yield strengths of the Mg-Zn/5TCP and Mg-Zn/10TCP composite scaffolds were about two times as high as that of the Mg-Zn scaffolds. The mechanical properties of the composite scaffolds fluctuated over the biodegradation period of 28 d, but the strengths and elastic moduli remained in the range of the mechanical properties of the cancellous bone. The direct cultures of preosteoblasts on the Mg-Zn/5TCP and Mg-Zn/10TCP specimens showed significantly improved cytocompatibility, as compared to Mg-Zn. The cells spread very well on the composite scaffolds with a brushite layer. The ALP activity was also significantly higher for the composites as compared to the control group (*i.e.*, Mg-Zn alloy). The presented results clearly show that the Mg-based composite scaffolds developed in this research satisfy many of the requirements of ideal bone substitutes and should be further developed towards potential clinical application.

References

- [1] Q. Zhang, W. Zhang, Z. Zhang, L. Zhang, H. Chen, M. Hao, J. Deng, P. Tang, Femoral nonunion with segmental bone defect treated by distraction osteogenesis with monolateral external fixation, *J. Orthop. Surg. Res.* 12 (2017) 183.
- [2] L. Ye, J. Xu, J. Mi, X. He, Q. Pan, L. Zheng, H. Zu, Z. Chen, B. Dai, X. Li, Q. Pang, L. Zou, L. Zhou, L. Huang, W. Tong, G. Li, L. Qin, Biodegradable magnesium combined with distraction osteogenesis synergistically stimulates bone tissue regeneration via CGRP-FAK-VEGF signaling axis, *Biomaterials.* 275 (2021) 120984.
- [3] F. Witte, The history of biodegradable magnesium implants: a review, *Acta Biomater.* 6 (2010) 1680-1692.
- [4] L. H. N. Dang, Y. K. Kim, S. Y. Kim, K. J. Lim, K. Bode, M. H. Lee, K. B. Lee, Radiographic and histologic effects of bone morphogenetic protein-2/hydroxyapatite within bioabsorbable magnesium screws in a rabbit model, *J. Orthop. Surg. Res.* 14 (2019) 117.
- [5] V. K. Bommala, M. G. Krishna, C. T. Rao, Magnesium matrix composites for biomedical applications: A review, *J. Magnes. Alloy.* 7 (2019) 72-79.
- [6] M. Shahin, K. Munir, C. Wen, Y. Li, Magnesium matrix nanocomposites for orthopedic applications: A review from mechanical, corrosion, and biological perspectives, *Acta Biomater.* 96 (2019) 1-19.
- [7] R. Radha, D. Sreekanth, Insight of magnesium alloys and composites for orthopedic implant applications - A review, *J. Magnes. Alloy.* 5 (2017) 286-312.
- [8] S. Shadanbaz, G. J. Dias, Calcium phosphate coatings on magnesium alloys for biomedical applications: A review, *Acta Biomater.* 8 (2012) 20-30.
- [9] H. Hornberger, S. Virtanen, A. R. Boccaccini, Biomedical coatings on magnesium alloys - A review, *Acta Biomater.* 8 (2012) 2442-2455.
- [10] K. Kusnierczyk, M. Basista, Recent advances in research on magnesium alloys and magnesium-calcium phosphate composites as biodegradable implant materials, *J. Biomater. Appl.* 31 (2017) 878-900.
- [11] K. Yu, L. J. Chen, J. Zhao, S. J. Li, Y. L. Dai, Q. Huang, Z. M. Yu, In vitro corrosion behavior and in vivo biodegradation of biomedical β -Ca₃(PO₄)₂/Mg-Zn composites, *Acta Biomater.* 8 (2012) 2845-2855.
- [12] X. L. Ma, L. H. Dong, X. Wang, Microstructure, mechanical property and corrosion behavior of co-continuous β -TCP/MgCa composite manufactured by suction casting, *Mater. Des.* 56 (2014) 305-312.
- [13] X. Wang, L. H. Dong, J. T. Li, X. L. Li, X. L. Ma, Y. F. Zheng, Microstructure, mechanical property and corrosion behavior of interpenetrating (HA+ β -TCP)/MgCa composite fabricated by suction casting, *Mater. Sci. Eng. C-Mater. Biol. Appl.* 33 (2013) 4266-4273.
- [14] H. R. Zheng, Z. Li, C. You, D. B. Liu, M. F. Chen, Effects of MgO modified β -TCP nanoparticles on the microstructure and properties of β -TCP/Mg-Zn-Zr composites, *Bioact. Mater.* 2 (2017) 1-9.
- [15] D. B. Liu, Y. B. Zuo, W. Y. Meng, M. F. Chen, Z. Fan, Fabrication of biodegradable nano-sized β -TCP/Mg composite by a novel melt shearing technology, *Mater. Sci. Eng. C-Mater. Biol. Appl.* 32 (2012) 1253-1258.
- [16] Z. Cui, Y. Zhang, Y. Cheng, D. Gong, W. Wang, Microstructure, mechanical, corrosion properties and cytotoxicity of betacalcium polyphosphate reinforced ZK61 magnesium

alloy composite by spark plasma sintering, *Mater. Sci. Eng. C-Mater. Biol. Appl.* 99 (2019) 1035-1047.

[17] Y. Zhang, H. Yang, S. Lei, S. Zhu, J. Wang, Y. Sun, S. Guan, Preparation of biodegradable Mg/ β -TCP biofunctional gradient materials by friction stir processing and pulse reverse current electrodeposition, *Acta Metall. Sin.-Engl. Lett.* 33 (2019) 103-114.

[18] A. A. Zadpoor, Bone tissue regeneration: the role of scaffold geometry, *Biomater. Sci.* 3 (2015) 231-245.

[19] Y. Li, P. Pavanram, J. Zhou, K. Lietaert, P. Taheri, W. Li, H. San, M. A. Leeflang, J. M. C. Mol, H. Jahr, A. A. Zadpoor, Additively manufactured biodegradable porous zinc, *Acta Biomater.* 101 (2020) 609-623.

[20] A. Zadpoor, Current trends in metallic orthopedic biomaterials: from additive manufacturing to bio-functionalization, infection prevention, and beyond, *Int. J. Mol. Sci.* 19 (2018) 2684.

[21] A. P. Moreno Madrid, S. M. Vrech, M. A. Sanchez, A. P. Rodriguez, Advances in additive manufacturing for bone tissue engineering scaffolds, *Mater. Sci. Eng. C-Mater. Biol. Appl.* 100 (2019) 631-644.

[22] Y. Zamani, H. Ghazanfari, G. Erabi, A. Moghanian, B. Fakić, S. M. Hosseini, B. P. M. Fakić, A review of additive manufacturing of Mg-based alloys and composite implants, *J. Compos. Compd.* 2 (2021) 71-83.

[23] Y. Yin, Q. Huang, L. Liang, X. Hu, T. Liu, Y. Weng, T. Long, Y. Liu, Q. Li, S. Zhou, H. Wu, In vitro degradation behavior and cytocompatibility of ZK30/bioactive glass composites fabricated by selective laser melting for biomedical applications, *J. Alloys Compd.* 785 (2019) 38-45.

[24] C. J. Shuai, Y. Z. Zhou, Y. W. Yang, P. Feng, L. Liu, C. X. He, M. C. Zhao, S. Yang, C. D. Gao, P. Wu, Biodegradation resistance and bioactivity of hydroxyapatite enhanced Mg-Zn composites via selective laser melting, *Materials.* 10 (2017) 307-319.

[25] Y. Yang, C. Lu, L. Shen, Z. Zhao, S. Peng, C. Shuai, In-situ deposition of apatite layer to protect Mg-based composite fabricated via laser additive manufacturing, *J. Magnes. Alloy.* (2021), in press.

[26] Y. Yang, C. Lu, S. Peng, L. Shen, D. Wang, F. Qi, C. Shuai, Laser additive manufacturing of Mg-based composite with improved degradation behaviour, *Virtual Phys. Prototy.* 15 (2020) 278-293.

[27] Y. Li, J. Zhou, P. Pavanram, M. A. Leeflang, L. I. Fockaert, B. Pouran, N. Tumer, K. U. Schroder, J. M. C. Mol, H. Weinans, H. Jahr, A. A. Zadpoor, Additively manufactured biodegradable porous magnesium, *Acta Biomater.* 67 (2018) 378-392.

[28] J. Dong, Y. Li, P. Lin, M. A. Leeflang, S. Van Asperen, K. Yu, N. Tumer, B. Norder, A. A. Zadpoor, J. Zhou, Solvent-cast 3D printing of magnesium scaffolds, *Acta Biomater.* 114 (2020) 497-514.

[29] H. S. Ma, T. Li, Z. G. Huan, M. Zhang, Z. Z. Yang, J. W. Wang, J. Chang, C. T. Wu, 3D printing of high-strength bioscaffolds for the synergistic treatment of bone cancer, *NPG Asia Mater.* 10 (2018) 31-44.

[30] J. Li, C. Deng, W. Liang, F. Kang, Y. Bai, B. Ma, C. Wu, S. Dong, Mn-containing bioceramics inhibit osteoclastogenesis and promote osteoporotic bone regeneration via scavenging ROS, *Bioact. Mater.* 6 (2021) 3839-3850.

- [31] J. Dong, N. Tümer, N.E. Putra, J. Zhu, Y. Li, M.A. Leeflang, P. Taheri, L.E. Fratila-Apachitei, J.M.C. Mol, A.A. Zadpoor, J. Zhou, Extrusion-based 3D printed magnesium scaffolds with multifunctional MgF₂ and MgF₂-CaP coatings, *Biomater. Sci.* 9 (2021) 7159-7182.
- [32] J. Dong, N. Tümer, M. A. Leeflang, P. Taheri, L. E. Fratila-Apachitei, J. M. C. Mol, A. A. Zadpoor, J. Zhou, Extrusion-based additive manufacturing of Mg-Zn alloy scaffolds, *J. Magnes. Alloy.* 10 (2021) 2491-2509.
- [33] F. Khorashadizade, S. Abazari, M. Rajabi, H. R. Bakhsheshi-Rad, A. F. Ismail, S. Sharif, S. Ramakrishna, F. Berto, Overview of magnesium-ceramic composites: Mechanical, corrosion and biological properties, *J. Mater. Res. Technol.* 15 (2021) 6034-6066.
- [34] G. Parande, V. Manakari, H. Gupta, M. Gupta, Magnesium- β -tricalcium phosphate composites as a potential orthopedic implant: a mechanical/damping/immersion perspective, *Metals.* 8 (2018) 343-360.
- [35] Y. Wang, Z. Wu, H. Zhou, Z. Liao, H. Zhang, Corrosion properties in a simulated body fluid of Mg/ β -TCP composites prepared by powder metallurgy, *Int. J. Miner. Metall.* 19 (2012) 1040-1044.
- [36] R. Del Campo, B. Savoini, A. Munoz, M. A. Monge, G. Garces, Mechanical properties and corrosion behavior of Mg-HAP composites, *Journal of the Mechanical Behavior of Biomedical Materials.* 39 (2014) 238-246.
- [37] M. Rashad, F. Pan, A. Tang, M. Asif, S. Hussain, J. Gou, J. Mao, Improved strength and ductility of magnesium with addition of aluminum and graphene nanoplatelets (Al+GNPs) using semi powder metallurgy method, *J. Ind. Eng. Chem.* 23 (2015) 243-250.
- [38] M. Rashad, F. Pan, A. Tang, Y. Lu, M. Asif, S. Hussain, J. She, J. Gou, J. Mao, Effect of graphene nanoplatelets (GNPs) addition on strength and ductility of magnesium-titanium alloys, *J. Magnes. Alloy.* 1 (2013) 242-248.
- [39] M. Rashad, F. Pan, H. Hu, M. Asif, S. Hussain, J. She, Enhanced tensile properties of magnesium composites reinforced with graphene nanoplatelets, *Mater. Sci. Eng. A-Struct. Mater. Prop. Microstruct. Process.* 630 (2015) 36-44.
- [40] D. B. Liu, Y. Huang, P. B. Prangnell, Microstructure and performance of a biodegradable Mg-1Ca-2Zn-1TCP composite fabricated by combined solidification and deformation processing, *Mater. Lett.* 82 (2012) 7-9.
- [41] Y. Huang, D. B. Liu, L. Anguilano, C. You, M. F. Chen, Fabrication and characterization of a biodegradable Mg-2Zn-0.5Ca/1 beta-TCP composite, *Mater. Sci. Eng. C-Mater. Biol. Appl.* 54 (2015) 120-132.
- [42] G. A. Yakaboylu, E. M. Sabolsky, Determination of a homogeneity factor for composite materials by a microstructural image analysis method, *J. Microsc.* 266 (2017) 263-272.
- [43] N. Barekar, S. Tzamtzis, B. K. Dhindaw, J. Patel, N. Hari Babu, Z. Fan, Processing of aluminum-graphite particulate metal matrix composites by advanced shear technology, *J. Mater. Eng. Perform.* 18 (2009) 1230-1240.
- [44] V. Karageorgiou, D. Kaplan, Porosity of 3D biomaterial scaffolds and osteogenesis, *Biomaterials.* 26 (2005) 5474-5491.
- [45] A. Oyane, Hyun. Kim, T. Furuya, T. Kokubo, T. Miyazaki, T. Nakamura, Preparation and assessment of revised simulated body fluids, *J. Biomed. Mater. Res. Part A.* 65A (2003) 188-195.

- [46] D. H. Napper, Steric stabilization, *J. Colloid Interface Sci.* 58 (1977) 390-407.
- [47] Melvin D. Croucher, M. L. Hair, Effect of free volume on the steric stabilization of nonaqueous latex dispersions, *J. Colloid Interface Sci.* 81 (1981) 257-265.
- [48] S. Elbasuney, Sustainable steric stabilization of colloidal titania nanoparticles, *Appl. Surf. Sci.* 409 (2017) 438-447.
- [49] K. Narita, E. Kobayashi, T. Sato, Sintering behavior and mechanical properties of magnesium/beta-tricalcium phosphate composites sintered by spark plasma sintering, *Mater. Trans.* 57 (2016) 1620-1627.
- [50] S. Naddafdezfuli, J. C. Brouwer, J. M. C. Mol, F. C. T. Van Der Helm, J. Zhou, Biodegradation and mechanical behavior of an advanced bioceramic-containing Mg matrix composite synthesized through in-situ solid-state oxidation, *Journal of the Mechanical Behavior of Biomedical Materials.* 80 (2018) 209-221.
- [51] K. Narita, S. Hiromoto, E. Kobayashi, T. Sato, Effects of incorporating β -tricalcium phosphate with reaction sintering into Mg-based composites on degradation and mechanical integrity, *Metals.* 11 (2021) 227-243.
- [52] K. Matsunaga, T. Kubota, K. Toyoura, A. Nakamura, First-principles calculations of divalent substitution of Ca(2+) in tricalcium phosphates, *Acta Biomater.* 23 (2015) 329-337.
- [53] M. Salehi, S. Maleksaedi, M. a. B. Sapari, M. L. S. Nai, G. K. Meenashisundaram, M. Gupta, Additive manufacturing of magnesium-zinc-zirconium (ZK) alloys via capillary-mediated binderless three-dimensional printing, *Mater. Des.* 169 (2019) 107683.
- [54] G. Levi, S. Avraham, A. Zilberov, M. Bamberger, Solidification, solution treatment and age hardening of a Mg-1.6wt.% Ca-3.2wt.% Zn alloy, *Acta Mater.* 54 (2006) 523-530.
- [55] P. Jiang, C. Blawert, M. L. Zheludkevich, The corrosion performance and mechanical properties of Mg-Zn based alloys—A review, *Corros. Mater. Degrad.* 1 (2020) 92-158.
- [56] C. Gao, M. Yao, S. Li, P. Feng, S. Peng, C. Shuai, Highly biodegradable and bioactive Fe-Pd-bredigite biocomposites prepared by selective laser melting, *J. Adv. Res.* 20 (2019) 91-104.
- [57] H. Li, S. Qin, Y. Ma, J. Wang, Y. Liu, J. Zhang, Effects of Zn content on the microstructure and the mechanical and corrosion properties of as-cast low-alloyed Mg-Zn-Ca alloys, *Int. J. Miner. Metall.* 25 (2018) 800-809.
- [58] D. Zander, N. A. Zumdick, Influence of Ca and Zn on the microstructure and corrosion of biodegradable Mg-Ca-Zn alloys, *Corros. Sci.* 93 (2015) 222-233.
- [59] Q. Dong, X. Zhou, Y. Feng, K. Qian, H. Liu, M. Lu, C. Chu, F. Xue, J. Bai, Insights into self-healing behavior and mechanism of dicalcium phosphate dihydrate coating on biomedical Mg, *Bioact. Mater.* 6 (2021) 158-168.
- [60] M. H. Salimi, J. C. Heughebaert, G. H. Nancollas, Crystal growth of calcium phosphates in the presence of magnesium ions, *Langmuir.* 1 (1985) 119-122.
- [61] E. Aghion, Y. Perez, Effects of porosity on corrosion resistance of Mg alloy foam produced by powder metallurgy technology, *Mater. Charact.* 96 (2014) 78-83.
- [62] K. X. Kuah, D. J. Blackwood, W. K. Ong, M. Salehi, H. L. Seet, M. L. S. Nai, S. Wijesinghe, Analysis of the corrosion performance of binder jet additive manufactured magnesium alloys for biomedical applications, *J. Magnes. Alloy.* 10 (2021) 1296-1310.

- [63] J. Capek, D. Vojtech, Properties of porous magnesium prepared by powder metallurgy, *Mater. Sci. Eng. C-Mater. Biol. Appl.* 33 (2013) 564-569.
- [64] M. Yazdimamaghani, M. Razavi, D. Vashae, K. Moharamzadeh, A. R. Boccaccini, L. Tayebi, Porous magnesium-based scaffolds for tissue engineering, *Mater. Sci. Eng. C-Mater. Biol. Appl.* 71 (2017) 1253-1266.
- [65] M. Q. Cheng, T. Wahafu, G. F. Jiang, W. Liu, Y. Q. Qiao, X. C. Peng, T. Cheng, X. L. Zhang, G. He, X. Y. Liu, A novel open-porous magnesium scaffold with controllable microstructures and properties for bone regeneration, *Sci. Rep.* 6 (2016) 24134.
- [66] H. Y. Zhuang, Y. Han, A. L. Feng, Preparation, mechanical properties and in vitro biodegradation of porous magnesium scaffolds, *Mater. Sci. Eng. C-Mater. Biol. Appl.* 28 (2008) 1462-1466.
- [67] R. Zeng, W. Dietzel, F. Witte, N. Hort, C. Blawert, Progress and challenge for magnesium alloys as biomaterials, *Adv. Eng. Mater.* 10 (2008) B3-B14.
- [68] D. Liu, G. Xu, S. S. Jamali, Y. Zhao, M. Chen, T. Jurak, Fabrication of biodegradable HA/Mg-Zn-Ca composites and the impact of heterogeneous microstructure on mechanical properties, in vitro degradation and cytocompatibility, *Bioelectrochemistry.* 129 (2019) 106-115.
- [69] Z. Cui, W. Li, L. Cheng, D. Gong, W. Cheng, W. Wang, Effect of nano-HA content on the mechanical properties, degradation and biocompatible behavior of Mg-Zn/HA composite prepared by spark plasma sintering, *Mater. Charact.* 151 (2019) 620-631.
- [70] Y. Deng, Y. Yang, C. Gao, P. Feng, W. Guo, C. He, J. Chen, C. Shuai, Mechanism for corrosion protection of beta-TCP reinforced ZK60 via laser rapid solidification, *Int. J. Bioprinting.* 4 (2018) 124.
- [71] Y. Yan, Y. Kang, D. Li, K. Yu, T. Xiao, Y. Deng, H. Dai, Y. Dai, H. Xiong, H. Fang, Improvement of the mechanical properties and corrosion resistance of biodegradable beta-Ca₃(PO₄)₂/Mg-Zn composites prepared by powder metallurgy: the adding beta-Ca₃(PO₄)₂, hot extrusion and aging treatment, *Mater. Sci. Eng. C-Mater. Biol. Appl.* 74 (2017) 582-596.
- [72] Q. Yuan, Y. Huang, D. Liu, M. Chen, Effects of solidification cooling rate on the corrosion resistance of a biodegradable beta-TCP/Mg-Zn-Ca composite, *Bioelectrochemistry.* 124 (2018) 93-104.
- [73] S. L. Sing, W. Y. Yeong, F. E. Wiria, B. Y. Tay, Characterization of titanium lattice structures fabricated by selective laser melting using an adapted compressive test method, *Experimental Mechanics.* 56 (2016) 735-748.
- [74] C. Chang, J. Huang, X. Yan, Q. Li, M. Liu, S. Deng, J. Gardan, R. Bolot, M. Chemkhi, H. Liao, Microstructure and mechanical deformation behavior of selective laser melted Ti6Al4V ELI alloy porous structures, *Mater. Lett.* 277 (2020) 128366.
- [75] S. M. Chowdhury, D. L. Chen, S. D. Bhole, X. Cao, E. Powidajko, D. C. Weckman, Y. Zhou, Tensile properties and strain-hardening behavior of double-sided arc welded and friction stir welded AZ31B magnesium alloy, *Materials Science and Engineering: A.* 527 (2010) 2951-2961.
- [76] N. Zou, Q. Li, Mechanical properties of lightweight porous magnesium processed through powder metallurgy, *Jom.* 70 (2018) 650-655.

- [77] H. Dieringa, Applications: magnesium-based metal matrix composites (MMCs), in *Fundamentals of Magnesium Alloy Metallurgy*, edited by Mihriban Pekguleryuz, Karl Kainer, and Aslan Kaya, 2013, pp. 317-341.
- [78] A. L. Feng, Y. Han, Mechanical and in vitro degradation behavior of ultrafine calcium polyphosphate reinforced magnesium-alloy composites, *Mater. Des.* 32 (2011) 2813-2820.
- [79] E. Perilli, M. Baleani, C. Ohman, R. Fognani, F. Baruffaldi, M. Viceconti, Dependence of mechanical compressive strength on local variations in microarchitecture in cancellous bone of proximal human femur, *J. Biomech.* 41 (2008) 438-446.
- [80] A. Liu, M. Sun, H. Shao, X. Yang, C. Ma, D. He, Q. Gao, Y. Liu, S. Yan, S. Xu, Y. He, J. Fu, Z. Gou, The outstanding mechanical response and bone regeneration capacity of robocast dilute magnesium-doped wollastonite scaffolds in critical size bone defects, *J Mater Chem B.* 4 (2016) 3945-3958.
- [81] H. Yang, B. Jia, Z. Zhang, X. Qu, G. Li, W. Lin, D. Zhu, K. Dai, Y. Zheng, Alloying design of biodegradable zinc as promising bone implants for load-bearing applications, *Nat. Commun.* 11 (2020) 401.
- [82] W. Wang, G. Jia, Q. Wang, H. Huang, X. Li, H. Zeng, W. Ding, F. Witte, C. Zhang, W. Jia, G. Yuan, The in vitro and in vivo biological effects and osteogenic activity of novel biodegradable porous Mg alloy scaffolds, *Mater. Des.* 189 (2020) 108514.
- [83] A. L. Di Virgilio, M. Reigosa, M. F. De Mele, Biocompatibility of magnesium particles evaluated by in vitro cytotoxicity and genotoxicity assays, *J. Biomed. Mater. Res. Part B.* 99 (2011) 111-119.
- [84] D. Li, D. Zhang, Q. Yuan, L. Liu, H. Li, L. Xiong, X. Guo, Y. Yan, K. Yu, Y. Dai, T. Xiao, Y. Li, C. Wen, In vitro and in vivo assessment of the effect of biodegradable magnesium alloys on osteogenesis, *Acta Biomater.* 141 (2021) 454-465.
- [85] Y. Yu, K. Liu, Z. Wen, W. Liu, L. Zhang, J. Su, Double-edged effects and mechanisms of Zn²⁺ microenvironments on osteogenic activity of BMSCs: osteogenic differentiation or apoptosis, *RSC Adv.* 10 (2020) 14915-14927.
- [86] H. Gu, F. Guo, X. Zhou, L. Gong, Y. Zhang, W. Zhai, L. Chen, L. Cen, S. Yin, J. Chang, L. Cui, The stimulation of osteogenic differentiation of human adipose-derived stem cells by ionic products from akermanite dissolution via activation of the ERK pathway, *Biomaterials.* 32 (2011) 7023-7033.

Supplementary material

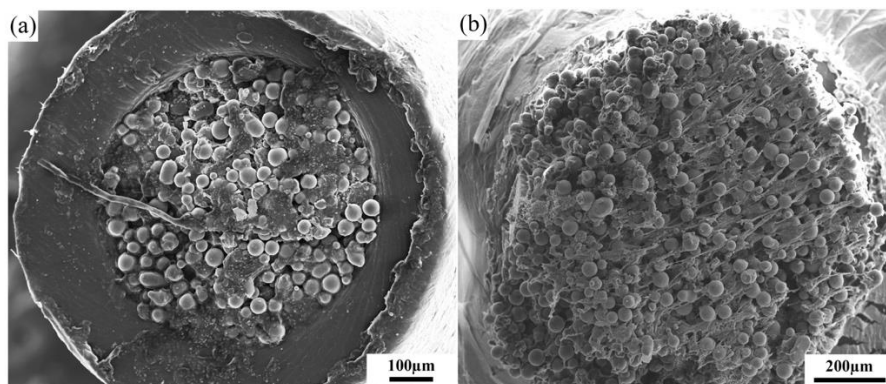


Figure S5.1 The SEM images of the cross section of the nozzle used in 3D printing: (a) printing with the Mg-Zn/10TCP_93% ink and (b) printing with the Mg-Zn/10TCP_95% ink.

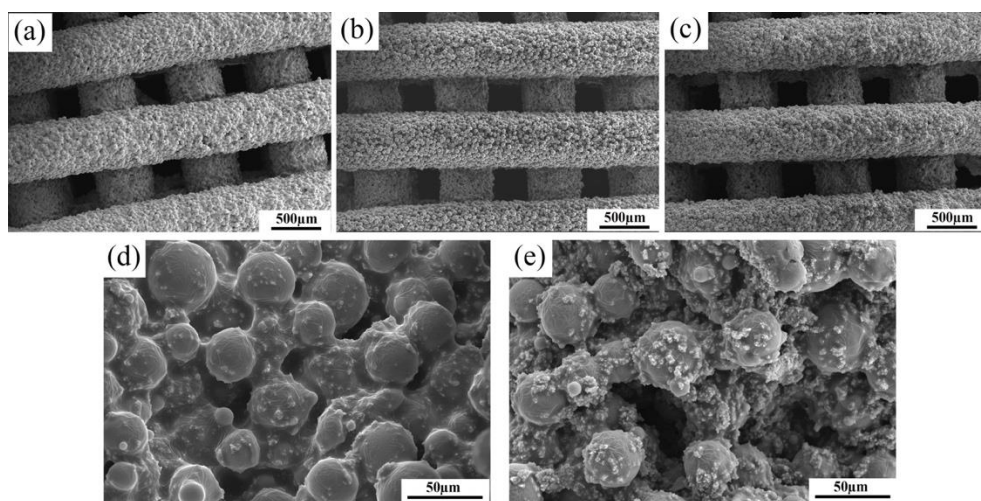


Figure S5.2 The morphologies of the as-printed composite scaffolds: (a) Mg-Zn/5TCP, (b) Mg-Zn/10TCP, (c) Mg-Zn/15TCP, and the close-up views: (d) Mg-Zn/5TCP and (e) Mg-Zn/15TCP.

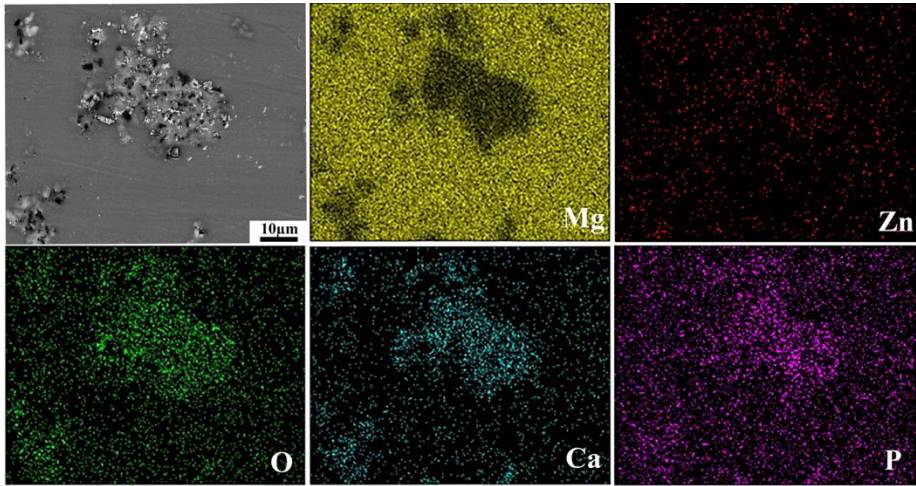


Figure S5.3 The phases and elemental distributions in the Mg-Zn/15TCP specimens.

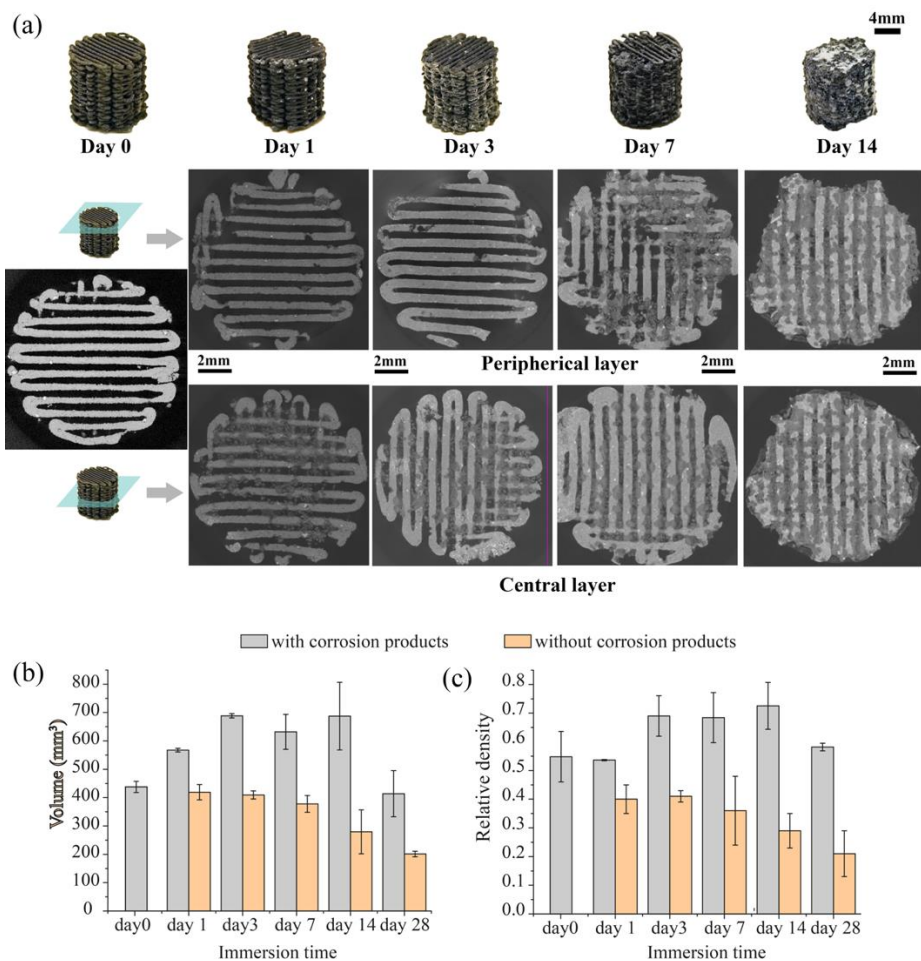


Figure S5.4 The *in vitro* degradation behavior of the Mg-Zn/5TCP specimens: (a) the macrographs and 2D images from the μ CT reconstructions, (b-c) the changes in the volumes and relative densities of the degraded scaffolds with and without corrosion products with immersion time.

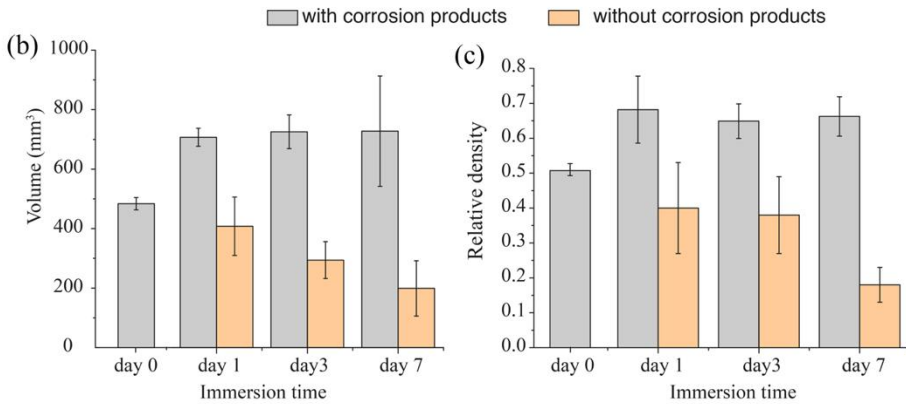
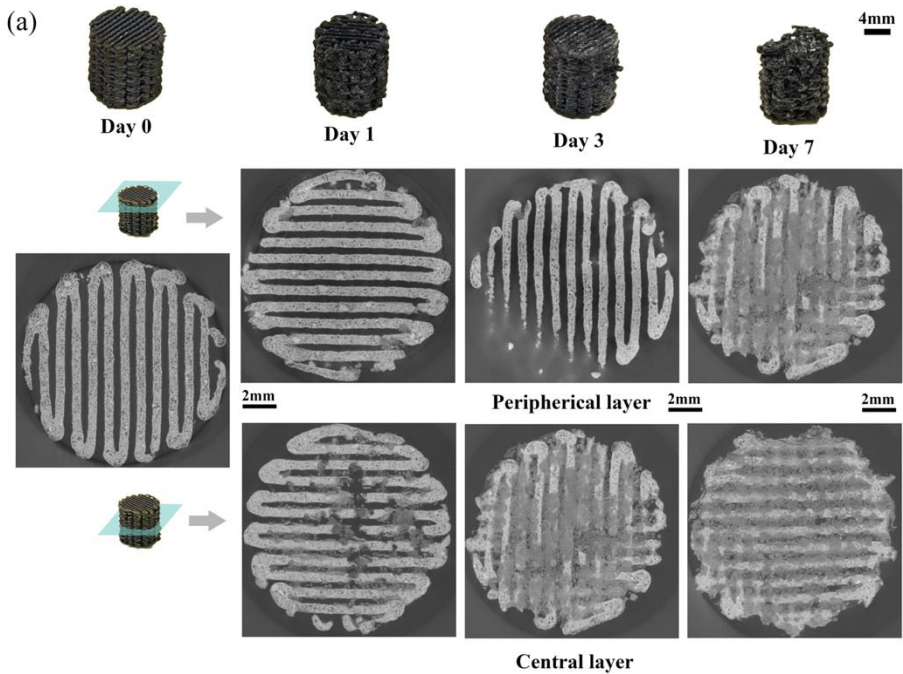


Figure S5.5 The *in vitro* biodegradation behavior of the Mg-Zn/15TCP specimens: (a) macrographs and 2D μ CT slices from the reconstructions, (b-c) the changes in the volumes and relative densities of the biodegraded scaffolds with and without corrosion products with immersion time.

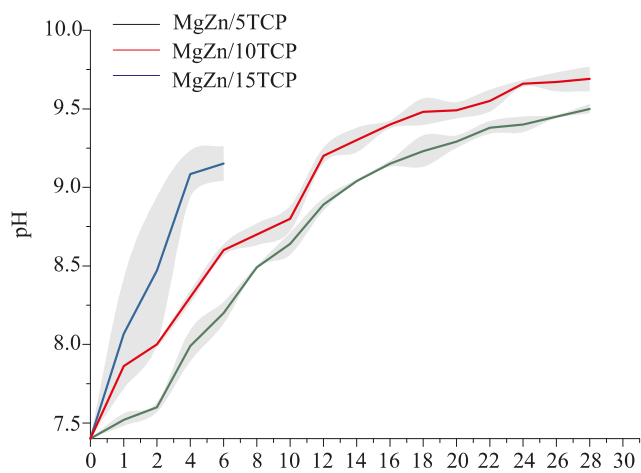


Figure S5.6 The pH variations with immersion time during the *in vitro* degradation of the Mg-Zn/TCP specimens.

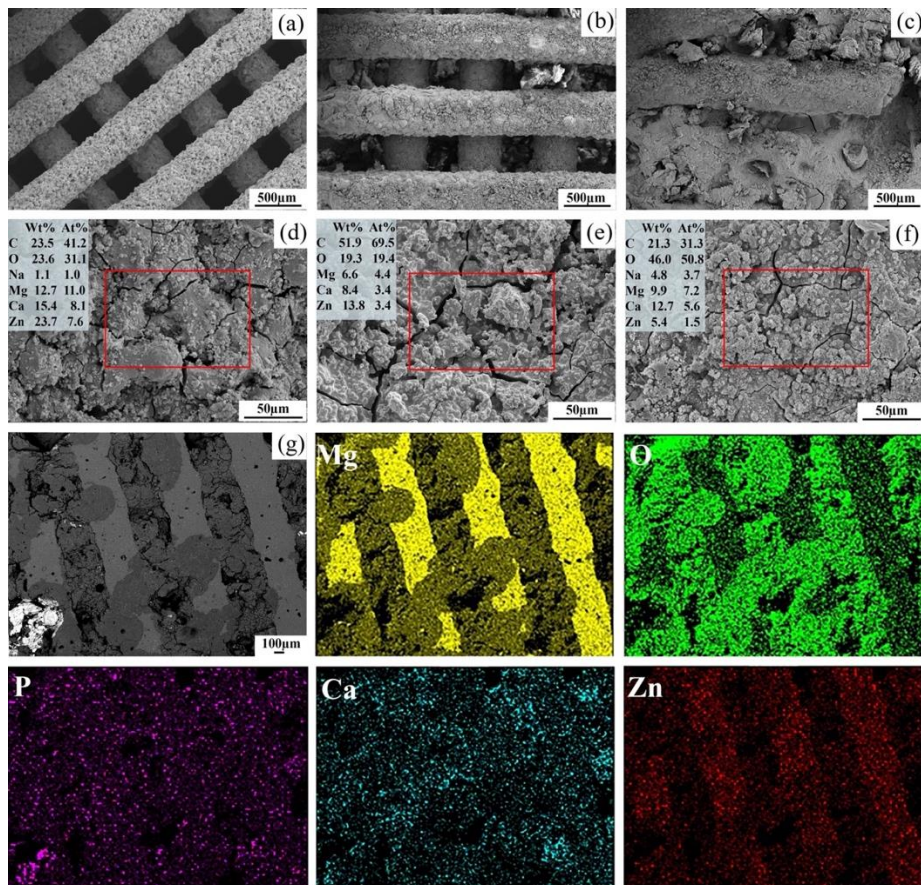


Figure S5.7 The morphologies and chemical compositions of the biodegradation products on the Mg-Zn/5TCP specimens: on the periphery after 1 d (a and d), 7 d (b and e), 14 d (c and f) of biodegradation, and (g) at the center of the scaffolds after 14 d of biodegradation and the corresponding EDS mapping. The boxed area and values indicate where the EDS analyses were performed and the corresponding elemental compositions, respectively.

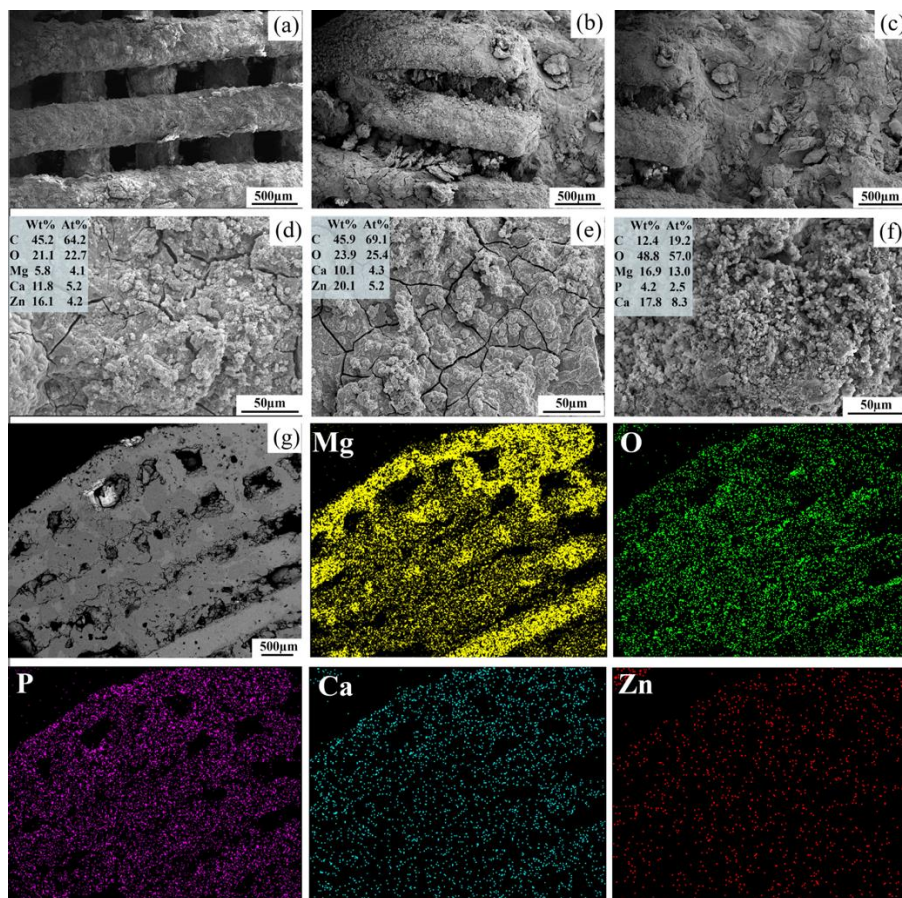


Figure S5.8 The morphologies and chemical compositions of the biodegradation products on the Mg-Zn/15TCP specimens: on the periphery after 1 d (a and d), 3 d (b and e), 7 d (c and f) of biodegradation, and (g) at the center of the scaffolds after 7 d of biodegradation and corresponding EDS mapping. The boxed area and values indicate where the EDS analyses were performed and the corresponding elemental compositions, respectively.

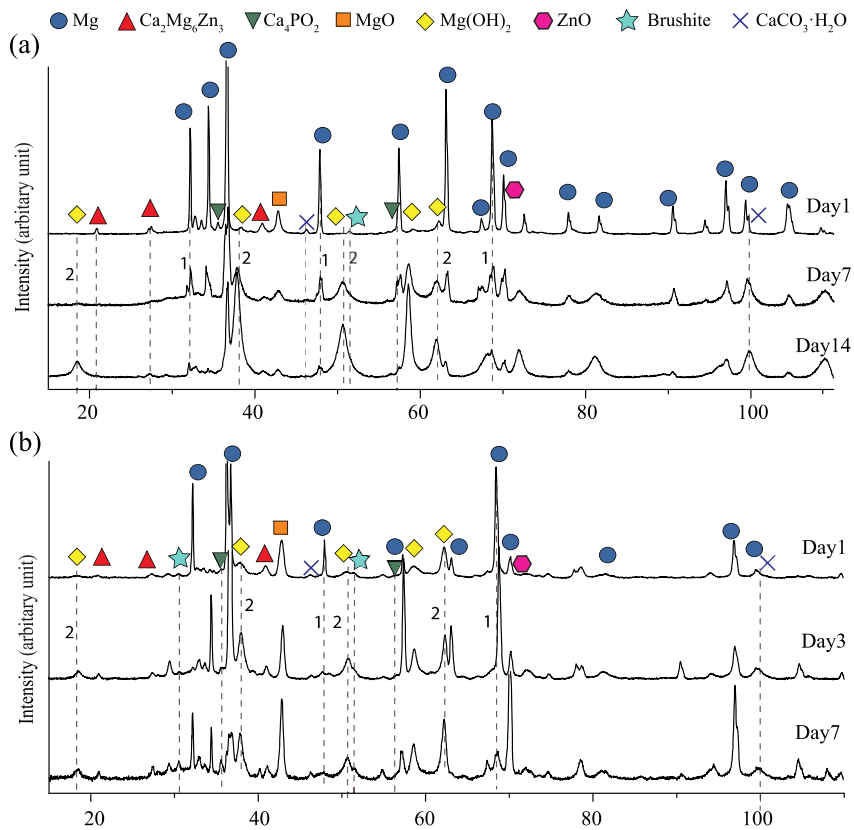


Figure S5.9 XRD patterns: (a) Mg-Zn/5TCP after 1, 7, and 14 d of biodegradation, and (b) Mg-Zn/15TCP after 1, 3, and 7 d of biodegradation.

Experimental methods for the Prestoblué assay:

The extracts of Mg-Zn/5TCP, Mg-Zn/10TCP and Mg-Zn/15TCP scaffolds were prepared by immersing the sterilized composite scaffolds in the α -MEM under the physiological conditions for 72 h. MC3T3-E1 cells (1×10^4 cells) were seeded in a 24 well plate and cultured in the α -MEM for 24 h. The α -MEM was then exchanged with the diluted extracts. The original α -MEM (without ascorbic acid, but with 10% FBS, 1% p/s) served as the negative control. After 1, 3, and 7 days of cell culture, the extracts were replaced with fresh α -MEM (without ascorbic acid, but with 10% FBS, 1% p/s) to prevent any interference between the extract and the assay. At the indicated time points, 50 μ L Prestoblué reagent was added per well, prior to incubation at 37 °C for 1 h. Absorbance values were measured using a Victor X3 microplate reader (PerkinElmer, The Netherlands) over a wavelength range of 530 – 590 nm. The average metabolic activity of the cells was calculated using:

$$\text{Metabolic activity} = \frac{\text{Absorbance (Mg specimen)}}{\text{Absorbance (negative control)}} \times 100\% \quad (1)$$

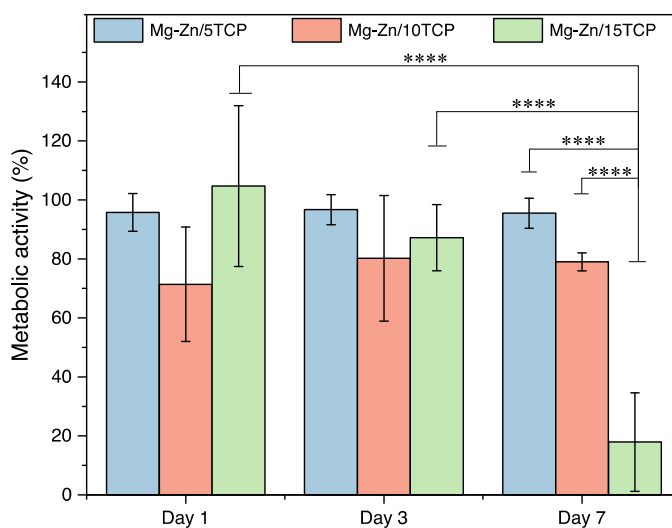


Figure S5.10 Metabolic activities of preosteoblasts cultured in the extracts of Mg-Zn/5TCP, Mg-Zn/1-TCP and Mg-Zn/15TCP.

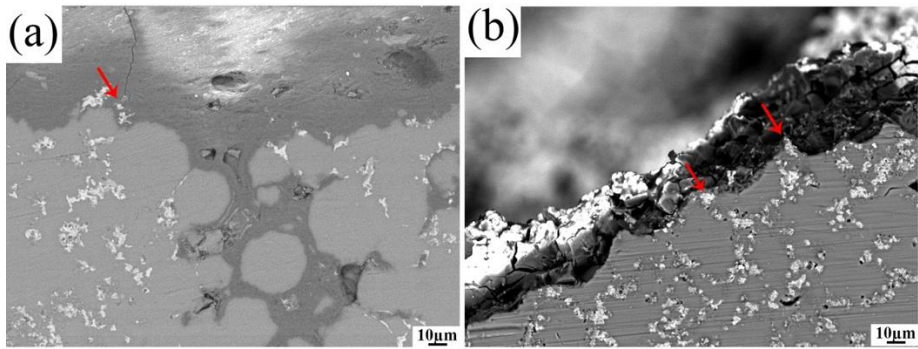


Figure S5.11 The SEM images of the biodegraded composite scaffolds: (a) Mg-Zn/5TCP after 14 d of biodegradation and (b) Mg-Zn/10TCP after 14 d of biodegradation.

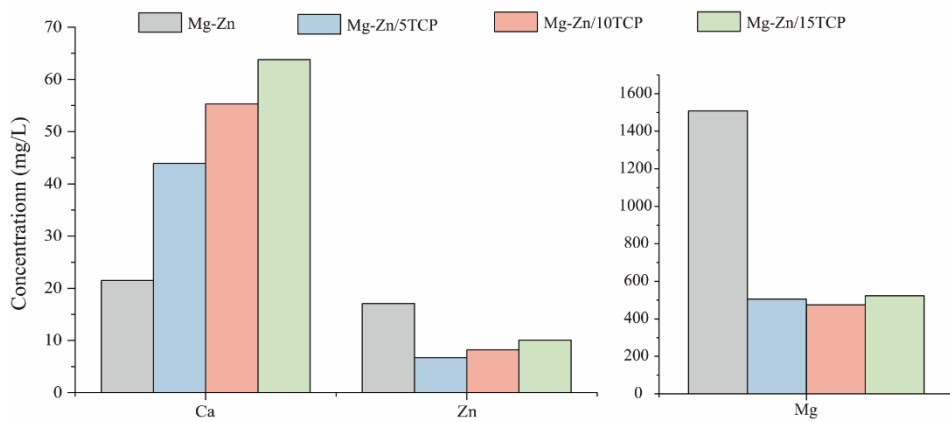


Figure S5.12 The Ca, Zn and Mg concentrations in the culture medium after 3 d of immersion.

Toughness of the Mg-Zn/TCP scaffolds

Method:

In general, toughness can be indicated by the energy absorption in quasi-static compression test [1]. The energy absorption ($U(\varepsilon)$, J cm^{-3}) is the energy per unit volume absorbed by a material under mechanical stress, and it is calculated as the area under the compressive stress-strain ($\sigma - \varepsilon$) curve:

$$U(\varepsilon) = \int_0^{\varepsilon} \sigma(\varepsilon) d\varepsilon$$

where $\sigma(\text{MPa})$ and ε are the engineering stress and strain, respectively.

The toughness (U_T , J cm^{-3}) is the energy absorption up to the point of fracture, $F(\varepsilon_T, \sigma_T)$.

Results:

Based on the obtained stress-strain curves of the Mg-Zn/TCP scaffolds, the toughness values were calculated to be $4.2 \pm 0.4 \text{ J cm}^{-3}$ for Mg-Zn/5TCP, $4.2 \pm 0.2 \text{ J cm}^{-3}$ for Mg-Zn/10TCP and $1.7 \pm 0.6 \text{ J cm}^{-3}$ for Mg-Zn/15TCP. Mg-Zn/15TCP showed the lowest toughness due to significantly increased Mg-bioceramic interface and agglomeration of β -TCP particles in the matrix.

Table S5.1 Comparisons between the relative densities of the fabricated Mg-Zn/TCP composite scaffolds in this study and those of the Mg-based composites in other studies.

Materials	Technique	Relative density	Reference
Mg-Zn/(2.5-10 wt%)HA	Selected laser melting	95.5%-97.7%	[2]
ZK60/5 wt% bioglass	Laser powder bed fusion	97.1%	[3]
ZK60/5 wt% bioglass	Laser powder bed fusion	86.7%-97.6%	[4]
Mg-20 vol% bredigite	Powder metallurgy	96.6%-98.7%	[5]
Mg-6Zn/10 wt% β -TCP	Powder metallurgy	97.6%	[6]
ZK61/(5-15wt%) β -TCP	Spark plasma sintering	86.3%-95.6%	[7]
ZK60/(4-12 wt%) β -TCP	Laser rapid solidification	88.5-97.6%	[8]
Mg-Zn/5 wt% β -TCP	Ink extrusion-based AM	99.9%	this study
Mg-Zn/10 wt% β -TCP	Ink extrusion-based AM	99.7%	this study
Mg-Zn/15 wt% β -TCP	Ink extrusion-based AM	93.1%	this study

References

- [1] A. A. Chernousov, B. Y. B. Chan, Optimizing in-situ nitridation in piled aluminum flakes for novel closed cell composites with high fracture stress and toughness, *Mater. Des.* 150 (2018) 113-123.
- [2] C. J. Shuai, Y. Z. Zhou, Y. W. Yang, P. Feng, L. Liu, C. X. He, M. C. Zhao, S. Yang, C. D. Gao, P. Wu, Biodegradation resistance and bioactivity of hydroxyapatite enhanced Mg-Zn composites via selective laser melting, *Materials*. 10 (2017) 307-319.
- [3] Y. Yang, C. Lu, L. Shen, Z. Zhao, S. Peng, C. Shuai, In-situ deposition of apatite layer to protect Mg-based composite fabricated via laser additive manufacturing, *J. Magnes. Alloy.* (2021), in press.
- [4] Y. Yang, C. Lu, S. Peng, L. Shen, D. Wang, F. Qi, C. Shuai, Laser additive manufacturing of Mg-based composite with improved degradation behavior, *Virtual Phys. Prototy.* 15 (2020) 278-293.
- [5] S. Naddafdezfuli, J. C. Brouwer, J. M. C. Mol, F. C. T. Van Der Helm, J. Zhou, Biodegradation and mechanical behavior of an advanced bioceramic-containing Mg matrix composite synthesized through in-situ solid-state oxidation, *J. Mech. Behav. Biomed. Mater.* 80 (2018) 209-221.
- [6] Y. Yan, Y. Kang, D. Li, K. Yu, T. Xiao, Y. Deng, H. Dai, Y. Dai, H. Xiong, H. Fang, Improvement of the mechanical properties and corrosion resistance of biodegradable β -Ca₃(PO₄)₂/Mg-Zn composites prepared by powder metallurgy: the adding β -Ca₃(PO₄)₂, hot extrusion and aging treatment, *Mater. Sci. Eng. C-Mater. Biol. Appl.* 74 (2017) 582-596.
- [7] Z. Cui, Y. Zhang, Y. Cheng, D. Gong, W. Wang, Microstructure, mechanical, corrosion properties and cytotoxicity of beta-calcium polyphosphate reinforced ZK61 magnesium alloy composite by spark plasma sintering, *Mater. Sci. Eng. C-Mater. Biol. Appl.* 99 (2019) 1035-1047.
- [8] Y. Deng, Y. Yang, C. Gao, P. Feng, W. Guo, C. He, J. Chen, C. Shuai, Mechanism for corrosion protection of β -TCP reinforced ZK60 via laser rapid solidification, *Int. J. Bioprinting.* 4 (2018) 124.

6

General conclusions, discussion, and recommendations

6.1. General conclusions

In this thesis work, we, for the first time, successfully employed extrusion-based 3D printing techniques to fabricate biodegradable porous Mg and Mg-based scaffolds for application in orthopedics. We started with the optimization of the formulated binder system, the printing process, and the subsequent liquid-phase sintering process for the AM of Mg and Mg-based scaffolds. On this basis, a series of Mg and Mg-based porous scaffolds, including Mg alloy and Mg matrix composite scaffolds were successfully fabricated. Then, we conducted comprehensive studies on the microstructure, geometrical characteristics, *in vitro* biodegradation behavior, mechanical properties, and the *in vitro* biodegradation and the responses of preosteoblast MC3T3-E1 cells to the fabricated scaffolds to evaluate the ability of the fabricated scaffolds to satisfy the requirements of ideal bone-substituting biomaterials. By modifying the alloy composition and adding bioceramic components, the properties of the Mg scaffolds required were significantly improved as compared to those of the pure Mg specimens. The fabricated Mg-matrix composite scaffolds were shown to be the most promising materials to be further developed for bone substitution. Surface modification could also contribute to bringing the fabricated Mg scaffolds closer to meeting the requirements. Therefore, with proper material design and surface modification, the Mg-based scaffolds fabricated using extrusion-based 3D printing technique constitute a new category of porous Mg-based biomaterials that hold great promise for application as bone substitutes. The main findings of the thesis work are summarized below:

1. With the choice of a formulated binder system and the adoption of a liquid-phase sintering strategy, extrusion-based 3D printing can be used to fabricate biodegradable porous Mg-based materials with fully interconnected and hierarchical pore structures.
2. The microstructure of the ink extrusion-based 3D printed Mg is featured by fully equiaxed grains. Introducing the alloying element Zn and a bioceramic (β -TCP) into Mg had great effects on the microstructure of the specimens, resulting in the generation of the second phase (MgZn_2) and reaction phases ($\text{Ca}_2\text{Mg}_6\text{Zn}_3$ and $\text{Ca}_4\text{P}_2\text{O}$), respectively.
3. Alloying and compositing can decrease the biodegradation rate of the 3D printed Mg scaffolds to a great extent. As compared with the pure Mg scaffolds, the biodegradation rate of the Mg-Zn scaffolds was decreased by 81%. With the addition of 5 wt% β -TCP micro-particles into the Mg-Zn scaffolds, the biodegradation rate decreased further, reaching the range of the ideal biodegradation rates suggested for bone substitutes. However, the corrosion resistance of the Mg-Zn/ β -TCP scaffolds deteriorated when compositing with more than 10 wt% β -TCP.

4. Alloying and compositing can enhance the mechanical properties of the ink extrusion-based 3D printed Mg scaffolds. The mechanical properties of the Mg-based scaffolds (porosity = 50%) fall into the range of the reported values of the trabecular bone, even after 4 weeks of *in vitro* biodegradation. As compared with the pure Mg scaffolds, both the yield strength and elastic modulus of the Mg-Zn alloy scaffolds increase significantly and are about three times as high as those of the pure Mg scaffolds. With β -TCP micro-particles added to the Mg-Zn scaffolds, the yield strength and elastic modulus increase further.

5. The Mg-Zn scaffolds exhibit moderate toxicity when cultured directly with preosteoblasts. After compositing with β -TCP micro-particles, the scaffolds exhibit improved *in vitro* biocompatibility and indirect osteogenic ability.

6. Multi-functional coatings applied to the Mg scaffolds can also decrease their biodegradation rate and improve their biocompatibility. The MgF_2 interlayer can evenly cover the surfaces of the scaffold struts with micropores at the periphery and those in the center, which contributes to decreasing the biodegradation rate of the scaffolds. The CaP coating as the outer layer provides a preferable surface for cell adhesion.

6.2. General discussion

Here, we reflect on the work performed within this thesis with respect to both main research questions identified in Chapter 1:

Question 1: “Can we use ink extrusion-based 3D printing techniques to manufacture biodegradable Mg-based scaffolds with geometrically-ordered and fully interconnected porous structure successfully?”

Indeed, we successfully developed the ink extrusion-based 3D printing technique to fabricate biodegradable pure Mg, Mg-Zn alloy and Mg-based composite scaffolds with a geometrically ordered and fully interconnected pore structure. In Chapter 2, we demonstrate the feasibility of using this technique to fabricate the Mg scaffolds. This involves the development of a suitably formulated binder system, the definition of an applicable printability window, and the adoption of a liquid-phase sintering strategy.

Question 2: “Can we fabricate porous Mg-based scaffolds with the desired properties for potential use as bone substitutes?”

In Chapters 3-5, we describe in detail the characteristics of the fabricated pure Mg, Mg-Zn alloy, and Mg-Zn-based composite scaffolds in terms of their biodegradation behavior, mechanical properties, and *in vitro* biodegradation behavior, as well as their compatibility with preosteoblasts. Comparing the three strategies applied in this thesis to

improve the performance of the Mg scaffolds, namely, alloying, compositing, and surface modification, the Mg-Zn/ β -TCP scaffolds with an appropriate β -TCP addition stand out as the most promising material to be developed further as bone substitutes. However, further research to assess osteogenesis *in vitro* and *in vivo* needs to be performed to confirm the potential to promote bone formation.

The main findings with respect to material processing, the performance of the Mg-based scaffold materials, and their functionality are highlighted and discussed below:

6.2.1. Material processing

The biodegradable porous Mg-based scaffolds presented in this thesis have precisely controlled geometries of the designed structure, suggesting that extrusion-based 3D printing can, indeed, be used as an alternative to PBF to fabricate biodegradable Mg-based materials. The whole manufacturing process avoids the use of laser or other thermal energy sources, which eliminates the safety concerns and the risk of the oxidation of Mg powder particles that has been commonly encountered during PBF processes. Moreover, extrusion-based 3D printing can work with multiple materials by simply mixing different components within a suitable binder to form a printable ink, which enables the fabrication of tailor-made Mg-based materials with multiple advanced functionalities as demonstrated in Chapter 5. The successful development of ink extrusion-based 3D printing to fabricate Mg-based materials is expected to contribute to the further development of AM Mg-based materials and to open up a new route for the fabrication of porous multi-materials for potential use in biomedicine as well as in other fields.

6.2.1.1. 3D Printing

For the ink extrusion-based 3D printing of a Mg-based porous structure, developing a suitable binder formulation is an exceptionally challenging step (Chapter 2). That is because there are limited choices regarding the binder components to avoid interactions and to ensure proper rheological behavior and sinterability. When printing multi-materials or composite materials, understanding the chemistry of additional components and ensuring homogenous distributions of these components in the ink feedstock, are both essential for selecting a proper binder system (Chapters 4 and 5). In addition to the chemistry of the binder, its rheological properties must be considered. Any change in the percentage of the loaded powder, powder particle size, or ink components can affect the rheological properties of the Mg powder containing ink. The ink formulation may subsequently need to be (fine-)tuned, based on rheological evaluations and the printability of the ink.

6.2.1.2. Post processing

During the post-AM debinding and sintering, an inert atmosphere is crucial for protecting the printed Mg scaffolds with large surface area from oxidation. During debinding, an appropriate gas flow rate is of great importance to carry the pyrolysis products (*i.e.*, decomposed binder) away from the scaffold surfaces. Post-AM sintering is a specially challenging step for the fabrication of Mg scaffolds because the inherent oxide layer on the Mg powder particles tend to retard atom diffusion, Mg has a low melting point, and a solid-liquid two phase region is absent in the phase diagram. In this thesis work, we explored a pressure-less sintering strategy (*i.e.*, liquid-phase sintering) for the sintering of the Mg scaffolds and achieved neck formation between Mg powder particles (Chapter 2). In the case of Mg-based alloys and Mg alloy-based composites, a sintering temperature range can be defined by calculating the liquid fraction using the thermodynamic equilibrium. The sintering scheme can be optimized according to the density and fidelity of scaffold struts (Chapters 4 and 5). This sintering strategy can be readily extended to any other Mg alloys or Mg alloy-based composite scaffolds printed using extrusion-based 3D printing techniques or any other techniques that need post-AM processing, such as binder jetting. The shrinkage occurring during liquid-phase sintering should be considered at the stage of geometrical design prior to 3D printing. When fabricating Mg-based composite scaffolds, the wettability between the liquid Mg phase and the added components should be well understood, as it greatly influences the sinterability of the scaffolds (Chapter 5).

By choosing a proper liquid-phase sintering condition and ensuring the wettability between the material components, high levels of densification of extrusion-based 3D printed scaffolds can be achieved (up to 99.9%, Chapter 5). Such high levels of densification are ordinarily only possible with PBF, in which the high power of laser results in full melting [1, 2]. Achieving such high levels of densification is of great significance for the development of 3D printed Mg-based scaffolds, as the high power of laser can be fully avoided, thereby resolving most safety issue. Moreover, using this technique, the densification of struts can be controlled and adjusted through the generation of different fractions of liquid Mg. Therefore, combined with the designed macropores, a hierarchical porous structure can be obtained (Chapters 2, 4 and 5).

Regarding the microstructure of the printed Mg parts, unlike the columnar grain structure typically formed during the PBF processes, the microstructure of Mg-based scaffolds made with ink extrusion-based 3D printing features fully equiaxed grains, which is beneficial in terms of a broad range of properties [3]. Nevertheless, the grain size of extrusion-based 3D printed Mg is generally larger than that of PBF Mg, due to the rapid solidification and cooling involved in the latter 3D printing process [4, 5].

6.2.1.3. Limitations

The liquid-phase sintering strategy adopted here is only applicable to pre-alloyed powders as the starting materials (e.g., the pre-alloyed Mg-Zn powder used in Chapters 4 and 5), but not mixed elemental powders. Considering the limited availability of pre-alloyed Mg powders with compositions suitable for implant applications, the fabrication of *in-situ* alloyed scaffolds is of great interest. While ink extrusion-based 3D printing provides a straightforward way for extruding multi-material-containing inks (e.g., the inks containing Mg powder and Zn powder) to create green bodies, pressure-free sintering of such green bodies is quite challenging especially when the difference in the melting temperature between Mg and the alloying element is large. A new sintering strategy is yet to be developed for sintering *in situ*-alloyed scaffolds. Nano-sized elemental powders and longer sintering time may be helpful for effective sintering to realize alloying during sintering.

The main limitation of ink extrusion-based 3D printing for the manufacturing of Mg-based materials lies in its printing resolution, which is strongly dependent on the nozzle size and powder particle sizes. In addition, it is not always possible to use this technique to print structures with large overhangs or high aspect ratios, as the right combination of rheological properties, solidification kinetics of the inks, and the printing parameters may not be easily achievable.

6.2.1.4. Surface modification

Regarding the surface modification applied to Mg scaffolds, ensuring consistent quality of coatings throughout the porous structure is essential for the overall properties of the resulting materials especially their biodegradation behavior. The coating located around the periphery and at the center of the scaffolds as well as strut surfaces with open micropores must be individually examined. Considering the geometric complexities of the surfaces in a porous structure, a coating method that allows the coating agent to flow into the macro-porous structure and micropores in the struts and results in uniform coverage of the strut surfaces is preferred. The HF conversion method used in Chapter 3 allowed for homogeneous coating of the porous Mg structure, while the hydrothermal deposition method failed to coat the struts at the center of the scaffolds with a HA layer due to the limited diffusivity of the CaP compounds in the solution to flow through the macropores into the scaffold center [6]. Geometrical design can be a useful tool to facilitate the flow of the coating material and, thus, to achieve homogeneous coating, for instance, by designing functionally graded porous structures with larger macropores around the periphery of the specimens and finer pores in the interior.

6.2.2. Performance of the scaffolds

A biodegradable bone implant should provide sufficient mechanical support for 12 - 24 weeks while being completely absorbed within 1-2 years, depending on the natural duration of bone healing at different implantation sites [7, 8]. The degradation rate is expected to be 0.2 - 0.5 mm/y for an ideal bone implant [9]. Mg generally degrades too fast. Recent research efforts have been directed towards decreasing the degradation rate of Mg, mainly through alloying, compositing, and surface modification. In this thesis, all these three strategies were successfully employed and proven to be effective in decreasing the degradation rate of ink extrusion-based 3D printed Mg scaffolds to different extents (Chapters 3, 4 and 5). While the MgF₂ and HA coatings could effectively protect the pure Mg scaffolds from corroding in the simulated body fluid, accelerated corrosion would occur when the coatings broke down or became penetrated through (Chapter 3). Through compositing with a bioceramic, the Mg-Zn/5 wt% β -TCP composite scaffolds possessed the lowest degradation rate among all the scaffolds that were manufactured by ink extrusion-based 3D printing, reaching the desired range biodegradation rates (*i.e.*, 0.2 - 0.5 mm/y) (Chapter 5).

Figure 6.1a compares the biodegradation rate between the Mg-based materials fabricated using ink extrusion-based 3D printing in this thesis and those with similar compositions fabricated using other AM techniques (*e.g.*, laser powder bed fusion (L-PBF) and binder jetting [1, 4, 5, 10, 11]) and conventional fabrication techniques [11-16]. The degradation rates of the Mg scaffolds (except the pure Mg scaffolds) manufactured by ink extrusion-based 3D printing with a high porosity (around 50%) and a geometrically ordered structure are similar to or even lower than those of bulk or near-bulk materials fabricated by casting/extrusion and powder metallurgy. While L-PBF AM can be used to print Mg alloys and their composites, most of the studies are limited to bulk Mg without any geometrically ordered designs, except for two studies on WE43 scaffolds with porosities of 64% [4] and 75% [17]. The latter study did not provide the data about the corrosion rates of the fabricated WE43 scaffolds. Therefore, it is not included in Figure 6.1a. Most L-PBF-fabricated Mg, even with a solid structure, showed quite high degradation rates.

Degradation rate is directly related to the biological behavior of the scaffolds. Among all the fabricated Mg scaffolds, the Mg-Zn/bioceramic composite scaffolds exhibited the best biocompatibility (Chapter 5). The addition of β -TCP particles to the scaffolds helped with the formation of an appetite layer on the strut surfaces, which facilitated cell attachment and proliferation. In the studies presented in this dissertation, the osteogenic ability of the scaffolds was evaluated by performing ALP tests and Alizarin red S staining. Gene expression analysis should be performed to better understand the osteogenic mechanism of the fabricated scaffolds. In addition, the fluorescence microscope was employed for observing cells residing on the scaffolds, which has a limitation in focusing

on multi-layer cells or for observing cells inside pores. Confocal microscopes can be used for better observation of the cells growing on/inside the scaffolds.

The mechanical properties of the ink extrusion-based 3D printed scaffolds fall into the range of those of Mg foams with similar porosities prepared using other AM techniques [4, 17] and conventional powder metallurgy methods [18-24], although high power laser or compaction step is employed in these techniques, in contrast to the pressureless sintering performed in this study (Figure 6.1b). The mechanical properties of the fabricated Mg scaffolds fall in the range of those of the trabecular bone [25] but are far away from those of the cortical bone (*i.e.*, yield strength = 90 - 120 MPa [26]).

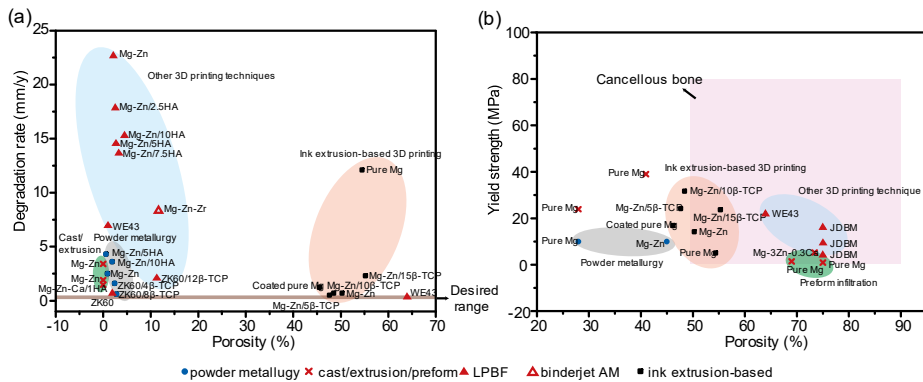


Figure 6.1 Comparisons between the biodegradation rate (a) and yield strength (b) of the Mg-based materials fabricated through ink extrusion-based 3D printing in this thesis and the values reported in the literature for other fabrication techniques.

Both materials and the geometrical design of fabricated scaffolds play important roles in determining the mechanical properties of the fabricated scaffolds. Therefore, new strategies need to be developed for both material and structure design, as suggested below.

6.2.2.1. Materials perspective

From the materials perspective, the choices of alloying element(s) and proper reinforcing particles are of critical importance for adjusting the degradation behavior, mechanical properties, and the biological responses of relevant cells to Mg-based scaffolds. The properties of Mg-based scaffolds are strongly influenced by the porosity, second phase particles (and their distribution), the dispersion of reinforcing particles, the wettability and interface bonding between the Mg matrix and the reinforcing phase, and the characteristics of the formed corrosion products (*e.g.*, protective ability, stability and the biocompatibility) (Chapters 3, 4 and 5).

In the studies presented in this thesis, we only focused on pure Mg and Mg-Zn scaffolds. In the future, other promising Mg alloys or composites that have been chosen and studied for bone implants in the bulk form can also be fabricated by using the ink extrusion-based 3D printing technique used here. WE43, for example, has already been used for commercial biodegradable coronary stents and bone screws [27], and L-PBF-fabricated WE43 scaffolds with a porosity of 64% showed a degradation rate within the desired range for bone substitutes [4]. Some rare earth elements that are effective in enhancing the corrosion resistance and mechanical properties of Mg, such as Y and Nd, may be added to Mg [28]. Heat treatment can be introduced for the dissolution of second-phase particles into the Mg matrix to decrease the galvanic corrosion of the Mg scaffolds [29]. Moreover, hot isostatic pressing (HIP) can be used to improve the density of scaffold struts, thereby decreasing the surface area exposed to the electrolyte and enhancing the strength of the material. Other types of reinforcements, such as bioglass that have good wettability with Mg and help form a protective corrosion product layer on Mg can be also added into the scaffolds to further improve their mechanical properties, biocompatibility, and osteogenic ability [30, 31]. Multi-reinforcing particles, such as bioceramic and graphene-based particles, can be also added into the fabricated material to achieve multiple functionalities for bone substitution.

6.2.2.2. Structure design perspective

From a design perspective, we found that the stable corrosion products could be entrapped inside the designed macropores between the struts in a geometrically ordered Mg structure, thereby improving the integrity of the scaffolds and retarding the progress of the corrosion process (Chapters 4 and 5). However, this caused crevice corrosion at the center of the scaffolds, resulting in different local corrosion rates between the center and periphery of the scaffolds (Chapter 4 and 5). Functionally graded structures can be designed to reach a consistent degradation rate throughout the whole scaffold. For example, the periphery of Mg scaffolds can be designed to have a lower porosity or smaller macropore size, while the central part of the scaffolds can be designed to have a higher porosity or larger macropore size. Such a design can also benefit the bone ingrowth due to sufficient mass transport to the center of the scaffolds.

It has been reported that pore geometry can greatly influence the mechanical properties of extrusion-based 3D printed materials [32]. While a low porosity will benefit the mechanical properties, it may not be favorable for cells due to low permeability. Pore shape and pore size can affect the adhesion and proliferation of cells [33]. In this thesis, we chose only one design with a rectangle pore shape (*i.e.*, a lay-down pattern with angles of 0 and 90°) and the same pore size and porosity for all the fabricated Mg-based scaffolds. More systematic studies regarding the geometrical design are needed to understand the relationships between the pore geometry and mechanical, biodegradation, and biological

properties of Mg-based scaffolds, paving the way for the optimization of the geometrical design. In addition to lattice structures, biomimetic structures can also be designed and achieved by ink extrusion-based 3D printing. Examples include tree-like [34] structures and lotus root-like struts [35] that can be used for different biomedical functions.

The role of the surface curvature of the designed scaffolds should be also considered, because that would allow for investigating the cell-geometry interactions [36]. To better mimic the native bone tissue, mechanical and biochemical gradients are also critically important for an ideal bone implant [37], which can be achieved by combining multi-materials and/or designing different pore shapes, pore sizes, or porosities in one scaffold [38].

6.2.3. Functionality

Treating critical-size bony defects may, in many cases, require the assistance of multi-functional porous bone implants. In addition to bone regeneration, additional functions (*e.g.*, eliminating residual cancer cells to suppress tumor recurrence) may also be necessary for bone defect healing after bone tumor resection surgery [39]. By taking advantage of the flexibility in designing and tuning the ink components in extrusion-based 3D printing technique, implants with additional functionalities can be obtained by adding various agents into the inks. Adding magnetothermal or photothermal agents, such as Fe-doped ceramic [40] or graphene-based materials [41], into Mg scaffolds can endow the scaffolds with magnetothermal or photothermal functionalities for tumor therapy while maintaining their osteogenic ability.

Bacterial infections pose a significant risk during bone transplantation surgeries. Because of severe infection, many bone grafting surgeries fail, although bone grafts exhibit conspicuous successes *in vitro* [42]. It is, therefore, important to fabricate scaffolds with antibacterial functions, while maintaining the bone regeneration ability of biomaterials. Adding an appropriate amount of silver (Ag) or copper (Cu) particles into Mg scaffolds is expected to induce antibacterial and bone-forming activities [43].

With proper agents selected as ink components, Mg-based scaffolds can be designed and developed to possess multi-functionalities for overcoming most challenges in bone substitution. For evaluating the multi-functions of the scaffolds, a cell co-culture system can be developed and employed. For example, mesenchymal stem cells-Schwann cells co-culture system can be used to study osteogenic and neurogenic differentiation [34], while mesenchymal stem cells-endothelial cells co-culture system can be employed to simultaneously investigate osteogenesis and angiogenesis [44].

6.3. Recommendations

While this thesis work has made contributions to the development of 3D printed porous Mg implants, it is only the first step to demonstrate the great potential of ink extrusion-based 3D printing for the fabrication of porous Mg scaffolds for biomedical applications. Some aspects of the Mg scaffolds that have been fabricated using this technique are yet to be understood. In this subsection, some general and specific recommendations for future work are presented.

1. The ink extrusion-based 3D printing technique for Mg-based scaffold fabrication needs to be further investigated to obtain biomaterials with the whole range of the desired properties, including degradable and mechanical properties.

2. For the optimization of extrusion-based 3D printing of Mg-based materials, the relationship between the structural design and resulting properties should be systematically investigated and established using both experimental and numerical approaches.

3. Taking advantage of extrusion-based 3D printing, various functions, such as cancer treatment cancer and infection prevention, can be achieved by simply incorporating various functional agents into the scaffolds. The potential of manufacturing multi-functional Mg scaffolds can then be fully explored.

4. *In vitro* evaluation of Mg scaffolds cannot fully reflect the complex *in vivo* situation. *In vivo* animal tests are, therefore, needed to evaluate the performance of extrusion-based 3D printed Mg-based scaffolds in actual service situations.

Some specific recommendations are also made:

Fabrication

1. The influences of powder loading percentage, powder particle size, debinding, and sintering parameters on the densification of extrusion-based 3D printed Mg should be systematically investigated for further optimization of the resultant properties.

2. Post-processing, such as heat treatment and HIP, can be applied to optimize the microstructure and density of Mg scaffold struts, thereby improving their properties.

3. The approach to apply coatings on the fabricated Mg scaffolds should be optimized to ensure their consistent quality throughout the porous Mg structure.

4. If micro/nano-sized particles are added into the material composition of Mg scaffolds, the balance between particle dispersion and printability should be optimized to accommodate higher volume percentages of reinforcing particles (*e.g.*, by adding a surfactant to the ink formulation).

5. *In-situ* alloying during sintering in combination with ink extrusion-based 3D printing should be explored to obtain Mg alloy scaffolds with tailor-made compositions.

Properties

1. Non-toxic alloying elements other than Zn or reinforcing particles should be considered to be incorporated into Mg scaffolds to further decrease their biodegradation rate, increase their mechanical strength, and improve their biological responses.

2. The degradation behavior of Mg-based scaffolds should be evaluated in more sophisticated *in vitro* environments with atmosphere control and dynamic flow of the simulated body fluid, which will be closer to the *in vivo* condition.

3. The osteogenic behavior of the fabricated Mg-based scaffolds needs to be systematically studied *in vitro*. In addition to the tests performed in this thesis, more tests (*e.g.*, real-time polymerase chain reaction (PCR)) need to be designed and performed to understand the impact of Mg scaffolds on the expression levels of osteogenesis-related genes.

4. The fatigue behavior is of critical importance for load-bearing orthopedic implants that experience millions of loading cycles per year. The fatigue behavior of the fabricated Mg-based scaffolds needs to be investigated in the simulated body fluid.

Design

1. Topological design, such as functionally graded porous structures, can be used as a tool to tune the degradation behavior and mechanical properties of Mg-based scaffolds.

2. With multi-nozzles, the scaffolds can be designed and printed to have compositional gradients to achieve mechanical or degradation gradients within one structure.

3. Other biomimetic designs, such as tree-like structures and lotus root-like struts, can be adopted for the design of Mg scaffolds to improve their osteogenesis and angiogenesis behaviors

Functionalities

1. In addition to osteogenesis, the fabricated Mg-based scaffolds should be equipped with more functionalities for the treatment of bone-related diseases, for example, by adding photothermally responsive agents for tumor therapy or by adding anti-bacterial agents to treat implant-associated infections.

2. In addition to implants, ink extrusion-based 3D printed biodegradable Mg materials can be developed to function as biosensors (*e.g.*, piezoelectric biosensors) by incorporating piezoelectric ceramic into their material composition.

References

- [1] C. J. Shuai, Y. Z. Zhou, Y. W. Yang, P. Feng, L. Liu, C. X. He, M. C. Zhao, S. Yang, C. D. Gao, P. Wu, Biodegradation resistance and bioactivity of hydroxyapatite enhanced Mg-Zn composites via selective laser melting, *Materials*. 10 (2017) 307-319.
- [2] Y. Yang, C. Lu, L. Shen, Z. Zhao, S. Peng, C. Shuai, In-situ deposition of apatite layer to protect Mg-based composite fabricated via laser additive manufacturing, *J. Magnes. Alloy*. (2021), in press.
- [3] D. Zhang, D. Qiu, M. A. Gibson, Y. Zheng, H. L. Fraser, D. H. Stjohn, M. A. Easton, Additive manufacturing of ultrafine-grained high-strength titanium alloys, *Nature*. 576 (2019) 91-95.
- [4] Y. Li, J. Zhou, P. Pavanram, M. A. Leeflang, L. I. Fockaert, B. Pouran, N. Tumer, K. U. Schroder, J. M. C. Mol, H. Weinans, H. Jahr, A. A. Zadpoor, Additively manufactured biodegradable porous magnesium, *Acta Biomater*. 67 (2018) 378-392.
- [5] C. L. Wu, W. Zai, H. C. Man, Additive manufacturing of ZK60 magnesium alloy by selective laser melting: Parameter optimization, microstructure and biodegradability, *Mater. Today Commun*. 26 (2021) 101922.
- [6] J. Dong, N. Tümer, N.E. Putra, J. Zhu, Y. Li, M.A. Leeflang, P. Taheri, L.E. Fratila-Apachitei, J.M.C. Mol, A.A. Zadpoor, J. Zhou, Extrusion-based 3D printed magnesium scaffolds with multifunctional MgF₂ and MgF₂-CaP coatings, *Biomater. Sci*. 9 (2021) 7159-7182.
- [7] Y. F. Zheng, X. N. Gu, F. Witte, Biodegradable metals, *Mater. Sci. Eng. R Rep*. 77 (2014) 1-34.
- [8] J. Venezuela, M. S. Dargusch, The influence of alloying and fabrication techniques on the mechanical properties, biodegradability and biocompatibility of zinc: A comprehensive review, *Acta Biomater*. 87 (2019) 1-40.
- [9] C. Gao, M. Yao, S. Li, P. Feng, S. Peng, C. Shuai, Highly biodegradable and bioactive Fe-Pd-bredigite biocomposites prepared by selective laser melting, *J. Adv. Res*. 20 (2019) 91-104.
- [10] K. X. Kuah, D. J. Blackwood, W. K. Ong, M. Salehi, H. L. Seet, M. L. S. Nai, S. Wijesinghe, Analysis of the corrosion performance of binder jet additive manufactured magnesium alloys for biomedical applications, *J. Magnes. Alloy*. 10 (2021) 1296-1310.
- [11] Y. Deng, Y. Yang, C. Gao, P. Feng, W. Guo, C. He, J. Chen, C. Shuai, Mechanism for corrosion protection of beta-TCP reinforced ZK60 via laser rapid solidification, *Int. J. Bioprinting*. 4 (2018) 124.
- [12] J. Yu, J. Wang, Q. Li, J. Shang, J. Cao, X. Sun, Effect of Zn on microstructures and properties of Mg-Zn alloys prepared by powder metallurgy method, *Rare Metal Mat. Eng*. 45 (2016) 2757-2762.
- [13] M. E. Moussa, H. I. Mohamed, M. A. Waly, G. S. Al-Ganainy, A. B. Ahmed, M. S. Talaat, Comparison study of Sn and Bi addition on microstructure and bio-degradation rate of as-cast Mg-4wt% Zn alloy without and with Ca-P coating, *J. Alloys Compd*. 792 (2019) 1239-1247.
- [14] W. Jiang, J. Wang, W. Zhao, Q. Liu, D. Jiang, S. Guo, Effect of Sn addition on the mechanical properties and bio-corrosion behavior of cytocompatible Mg-4Zn based alloys, *J. Magnes. Alloy*. 7 (2019) 15-26.

- [15] D. Liu, G. Xu, S. S. Jamali, Y. Zhao, M. Chen, T. Jurak, Fabrication of biodegradable HA/Mg-Zn-Ca composites and the impact of heterogeneous microstructure on mechanical properties, in vitro degradation and cytocompatibility, *Bioelectrochemistry*. 129 (2019) 106-115.
- [16] Z. Cui, W. Li, L. Cheng, D. Gong, W. Cheng, W. Wang, Effect of nano-HA content on the mechanical properties, degradation and biocompatible behavior of Mg-Zn/HA composite prepared by spark plasma sintering, *Mater. Charact.* 151 (2019) 620-631.
- [17] Y. Wang, P. Fu, N. Wang, L. Peng, B. Kang, H. Zeng, G. Yuan, W. Ding, Challenges and solutions for the additive manufacturing of biodegradable magnesium implants, *Engineering*. 6 (2020) 1267-1275.
- [18] X. N. Gu, W. R. Zhou, Y. F. Zheng, Y. Liu, Y. X. Li, Degradation and cytotoxicity of lotus-type porous pure magnesium as potential tissue engineering scaffold material, *Mater. Lett.* 64 (2010) 1871-1874.
- [19] J. Capek, D. Vojtech, Effect of sintering conditions on the microstructural and mechanical characteristics of porous magnesium materials prepared by powder metallurgy, *Mater. Sci. Eng. C-Mater. Biol. Appl.* 35 (2014) 21-28.
- [20] G. Jia, Y. Hou, C. Chen, J. Niu, H. Zhang, H. Huang, M. Xiong, G. Yuan, Precise fabrication of open porous Mg scaffolds using NaCl templates: Relationship between space holder particles, pore characteristics and mechanical behavior, *Mater. Des.* 140 (2018) 106-113.
- [21] Q. Dong, Y. Li, H. Jiang, X. Zhou, H. Liu, M. Lu, C. Chu, F. Xue, J. Bai, 3D-cubic interconnected porous Mg-based scaffolds for bone repair, *J. Magnes. Alloy.* 9 (2021) 1329-1338.
- [22] N. T. Kirkland, I. Kolbeinsson, T. Woodfield, G. J. Dias, M. P. Staiger, Synthesis and properties of topologically ordered porous magnesium, *Mater. Sci. Eng. B-Adv. Funct. Solid-State Mater.* 176 (2011) 1666-1672.
- [23] Z. S. Seyedraoufi, S. Mirdamadi, Synthesis, microstructure and mechanical properties of porous Mg-Zn scaffolds, *J. Mech. Behav. Biomed. Mater.* 21 (2013) 1-8.
- [24] Y. Yan, Y. Kang, D. Li, K. Yu, T. Xiao, Y. Deng, H. Dai, Y. Dai, H. Xiong, H. Fang, Improvement of the mechanical properties and corrosion resistance of biodegradable β -Ca₃(PO₄)₂/Mg-Zn composites prepared by powder metallurgy: the adding β -Ca₃(PO₄)₂, hot extrusion and aging treatment, *Mater. Sci. Eng. C-Mater. Biol. Appl.* 74 (2017) 582-596.
- [25] M. H. Kang, H. Lee, T. S. Jang, Y. J. Seong, H. E. Kim, Y. H. Koh, J. Song, H. D. Jung, Biomimetic porous Mg with tunable mechanical properties and biodegradation rates for bone regeneration, *Acta Biomater.* 84 (2019) 453-467.
- [26] S. C. Cifuentes, E. Frutos, J. L. González-Carrasco, M. Muñoz, M. Multigner, J. Chao, R. Benavente, M. Lieblisch, Novel PLLA/magnesium composite for orthopedic applications: A proof of concept, *Mater. Lett.* 74 (2012) 239-242.
- [27] Biodegradable magnesium-based screw clinically equivalent to titanium screw in hallux valgus surgery: short term results of the first prospective, randomized, controlled clinical pilot study, *Biomed. Eng. Online*. 12 (2013) 62.
- [28] H. Li, P. Wang, G. Lin, J. Huang, The role of rare earth elements in biodegradable metals: A review, *Acta Biomater.* 129 (2021) 33-42.

- [29] J. Chang, X. Guo, P. Fu, L. Peng, W. Ding, Effect of heat treatment on corrosion and electrochemical behaviour of Mg–3Nd–0.2Zn–0.4Zr (wt.%) alloy, *Electrochimica Acta*. 52 (2007) 3160-3167.
- [30] V. K. Bommala, M. G. Krishna, C. T. Rao, Magnesium matrix composites for biomedical applications: A review, *J. Magnes. Alloy*. 7 (2019) 72-79.
- [31] H. Zhou, B. Liang, H. Jiang, Z. Deng, K. Yu, Magnesium-based biomaterials as emerging agents for bone repair and regeneration: from mechanism to application, *J. Magnes. Alloy*. 9 (2021) 779-804.
- [32] S. I. Roohani-Esfahani, P. Newman, H. Zreiqat, Design and fabrication of 3D printed scaffolds with a mechanical strength comparable to cortical bone to repair large bone defects, *Sci. Rep.* 6 (2016) 19468.
- [33] A. A. Zadpoor, Additively manufactured porous metallic biomaterials, *J. Mater. Chem. B*. 7 (2019) 4088-4117.
- [34] M. Zhang, C. Qin, Y. Wang, X. Hu, J. Ma, H. Zhuang, J. Xue, L. Wan, J. Chang, W. Zou, C. Wu, 3D printing of tree-like scaffolds for innervated bone regeneration, *Addit. Manuf.* 54 (2022).
- [35] C. Feng, W. J. Zhang, C. J. Deng, G. L. Li, J. Chang, Z. Y. Zhang, X. Q. Jiang, C. T. Wu, 3D printing of lotus root-like biomimetic materials for cell delivery and tissue regeneration, *Adv. Sci.* 4 (2017) 1700401.
- [36] S. J. P. Callens, R. J. C. Uyttendaele, L. E. Fratila-Apachitei, A. A. Zadpoor, Substrate curvature as a cue to guide spatiotemporal cell and tissue organization, *Biomaterials*. 232 (2020) 119739.
- [37] L. G. Bracaglia, B. T. Smith, E. Watson, N. Arumugasaamy, A. G. Mikos, J. P. Fisher, 3D printing for the design and fabrication of polymer-based gradient scaffolds, *Acta Biomater.* 56 (2017) 3-13.
- [38] B. Zhang, L. Guo, H. Chen, Y. Ventikos, R. J. Narayan, J. Huang, Finite element evaluations of the mechanical properties of polycaprolactone/hydroxyapatite scaffolds by direct ink writing: Effects of pore geometry, *J. Mech. Behav. Biomed. Mater.* 104 (2020) 103665.
- [39] J. Long, W. Zhang, Y. Chen, B. Teng, B. Liu, H. Li, Z. Yao, D. Wang, L. Li, X. F. Yu, L. Qin, Y. Lai, Multifunctional magnesium incorporated scaffolds by 3D-Printing for comprehensive postsurgical management of osteosarcoma, *Biomaterials*. 275 (2021) 120950.
- [40] H. Zhuang, R. Lin, Y. Liu, M. Zhang, D. Zhai, Z. Huan, C. Wu, Three-dimensional-printed bioceramic scaffolds with osteogenic activity for simultaneous photo/magnetothermal therapy of bone tumors, *ACS Biomater. Sci. Eng.* 5 (2019) 6725-6734.
- [41] H. Ma, C. Jiang, D. Zhai, Y. Luo, Y. Chen, F. Lv, Z. Yi, Y. Deng, J. Wang, J. Chang, C. Wu, A bifunctional biomaterial with photothermal effect for tumor therapy and bone regeneration, *Adv. Funct. Mater.* 26 (2016) 1197-1208.
- [42] Y. L. Zhang, D. Zhai, M. C. Xu, Q. Q. Yao, H. Y. Zhu, J. Chang, C. T. Wu, 3D-printed bioceramic scaffolds with antibacterial and osteogenic activity, *Biofabrication*. 9 (2017) 025037.
- [43] E. Zhang, X. Zhao, J. Hu, R. Wang, S. Fu, G. Qin, Antibacterial metals and alloys for potential biomedical implants, *Bioact. Mater.* 6 (2021) 2569-2612.

[44] H. Qi, K. Wang, M. Li, Y. Zhang, K. Dong, S. Heise, A. R. Boccaccini, T. Lu, Co-culture of BMSCs and HUVECs with simvastatin-loaded gelatin nanosphere/chitosan coating on Mg alloy for osteogenic differentiation and vasculogenesis, *Int. J. Biol. Macromol.* 193 (2021) 2021-2028.

CURRICULUM VITAE

Sept. 19, 1993

Born in Liaoning province, China

Education/Work experience

Sept. 2018 - current

Ph.D. at Dept. of Biomechanical Engineering
Delft University of Technology, Delft, The Netherlands

Sept. 2015 - June 2018

M.Sc. at Institute of Metal Research,
Chinese Academy of Sciences, Shenyang, China

Sept. 2011 - June 2015

B.Sc. at Dept. of Materials Science and Engineering,
Shenyang University of Technology, Shenyang, China

LIST OF PUBLICATIONS

1. **J. Dong**, P. Lin, N.E. Putra, N. Tümer, M.A. Leeftang, Z. Huan, L.E. Fratila-Apachitei, J. Chang, A.A. Zadpoor, J. Zhou, Extrusion-based 3D printed Mg-Zn/bioceramic scaffolds, *Acta Biomaterialia*, 151 (2022), 628-646.
2. **J. Dong**, N. Tümer, N.E. Putra, J. Zhu, Y. Li, M.A. Leeftang, P. Taheri, L.E. Fratila-Apachitei, J.M.C.Mol, A.A. Zadpoor, J. Zhou, Extrusion-based 3D printed magnesium scaffolds with multifunctional MgF₂ and MgF₂-CaP coatings, *Biomaterials Science*, 9 (2021), 7159-7182.
3. **J. Dong**, N. Tümer, M.A. Leeftang, P. Taheri, L.E. Fratila-Apachitei, J.M.C. Mol, A.A. Zadpoor, J. Zhou, Extrusion-based 3D printed Mg-Zn scaffolds, *Journal of magnesium and alloys*, 10 (2021), 2491-2509.
4. Y. Li, W. Li, FSL Bobbert, **J. Dong**, Corrosion fatigue behavior of additively manufactured biodegradable porous zinc, *Acta Biomaterialia*, 106 (2020), 439-449.
5. **J. Dong**, Y. Li, P. Lin, M.A. Leeftang, S.van. Asperen, K. Yu, N. Tümer, B. Norder, A.A. Zadpoor, J. Zhou, Solvent-cast 3D printing of magnesium scaffolds, *Acta Biomaterialia*, 114 (2020) 497-514.
6. W. Wang, K.C. Nune, L. Tan, N. Zhang, **J. Dong**, J. Yan, R.D.K. Misra, K. Yang, Bone regeneration of hollow tubular magnesium-strontium scaffolds in critical-size segmental defects: Effect of surface coatings, *Materials Science and Engineering: C*, 100 (2019), 297-307.
7. J. Chen, **J. Dong**, H. Fu, H. Zhang, L. Tan, D. Zhao, K. Yang, In vitro and in vivo studies on the biodegradable behaviour and bone response of Mg₆₉Zn₂₇Ca₄ metal glass for treatment of bone defect, *Journal of Materials Science & Technology*, 35 (2019), 2254-2262.
8. **J. Dong**, L. Tan, Y. Ren, K. Yang, Effect of microstructure on corrosion behaviour of Mg-Sr alloy in simulated biological fluid, *Acta Metallurgica Sinica (English Letters)*, 32 (2018), 305-320.
9. **J. Dong**, L. Tan, J. Yang, Y. Wang, J. Chen, W. Wang, D. Zhao, K. Yang, In vitro and in vivo studies on degradation and bone response of Mg-Sr alloy for treatment of bone defect, *Materials Technology*, 33 (2018), 387-397.

10. L. Tan, **J. Dong**, J. Chen, K. Yang, Development of magnesium alloys for biomedical applications: structure, process to property relationship, *Materials Technology*, 33 (2018), 235-243.
11. **J. Dong**, L. Tan, K. Yang, Research of biodegradable Mg-based metals as bone graft substitutes, *Acta Metallurgica Sinica*, 53(2017), 1197-1206.
12. H. Zhao, Y. Ren, **J. Dong**, X. Fan, K. Yang, Effect of cold deformation on the friction–Wear property of a biomedical nickel-free high-nitrogen stainless steel, *Acta Metallurgica Sinica (English Letters)*, 29 (2016), 217-227.
13. Y. Ren, J. li, **J. Dong**, K. Yang, A zinc alloy for MR-compatible applications, China Patent, ZL201510542175.X.

ACKNOWLEDGEMENTS

In September 2018, I came to the Netherlands and started my PhD journey. It has been a challenging, yet memorable journey in my whole life. Without the support from my colleagues, friends and family members, I would not have enjoyed my PhD journey as much as I have. Here, I would like to express my sincere gratitude to all the people who have accompanied me during this four-year journey.

First, I would like to thank my promoters, Prof. Amir Zadpoor and Dr. Jie Zhou, for their great supervision and support. Amir, when I talked about some ideas with you, you were always open to them and supported me as much as possible. Jie, thank you very much for your support each step of the journey. Whenever I encountered problem or obstacles, you always helped me solve them as soon as possible. You motivated and inspired me a lot when I struggled with my research, especially during the first year of my PhD. I have benefited a lot from your guidance and from the discussions that always let me see a clear path forward.

I would like to thank Dr. Lidy E. Fratila-Apachitei for her substantial support with regard to the cell culture tests in this thesis and for her very constructive comments on the biological part of my manuscripts.

I also would like to thank Prof. Arjan Mol for providing me with great convenience to perform the electrochemical tests in the corrosion lab. I really appreciate the comments from him and from Dr. Peyman Taheri on the electrochemical studies in this thesis.

I am also grateful for the help and support from Prof. Jiang Chang and Dr. Zhiguang Huan who kindly recommended and provided the bioceramic powder for part of the work in this dissertation and commented on my manuscript. Zhiguang, thank you for always patiently answering my questions regarding bioceramics.

I would like to express my great appreciation to my former supervisor, Prof. Ke Yang, who has been supporting me ever since my master studies. He always encourages me whenever I have struggles either in research or in life.

I would like to express my appreciation to Mr. Sander Leeftang who has provided all the technical support and training needed on this project. I also would like to thank Maria and Michelle for their help in cell culture tests, Mr. Sander van Asperen for metallographic analysis and coating preparation, Mrs. Agnieszka Kooijman for electrochemical tests, Mr. Michel van den Brink for ICP analysis and powder size distribution analysis, Mr. Arjan Thijssen for micro-CT analysis, Mr. Richard Huizenga and Mr. Ruud Hendrikx for XRD

analysis, Mr. Kees Kwakernaak for SEM training, Mr. Ben Norder for TGA analysis, and Mr. Bart Boshuizen for XPS analysis.

I would like to thank the China Scholarship Council (CSC) for financial support.

I am grateful for the help from Peng Lin at the Department of Engineering Structures for viscosity tests and Jianing at the Department of Materials Science and Engineering for coating preparation. I also would like to thank Kui Yu who always gives me great support and encouragement. I have been so lucky that I have met these nice people on campus and become their friends. Whenever I need help, each of them gives me selfless help in research or in daily life.

I would like to thank all my past and present colleagues in the group. Nazli, thanks for your help in CT data processing. Yageng, you helped me a lot in becoming familiar with the group and with the Netherlands at the beginning of my PhD. I am also grateful for your help in coating preparation and for teaching me how to structure a good paper when I wrote my first paper.

Helda, we have shared the office for 3.5 years. I have enjoyed all the nice conversations (sometimes in a mixture of Persian, Chinese and Dutch) and delicious Persian dinners with you and Amirhossein. Vahid (and Saeede), you are a nice friend. Thank you for giving me a lot of useful advice on my life and career, and I really enjoy the time when we gathered together. Kirsten, you are an amazing friend. It is always a pleasure to be with you. I have enjoyed all the chats with you in my/your office, during lunch, during walking and at parties. You and Niko have brought me a lot of words that I would never have known how to say in English. Niko, most of my PhD time, we have worked together and always shared our progress with each other. Jinlai, we have become very good friends since you joined the group. Thank you and Jinyang for bringing me a lot of joy and giving me a lot of favors. Keyu, we have communicated a lot since you joined our group and wish you a successful and happy PhD journey.

I have enjoyed all the nice conversations about the Iranian culture and Persian language, with my Iranian colleagues, Mahdiyeh, Mohammad, Khashayar, Mahya, Vahid, Ebrahim and Helda. Khashayar, thank you and (Sara) for all the nice conversations and delicious Persian food. I would never forget the joyful atmosphere when we danced together.

The party and drinks (always only two for me, orange juice and Tequila) time I spent with Pier, Niko, Katerina, Judith, Monika, Kirsten, Pedro, Jelle, Merle, Chunfeng and Mauricio made my PhD life much colorful. I have enjoyed all the casual chats, jokes and talking about different cultures with these people.

I also would like to thank my other colleagues, past and present, Mohammad, Sebastien, Ingmar, Pedro, Hongshan, Julian, Juan, Shahram, Jette, Dirk, Yujiang, Lorenzo, Zhen, Anneke, Eline, Jonathan, and my students Francesco, Ziyi and Sohrab.

I would like to extend my gratitude to other friends of mine who have accompanied and supported me during my PhD journey. Yan, we have been very close friends for 10 years. We have supported and motivated each other during master and PhD studies. We always discuss the research, life, love and future, even over a distance of more than 5000 km. Zhaoying (Dingding), I am very happy for having you as my close friend and my (previous) neighbor. I still feel happy and warm when I recall those times when we cycled together, enjoyed ice cream after work, and enjoyed sunny weekends with nice food. Most importantly, without you, I would not have met my love. Jiayi, you are a great and generous friend. I enjoyed the amazing trips and views in Iceland with you during that Christmas. Tian (Tao), Tian (Wang), Meng and Xiaogeng, thank you for accompanying me during my first year of PhD, letting me not feel lonely when I just arrived at the Netherlands. Hui (and families), I am grateful that I met you and Wei (Prof. Xu) in Delft. Thank you for helping me solve different kinds of difficulties in my daily life. Huanan and Tianchi, thank you for all your nice and useful advice on my life.

Very special thanks to my husband, Hesheng, for his love and constant support. Hesheng, I feel so lucky that I met you, my Mr. Right, in that summer. You have been my warm partner, smart adviser, and spiritual soulmate. You make me feel the warmth of home when I feel homesick, and lift my spirits when I feel down. Your love is the greatest gift that I have ever been given during my PhD journey.

最后，我要由衷的感谢我的家人，特别是最爱的妈妈。感谢您在我成长过程中无微不至的关心和对我做任何决定的无条件支持，没有您的教育和支持，我不会有能力和勇气走到今天。在我读博的 4 年里，为了能更多的陪伴我和照顾我，您不顾及长时间的飞行，倒时差的难受以及语言不通，独自一人千里迢迢飞来荷兰 3 次。我很怀念那段我们挤在 20 平米小屋里一起吃饭，聊天，看电视的日子，那段时光让我感受到母女之外，我们也能成为无话不谈的朋友。我很开心和幸福能够成为您的女儿。

同时，我也要感谢我的其他亲人们，大姨，二姨和三姨以及我的哥哥姐姐，在我读博期间对我的关心和问候，以及对我妈妈的照顾。特别是我的大姨，您对我的爱体现在每一条问候和祝福的微信上，我永远也不会忘记您对我说的那些真挚的话。我也要感谢我的婆婆，感谢您对待女儿一样对我的关心和挂念，和我所有决定的支持，您对我的爱让我觉得倍加温暖。